

AFRL-SN-HS-TR-2004-031

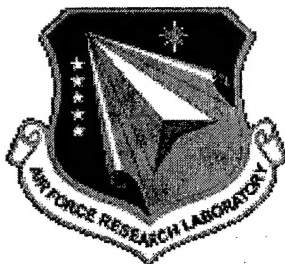
**THE GEODESIC SPHERE PHASED ARRAY ANTENNA FOR SATELLITE
COMMUNICATION AND AIR/SPACE SURVEILLANCE – PART 1**

**Dr. Boris Tomasic
Mr. John Turtle
AFRL/SNHA
80 Scott Drive
Hanscom AFB MA 01731-2909**

**Dr. Shiang Liu
The Aerospace Corporation
P.O. Box 92957
Los Angeles CA 90009**

IN-HOUSE Technical Report: 1 Jan 2000 – 1 Jan 2004

APPROVED FOR PUBLIC RELEASE DISTRIBUTION UNLIMITED



**AIR FORCE RESEARCH LABORATORY
Sensors Directorate
Electromagnetics Technology Division
80 Scott Drive
Hanscom AFB MA 01731-2909**

20040910 066

TECHNICAL REPORT

Title: *The Geodesic Sphere Phased Array Antenna for Satellite Communication and Air/Space Surveillance - Part I*

Unlimited, Statement A

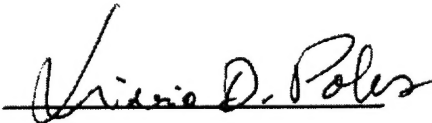
NOTICE

USING GOVERNMENT DRAWINGS, SPECIFICATIONS, OR OTHER DATA INCLUDED IN THIS DOCUMENT FOR ANY PURPOSE OTHER THAN GOVERNMENT PROCUREMENT DOES NOT IN ANY WAY OBLIGATE THE US GOVERNMENT. THE FACT THAT THE GOVERNMENT FORMULATED OR SUPPLIED THE DRAWINGS, SPECIFICATIONS, OR OTHER DATA DOES NOT LICENSE THE HOLDER OR ANY OTHER PERSON OR CORPORATION; OR CONVEY ANY RIGHTS OR PERMISSION TO MANUFACTURE, USE, OR SELL ANY PATENTED INVENTION THAT MAY RELATE TO THEM.

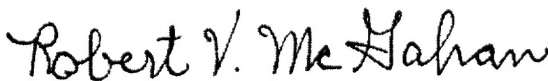
THIS TECHNICAL REPORT HAS BEEN REVIEWED AND IS APPROVED FOR PUBLICATION.



Boris Tomasic, AFRL/SNHA



Livio D. Poles
Chief, Antenna Technology Branch
AFRL/SNHA 80 Scott Drive
Hanscom AFB MA 01731-3010



Dr. Robert V. McGahan, Technical Advisor
Electromagnetics Technology Division
Air Force Research Laboratory - AFRL/SNH
80 Scott Drive, Hanscom AFB MA 01731-2909

REPORT DOCUMENTATION PAGE			Form Approved OMB No. 0704-0188	
Public reporting burden for this collection of information is estimated to average 1 hour per response, including the time for reviewing instructions, searching existing data sources, gathering and maintaining the data needed, and completing and reviewing this collection of information. Send comments regarding this burden estimate or any other aspect of this collection of information, including suggestions for reducing this burden to Department of Defense, Washington Headquarters Services, Directorate for Information Operations and Reports (0704-0188), 1215 Jefferson Davis Highway, Suite 1204, Arlington, VA 22202-4302. Respondents should be aware that notwithstanding any other provision of law, no person shall be subject to any penalty for failing to comply with a collection of information if it does not display a currently valid OMB control number. PLEASE DO NOT RETURN YOUR FORM TO THE ABOVE ADDRESS.				
1. REPORT DATE (DD-MM-YYYY) 24-04-2003		In-House Report		3. DATES COVERED (From - To) 1 Jan 2000 - 1 Jan 2004
4. TITLE AND SUBTITLE The Geodesic Sphere Phased Array Antenna for Satellite Communication and Air/Space Surveillance - Part I			5a. CONTRACT NUMBER	
			5b. GRANT NUMBER	
			5c. PROGRAM ELEMENT NUMBER 62204F	
6. AUTHOR(S) Boris Tomasic, John Turtle and Shiang Liu			5d. PROJECT NUMBER 4916	
			5e. TASK NUMBER HA	
			5f. WORK UNIT NUMBER 01	
7. PERFORMING ORGANIZATION NAME(S) AND ADDRESS(ES) B. Tomasic and J. Turtle AFRL/SNHA 80 Scott Drive Hanscom AFB, MA 01731-2909			S. Liu The Aerospace Corporation P.O. Box 92957 Los Angeles, CA 90009	
8. PERFORMING ORGANIZATION REPORT AFRL/SNHA 80 Scott Drive Hanscom AFB, MA 01731-2909				
9. SPONSORING / MONITORING AGENCY NAME(S) AND ADDRESS(ES) Electromagnetics Technology Division Sensors Directorate Air Force Research Laboratory 80 Scott Drive Hanscom AFB MA 01731-2909			10. SPONSOR/MONITOR'S ACRONYM(S) AFRL/SNHA	
			11. SPONSOR/MONITOR'S REPORT NUMBER(S)	
12. DISTRIBUTION / AVAILABILITY STATEMENT DISTRIBUTION UNLIMITED. APPROVED FOR PUBLIC RELEASE. OTHER REQUESTS FOR THIS DOCUMENT SHALL BE REFERRED TO DTIC-OMI, 8725, JOHN J. KINGMAN RD. FT BELVOIR, VA 22060-6218				
13. SUPPLEMENTARY NOTES				
14. ABSTRACT This report presents a highly desirable, but up to this day not practical, spherical phased array antenna design that provides hemispherical coverage. Consequently it can be used for simultaneous communication and control with multiple satellites and air/space surveillance in the entire sky. The proposed spherical phased array antenna structure consists of a number of near-equilateral triangular planar subarrays arranged in an icosahedral geodesic dome configuration. This novel architecture design, "the geodesic dome phased array antenna" preserves all the advantages of spherical phased array antennas while fabrication is based on its well developed, easily manufactured, and affordable planar array technology.				
15. SUBJECT TERMS Spherical phased array antennas, geodesic dome, satellite communication, space and air surveillance				
16. SECURITY CLASSIFICATION OF: Unclassified			17. LIMITATION OF ABSTRACT SAR	18. NUMBER OF PAGES 176
a. REPORT Unclassified	b. ABSTRACT Unclassified	c. THIS PAGE Unclassified	19a. NAME OF RESPONSIBLE PERSON Dr. Boris Tomasic	
			19b. TELEPHONE NUMBER (include area code) 781-377-2055	

Abstract

This paper presents a highly desirable, but up to this day not practical, spherical phased array antenna design that provides hemispherical coverage. Consequently it can be used for simultaneous communication and control with multiple satellites and air/space surveillance in the entire sky. The proposed spherical phased array antenna structure consists of a number of near-equilateral triangular planar subarrays arranged in an icosahedral geodesic dome configuration. This novel architecture design, "the geodesic dome phased array antenna" preserves all the advantages of spherical phased array antennas while fabrication is based on its well developed, easily manufactured, and affordable planar array technology.

⁰This work was supported by Air Force Research Laboratory under Project 6.2 and Aerospace Corporation under AFSPC/SMC contract FA8802-04-C-0001.

B. Tomasic is with Air Force Research Laboratory, Sensors Directorate, Electromagnetics Technology Division, Antenna Technology Branch, 80 Scott Road, Hanscom AFB, MA 01731.

J. Turtle is with Air Force Research Laboratory, Sensors Directorate, Electromagnetics Technology Division, Antenna Technology Branch, 80 Scott Road, Hanscom AFB, MA 01731.

S. Liu is with The Aerospace Corporation, P.O. Box 92957, Los Angeles, CA 90009

Contents

Abstract	iii
Contents	iv
1 Introduction	1
2 Spherical Arrays	4
2.1 Principle of Operation	4
2.2 Why Spherical Arrays?	4
2.3 Comparison with Other Array Architectures	5
2.4 Basic Design Parameters	8
2.4.1 Active Sector	8
2.4.2 Element Field Pattern	9
2.4.3 Element Gain	10
2.4.4 Array Far-Field	10
2.4.5 On-Off Switch	10
2.4.6 Excitation/Beamsteering	11
2.4.7 Array Gain	11
2.4.8 Polarization	13
2.4.9 Instantaneous Bandwidth	17
2.4.10 Mismatch Losses	18
2.5 Numerical Simulation	19
2.5.1 Computer Code	19
2.5.2 Calculated Array Patterns	20
3 Geodesic Dome Phased Array Antenna	48
3.1 Antenna Architecture	48
3.2 Geodesic Dome Structure - Background	50
4 Geodesic Dome Antenna Structure	62
4.1 Global Coordinate System	62
4.1.1 Counting Icosa's	62
4.1.2 Counting Sub-Icosa's	62
4.1.3 Class I, Method 1, $6\sqrt{2}$ Icosahedral Coordinates	62
4.1.4 Class I, Method 1, $6\sqrt{2}$ Chord Lengths	63
4.1.5 Sub-Icosas (Panel) Types	63
4.2 Local Coordinate System	64
4.2.1 Sub-Icosa (panel) in Local Coordinate System	64
4.2.2 Sub-Icosa Base	67
4.3 Reference Coordinate System	68
4.3.1 Sub-Icosa in Reference Coordinates	69
4.3.2 Fitting Equilateral Triangle Into Sub-Icosa Triangle	69

4.3.3	Counting the Array Elements in Reference Coordinate System (x'_{NM}, y'_{NM})	72
4.3.4	Location of the Array Elements in Reference Coordinates	72
4.3.5	Location of the Array Elements in Local Coordinates	73
4.3.6	Location of the Array Elements in Global Coordinates	74
5	Geodesic Dome Array Beamsteering and Radiation Pattern	116
5.1	Element Pattern	116
5.1.1	Element Pattern in Reference Coordinates	116
5.1.2	Element Pattern in Local Coordinates	116
5.1.3	Element Pattern in Global Coordinates	117
5.2	Far-Field	118
5.2.1	On-Off Switch	119
5.2.2	Element Voltage Excitation Coefficients	121
5.3	Array Gain	121
6	Computer Codes	128
6.1	Code 1	128
6.1.1	Input	128
6.1.2	Output	128
6.2	Code 2	129
6.2.1	Input	129
6.2.2	Output	130
Appendix A:	Element Patterns in Source (Local) Coordinates	155
A.1	Far-Field of Two Crossed Dipoles	155
A.2	Approximate Expressions for Array Element Patterns	156
Appendix B:	Spherical Array Analysis	157
B.1	Array Model	157
B.2	Global and Local Coordinate Systems	157
B.3	Coordinate Transformation Relations	158
B.4	Element Patterns in Local Coordinates	159
B.5	Element Patterns in Global Coordinates	159
B.6	An Example	160
Appendix C:	Maximum Gain Theorem for Conformal Arrays	165
C.1	The Theorem	165
C.2	Proof	166
Bibliography		171

Chapter 1

Introduction

Within the next decade there will be a dramatic increase in the number of commercial and military satellite constellations providing world-wide telecommunication, environmental, navigation, and surveillance services [1]. The satellites, in LEO, MEO, and GEO orbits, will need a number of ground stations to serve as gateways for payload message/data routing and/or as control centers for satellite tracking, telemetry, and command (TT&C) operations. A typical ground station will require one or more large high performance antennas with hemispherical coverage for communicating with LEO and MEO satellites during the brief interval from their rise above the horizon until they set below the horizon.

Three main types of antennas can be used for satellite ground stations: mechanically steered reflector antennas, electronically steerable arrays (ESA), and microwave lens antennas. Although mechanically steered reflectors are most widely used for satellite communications, ESA are the optimum choice for this application because they can provide multi-function, multiple simultaneous beams, have high reliability with graceful degradation, require low maintenance, and have low life cycle cost. With rapidly emerging Microwave Monolithic Integrated Circuits (MMIC) and multilayer beamforming and beam steering technologies, large ESA are viable candidates for ground station antennas, and by using commercial off-the-shelf components they could be also affordable.

Because hemispherical coverage is required for ground station antennas, only a few potential array architectures are suitable [33]. These can be classified into three major groups: (1) multi-face planar arrays, (2) curved surface or conformal arrays [12, 13, 14], and (3) lens arrays/antennas. In [2, 3, 4] we present design trade-offs for these array architectures. We have shown that a spherical array is the optimal choice for ground-based satellite control antennas in terms of performance and cost. It is a natural array geometry that provides scan independent hemispherical coverage with a uniform gain pattern. We show that a spherical array requires about 20% fewer elements than a comparable multi-planar phased array [3]. It is also shown that spherical arrays exhibit significantly larger instantaneous bandwidths and have lower polarization and mismatch losses than other types of array architectures. However, fabrication and assembly including implementing multi-beamforming networks, is much more difficult for curved array surfaces than for planar arrays and consequently spherical arrays are very expensive. This is the main reason that up to this date large spherical phased arrays have not been implemented in practice.

A novel architecture design, "The Geodesic Dome Phased Array Antenna" that preserves

all the advantages of spherical phased arrays for hemispherical coverage while maintaining the ease of fabrication afforded by well-developed planar array technology was invented and proposed in [3] by Boris Tomasic. The invention, therefore provides desired spherical phased array performance using affordable planar array technology. This invention is also described in [3], TT&C Phased Array Antenna Survey, Attachment 3, Section 4, which was sent out to many government agencies and DoD contractors, and cited in SBIR Topic AF99-244. The geodesic dome array was also analyzed and described in [4]. In this design, the spherical array is constructed with many near-equitriangular planar subarrays arranged in an icosahedral geodesic dome configuration. This "faceted" dome antenna provides a communication function for SATOPS and a radar function for air/space surveillance with full hemispherical coverage while exhibiting the following advantages over the conventional pyramid-like and conformal array structures:

1. Keeping the architecture locally planar and globally spherical allows the array to be constructed using flat (panel) subarrays which are assembled to form the hemispherical dome structure. This is technically and economically viable because the design avoids the fabrication complexity associated with conformal (curved) arrays since the subarray fabrication is based on well-developed, easily manufacturable planar array technology. Moreover, the geodesic dome is a practically realizable structure with well-known mechanical design and fabrication techniques [8, 9];

2. The Geodesic Dome antenna preserves all the advantages of spherical phased arrays [5, 6, 7] such as: uniform beams over a hemisphere; high gain, high instantaneous bandwidth, low mismatch and polarization losses, and low life cycle cost. Above all, it requires about 20% fewer radiating elements and transmit/receive (T/R) modules than other array configurations.

We have designed a geodesic dome phased array antenna that meets the basic requirements for Space-Ground Link System (SGLS) and Unified S-band (USB) satellite operation, [19] to [26]. The antenna, about 10 m in diameter, will support two independent Tx beams and two independent Rx beams. It consists of 675 flat panel/facets (subdivision frequency $\nu = 6$). One of the panel subarrays was fabricated and tested by AFRL/SNH. Each panel consists of a multi-layer beamforming network (BFN), 78 wide-band circularly polarized (CP) radiating elements and T/R modules, a beamsteering antenna controller/computer (ACC), and software that will integrate the geodesic dome antenna with control computers in the existing US Air Force Satellite Control Network. The controller, in addition to performing the present dish antenna functions, will be capable of exploiting all "nice" features of a phased array antenna such as multiple, simultaneous, independent beams, fast beam switching/steering, adaptive pattern control, etc., for improved SATOPS.

The report is organized in two parts. In part I, we present an extensive theoretical analysis of spherical arrays, describe the geodesic dome structure and present the analysis for excitation, beamsteering and far-field patterns of the geodesic dome array antenna. In part II we describe the system aspects of the full dome array for SGLS and USB for satellite TT&C, and radar for air and space surveillance. We focus on design, development and demonstration of the basic building block, a flat panel subarray, for SGLS and USB TT&C satellite operations (SATOPS). Specifically, we describe design, development and fabrication of the radiating elements, multi-layer beamforming network, T/R modules and beamsteering controller/computer. Theoretical and measured subarray patterns for transmit and receive

beams will be also given.

Part I of this report consists of 6 Chapters. In Chapter 2, we describe conventional spherical arrays and their principle of operation. Basic design parameters such as element field pattern, array far-field, active sector, On-Off switch, excitation and beamsteering are discussed in great detail. Also we derive expressions for polarization loss, instantaneous bandwidth and mismatch losses in spherical arrays. In short, this chapter treats all relevant design aspects of the spherical arrays in multi-dimensional trade space, that will serve as a basis in the analysis of the geodesic dome antenna. In Chapter 3, we give background on geodesic dome antenna. The geodesic dome structure is treated in Chapter 4. The array beamsteering and radiation patterns were computed in Chapter 5, while in Chapter 6 we describe the computer codes and present some representative numerical data.

Chapter 2

Spherical Arrays

2.1 Principle of Operation

The general configuration for spherical arrays consists of a large number of radiating elements placed on a spherical surface, as schematically shown in Figure 2.1. The basic theoretical and experimental aspects of spherical phased arrays are given in [5, 6, 7]. For a given beam direction only a sector of the array elements is excited while all other elements are turned off. The active sector is the area encompassed by a cone with the cone angle of $2\alpha_{max}$ degrees, and with the cone axis coinciding with the antenna beam direction. The active part (sector) is defined as that part of the sphere that is turned on to receive (or transmit) electromagnetic energy. Beam scanning is accomplished by activating different sectors of the spherical surface, Figure 2.1. All array elements in the active sector are phased to produce an equi-phase front normal to the desired beam axis. Thus each array element must have an RF On/Off switch and a phase shifter. The radiating elements in the active sector are assumed to have symmetry in the plane perpendicular to the axis of the cone (antenna beam), and consequently a spherical array can be used to cover the hemisphere with practically identical beams. Thus in contrast to other array configurations, which suffer from beam degradation as the beam is steered over wide angular regions, spherical arrays can provide uniform patterns and gain over the entire sky. In order to provide full hemispherical coverage using a 120 degree active sector, the size of the spherical array must be 93% of the full sphere.

2.2 Why Spherical Array?

First question becomes when and why do we use spherical array. To answer this question we present a simple comparison between a planar and spherical arrays in terms of required area, which translates into number of array elements and ultimately the array cost. We begin by considering a planar array of circular aperture with radius a and area $A_p = \pi a^2$ as shown in Figure 2.2. We assume that the array is required to scan in a cone with angle α_{max} measured from z -axis. The peak array gain at θ_0 is

$$G_p(\theta_0) = 4\pi \frac{A_p}{\lambda^2} \cos \theta_0 \quad (2.1)$$

Similarly, in reference to Figure 2.3, the gain of the spherical array is

$$G(\alpha_{max}) = 4\pi \frac{A'(\alpha_{max})}{\lambda^2} \quad (2.2)$$

where the projected area of active sector is

$$A'(\alpha_{max}) = \pi R^2 \sin^2 \alpha_{max} \quad (2.3)$$

By equating (2.1) and (2.2), the radius of the spherical array must be

$$R = \frac{a}{\sin \alpha_{max}} \sqrt{\cos \theta_0}. \quad (2.4)$$

The area of the spherical array normalized to its planar counterpart is therefore

$$\frac{A(\alpha_{max})}{A_p} = 2 \frac{1 - \cos(\theta_0 + \alpha_{max})}{\sin^2 \alpha_{max}} \cos \theta_0. \quad (2.5)$$

Figure 2.4 plots the equation (2.5) for $\alpha_{max} = 60^\circ$ and 90° from where we can see that for scan angles up to roughly 75 degrees the planar array area is smaller than the spherical, and consequently of lower cost. For scan angles greater than 75 degrees the spherical array area becomes smaller than the planar and therefore is a better solution for this application. It is worth mentioning that in this simple comparison only $\cos \theta$ scan loss is taken into account. In practice, because of additional mismatch and polarization losses, planar arrays are not used to scan beyond 60 to 70 degrees from broadside. Thus, spherical arrays complement planar arrays in the sense that for small scan angles ($\leq 60^\circ$) planar arrays are more efficient than spherical while for scan angles roughly greater than 60° spherical arrays are more efficient than planar arrays.

2.3 Comparison with Other Array Architectures

As shown above a single planar array cannot be used for wide scan angles. In this case we must resort to the alternative array configurations such as conformal arrays or geometries consisting of two or more planar faces. Three faces are the minimum required for hemisphere coverage. Each face scans throughout a portion of the sector, thereby minimizing the maximum required scan angle and limiting the degradation in performance caused by scanning the beam. In general, as shown in [27] and below, the greater the number of faces, the better the overall antenna performance. In [27, 28, 32, 34, 35] it is also shown that by increasing the number of faces, less elements are needed for a given array performance. (In the limiting case a multi face planar array geometry converges into spherical array which gives the best performance with minimum number of array elements.)

In the remaining part of this section we show that in the limiting case, a multi-face planar array geometry converges into a spherical array which gives the best performance with the minimum number of array elements. For convenience, but with no loss of generality, we consider a simple two-dimensional (circular) array in the x - z plane with n_{max} number of elements as shown in Figure 2.5. We also assume that the elements are uniformly spaced at

$\lambda/2$ distance and are equally excited and phased so as to produce a main beam in z-direction. The element gain which we assume to be the same for all elements is

$$g(\theta) = G_{cell} \cos \theta \quad (2.6)$$

where θ is the field angle counted from the local element normal. In (2.6), the unit cell area gain is

$$G_{cell} = \frac{4\pi A_{cell}}{\lambda^2} \quad (2.7)$$

with A_{cell} being the cell area.

Thus, the circular array peak gain is

$$G_{max} = \sum_{n=1}^{n_{max}} \delta_n g_n(\theta_n - \theta_0) \quad (2.8)$$

where the Kronecker delta is

$$\delta_n = \begin{cases} 1 & \text{if } |\theta_n - \theta_0| < \frac{\pi}{2} \\ 0 & \text{otherwise} \end{cases} \quad (2.9)$$

and θ_0 specifies the beam direction measured from the z-axis. The array gain pattern for the selected case $n_{max} = 96$ and $\theta_0 = 0^\circ$ is shown in Figure 2.6. Figure 2.7 shows the peak gain vs. scan angle θ_0 . As expected, because the array geometry is independent of angle θ , the gain pattern is uniform (independent of θ) and the peak gain is also practically independent of scan angle θ_0 .

A polygon approximation to a circular array is shown in Figure 2.8. There are N_{max} sides with $N = 1, 2, \dots, N_{max}$ being the sector serial number. The total number of array elements on the polygon is the same as on a circle. Now, we compute the peak gain of the polygon-shaped array. The peak gain is no longer constant vs. scan angle θ_0 , but periodically varies between G_{min} and G_{max} to be determined below.

The peak gain of the N_{max} -polygon array is

$$G(\theta_0) = G_{cell} \frac{n_{max}}{N_{max}} 2 \sum_{N=1}^{N_{max}} \delta_N(\alpha) \cos \alpha \quad (2.10)$$

where $\alpha = \theta_N - \theta_0$ and Kronecker delta is

$$\delta_N(\alpha) = \begin{cases} 1 & \text{if } |\alpha| < \frac{\pi}{2} \\ 0 & \text{otherwise} \end{cases} \quad (2.11)$$

We distinguish two cases:

(1) Even-sided polygon with two sub-cases

(1a) Number of sectors given by $N_{max} = 4(m + 1)$, where $m = 0, 1, 2, \dots$ i.e., $N_{max} = 4, 8, 12, 16, 20, \dots$. In this case the maximum peak gain is at $\theta_0 = \pi/N_{max}$ and minimum gain occurs at $\theta = 0$.

(1b) Number of sectors given by $N_{max} = 4m + 6$, where $m = 0, 1, 2, \dots$ which means $N_{max} = 6, 10, 14, 18, 22, \dots$. In this case the maximum and the minimum gain are at $\theta_0 = 0$ and $\theta_0 = \pi/N_{max}$, respectively.

(2) Odd-sided polygon

For an odd sided polygon with number of sides $N_{max} = 3 + 2m$, where $m = 0, 1, 2, \dots$ which is $N_{max} = 3, 5, 7, 9, \dots$, the maximum gain is at $\theta_0 = 0^\circ, \pi/N_{max}$ while the minimum gain is at $\theta_0 = \pi/(2N_{max})$.

In all cases above $G(\theta_0)$ is a periodic function of θ_0 with period $\Delta\theta_N = 2\pi/N_{max}$.

Figure 2.9 shows an equilateral triangular array where only one side (red) is active. The gain patterns for a beam pointing at $\theta_0 = 0^\circ$ and $\theta_0 = 60^\circ$ are shown in Figure 2.10 and Figure 2.11, respectively. Notice that at $\theta_0 = 60^\circ$, the peak gain is maximum (about 20 dB) while at $\theta_0 = 0^\circ$ the peak gain is about 3 dB lower. This is explicitly shown in Figure 2.12, which shows that if one side of the triangle is active at the time the peak gain varies vs. scan angle θ_0 by about 3dB. As the beam scans in θ from 0 to 360 deg it must be handed over from one side to the next side. For single-sided active triangular array the hand-over angles are $\theta_0 = 0^\circ, 120^\circ$ and 240° .

In practice a large variation of the peak gain vs. angle is undesirable because the array size must be determined so as to meet minimum gain specs. Thus, in the triangle case it is better to have one or two (depend on scan angle) active sides as shown in Figure 2.13. In this case, according to (2.10) (case (2)), the peak gain is maximum at $\theta_0 = 0^\circ, 60^\circ$ and minimum at $\theta_0 = 30^\circ$. This is also seen in Figure 2.14 which shows the variation of the peak gain vs. scan angle θ_0 . Notice that the min peak gain is now only 0.6 dB below the maximum value. The array gain pattern for $\theta_0 = 0^\circ$ is shown in Figure 2.15 which is a substantial improvement over single-side active case.

Figure 2.16 shows a square array. From (2.10) (case (1a)) the minimum peak gain is at $\theta_0 = 0^\circ$ while maximum gain is at $\theta_0 = 45^\circ$. Figure 2.17 and Figure 2.18 show array gain pattern at $\theta_0 = 0^\circ$ and peak gain variation vs. θ_0 .

Figure 2.19 to Figure 2.21 show pentagon arrays and respective gain patterns for $\theta_0 = 0^\circ$ and peak gain variation vs. θ_0 . In this case the maximum peak gain is at $\theta_0 = 0^\circ$ and 36° while minimum peak gain occurs at $\theta_0 = 18^\circ$. As one may observe from Figure 2.14, Figure 2.18 and Figure 2.21 as the number of polygon sides increase the peak gain variation vs. θ_0 decreases and the minimum peak gain increases.

Continuing in the same fashion, Figure 2.22 to Figure 2.24 show the hexagon array with corresponding gain pattern for $\theta_0 = 0^\circ$, and peak gain variation as a function of θ_0 . Similarly, Figure 2.25 to Figure 2.27 show the same for a 12-sided polygon while Figure 2.28 to Figure 2.30 show the same for a 24-sided polygon. And, Figure 2.31 to Figure 2.33 show the same for a 48-sided polygon.

In summary we observe that the minimum peak gain of an N_{max} -polygon array increases with N_{max} and the peak gain variation decreases as a function of scan angle θ_0 . This is borne out in Figure 2.34 which shows the minimum and maximum peak gain variation vs. number of polygon sides, N_{max} . It is seen that in the limiting case when a polygon becomes circle ($N_{max} = n_{max}$), the maximum and minimum peak gain curves coincide into the constant gain line of a circular array. At the same time the minimum peak gain of the polygon array reaches the maximum possible value, that of a circular array.

Thus, we conclude that if omni scan coverage is required, the circular array is the optimal geometry, since it offers the best performance in comparison to polygon-type arrays with the same number of radiating elements.

In summary, the spherical array offers the optimal geometry for hemispherical coverage. Beside providing a uniform beam in a hemisphere it also requires minimum number of radiating elements in comparison to alternative array architectures consisting of multiple planar arrays or other conformal arrays.

Below we present a simple analysis and compare a spherical array with a conventional three-face pyramid structure. Figure 2.35 shows the array where each face consist of circular planar arrays of radius a . To cover a hemisphere each individual planar array must scan about 64 degrees from its local normal (broadside).

If area of the single face is

$$A_p = \pi a^2 \quad (2.12)$$

then the total array area is

$$A_\Delta = 3A_p. \quad (2.13)$$

Thus, if we set in (2.5) $A_p = A_\Delta/3$ and for sake of simplicity $\theta_0 = \pi/3$ we get

$$A(\alpha_{max}) = \frac{2}{3}A_\Delta \frac{1 - \cos(\frac{\pi}{3} + \alpha_{max})}{\sin^2 \alpha_{max}} \cos \frac{\pi}{3}. \quad (2.14)$$

We see that if $\alpha_{max} = 90^\circ$ then $A(\alpha_{max}) = 0.62A_\Delta$ and if $\alpha_{max} = 60^\circ$ then $A(\alpha_{max}) = 2/3A_\Delta$. Thus, a spherical array requires about 33% less array elements than the three-face pyramid.

Another candidate array configuration for hemispherical coverage is the Dome antenna [29, 30]. The pros and cons of the dome antenna are discussed in [31].

2.4 Basic Design Parameters

2.4.1 Active Sector

Once we have decided on a spherical array, the question becomes how big is the active sector or what is the optimum value of α_{max} . The array gain is

$$G(\alpha_{max}) = (kR)^2 \sin^2 \alpha_{max} \quad (2.15)$$

with the beamwidth

$$BW = 58^\circ \frac{\pi}{kR \sin \alpha_{max}}. \quad (2.16)$$

For the fixed G/BW , i.e.,

$$kR \sin \alpha_{max} = 58^\circ \pi \frac{G(\alpha_{max})}{BW} = C \quad (2.17)$$

we see that the active area must be

$$A(\alpha_{max}) = \frac{2\pi}{k^2} C^2 f(\alpha_{max}) \quad (2.18)$$

where

$$f(\alpha_{max}) = \frac{1 + \sin \alpha_{max}}{\sin^2 \alpha_{max}}. \quad (2.19)$$

As seen in Figure 2.37 the required active array area is the smallest when $\alpha_{max} = 90^\circ$. For practical reasons α_{max} is usually between 60 and 70 degrees.

2.4.2 Element Field Pattern

The far electric field produced by a single element is originally expressed in a local coordinate system $(r_{nm}, \theta_{nm}, \phi_{nm})$ with the origin at element (nm) as follows

$$\mathbf{e}_{nm}(\mathbf{r}_{nm}; t) = \mathbf{e}_{nm}(\theta_{nm}, \phi_{nm}) \frac{e^{j(\omega t - kr_{nm})}}{r_{nm}} \quad (2.20)$$

where

$$\mathbf{e}_{nm}(\theta_{nm}, \phi_{nm}) = \hat{\theta}_{nm} e_{\theta nm}(\theta_{nm}, \phi_{nm}) + \hat{\phi}_{nm} e_{\phi nm}(\theta_{nm}, \phi_{nm}) e^{j\delta}. \quad (2.21)$$

where $e_{\theta nm}$ and $e_{\phi nm}$ are the complex element pattern factors of the two field components. Basically they represent the field produced by a single element in a match-terminated spherical array environment where δ is the phase difference between the two components of the field. In general, the field is elliptically polarized. For a circularly polarized field $e_{\theta nm} = e_{\phi nm}$ and $\delta = \pm\pi/2$ where the plus sign corresponds to RHCP and the minus sign to LHCP of the outgoing wave.

We consider an elementary case, the rough approximation for the pattern of two CP crossed infinitesimal dipoles, which from Appendix A.4 is

$$\mathbf{e}_{nm}(\theta_{nm}, \phi_{nm}) = E_0 \sqrt{\cos \theta_{nm}} e^{\pm j\phi_{nm}} \frac{1}{\sqrt{2}} (\hat{\theta}_{nm} \pm j\hat{\phi}_{nm}) \quad (2.22)$$

where

$$E_0 = \sqrt{\frac{\zeta_0}{4\pi}} \sqrt{\frac{4\pi A_{cell}}{\lambda^2}}. \quad (2.23)$$

This pattern can be expressed in global coordinates (r, θ, ϕ) using coordinate transformation relation (B.12) as described in Appendix B.6, i.e.,

$$\mathbf{e}_{nm}(\theta, \phi) = -E_0 \sqrt{\cos \theta_{nm}} \frac{1}{\sqrt{2}} (\hat{\theta} \pm j\hat{\phi}) e^{\pm j\nu_{nm}(\theta, \phi)} e^{j\psi_{nm}} e^{\pm j\phi_{nm}} \quad (2.24)$$

where

$$\cos \theta_{nm} = \sin \alpha_n \sin \theta \cos(\phi - \beta_{nm}) + \cos \alpha_n \cos \theta \quad (2.25)$$

$$\cot \phi_{nm} = \frac{\cos \alpha_n \sin \theta \cos(\phi - \beta_{nm}) - \sin \alpha_n \cos \theta}{\sin \theta \sin(\phi - \beta_{nm})} \quad (2.26)$$

$$\psi_{nm} = kR \cos \theta_{nm} = kR [\sin \alpha_n \sin \theta \cos(\phi - \beta_{nm}) + \cos \alpha_n \cos \theta] \quad (2.27)$$

and

$$\tan \nu_{nm}(\theta, \phi) = \frac{\sin \alpha_n \sin(\phi - \beta_{nm})}{\cos \theta \sin \alpha_n \cos(\phi - \beta_{nm}) - \sin \theta \cos \alpha_n}. \quad (2.28)$$

2.4.3 Element Gain

Element gain is defined as

$$g_{nm}(\theta_{nm}, \phi_{nm}) = \frac{\mathbf{e}_{nm}(\mathbf{r}) \cdot \mathbf{e}_{nm}^*(\mathbf{r})}{\zeta_0 P_{0nm}} \quad (2.29)$$

where

$$P_{0nm} = \frac{|c_{nm}|^2}{4\pi r_{nm}^2} \quad (2.30)$$

and $\zeta_0 = 376.7 \Omega$ is the free space impedance. Thus,

$$g_{nm}(\theta_{nm}, \phi_{nm}) = \frac{4\pi}{\zeta_0} |\mathbf{e}_{nm}(\theta_{nm}, \phi_{nm})|^2. \quad (2.31)$$

Specifically, if \mathbf{e}_{nm} above is that of (2.24), we get

$$g_{nm} = G_{cell} \cos \theta_{nm} \quad (2.32)$$

where

$$G_{cell} = \frac{4\pi A_{cell}}{\lambda^2} \quad (2.33)$$

is the unit cell area gain.

2.4.4 Array Far-Field

The expression for the radiation pattern produced by the spherical array is obtained after combining the fields produced by the individual antenna elements at the far field point. Thus,

$$\mathbf{E}(\mathbf{r}; t) = \mathbf{E}(\theta, \phi) \frac{e^{j(\omega t - kr)}}{r} \quad (2.34)$$

where

$$\mathbf{E}(\theta, \phi) = \hat{\theta} E_\theta(\theta, \phi) + \hat{\phi} E_\phi(\theta, \phi) = \sum_{nm} \mathbf{E}_{nm}(\theta, \phi) \quad (2.35)$$

and

$$\mathbf{E}_{nm}(\theta, \phi) = \delta_{nm} c_{nm}(\theta_0, \phi_0) \mathbf{e}_{nm}(\theta, \phi). \quad (2.36)$$

Here, δ_{nm} are on-off switches, \mathbf{e}_{nm} are complex element patterns, and c_{nm} are element voltage excitation coefficients.

2.4.5 On-Off Switch

As already mentioned, δ_{nm} in (2.36), is an On-Off switch. This switch determines which element will be on or off for a particular beam direction. For example, if we define an active array region within cone with axis in (θ_0, ϕ_0) beam direction and with the cone angle α_{max} , then

$$\delta_{nm} = \begin{cases} 1 & \text{if } \gamma_{nm} \leq \alpha_{max} \\ 0 & \text{otherwise} \end{cases} \quad (2.37)$$

where γ_{nm} is the angle between the axis of the cone and the radial line passing thru the element (nm) . Since

$$\cos \gamma_{nm} = \hat{\mathbf{r}} \cdot \boldsymbol{\rho}_{nm} \quad (2.38)$$

where $\boldsymbol{\rho}_{nm}$ is the radial vector specifying the location of the (n, m) th element, see Figure 5.3, we can write

$$\begin{aligned} \cos \gamma_{nm} &= \sin \theta_0 \cos \phi_0 \sin \alpha_n \cos \beta_{nm} \\ &+ \sin \theta_0 \sin \phi_0 \sin \alpha_n \sin \beta_{nm} \\ &+ \cos \theta_0 \cos \alpha_n. \end{aligned} \quad (2.39)$$

2.4.6 Excitation/Beamsteering

The excitation coefficients are

$$c_{nm}(\theta_0, \phi_0) = |c_{nm}(\theta_0, \phi_0)| e^{j\chi_{nm}(\theta_0, \phi_0)} \quad (2.40)$$

where $|c_{nm}|$ depends on the desired aperture illumination function. The array elements are phased so that the pattern produced by the array has a maximum along the (θ_0, ϕ_0) direction. This means that $\chi_{nm}(\theta_0, \phi_0)$ must be of the opposite sign of the phase of $\mathbf{e}_{nm}(\theta_0, \phi_0)$. Specifically, for $\mathbf{e}_{nm}(\theta_0, \phi_0)$ of (2.24), the phase of the excitation coefficients is

$$\chi_{nm}(\theta_0, \phi_0) = -[\psi_{nm}(\theta_0, \phi_0) \pm \nu_{nm}(\theta_0, \phi_0) \pm \phi_{nm}(\theta_0, \phi_0)] \quad (2.41)$$

chosen so that $\text{Re}[E_{\phi nm}(\theta_0, \phi_0) \exp(j\omega t)] = 0$ when $\omega t = 0$. Thus when $\omega t = 0$ all the element's instantaneous fields point in the same $(\hat{\theta})$ direction.

2.4.7 Array Gain

The array gain is

$$G(\theta, \phi) = \frac{\mathbf{E}(\mathbf{r}) \cdot \mathbf{E}^*(\mathbf{r})}{\zeta_0 P_0} \quad (2.42)$$

where

$$P_0 = \frac{\sum_{nm} |c_{nm}|^2}{4\pi r^2} \quad (2.43)$$

Thus,

$$G(\theta, \phi) = \frac{4\pi}{\zeta_0} \frac{|\sum_{nm} c_{nm} \mathbf{e}_{nm}(\theta, \phi)|^2}{\sum_{nm} |c_{nm}|^2} \quad (2.44)$$

and consequently, the peak gain is

$$G(\theta_0, \phi_0) = \frac{4\pi}{\zeta_0} \frac{[\sum_{nm} |c_{nm}| |\mathbf{e}_{nm}(\theta_0, \phi_0)|]^2}{\sum_{nm} |c_{nm}|^2} \quad (2.45)$$

For an element pattern as given by (2.22) we get

$$G(\theta_0, \phi_0) = G_{\text{cell}} \frac{[\sum_{nm} |c_{nm}| \sqrt{\cos \theta_{nm}}]^2}{\sum_{nm} |c_{nm}|^2} \quad (2.46)$$

The expression (2.45) is maximum if we choose the excitation coefficients c_{nm} according to the Maximum Gain Theorem, (C.2), which is for convenience presented in Appendix C. Namely, in conformal arrays, in contrast to planar arrays, maximum gain is achieved not when elements are uniformly excited but when the magnitude of the voltage excitation coefficients is proportional to the magnitude of the complex element pattern (field) values in the main beam direction (θ_0, ϕ_0) , and the phase of the voltage excitation coefficients is such as to compensate for the different propagation paths and element phase pattern values in (θ_0, ϕ_0) , and the orientation of the radiating elements. In short, (2.45) is maximum when

$$|c_{nm}| \propto |e_{nm}(\theta_0, \phi_0)| \quad (2.47)$$

while the phase of c_{nm} must be that of (2.41). Thus, for a spherical array of radiators with an element pattern of (2.22), the maximum gain can be achieved if

$$|c_{nm}| = \sqrt{\cos \theta_{nm}}. \quad (2.48)$$

As an illustrative example, below we evaluate the array gain for (1) "equal-amplitude" excitation, i.e., $|c_{nm}| = 1$ and (2) "maximum gain excitation" as given by (2.48). Because the radiation pattern in a spherical array is independent of the beam pointing direction, with no loss of generality, we assume that all the elements in the active sector are phased so that the peak of the beam points in z -direction, i.e., $\theta_0 = \phi_0 = 0$.

In case (1), from (2.46)

$$G_u(0,0) = G_{cell} \frac{1}{N_a} [\sum_{nm} \sqrt{\cos \theta_{nm}}]^2 \quad (2.49)$$

where N_a is the number of elements in the active array sector, while in case (2)

$$G_{max}(0,0) = G_{cell} \sum_{nm} \cos \theta_{nm} = \sum_{nm} g_{nm}(0,0). \quad (2.50)$$

The above sums can be evaluated by replacing $\sum_n \sum_m$ with

$$\int_0^{2\pi} \int_0^{\alpha_{max}} R^2 \sin \alpha \, d\alpha \, d\beta. \quad (2.51)$$

Similarly, in (2.49), N_a is replaced by the active area i.e.,

$$N_a \rightarrow 2\pi R^2 (1 - \cos \alpha_{max}). \quad (2.52)$$

For $\alpha_{max} = \pi/3$ the ratio between (2.49) and (2.50) is

$$\frac{G_{max}(0,0)}{G_u(0,0)} = 1.0086 \quad (2.53)$$

Thus, in case of "maximum gain excitation" the gain is about 0.04 dB higher than if the array elements were excited uniformly. This increase in the gain is insignificant for any practical application.

2.4.8 Polarization

The far-field pattern of a single element in array is

$$\mathbf{E}_{nm}(\theta, \phi) = c_{nm}(\theta_0, \phi_0) \mathbf{e}_{nm}(\theta, \phi) \quad (2.54)$$

For the sake of simplicity in the previous analysis we assumed that the array element, radiates a CP wave in all directions, as expressed by (2.22). For a more realistic (physical) element, (2.22) is modified according to

$$\mathbf{e}_{nm}(\theta_{nm}, \phi_{nm}) = E_0 \sqrt{\cos \theta_{nm}} e^{\pm j \varphi_{nm}} \frac{1}{\sqrt{2}} (\hat{\theta}_{nm} \cos \theta_{nm} \pm j \hat{\phi}_{nm}) \quad (2.55)$$

which resembles the far-field radiated by two CP infinitesimal dipoles $\lambda/4$ above an infinite ground, Appendix A. The field is elliptically polarized everywhere except at the local zenith ($\theta_{nm} = 0$) where it is CP.

We express this field, see Appendix B.6 for details, in global coordinates as

$$\mathbf{e}_{nm}(\theta, \phi) = -[\hat{\theta} | e_{\theta nm}(\theta, \phi) | e^{\pm j \vartheta_{nm}(\theta, \phi)} \pm j \hat{\phi} | e_{\phi nm}(\theta, \phi) | e^{\pm j \varphi_{nm}(\theta, \phi)}] e^{j \psi_{nm}} e^{\pm j \phi_{nm}} \quad (2.56)$$

$$| e_{\theta nm}(\theta, \phi) | = \frac{1}{\sqrt{2}} E_0 \sqrt{\cos \theta_{nm}} | a_{nm} \cos \theta_{nm} \pm j b_{nm} | \quad (2.57)$$

$$| e_{\phi nm}(\theta, \phi) | = \frac{1}{\sqrt{2}} E_0 \sqrt{\cos \theta_{nm}} | a_{nm} \pm j b_{nm} \cos \theta_{nm} | \quad (2.58)$$

$$\tan \vartheta_{nm} = \frac{b_{nm}}{a_{nm} \cos \theta_{nm}} \quad (2.59)$$

$$\tan \varphi_{nm} = \frac{b_{nm} \cos \theta_{nm}}{a_{nm}} \quad (2.60)$$

where a_{nm} and b_{nm} are elements of the rotation matrix given by (B.9) and (B.10).

We rewrite (2.56) in the form

$$\mathbf{e}_{nm}(\theta, \phi) = -[\hat{\theta} | e_{\theta nm}(\theta, \phi) | e^{\pm j(\vartheta_{nm} - \varphi_{nm})} \pm j \hat{\phi} | e_{\phi nm}(\theta, \phi) |] e^{\pm j \nu_{nm}} e^{j \psi_{nm}} e^{\pm j \phi_{nm}} \quad (2.61)$$

where for convenience we set $\varphi_{nm} = \nu_{nm}$. In (2.54), the voltage excitation coefficients are

$$c_{nm}(\theta_0, \phi_0) = | c_{nm}(\theta_0, \phi_0) | e^{j \chi_{nm}(\theta_0, \phi_0)} \quad (2.62)$$

where, as already mentioned, to point the beam in the (θ_0, ϕ_0) direction, χ_{nm} must be

$$\chi_{nm}(\theta_0, \phi_0) = -[\psi_{nm}(\theta_0, \phi_0) \pm \nu_{nm}(\theta_0, \phi_0) \pm \phi_{nm}(\theta_0, \phi_0)]. \quad (2.63)$$

To observe the polarization effects we find the instantaneous far field of a single (nm) element in the (θ_0, ϕ_0) direction:

$$\tilde{\mathbf{E}}_{nm}(\theta_0, \phi_0; t) = \text{Re}\{\mathbf{E}_{nm}(\theta_0, \phi_0) e^{j \omega t}\} \quad (2.64)$$

where according to (2.54) using (2.62) and (2.63)

$$\mathbf{E}_{nm}(\theta_0, \phi_0) = - |c_{nm}(\theta_0, \phi_0)| [\hat{\theta} | e_{\theta nm}(\theta_0, \phi_0) | e^{\pm j(\vartheta_{nm}(\theta_0, \phi_0) - \varphi_{nm}(\theta_0, \phi_0))} \pm j \hat{\phi} | e_{\phi nm}(\theta_0, \phi_0) |] \quad (2.65)$$

Substituting (2.65) into (2.64) yields

$$\begin{aligned} \tilde{\mathbf{E}}_{nm}(\theta_0, \phi_0; t) = & - |c_{nm}(\theta_0, \phi_0)| \{ \hat{\theta} | e_{\theta nm}(\theta_0, \phi_0) | \cos[(\vartheta_{nm}(\theta_0, \phi_0) - \varphi_{nm}(\theta_0, \phi_0)) \pm \omega t] \\ & \mp \hat{\phi} | e_{\phi nm}(\theta_0, \phi_0) | \sin \omega t \} \end{aligned} \quad (2.66)$$

Thus in the plane perpendicular to the array beam direction, the instantaneous electric field $\tilde{\mathbf{E}}_{nm}$ traces an ellipse with tilt angle

$$\tau_{nm} = \frac{1}{2} \tan^{-1} \frac{\sin(2\gamma_{nm}) \cos[\pm \frac{\pi}{2} \mp (\vartheta_{nm} - \varphi_{nm})]}{\cos(2\gamma_{nm})} \quad (2.67)$$

where

$$\gamma_{nm} = \tan^{-1} \frac{|E_{\phi nm}|}{|E_{\theta nm}|} \quad (2.68)$$

The axial ratio is

$$R_{nm} = -\cot \epsilon_{nm} \quad (2.69)$$

where

$$\epsilon_{nm} = \frac{1}{2} \sin^{-1} \{ \sin(2\gamma_{nm}) \sin[\pm \frac{\pi}{2} \mp (\vartheta_{nm} - \varphi_{nm})] \}. \quad (2.70)$$

For simplicity we assume that we point a beam in z -direction, $(\theta_0, \phi_0) = (0, 0)$, with array active elements located within a cone angle $\alpha_{max} = 60^\circ$. Then only the top element, $(nm) = (00)$ with $\alpha_0 = 0, \beta_{00} = 0$ designated as the reference element, will be CP while all others will be elliptically polarized. Figure 2.39 shows in red the polarization circle of the reference element in the z =constant plane. As an illustrative example, the $\tilde{\mathbf{E}}_{00}$ vectors for $\omega t = 0, \pi/2, \pi$ and $\omega t = 3\pi/2$ are shown. In the same figure we also show the polarization ellipse of the $(n, m) = (38, 0)$ element with coordinates $(\alpha_n = 30.4^\circ, \beta_{n0} = 0^\circ)$; thus the element is located in the x - z plane. The instantaneous electric field vector $\tilde{\mathbf{E}}_{nm}$ is shown in blue for the same ωt parameter values. Notice that for $\omega t = 0, \pi/2, \pi$, and $3\pi/2$ both vectors are in sync while for other ωt values they point in slightly different direction resulting in a reduction of the array gain, or a so called polarization loss. In regions $0 \leq \omega t \leq \pi/2$ and $\pi \leq \omega t \leq 3\pi/2$ the $\tilde{\mathbf{E}}_{nm}$ is leading $\tilde{\mathbf{E}}_{00}$ while in regions $\pi/2 \leq \omega t \leq \pi$ and $3\pi/2 \leq \omega t \leq 2\pi$ $\tilde{\mathbf{E}}_{nm}$ is lagging $\tilde{\mathbf{E}}_{00}$. The element phasing was chosen according to (2.63) so that at $\omega t = 0$ all element instantaneous vectors align with the top element $(0, 0)$, as can be seen in Figure 2.39.

The axial ratio and orientation of the ellipse are indicative of the element pattern relation (2.55) and the element position in the array. Below we elaborate on the ellipse characteristics:

1. The radius of the red circle in Figure 2.39 is $E_0/\sqrt{2}$, see (2.55) where

$$E_0 = \sqrt{G_{cell}} = \sqrt{\frac{4\pi A_{cell}}{\lambda^2}}. \quad (2.71)$$

We assume a typical value for the cell area $A_{\text{cell}} = \lambda/2 \times \lambda/2$ which gives an area cell gain $G_{\text{cell}} = \pi$. Thus in (2.71), $E_0 = 1.2533$.

2. The ellipse axis depends on element location. For $(n, m) = (38, 0)$ element, the major axis of the polarization ellipse is smaller than the diameter of the red circle, and is due to the $\sqrt{\cos \theta_{nm}}$ factor in (2.55).

3. The ellipse axial ratio is determined by the factor $(\hat{\theta}_{nm} \cos \theta_{nm} \pm j\hat{\phi}_{nm})$ in (2.55). Thus the axial ratio is

$$R = \frac{1}{\cos \theta_{nm}} \quad (2.72)$$

or in our case, i.e., the z -directed beam

$$R = \frac{1}{\cos \alpha_n}. \quad (2.73)$$

For element $(38, 0)$ shown in Figure 2.39, $R = 1/\cos 30.4^\circ = 1.15$.

4. The ellipse tilt angle can be computed from (2.67) and for all elements lying in $(+x)$ - z plane it is 90° .

5. Note also that at $\omega t = 0$ both vectors point in the negative θ direction. Below we give a short explanation: It is assumed that at $\omega t = 0$ the single element has only $E_{\theta nm}$ in the local coordinate system. Because the $m = 0$ element is located in the x - z plane, $E_{\theta nm}$ lies also in the same plane as shown in Figure 2.43. The elements are phased so as to produce a beam in the z -direction $(\theta_0, \phi_0) = (0, 0)$, and therefore the corresponding local observation angles are $(\theta_{0nm}, \phi_{0nm}) = (\alpha_n, -\pi)$. Transforming this field into global coordinates gives $-E_\theta$, as illustrated in Figure 2.43.

Similarly, Figure 2.40 shows the polarization ellipse for the $(n, m) = (76, 0)$ element. This element is located at the edge of the active sector, more specifically at $(\alpha_n, \beta_{nm}) = (60.7^\circ, 0^\circ)$. Comparing this figure with Figure 2.39, we notice that the ellipse is much smaller because of the $\sqrt{\cos \alpha_n}$ factor and the axial ratio is about 3dB . This is not great but still acceptable performance.

As m increases the polarization ellipse starts rotating in the β_{nm} direction and makes a full circle as β_{nm} sweeps from zero to 2π . A snap shot in time of $\tilde{\mathbf{E}}_{nm}$ for the element $(nm) = (38, 16)$ with $\alpha_n = 30.4^\circ$, $\beta_{nm} = 29.2^\circ$ and the corresponding ellipse for $\omega t = 0, \pi/2, \pi, 3\pi/2$ is shown Figure 2.41. Because of different ellipse tilt angles as a function of element position (α_n, β_{nm}) the $\tilde{\mathbf{E}}_{nm}$ vectors do not rotate in sync vs. ωt . In addition, $\tilde{\mathbf{E}}_{nm}$ at some reference time, for example $\omega t = 0$, does not coincide. This, however, can be compensated for by imposing the proper phase of the excitation coefficients according to (2.63). In this case, at the peak of the beam, $\tilde{\mathbf{E}}_{nm}$ will align with $\tilde{\mathbf{E}}_{00}$ at four distinct points on the ellipse: $\omega t_1 = 0$, $\omega t_2 = \pi$,

$$\omega t_3 = \tan^{-1} \frac{|e_{\phi nm}| - \cos(\vartheta_{nm} - \varphi_{nm})}{\mp \sin(\vartheta_{nm} - \varphi_{nm})} \quad (2.74)$$

and $\omega t_4 = \omega t_3 + \pi$. For other ωt 's, the instantaneous vector fields $\tilde{\mathbf{E}}_{nm}$ from different array elements won't be exactly in sync, and therefore there will gain degradation due to polarization effects. For this particular element $\omega t_3 = 35.0474^\circ$ and $\omega t_4 = 215.0474^\circ$, see (2.74). Also notice that in the regions $0 \leq \omega t \leq \omega t_3$ and $\pi \leq \omega t \leq \omega t_4$, $\tilde{\mathbf{E}}_{38,16}$ is leading $\tilde{\mathbf{E}}_{00}$ while in regions $\omega t_3 \leq \omega t \leq \pi$ and $2\pi \leq \omega t \leq \omega t_4$ the $\tilde{\mathbf{E}}_{38,16}$ is lagging $\tilde{\mathbf{E}}_{00}$.

Figure 2.42 shows the same as Figure 2.41 except here the element is $(n, m) = (76, 29)$. This element has the following coordinates: $\alpha_n = 60.7^\circ$ and $\beta_{nm} = 30.7^\circ$. Furthermore, the four points in time where, the instantaneous electric field vectors align with the top CP element $(0, 0)$ are two fixed values $\omega t = 0, \pi$ and two element dependent values $\omega t_3 = 43.1548^\circ$ and $\omega t_4 = 223.1548^\circ$.

Below we evaluate the polarization efficiency (loss) in spherical arrays. We define the polarization efficiency in spherical arrays as the ratio of the peak gain with elliptically polarized elements to the peak gain of the array when all elements are circularly polarized. Thus, using (2.45) for the array gain, we get

$$p = \frac{[\sum_{nm} |c_{nm}| |e_{nm}(\theta_0, \phi_0)|]^2}{[\sum_{nm} |c_{nm}^{CP}| |e_{nm}^{CP}(\theta_0, \phi_0)|]^2} \quad (2.75)$$

where e_{nm} is given by (2.55) and e_{nm}^{CP} is given by (2.22). Under maximum gain condition, i.e., $|c_{nm}| = |e(\theta_0, \phi_0)_{nm}|$ and $|c_{nm}^{CP}| = |e(\theta_0, \phi_0)_{nm}^{CP}|$ and using transformation (2.51), (2.75) can be written in the form

$$p = \frac{[\int_0^{\alpha_{max}} \sin \alpha \cos \alpha \sqrt{\frac{1+\cos^2 \alpha}{2}} d\alpha]^2}{[\int_0^{\alpha_{max}} \sin \alpha \cos \alpha d\alpha]^2} \quad (2.76)$$

which gives

$$p = \frac{2 [2^{2/3} - (2 - \sin^2 \alpha_{max})^{3/2}]^2}{9 \sin^4 \alpha_{max}} \quad (2.77)$$

For $\alpha_{max} = \pi/3$, $p = 0.809$ and consequently the polarization loss is

$$L_p = -10 \log p = 0.92 \text{ dB}. \quad (2.78)$$

Evaluating the polarization loss in the planar array case, (2.75) is still valid and because all elements point in the same direction it can be further reduced to

$$p = \frac{|e_{nm}(\theta_0, \phi_0)|^2 [\sum_{nm} |c_{nm}|]^2}{|e_{nm}^{CP}(\theta_0, \phi_0)|^2 [\sum_{nm} |c_{nm}^{CP}|]^2} \quad (2.79)$$

In planar arrays maximum gain is obtained when $|c_{nm}| = 1$. Therefore,

$$p = \frac{|e_{nm}(\theta_0, \phi_0)|^2}{|e_{nm}^{CP}(\theta_0, \phi_0)|^2} \quad (2.80)$$

Substituting (2.55) and (2.22) into (2.80) yields

$$p = \frac{1 + \cos^2 \theta_0}{2} \quad (2.81)$$

which at 60° off broadside scan is $p = 0.625$, and polarization loss $L_p = 2.04 \text{ dB}$. Thus, the polarization losses of the spherical array are about half of the equivalent planar array at 60° off broadside scan.

2.4.9 Instantaneous Bandwidth

In planar arrays steered by phase shift rather than by time delay the beam will scan (squint) as the frequency changes. This beam squint with frequency results in a decrease in gain because the beam is no longer pointing in the desired direction. Expressions for the signal bandwidth of planar phased arrays are derived in [18, 12] where the bandwidth criteria is based on unacceptable gain loss due to change in scan angle with frequency. For example, if we define the frequency limits in which the beam squints by 1/4 of the beamwidth, and loses about 3/4 dB gain, the resulting bandwidth is given by

$$\frac{\Delta f}{f} = \frac{\lambda}{2L \sin \theta_0} \quad (2.82)$$

For $\theta_0 = 60^\circ$, this expression reduces to

$$\text{Bandwidth (\%)} \approx \text{Broadside Beamwidth (degrees)}. \quad (2.83)$$

Thus beam squint with frequency is the fundamental mechanism that limits the bandwidth of planar phased array. In spherical arrays there is no beam squint since the beam steering principle is different than in the planar arrays. However, in spherical arrays there is a beam broadening effect which causes gain loss as the frequency changes. Consequently, the bandwidth criteria for planar arrays developed in [18] do not apply in a spherical array case.

Below we develop the bandwidth criteria for a spherical array aperture. The criteria is based on the requirement that all elements in an active array sector contribute constructively to the total far field in the beam direction. This means that the difference in phase between the center element and the element at the edge of the active sector is not greater than $\pi/2$ as the frequency changes from f_0 to f . Thus, with the help of Figure 2.38 we write

$$|k_0 R(1 - \cos \alpha_{max}) - kR(1 - \cos \alpha_{max})| = \frac{\pi}{2} \quad (2.84)$$

From here

$$\frac{2\pi R}{c} |f_0 - f| (1 - \cos \alpha_{max}) = \frac{\pi}{2} \quad (2.85)$$

Setting $\Delta f = 2 |f_0 - f|$ and since $c = 2\pi f_0/k_0$, the instantaneous bandwidth of a spherical array is

$$\frac{\Delta f}{f_0} = \frac{\pi}{k_0 R(1 - \cos \alpha_{max})} \quad (2.86)$$

This criteria gives about 1 dB loss at the edge of the band. As an illustrative example, we consider a spherical array of 5 meter radius with an active sector cone angle $\alpha_{max} = 60^\circ$ and $f = 2$ GHz. In this case from (2.86), $\Delta f/f_0 = 3\%$ or $\Delta f = 60$ MHz. Comparing this with an equivalent planar array with the same projected circular aperture of radius $R \sin \alpha_{max}$, and with a broadside beamwidth of 1° ; according to (2.83), the signal bandwidth of the planar array is approximately 1%. In this case at 60° off-broadside scan a spherical array has about three times greater signal bandwidth than an equivalent planar array.

Figure 2.49 and Figure 2.50 show a $\phi = 0$ cut radiation pattern of a spherical array and an equivalent planar array with a beam pointing in $(\theta_0 = 60^\circ, \phi_0 = 0^\circ)$ direction for two

frequencies $f_0 = 2$ GHz, and $f_0 + 10$ MHz corresponding to 1% signal bandwidth. From Figure 2.50 notice that at f_0 the planar array has 3 dB scan loss while the spherical array has a scan independent gain pattern. As the frequency changes from 2.000 GHz to 2.010 GHz a planar array exhibits a beam shift, and an additional 1 dB loss, while a spherical array keeps pointing its beam in the same direction with only about 0.1 dB loss in gain.

2.4.10 Mismatch Losses

Let a_{nm} and b_{nm} be the voltages of the incident and reflected signals at the array element terminals. The total voltages, also called array excitation coefficients, c_{nm} are then

$$c_{nm} = a_{nm} + b_{nm} \quad (2.87)$$

In phased arrays the incident and reflected voltages are related via scan dependent active reflection coefficients,

$$b_{nm} = \Gamma_{nm}(\theta_0, \phi_0) a_{nm} \quad (2.88)$$

where

$$\Gamma_{nm}(\theta_0, \phi_0) = |\Gamma_{nm}(\theta_0, \phi_0)| e^{j\gamma_{nm}(\theta_0, \phi_0)}. \quad (2.89)$$

In spherical arrays, as in planar arrays, the excitation coefficients c_{nm} directly affect the array gain pattern, and are usually determined according to the desired pattern whether in regard to the sidelobe level or maximum gain condition. With known c_{nm} 's, the incident signal voltages must be

$$a_{nm} = \frac{c_{nm}}{1 + \Gamma_{nm}(\theta_0, \phi_0)}. \quad (2.90)$$

Mismatch losses are defined as the ratio of the input or available power to the power radiated by the antenna, i.e.,

$$L = \frac{P_{in}}{P_{rad}} = \frac{\sum_{nm} |a_{nm}|^2}{\sum_{nm} |a_{nm}|^2 (1 - |\Gamma_{nm}(\theta_0, \phi_0)|^2)}. \quad (2.91)$$

To estimate mismatch losses in spherical arrays and to compare them with an equivalent planar array, we assume a typical practical case where the elements are perfectly matched at broadside and have a reflection coefficient of 0.33 at 60° off-broadside scan. This corresponds to a $VSWR$ of 2 : 1 at $\theta_0 = 60^\circ$. For the in-between scan angles we approximate $|\Gamma_{nm}|^2 = 0.128 \sin \alpha_n$.

For the planar array with $\Gamma_{nm} = \Gamma$ and for maximum gain, i.e., uniform excitation ($c_{nm} = 1$), the mismatch losses are

$$L_p = \frac{1}{1 - |\Gamma(\theta_0 = 60^\circ)|^2} = 1.125 \quad (2.92)$$

which is about 0.51 dB.

To evaluate (2.91) for a spherical array, we replace \sum_{nm} by $\int_0^{2\pi} \int_0^{\alpha_{max}} R^2 \sin \alpha d\alpha d\beta$ which for uniform excitation gives

$$L = \frac{\int_0^{\alpha_{max}} |a(\alpha)|^2 \sin \alpha d\alpha}{\int_0^{\alpha_{max}} |a(\alpha)|^2 (1 - |\Gamma(\alpha)|^2) \sin \alpha d\alpha} \quad (2.93)$$

where

$$a(\alpha) = \frac{c(\alpha)}{1 + \Gamma(\alpha)}. \quad (2.94)$$

Specifically, for "equal amplitude excitation", $c(\alpha) = 1$, from (2.93) we get $L = 0.345$ dB while if we apply maximum gain excitation, i.e., $c(\alpha) = \cos^{1/2} \alpha$, the mismatch losses, $L = 0.322$ dB are almost half those of the equivalent planar array.

2.5 Numerical Simulation

2.5.1 Computer Code

A Matlab computer code was generated to evaluate the radiation characteristics of a spherical array and, for comparison, an equivalent planar array. The equivalent planar array has the same circular aperture size as the projected active sector on the $z=\text{constant}$ plane of the spherical array. The planar array has a uniform triangular grid with the same average cell area as that of the spherical array. The code calculates the radiation patterns in the $\phi=\text{const}$ plane vs. elevation angle θ as a function of geometry, element type, and excitation. We selected a typical element arrangement on a sphere consisting of a number of rings equally spaced in θ . Array elements are then uniformly distributed along each ring so that the element spacing in ϕ is as close as it can be to half of the free space wavelength ($\lambda_0/2$). Each ring of course contains a different number of elements, and the periodic element spacing on each ring varies slightly from ring-to-ring. Each element is designated by two indices (nm) and its position on the sphere by two angles, (α_n, β_{nm}) as illustrated in Figure B.2 and Figure B.3. The code can be easily adapted to any array element distribution on the sphere by setting new values for (α_n, β_{nm}) .

The radiation elements are specified by the element pattern, i.e., the radiated field of a single element in a mutually coupled spherical array environment. In the code the user can select one of three typical choices: isotropic, or element patterns as given by either (2.22) or (2.55). The code can easily adapt to any other element pattern values whether they are theoretical, computed by other codes or measured data.

There are two choices for the excitation, uniform or maximum gain excitation, see Appendix C. Thus, since there are three element patterns, we have three different maximum gain excitations. In addition to these preset choices, the user can input his own excitation if a low sidelobe level is desired or for adaptive pattern control.

In addition the user can select either left or right CP or EP, the beam pointing angles, and the size of the active sector.

The excitation of the equivalent planar array is unity.

The Matlab file is "SphereArray6.m". The code input parameters are:

f0=center frequency (GHz)

f=operating frequency (GHz)

R=sphere radius (m)

ActAngleDeg=active sector angle α_{max} (deg) - typical 60° .

Th0=main beam direction in elevation (deg)

Phi0=main beam direction in azimuth (deg)

PhiDegCut= (ϕ =constant) plane in which the pattern will be plotted

dth=elevation ring spacing (m)

dphi=azimuth element spacing in a ring (m)

sign=

1, for LHCP and LHEP

-1, for RHCP and RHEP

Polar=

1, for circular polarization

0, for elliptical polarization

Excite=

1, for unity excitation, $|c_{nm}| = 1$.

2, for $|c_{nm}| = \sqrt{\cos \theta}$,

3, for $|c_{nm}| = \sqrt{(\cos \theta \sqrt{\cos^2 \theta + 1})/2}$

Element=

1, for isotropic element

2, for element as given by element pattern relation (2.22), $g_{nm} = \cos \theta_{nm}$

3, for element as given by element pattern relation (2.55), $g_{nm} = \cos \theta_{nm}(\cos^2 \theta_{nm} + 1)/2$

MissLoss=

0, no mismatch losses

1, mismatch losses, $\sqrt{1 - |\Gamma_a|^2}$

The output of the code is a plot showing the array gain patterns of both spherical as well as planar arrays.

2.5.2 Calculated Array Patterns

Below we use the code described in the previous Subsection to demonstrate some of the features of spherical arrays. In all illustrations, sphere radius, $R = 10m$. The array grid, shown in Figure B.2 and Figure B.3, as described above consists of number of array rings. The z =constant rings are periodic in θ with spatial period $Rd\theta = \lambda_0/2$. The elements on each ring are also uniformly distributed in ϕ however, the spatial period varies slightly from ring to ring with an average period of $R \sin \alpha_n d\phi \simeq \lambda_0/2$. The number of elements on each ring is determined so that the element spacing in the ϕ direction is as close to $\lambda_0/2$ as possible while maintaining 2π periodicity. Thus, the average cell area is $(\lambda_0/2 \times \lambda_0/2)$ resulting in the same element area gain $G_{cell} = \pi$.

The center frequency is $f_0 = 2$ GHz in all cases unless otherwise stated. The active sector is defined by the cone angle $\alpha_{max} = 60^\circ$.

Figure 2.44 to Figure 2.47 compare the radiation pattern of the above described spherical array with an equivalent planar array that has the same circular aperture as that of the projected active spherical sector. Thus, the radius of the equivalent planar array is $R \sin \alpha_{max}$. Both arrays have identical elements and the same cell area, i.e. the same element gain $G_{cell} = \pi$.

Specifically, Figure 2.44 compares the radiation patterns of a spherical array with an equivalent planar array where the element pattern is CP as given by (2.22). Consequently, the element gain for both arrays is $g_{nm} = G_{cell} \cos \theta_{nm} = \pi \cos \theta_{nm}$. Furthermore both arrays

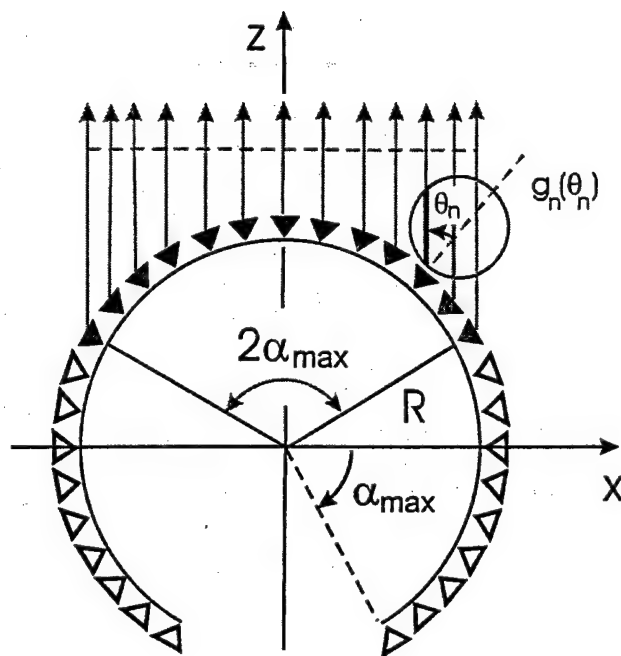


Figure 2.1: Schematic view of spherical array

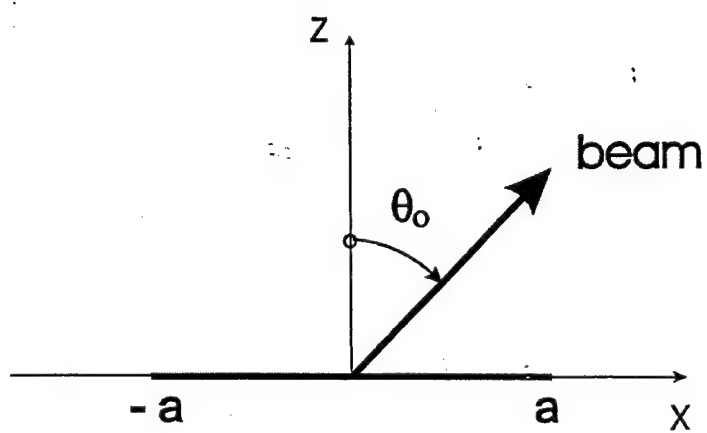


Figure 2.2: Planar array with circular aperture

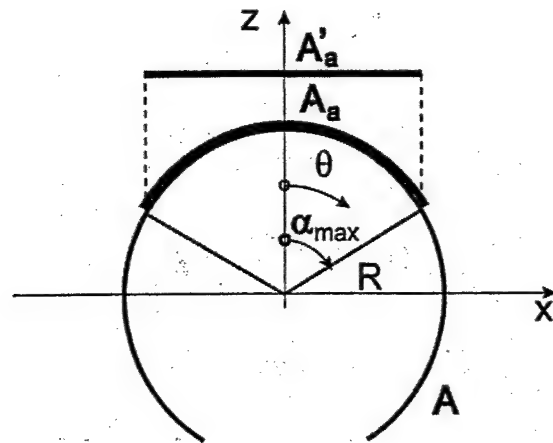


Figure 2.3: Schematic view of active sector

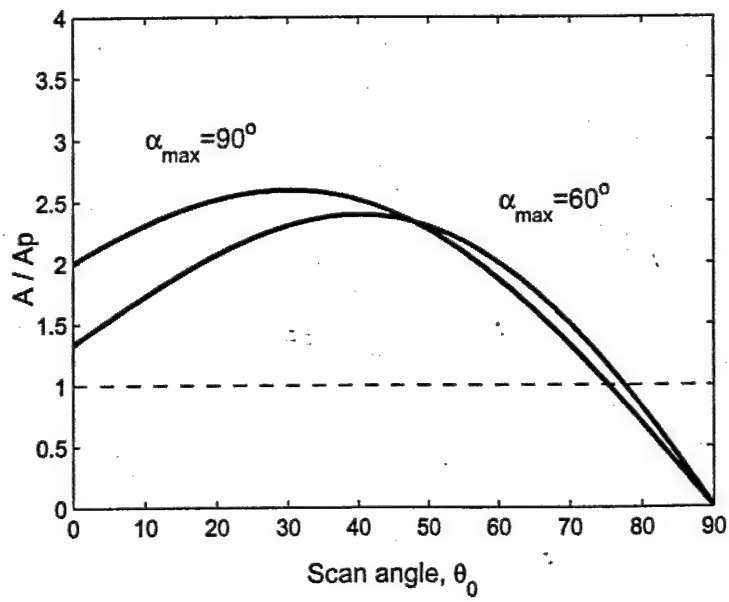


Figure 2.4: Spherical array area normalized to an equivalent planar array vs. scan angle θ_0

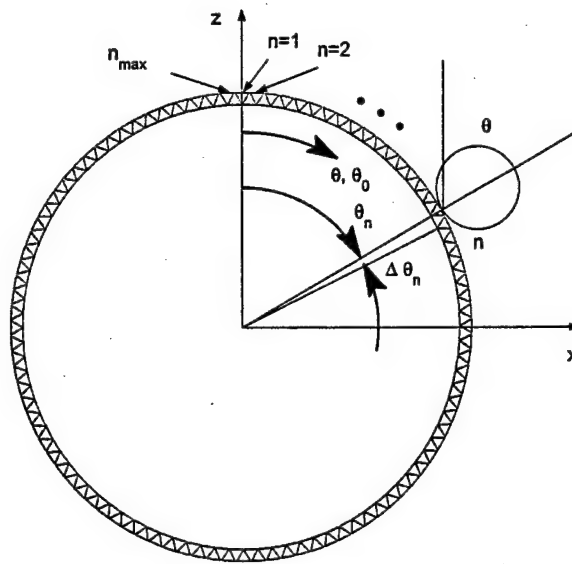


Figure 2.5: Circular array

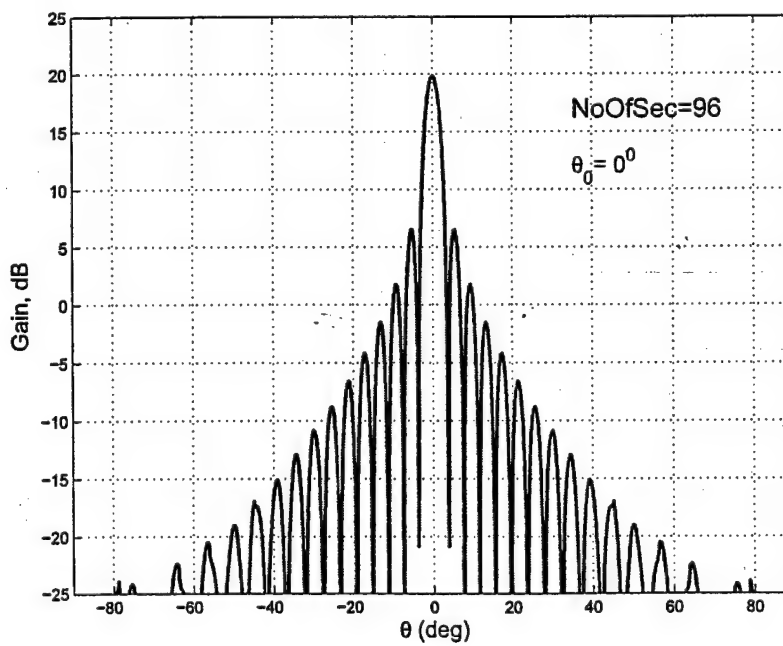


Figure 2.6: Gain pattern of 96-element circular array

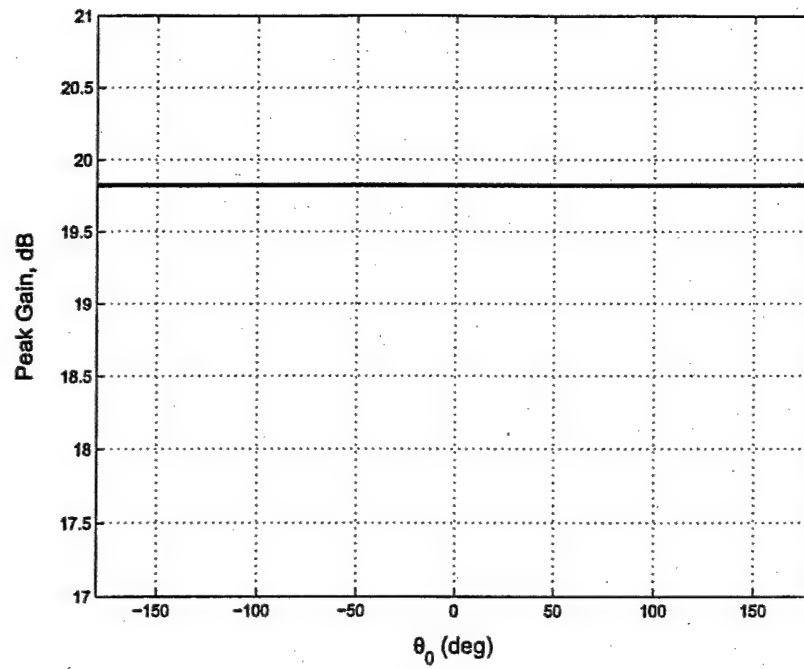


Figure 2.7: Peak gain vs. scan angle of 96-element circular array

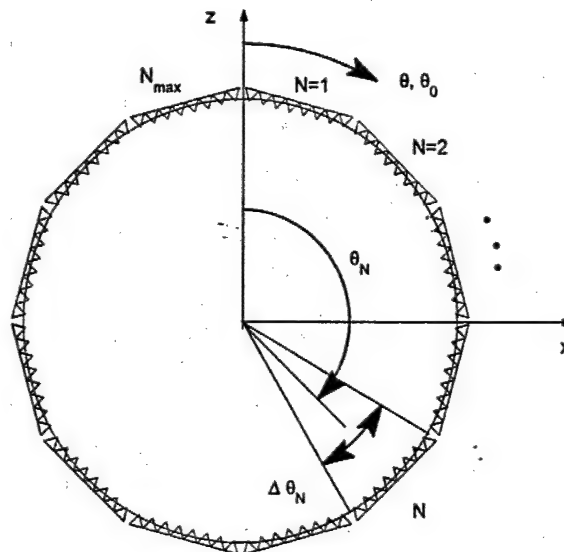


Figure 2.8: Polygon (multi-face linear) array

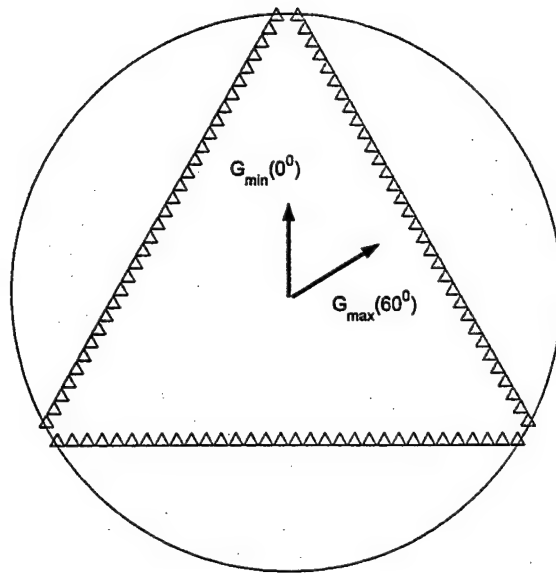


Figure 2.9: Triangular (3-face linear) array - face in red active

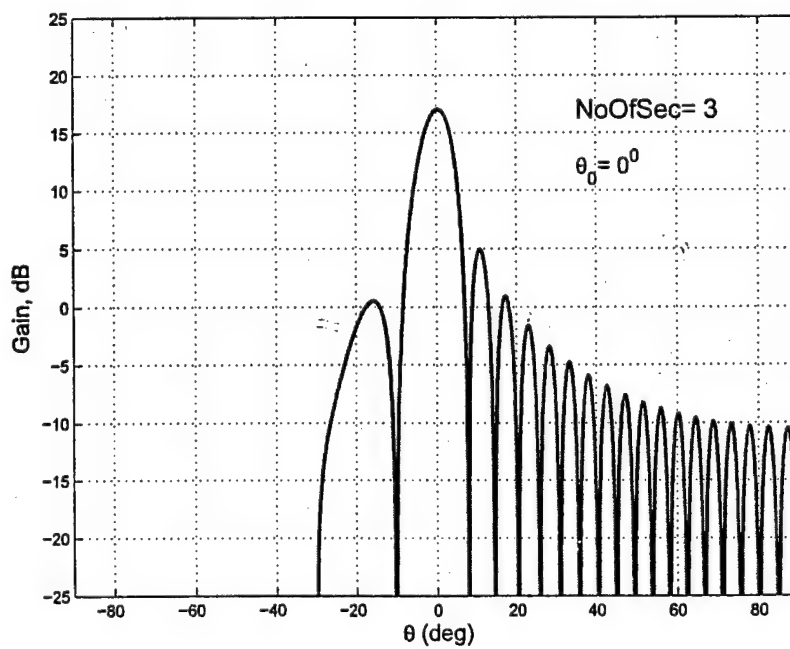


Figure 2.10: Array gain pattern of triangular array, single face active, $\theta_0 = 0^0$

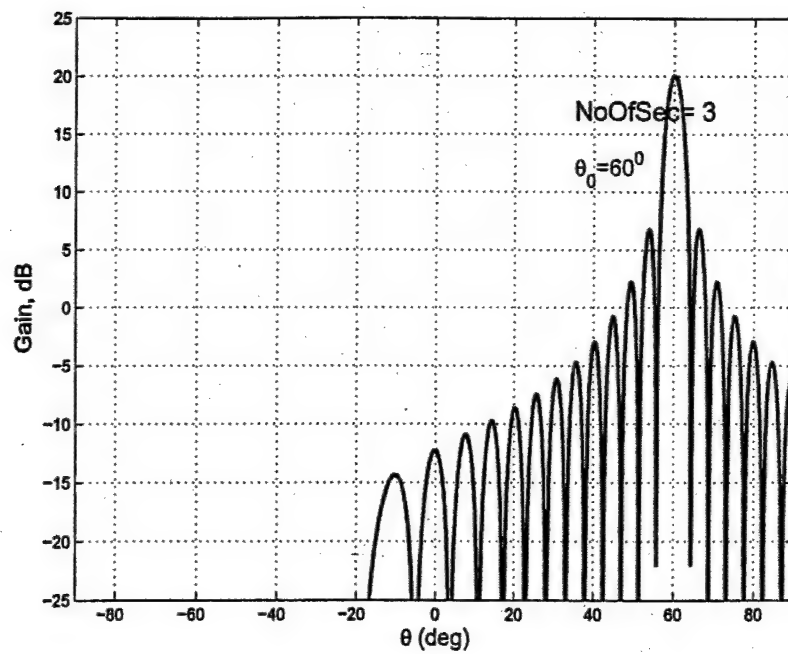


Figure 2.11: Array gain pattern of triangular array, single face active, $\theta_0 = 60^\circ$

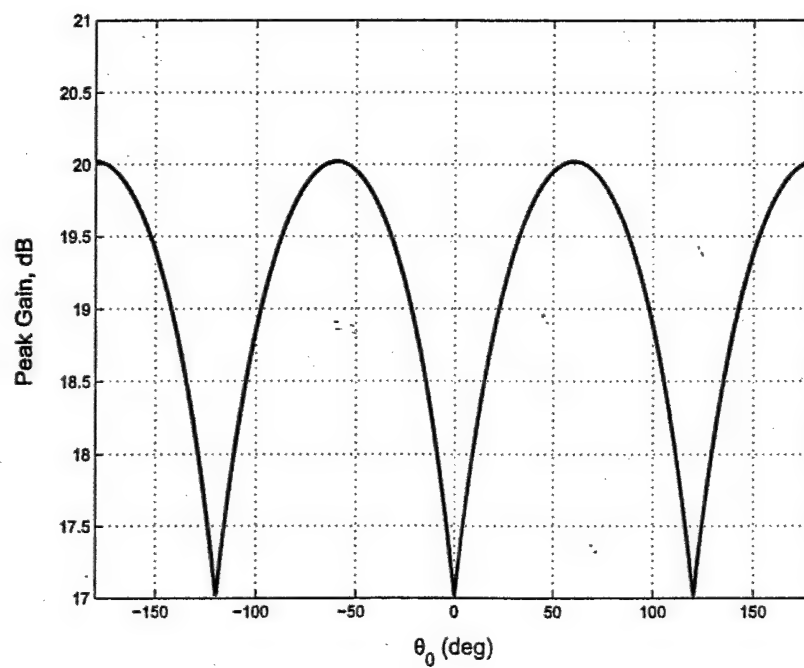


Figure 2.12: Peak gain vs. scan angle for triangular array, one face active at the time

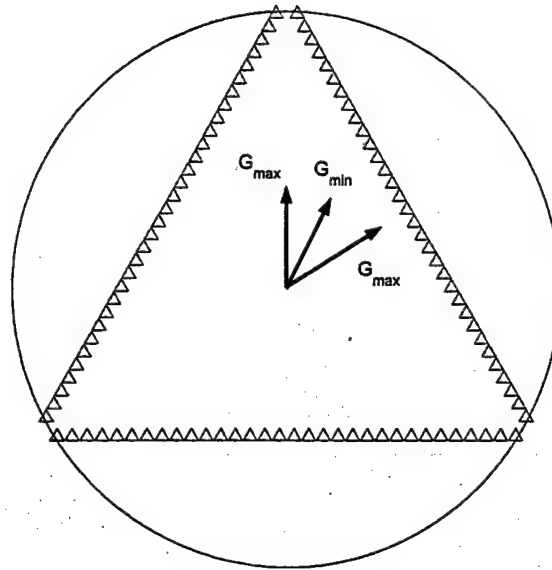


Figure 2.13: Triangular (3-face linear) array - two faces in red active

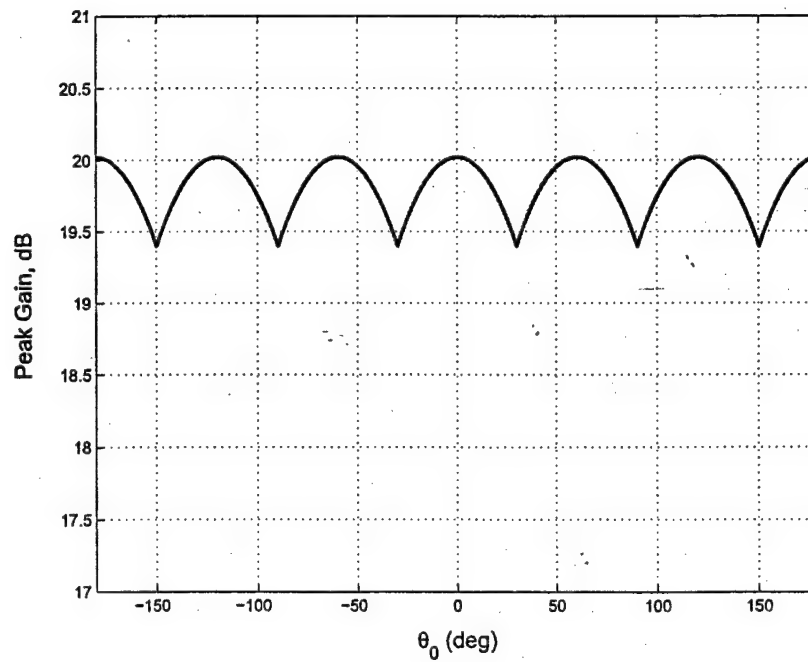


Figure 2.14: Peak gain vs. scan angle of triangular array, one or two faces active

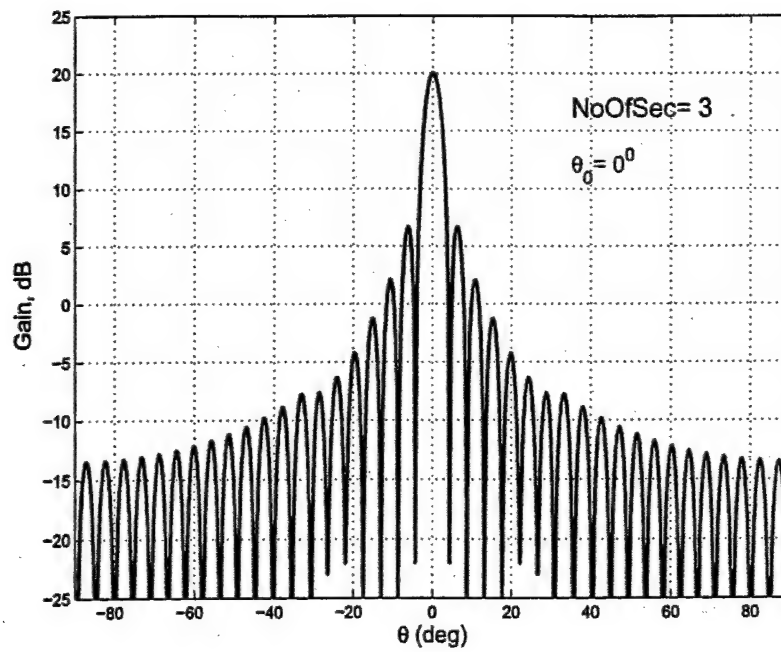


Figure 2.15: Gain pattern of triangular array - one or two faces active

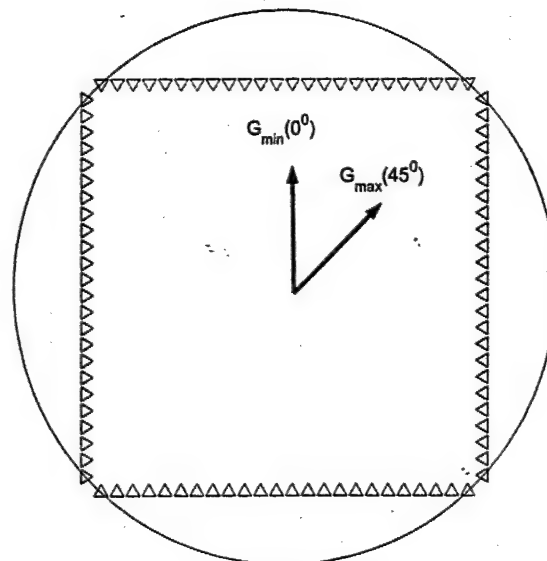


Figure 2.16: Square (4-face) linear array

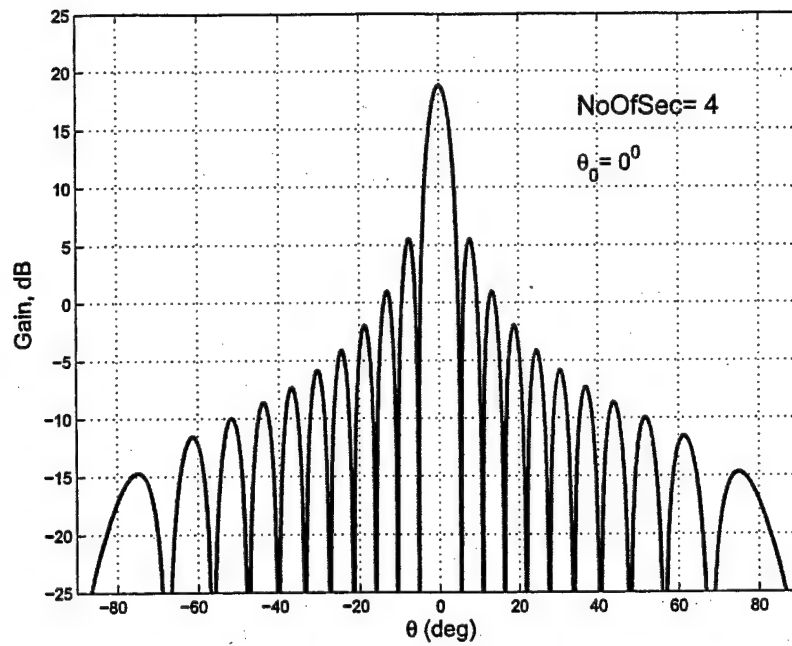


Figure 2.17: Gain pattern of square array

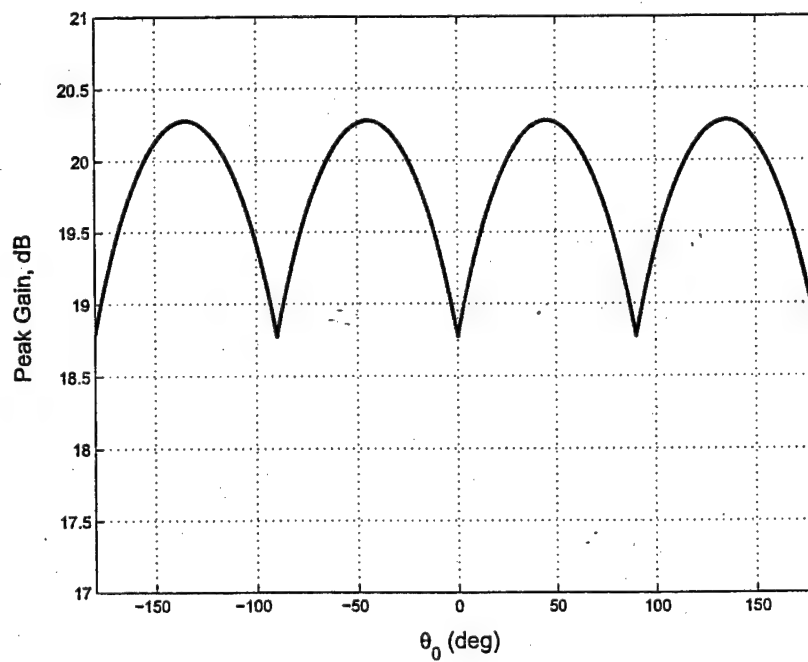


Figure 2.18: Peak gain vs. scan angle of square array

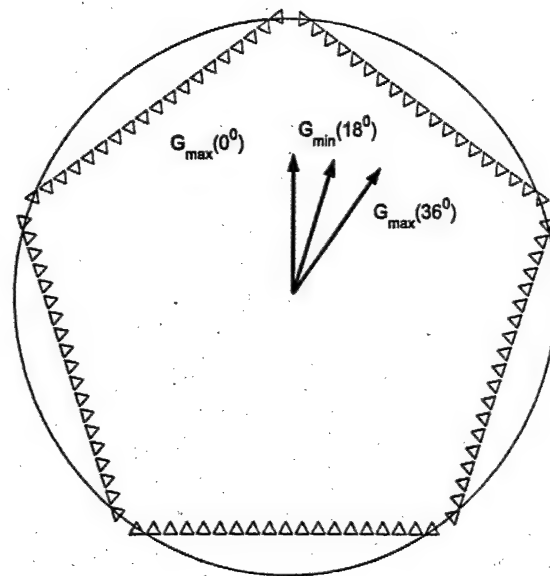


Figure 2.19: Pentagon (5-face) linear array

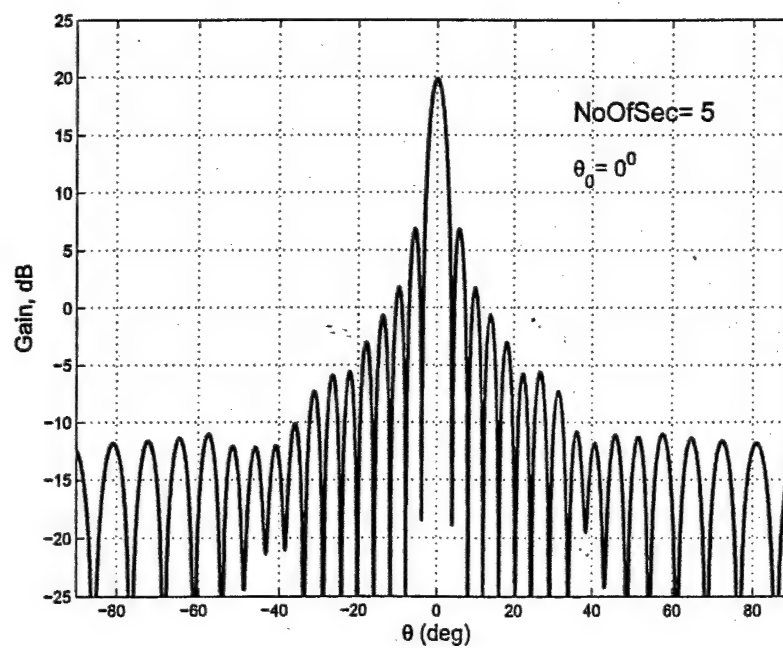


Figure 2.20: Gain pattern of pentagon array

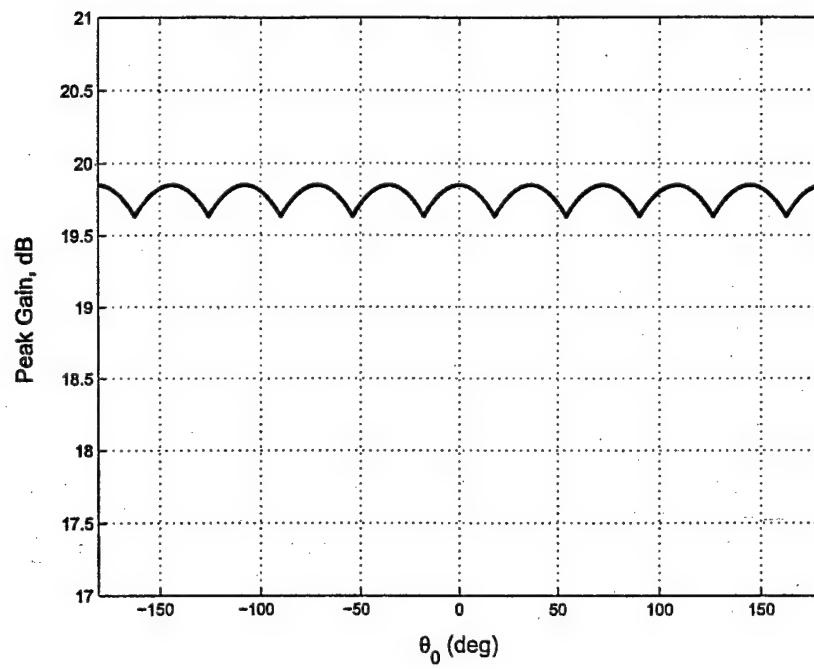


Figure 2.21: Peak gain vs. scan angle of pentagon array

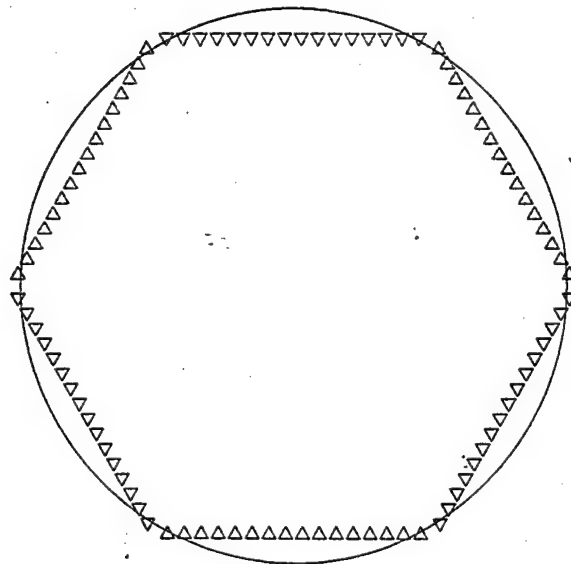


Figure 2.22: Hexagon (6-face) linear array

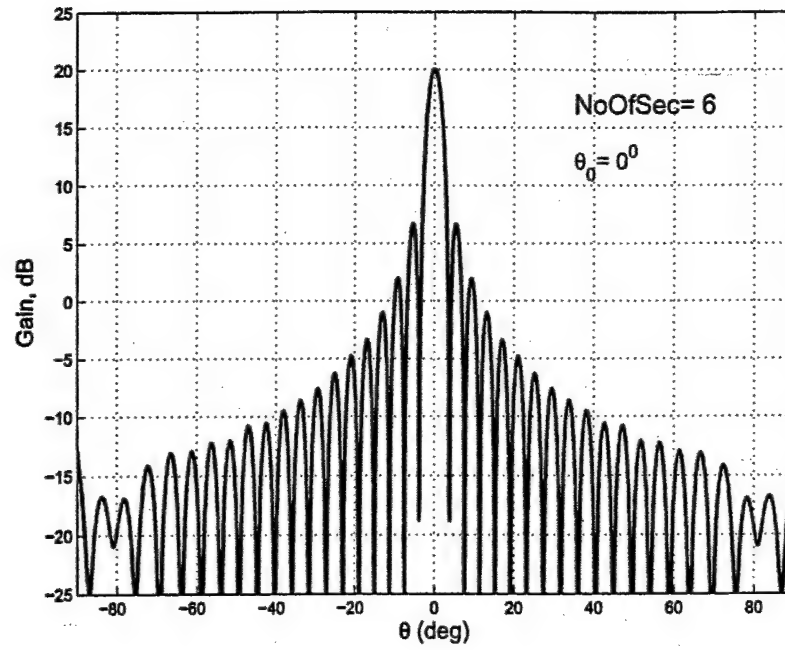


Figure 2.23: Gain pattern of hexagon array

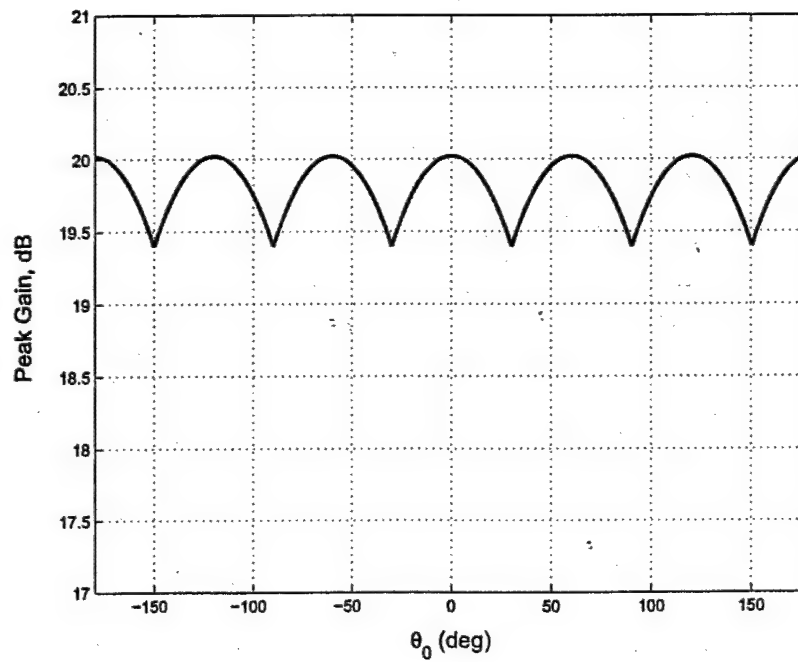


Figure 2.24: Peak gain vs. scan angle of hexagon array

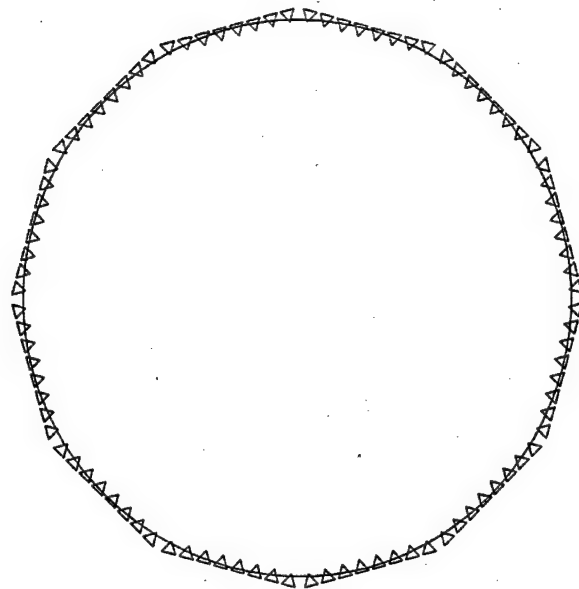


Figure 2.25: 12-gon (twelve-face) linear array

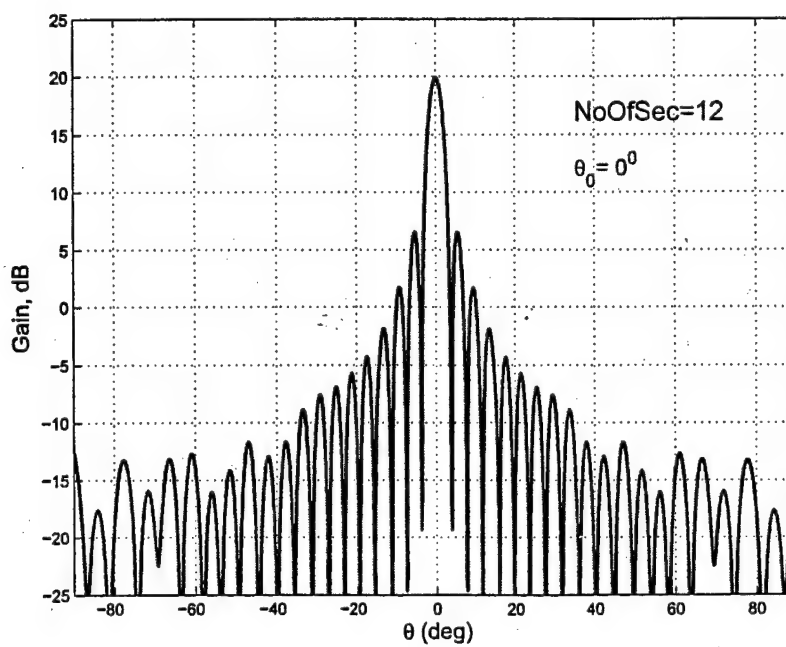


Figure 2.26: Gain pattern for of 12-gon array

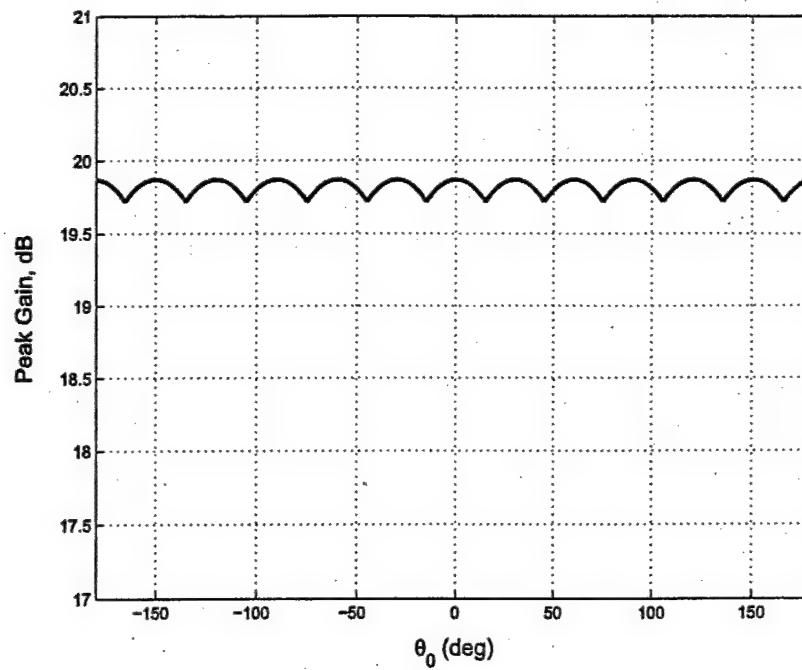


Figure 2.27: Peak gain vs. scan angle of 12-gon array

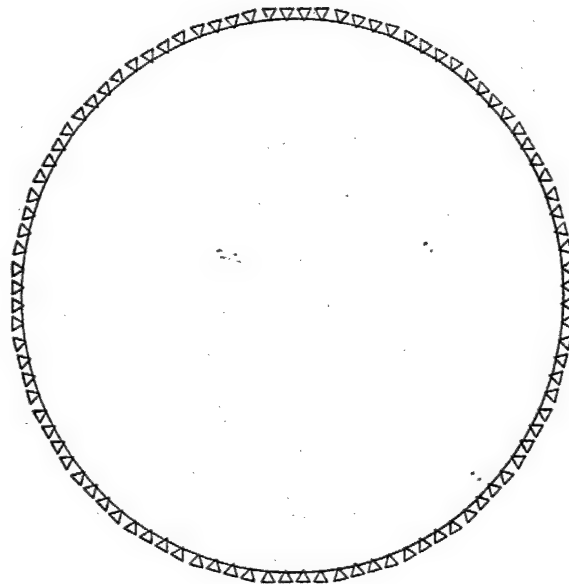


Figure 2.28: 24-gon (twenty four-face) linear array

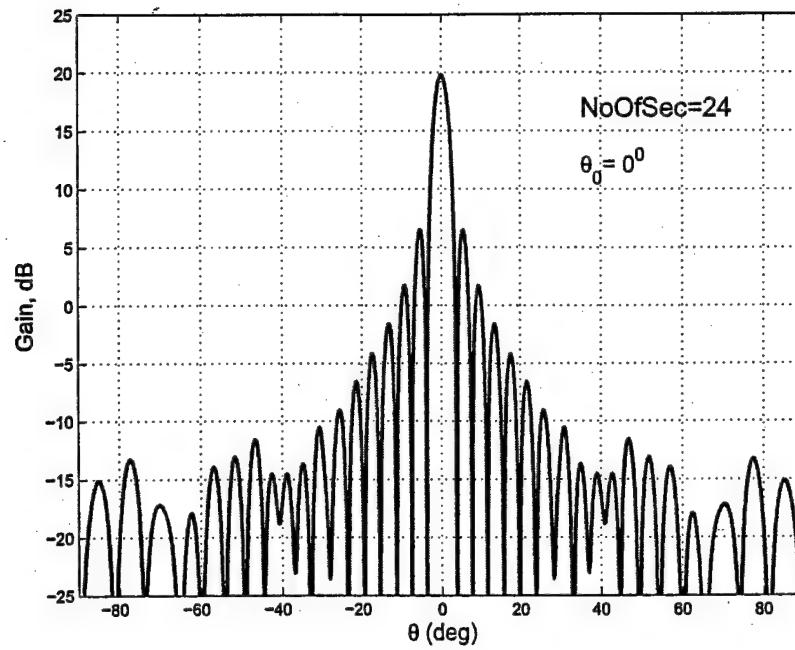


Figure 2.29: Gain pattern of 24-gon array

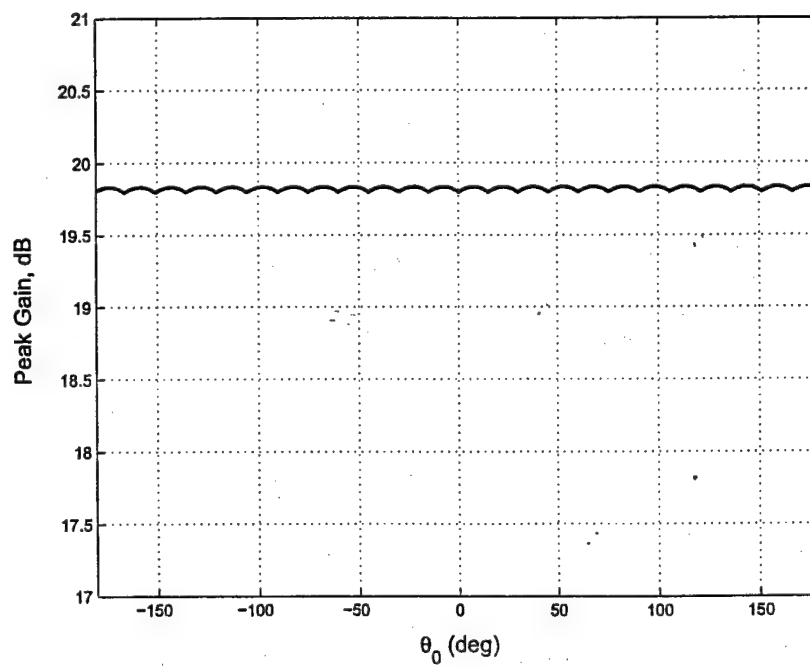


Figure 2.30: Peak gain vs. scan angle of 24-gon array

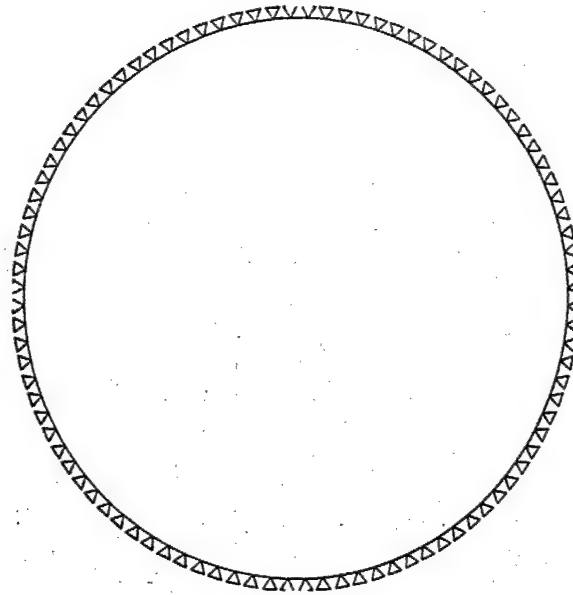


Figure 2.31: 48-gon (forty eight-face linear) array

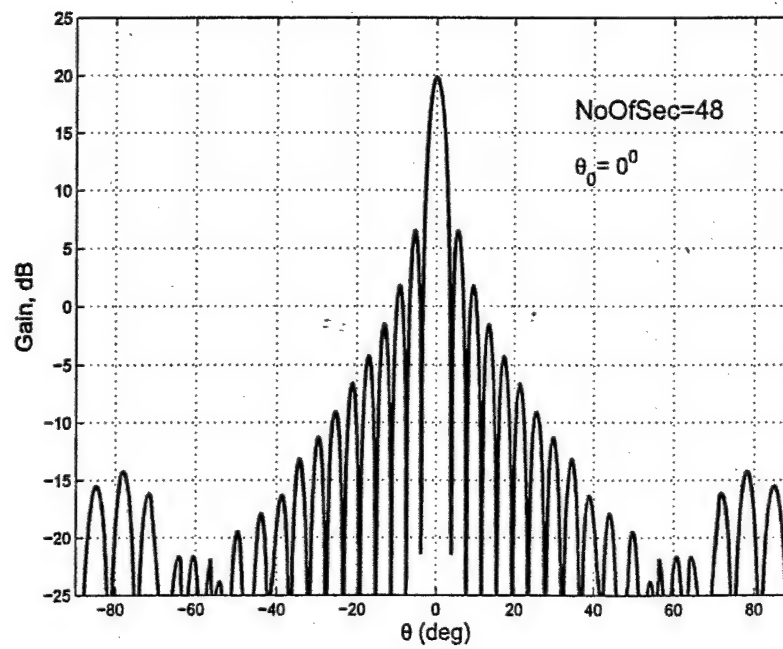


Figure 2.32: Gain pattern of 48-gon array

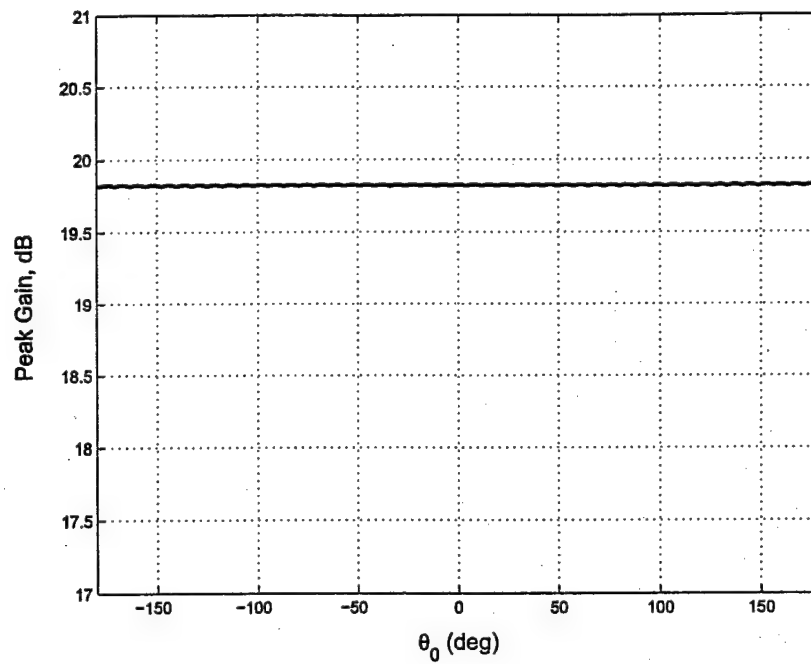


Figure 2.33: Peak gain vs. scan angle of 48-gon array

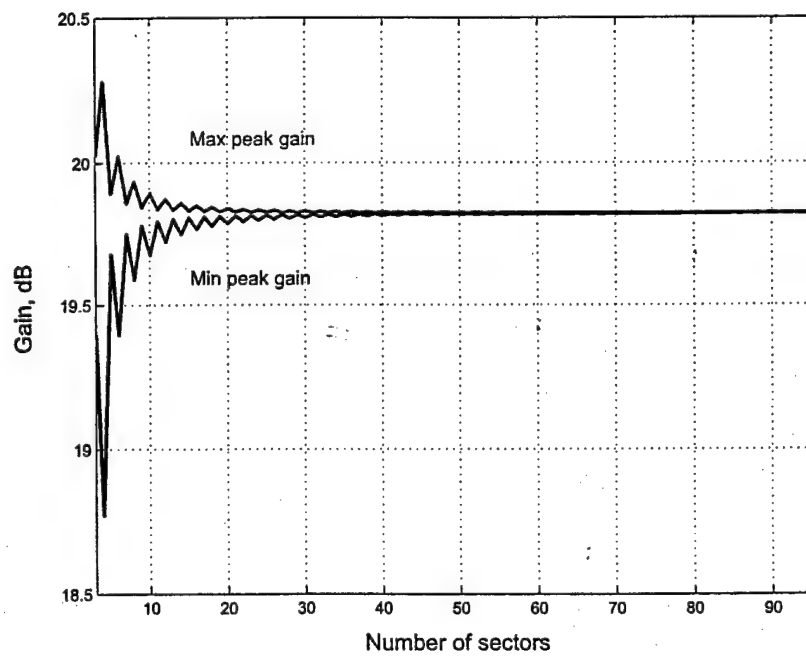


Figure 2.34: Minimum (blue) and maximum (red) array peak gain vs. number of polygon faces

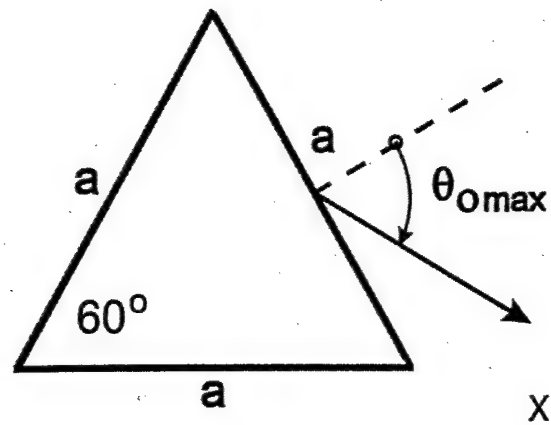


Figure 2.35: Pyramid type or three-face planar arrays

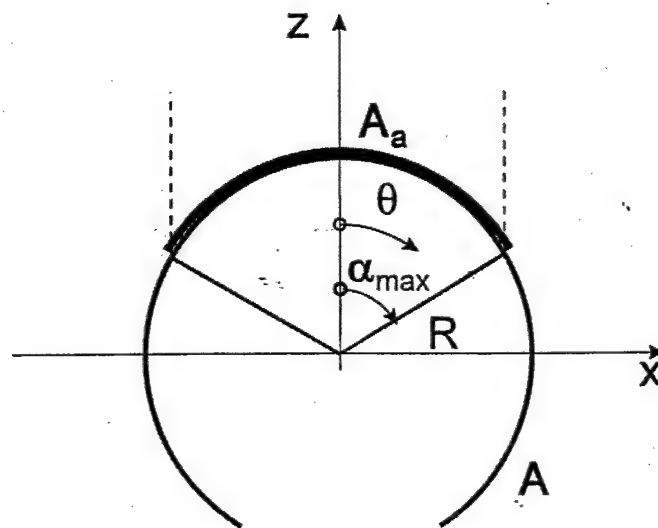


Figure 2.36: Spherical array showing active sector in red

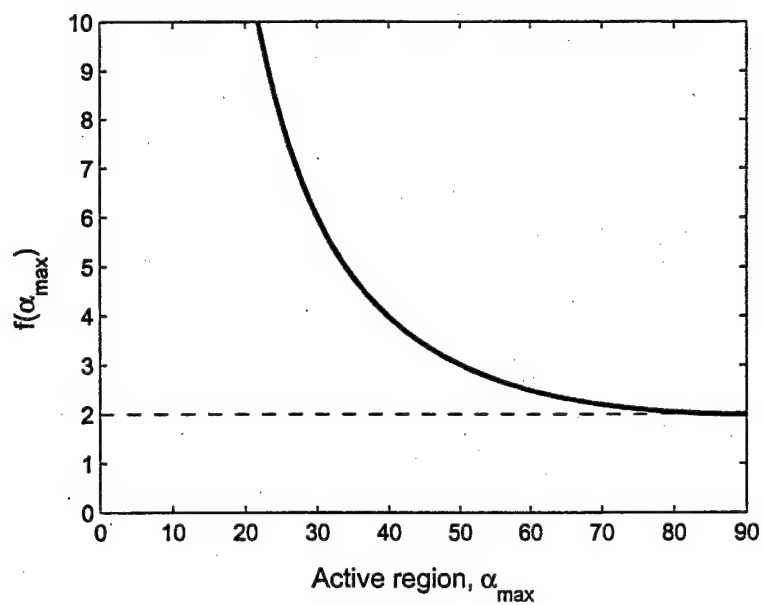


Figure 2.37: Active array area vs. α_{\max}

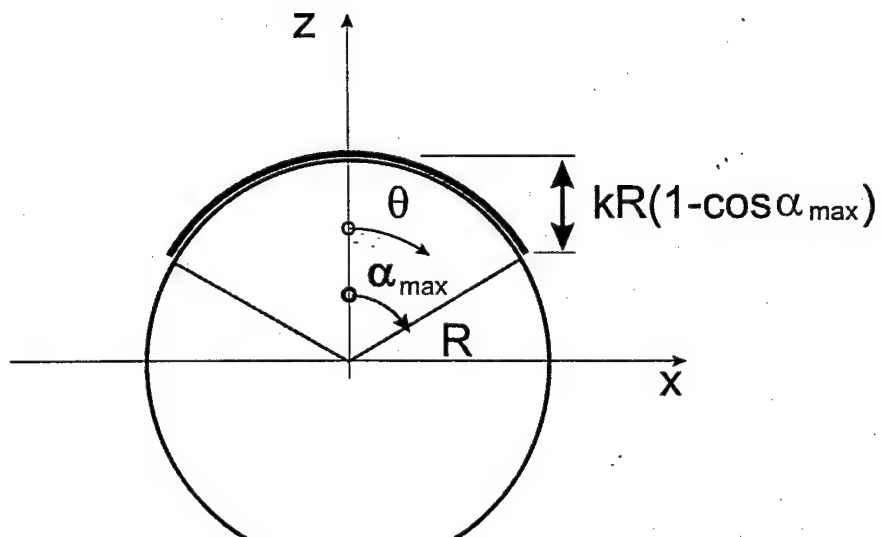


Figure 2.38: Spherical array showing relevant geometrical parameters

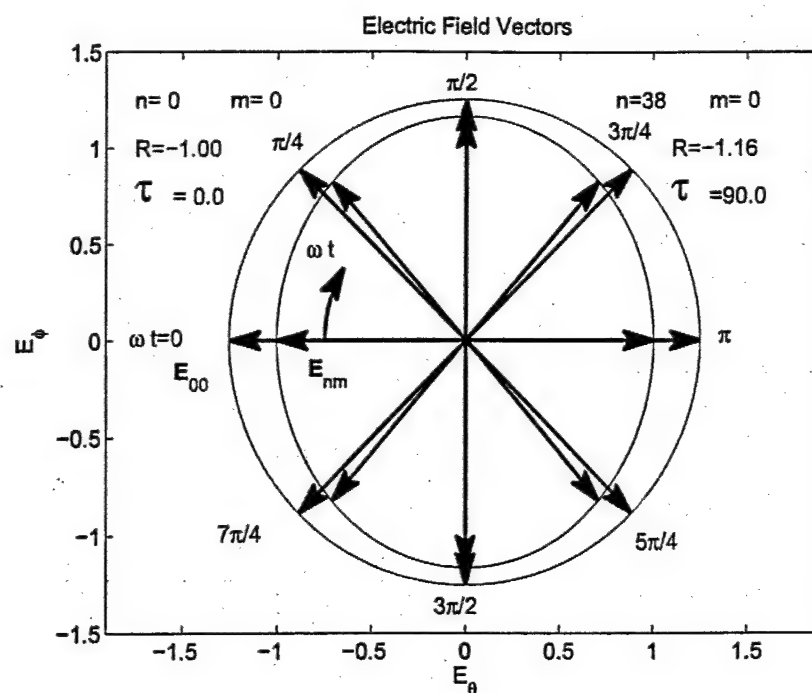


Figure 2.39: Polarization ellipse, for $(0,0)$ element (red) and $(38,0)$ element (blue)

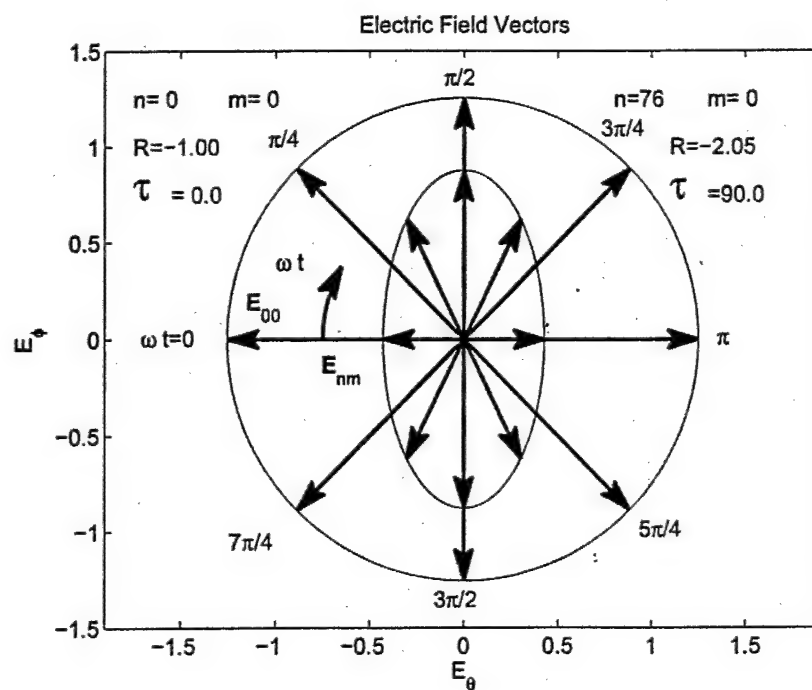


Figure 2.40: Polarization ellipse, for $(0,0)$ element (red) and $(76,0)$ element (blue)

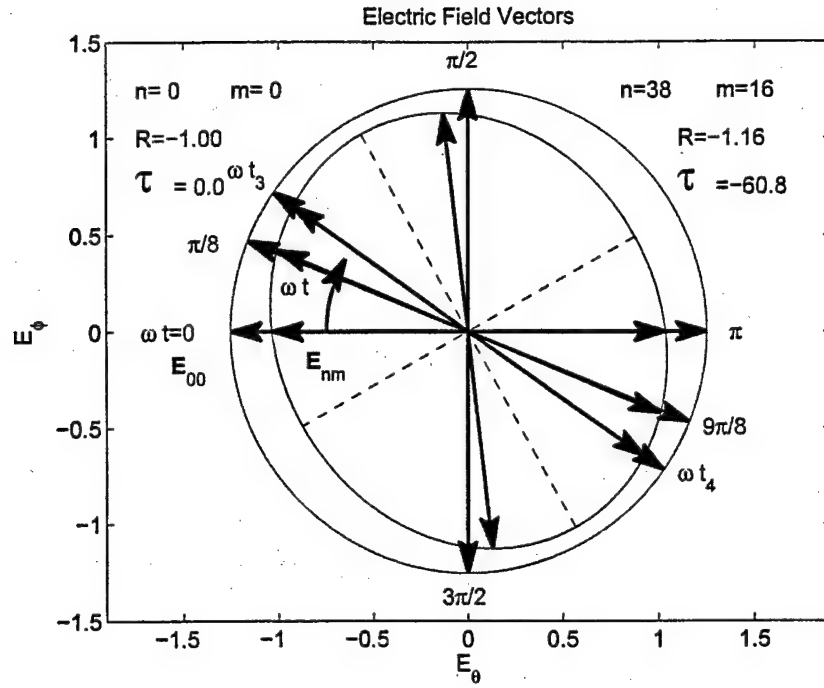


Figure 2.41: Polarization ellipse, for (0,0) element (red) and (38,16) element (blue)

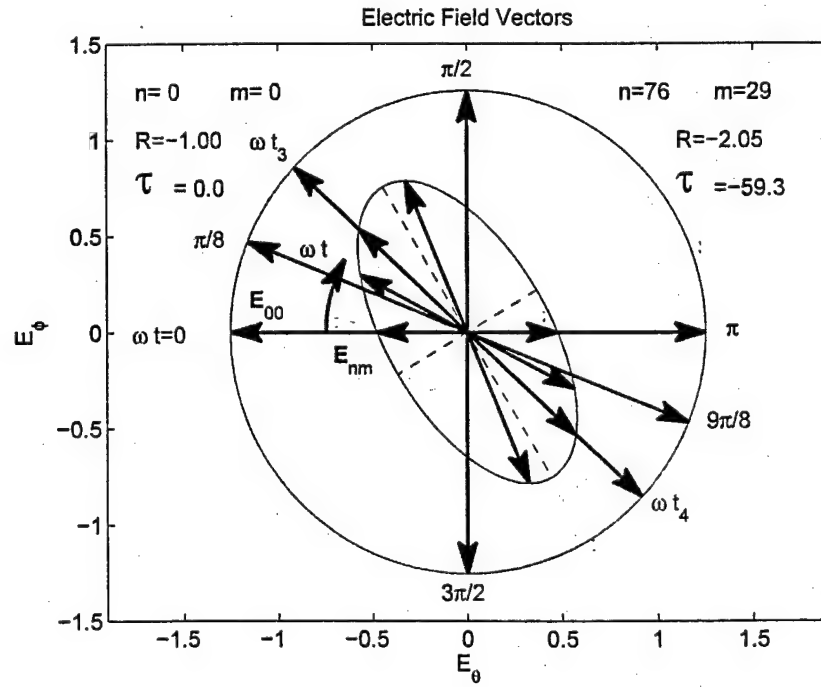


Figure 2.42: Polarization ellipse, for (0,0) element (red) and (76,29) element (blue)

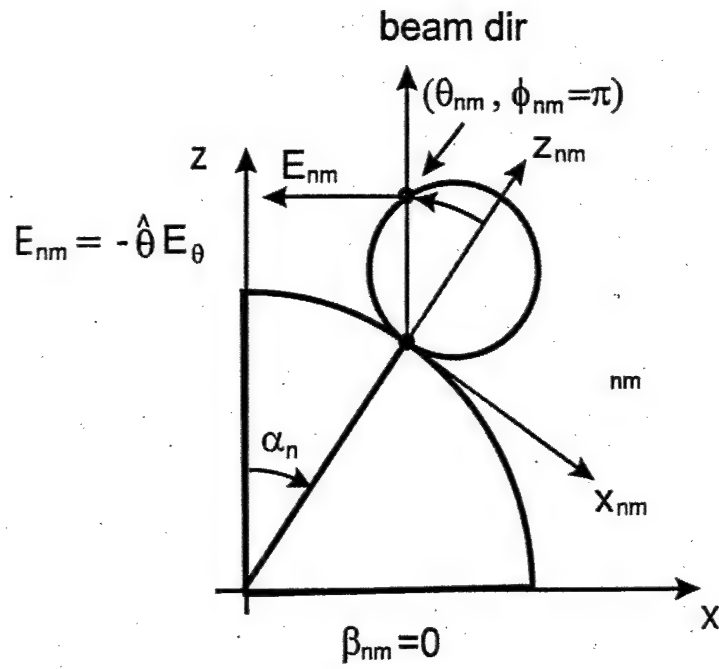


Figure 2.43: Electric field vector E_{nm} in x - z plane pertaining to $(n, m = 0)$ element

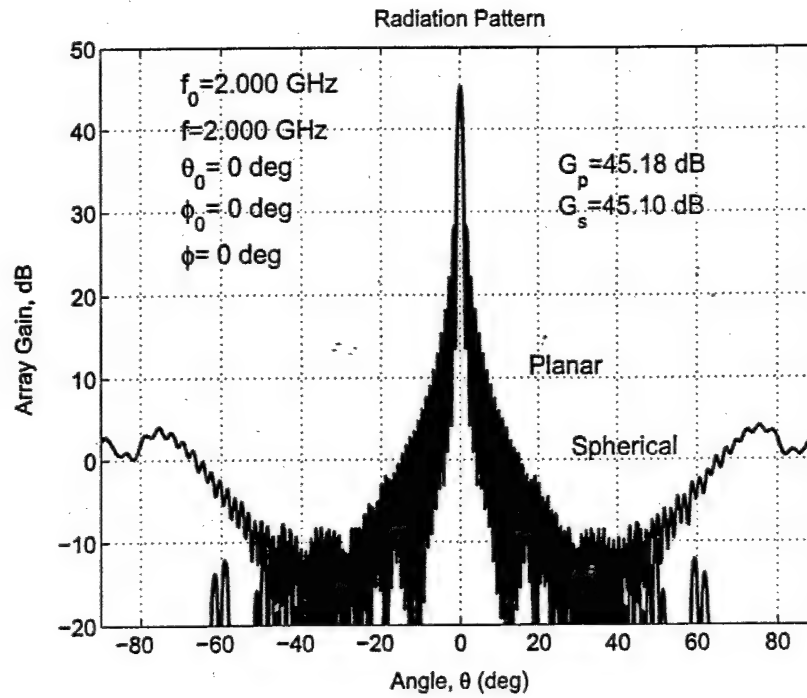


Figure 2.44: Radiation Pattern, $\phi = 0^\circ$ cut, $c_i = 1$

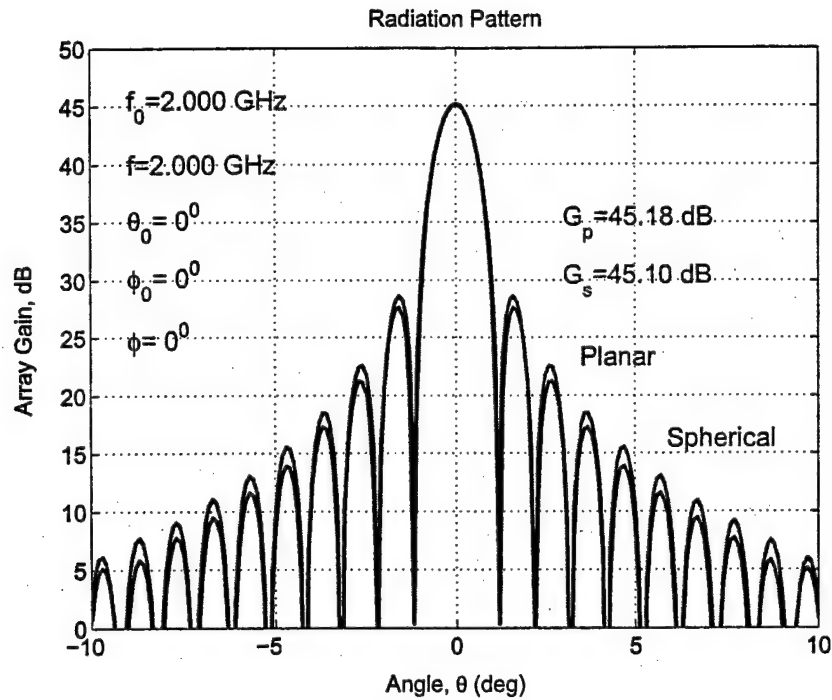


Figure 2.45: Radiation Pattern, $\phi = 60^\circ$ cut, $c_i = 1$, expanded scale

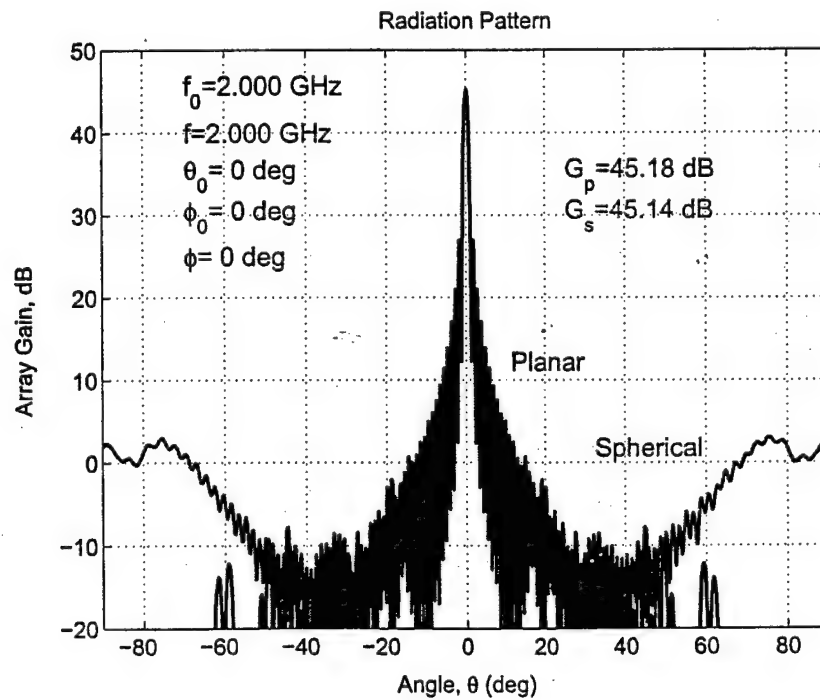


Figure 2.46: Radiation Pattern, $\phi = 0^\circ$ cut, $c_i = \sqrt{\cos \theta}$

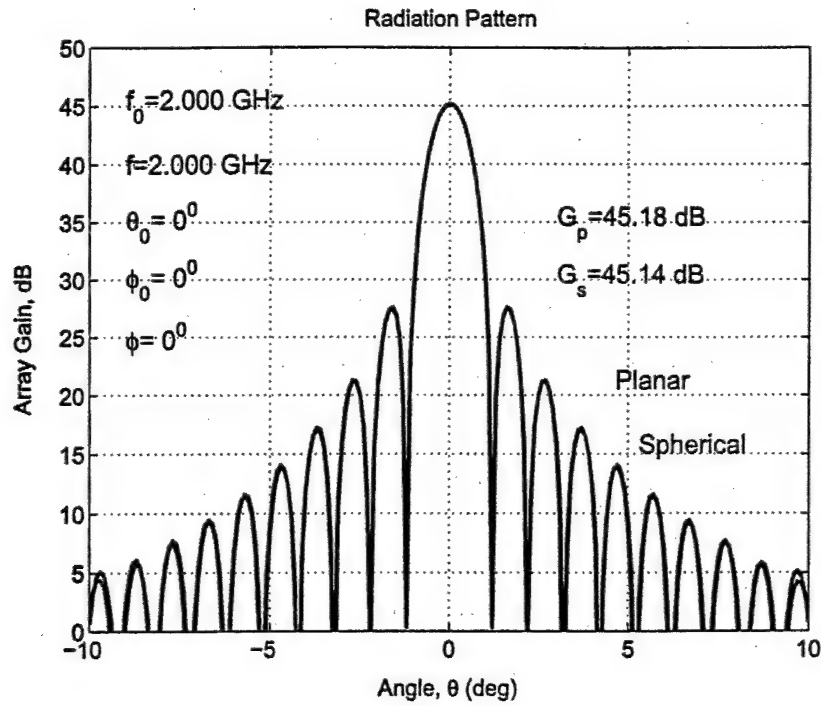


Figure 2.47: Radiation Pattern, $\phi = 0^\circ$ cut, $c_i = \sqrt{\cos \theta}$, expanded scale

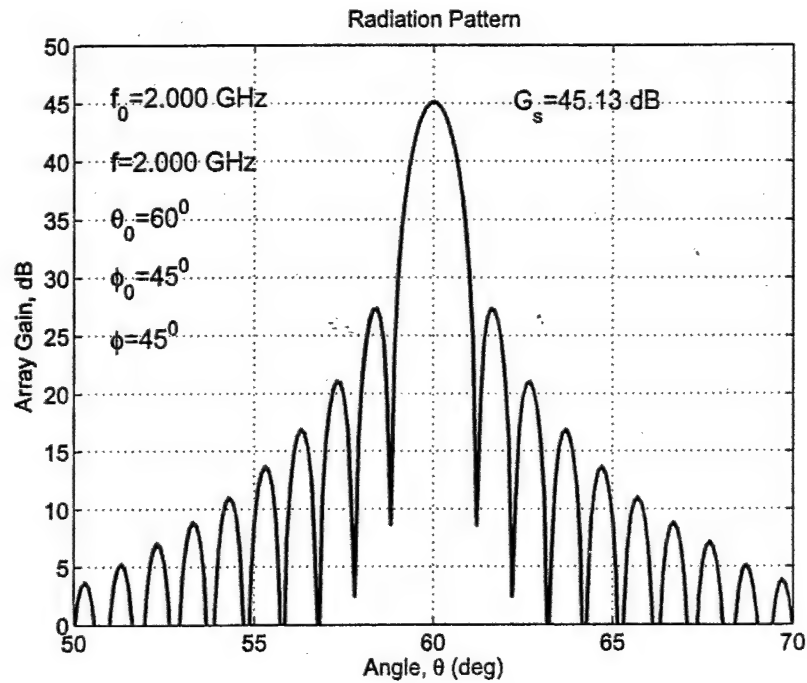


Figure 2.48: Radiation Pattern, $(\theta_0, \phi_0) = (60^\circ, 45^\circ)$, $\phi = 45^\circ$ cut

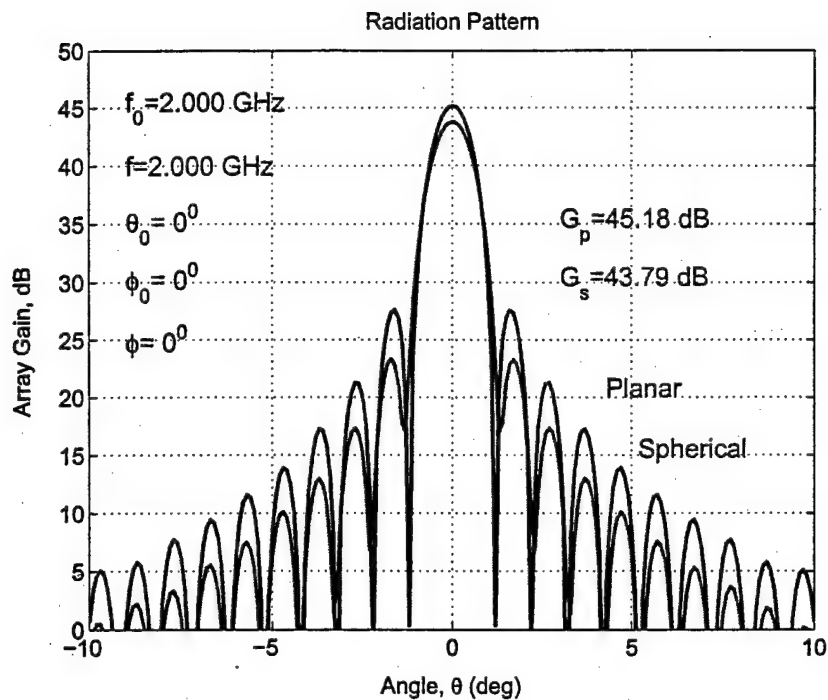


Figure 2.49: Radiation Pattern, $\phi = 0^\circ$ cut

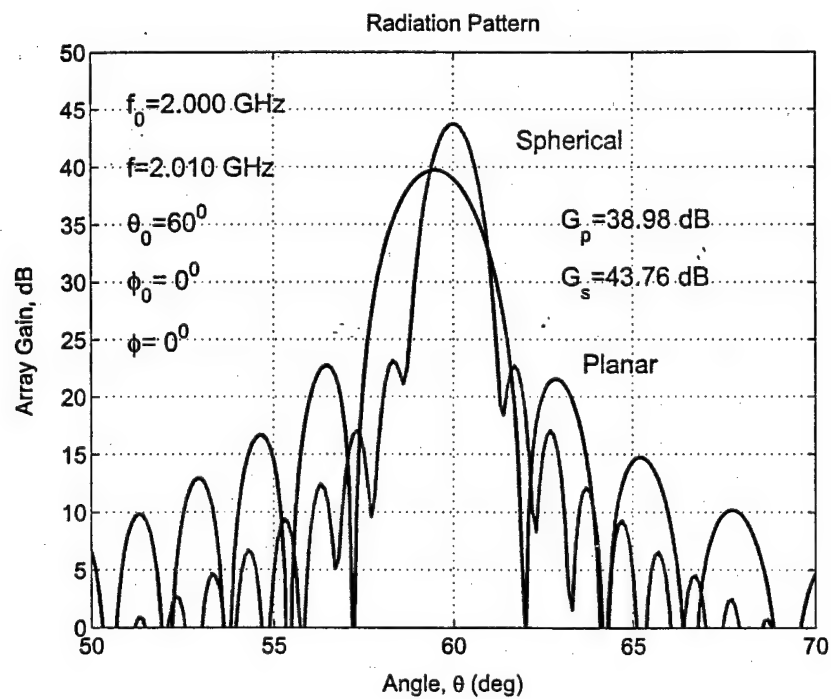


Figure 2.50: Radiation Pattern, $\phi = 60^\circ$ cut

Chapter 3

Geodesic Dome Phased Array Antenna

3.1 Antenna Architecture

In the previous chapter we showed that a spherical array is the optimum geometry for hemispherical coverage in terms of number of elements, which directly translates into array cost, and performance. With all these advantages, however, spherical arrays have not been used in practice primarily because the fabrication and assembly of the Beamforming Network (BFN), are much more difficult than for architectures based on planar array geometry.

In this chapter we propose a design architecture, the Geodesic Sphere/Dome (GS/D) Phased Array Antenna, that preserves all the advantages of spherical arrays while its fabrication is based on well developed, easily manufactured planar array technology [2, 3]. The GD phased array antenna structure consists of a number of near-equilateral triangular planar subarrays arranged in an icosahedral geodesic dome configuration. It is important to mention that the Geodesic Sphere Phased Array antenna architecture is not limited to the proposed icosahedron geometry, but can be derived from any one of the five regular polyhedra (platonic solids) or one of the 15 semi-regular polyhedra (Archimedean solids). As an illustrative example, a geodesic dome phased array antenna is shown in Figure 3.1. It consists of 300 near-equitriangular flat panel subarrays obtained by 4-frequency subdivision of the icosahedron. The dome rests on a building housing a computer and other operational and support equipment.

This "faceted" dome antenna provides full hemispherical coverage for gateway and control (TT&C) in satellite communication systems and/or radar for air/space surveillance while at the same time exhibiting the following advantages over the existing pyramid-like and conformal structures:

1. Keeping the architecture locally planar and globally spherical allows the array to be constructed in flat panel pieces and then assembled to form the hemispherical dome structure. This is technically and economically viable because:

- the design overcomes the fabrication complexity associated with conformal (curved) structures since the subarray fabrication is based on well-developed, easily manufactured planar array technology.

- the geodesic dome is an easily realized structure with well-known mechanical design and fabrication techniques.

2. The Geodesic Dome antenna preserves all the advantages of spherical phased arrays [3] such as:

- uniform beams over a hemisphere
- high gain
- high instantaneous bandwidth
- low mismatch and polarization losses
- low input power
- low life cycle cost
- requiring about 20% fewer radiating elements than other array configurations.

Thus the proposed Geodesic Dome architecture presents a highly desirable, but up to this day, impractical spherical array design that provides hemispherical coverage and consequently can be used for communications and control with multiple satellites over the entire sky. This optimum design is achieved by marrying two mature and well established technologies: flat panel phased array technology and geodesic dome structures.

Although in this report we consider the (spherical) geodesic dome antenna, another similar array configuration, the geodesic dome/cylinder that provides hemispherical coverage is shown in Figure 3.2. The top section (hemisphere or cap) is the same as in Fig. 1, while the bottom part of Figure 3.1 is replaced by the faceted cylinder. This configuration provides about 0.5 dB more gain at the horizon than full GD configuration which is highly desirable in satellite communications. In addition the dome/cylinder architecture may be easier to construct. However, in contrast to full dome, off-zenith beams are non-uniform.

3.2 Geodesic Dome Structure - Background

As previously mentioned, the geodesic sphere phased array antenna structure is based on one of the five regular polyhedra or on one of the 15 semi-regular polyhedra, all of which could be inscribed in a sphere [8, 9, 10, 11]. The five regular polyhedra, also known as platonic solids, have edges of the same length and identical polygon faces. They are the tetrahedron, cube, octahedron, dodecahedron, and icosahedron. Most geodesic domes are based on the spherical icosahedron, which is the result of the stereographic projection of the icosahedron onto its circumscribed sphere. The icosahedron shown in Figure 3.3 has 20 equilateral triangular faces, 12 apexes, and 30 edges. Thus, the use of the icosahedron as the basis for the geodesic subdivision of a sphere results in the division of the spherical surface into 20 equilateral spherical triangles. This is the maximum number of equilateral triangles into which a sphere can be divided. For a geodesic dome antenna requiring hemispherical coverage, the icosahedron can be truncated as shown in Figure 3.4. For most practical applications, however, an icosahedron is a poor or too crude approximation of a spherical surface. The spherical surface can be made smoother by increasing the number of flat panels (facets). This can be achieved by subdividing each of the 20 equilateral triangular faces of the icosahedron (also called icosas) into a number of smaller triangles, or subarrays in antenna terms. The number of triangles depends primarily on the required geodesic dome array performance and subarray architecture, and fabrication complexity and cost. This subdivision is referred to as a frequency, which is the number of segments into which the icosahedronal edge has been divided by a particular type of breakdown.

There are two basic types of subdivision, Class I (Alternate breakdown) and Class II (Triacon breakdown). Class I subdivision can be realized by two principal methods: Method 1 which is based on similarity of triangle shape and Method 2 based on similarity of triangle size.

In Class I Method 1, and a breakdown scheme with frequency ν , each edge of the spherical icosahedron is divided into ν equal segments, and the points of subdivision are joined with a three-way grid. Each face of the spherical icosahedron is thus divided into

$$N_{\Delta} = \sum_{n=1}^{\nu} (2n - 1) \quad (3.1)$$

smaller planar equilateral triangles, Figure 3.5. The division points are then radially projected (pushed) outward onto the surface of its circumscribing sphere, see Figure 3.6. Connecting these points with straight lines produces $20N_{\Delta}$ planar triangles (facets/subarrays) approximating the spherical surface. It must be pointed out that the triangles resulting from such subdivision are no longer equilateral and that the number of different triangles increases with frequency of subdivision. Class I, Method 2 is the same as Class I, Method 1, except instead each edge of equilateral triangle i.e., icosas is divided into ν equal segments, here the subtended angle by the edge of each icosas face is divided into ν equal angles.

We illustrate both methods on a simple example, icosas with 3ν subdivision frequency. The basic principle of subdivision for Method 1 is shown in Figure 3.7. In this figure, AB is the edge or side length of the equilateral triangle of Figure 3.5. The edge is divided into three equal sectors where $AC = CD = DB = AB/3$. The spherical coordinates of respective vertexes and chord factors are given in Table 3.1. Similarly, Method 2, divides

the θ coordinates equally down the edge of the icosahedron triangle, making all edge struts equal, as shown in Figure 3.8. In this figure $\alpha = \beta = \gamma = 63.435/3$. Table 3.2 shows the respective spherical coordinates of the vertices and chord lengths.

To observe the basic characteristics of both methods, we unfold a spherical sector corresponding to a single icosahedron. Twenty of either can be connected together to make a spherical dome. By simply observing the unfolded diagrams, Figure 3.9 and Figure 3.10, we see that in the case of equal chord factors along the icosahedron edge (Method 2), the small triangles vary less in size, but vary more in shape. Disregarding for the moment the corner triangles A, which are always a special case, we notice that the rest of the icosahedron face is shared by three each of two quite noticeably isosceles triangles, B and C. But when we vary the edge chord factors (Method 1) the corner triangles D stay virtually the same shape as before, while the rest of the icosahedron face divides itself into six identical triangles E, which come much closer to being equilateral than either B or C in the other diagram (see Figure 3.9).

In short, by letting the triangle sizes vary more we can keep their shapes more nearly constant. This seems preferable structurally as well from an array element arrangement perspective. To elaborate on the later, it is known that for hemispherical coverage, the array grid must be equilateral triangular. This means that the subarrays are also equilateral triangular. On the other hand, for efficient use of the aperture area, it is desirable to place the largest possible subarray into a subicosahedron triangle (dome facet). This can be achieved when a subicosahedron is as nearly equilateral as possible. In this case, the nonuniform space around the subarray is minimum.

Odd and even frequencies can be used for Class I. Figure 3.11 illustrates the subdivision of a spherical equilateral triangle with (a) 2-frequency, (b) 4-frequency and (c) 6-frequency subdivision. The characteristic of this subdivision type is that the dividing lines are parallel to the edges of the original triangles. A full dome using Class I, Method I, with subdivision frequency $\nu = 2$ is shown in Figure 3.12.

The Triacon breakdown scheme (Class II) is similar to the Alternate breakdown scheme except the dividing lines are perpendicular to the edges of the polyhedron face, Figure 3.13. As noted in [10], the Class II scheme does not really break down the icosahedron face from which it derives its frequency count, but smaller and nonequilateral triangle which consists of two icosahedron symmetry triangles ADE (in red) and CDE back to back, forming a diamond ADEC, as also shown in Figure 3.13 for 2ν subdivision frequency. A full sphere with 2ν Class II subdivision is shown in Figure 3.14. The two icosahedron facets are indicated with broken-lines, and the Class II triangle is filled in red color.

Further subdivision of the icosahedron face is possible according to the same scheme described above. An example of 4ν subdivision is shown in Figure 3.15.

Since Class II breakdown is based on symmetrical subdivision, only even frequencies are possible.

For geodesic dome phased array applications the Alternate breakdown is superior because the edges of the triangles lie on an equatorial circle, which leads to a simple design of a hemisphere with planar connections. The connection is an important criterion in the design of a geodesic dome antenna. Planar connection cannot be obtained with the Triacon breakdown scheme. Moreover, in the Alternate breakdown the resulting triangles are more nearly equilateral than in Triacon breakdown, which is preferable in subarray design.

Why icosahedron?

As already mentioned above, the geodesic dome antenna could, in principle, be constructed from any regular or semi-regular polyhedra. We selected the icosahedron as the basis for the geodesic dome antenna structure because of its distinct structural and electrical characteristics. In comparison to other polyhedra, icosahedron-based domes have the following advantages [10]:

- (1) lower subdivision frequency needed for comparable average chord factor, which results in a smaller number of required subarrays;
- (2) angles uniformly averaged among nearly equilateral triangles and less variation in the lengths of members for a comparable average chord factor, which results in a more uniform size and shape of the triangular subarrays;
- (3) curvature is more uniformly distributed, preserving uniform beams over a hemisphere;
- (4) simple truncation to a planar surface, allowing planar support structure.

Which Class?

Class I keeps component variations within narrower bounds, but at the cost of employing a larger inventory of different strut lengths. It permits odd as well as even frequencies. Class I icosahedra have uninterrupted equators at all even frequencies and the edges of the triangles lie on an equatorial great circle which facilitates a simple hemisphere connection with planar supporting structure. In the alternate breakdown, Class I, Method 1, the resulting triangles are more nearly-equilateral than in Class I, Method 2.

Class II yields even frequencies only. Used with icosahedron, it introduces some truncation problems, since any equator breaks through some of the subdividing triangles.

Which frequency?

The subdivision frequency depends on acceptable sphericity and the number and size of the subarrays. In general, to minimize the component inventory we use the lowest frequency we can. For our 10 m geodesic dome array, the driving factor is fabrication of the largest possible subarray. Triangular panels of 1 m on a side seem to be a challenging but not impossible task. With this in mind we found that subdivision frequency of 6 gives very good sphericity, with a relatively small number of facets (675) of reasonably large size.

Decision!

Based on the above factors, for our 10m dome we selected icosahedron using Class I, Method 1 breakdown scheme with subdivision frequency $\nu=6$. The Geodesic Dome phased array antenna is shown in Figure 3.16. More practical design, a hemisphere with cylindrical base is shown in Figure 3.17.

There are numerous publications and computer codes giving all the details (lengths and angles) for different configurations and subdivision types. A computer algorithm for obtaining the coordinates of vertices, chord factors, and dihedral angles of ν -frequency spherical icosahedral domes is given in [10].

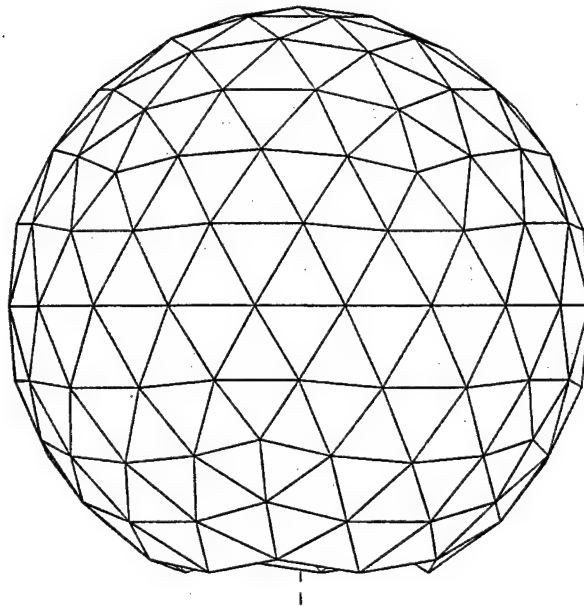


Figure 3.1: Geodesic dome phased array, subdivision frequency $\nu=4$

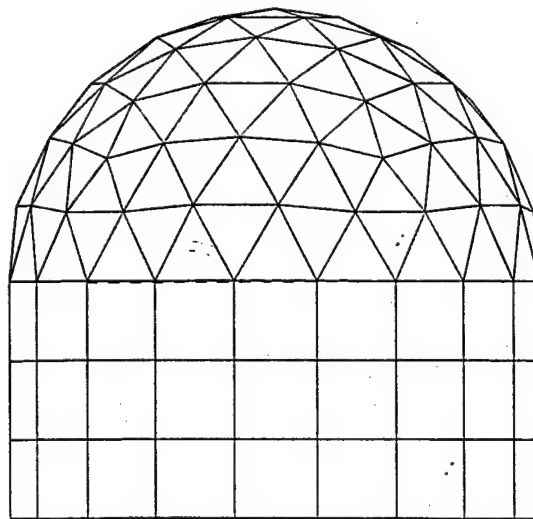


Figure 3.2: Geodesic dome/cylinder, subdivision frequency $\nu=4$

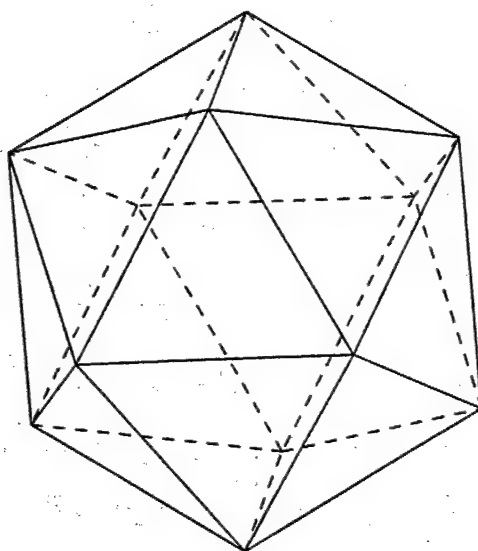


Figure 3.3: An icosahedron

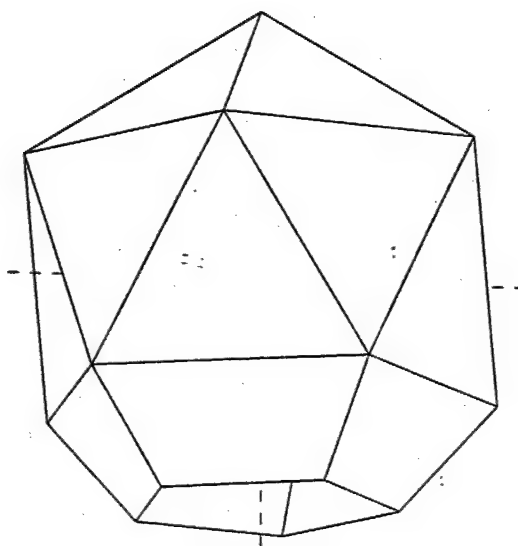


Figure 3.4: A truncated icosahedron

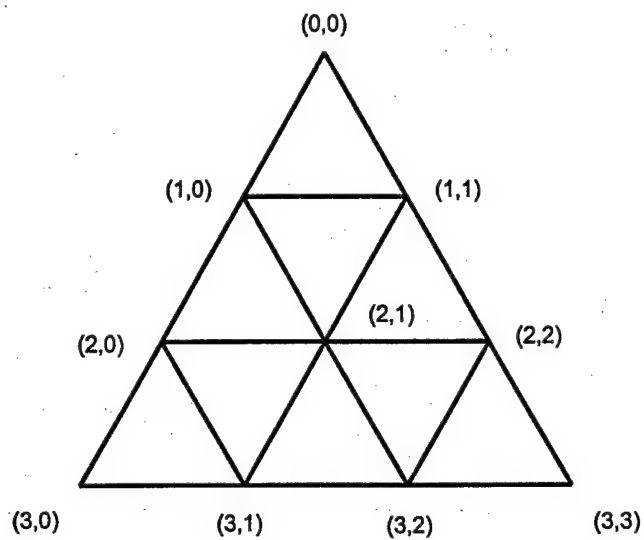


Figure 3.5: Equilateral triangle illustrating Class I-Method 1, 3ν subdivision

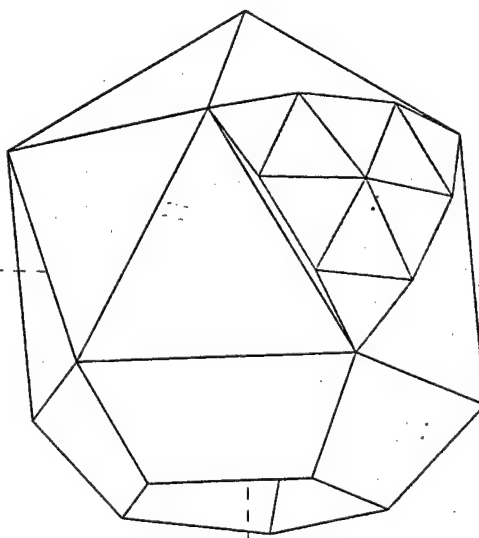


Figure 3.6: A truncated icosahedron showing sub-icosa triangles

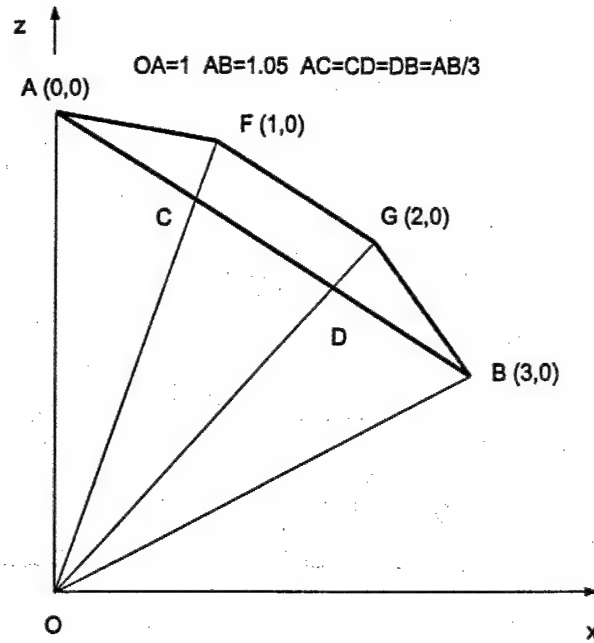


Figure 3.7: 3 ν Icosa illustrating Class I-Method 1 subdivision

	θ	ϕ	Chord factors	
0,0	0	0	0,0 / 1,0	0.348
1,0	20.077	0	1,0 / 2,0	0.403
2,0	43.358	0	1,0 / 1,1	0.403
3,0	63.435	0	2,0 / 2,1	0.412
1,1	20.077	72		
2,1	37.377	36		
3,1	59.008	22.386		
2,2	43.358	72		
3,2	59.008	49.614		
3,3	63.435	72		

Table 3.1: Coordinates of vertices and chord factors ($R=1$) for Icosa, Method 1, $\nu=3$

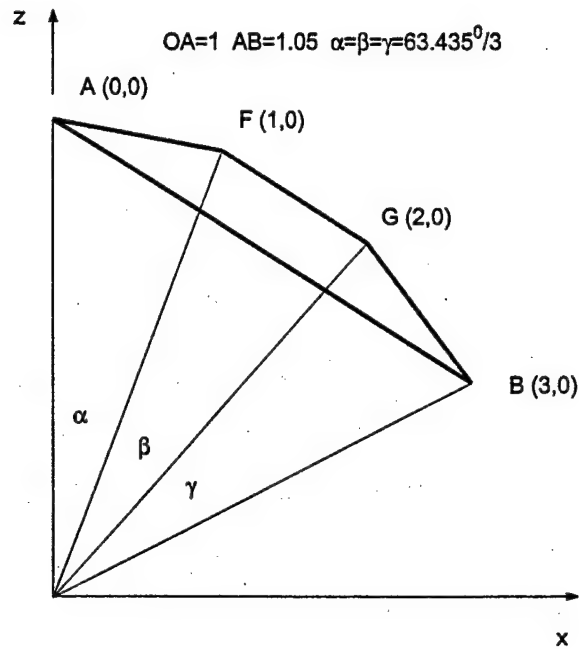


Figure 3.8: 3 ν Icosa illustrating Class I-Method 2 subdivision

	θ	ϕ	Chord factors	
0,0	0	0	0,0 / 1,0	0.367
1,0	21.145	0	1,0 / 2,0	0.367
2,0	42.29	0	1,0 / 1,1	0.424
3,0	63.435	0	2,0 / 2,1	0.404
1,1	21.145	72		
2,1	37.375	36		
3,1	58.881	23.624		
2,2	42.29	72		
3,2	58.881	48.375		
3,3	63.435	72		

Table 3.2: Coordinates of vertices and chord factors ($R=1$) for Icosa, Method 2, $\nu=3$

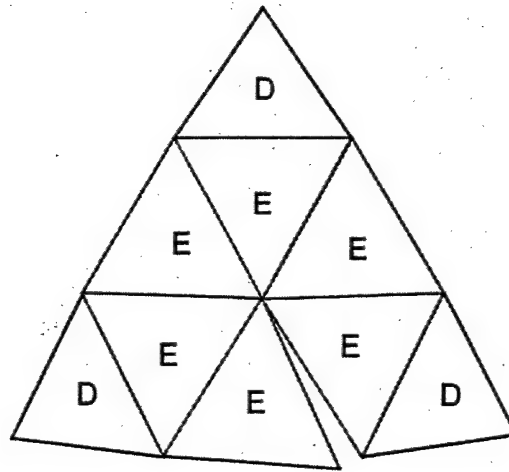


Figure 3.9: 3 ν Icosa, Method 1, Equal chords before projection

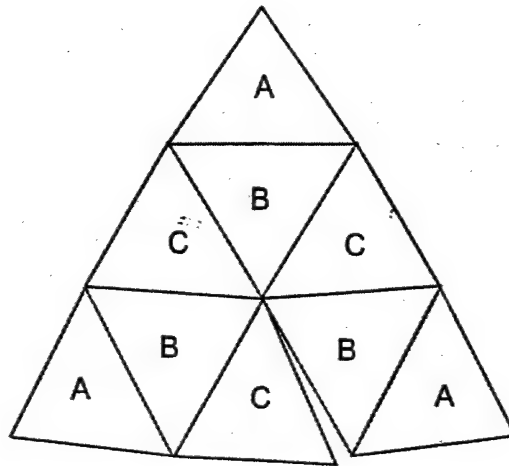


Figure 3.10: 3 ν Icosa, Method 2, Equal edge (angle) division

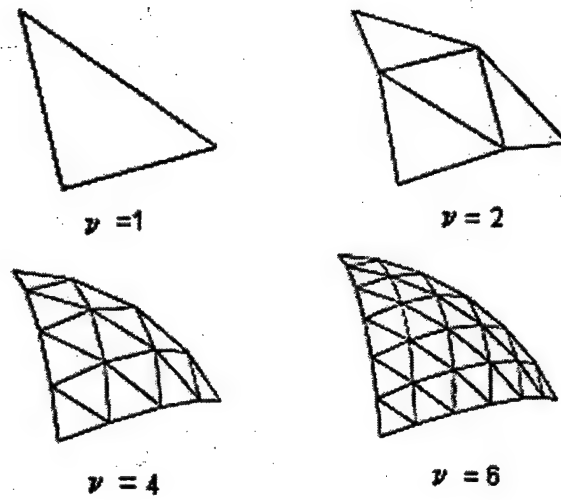


Figure 3.11: Frequency of subdivision - Class I, Method 1

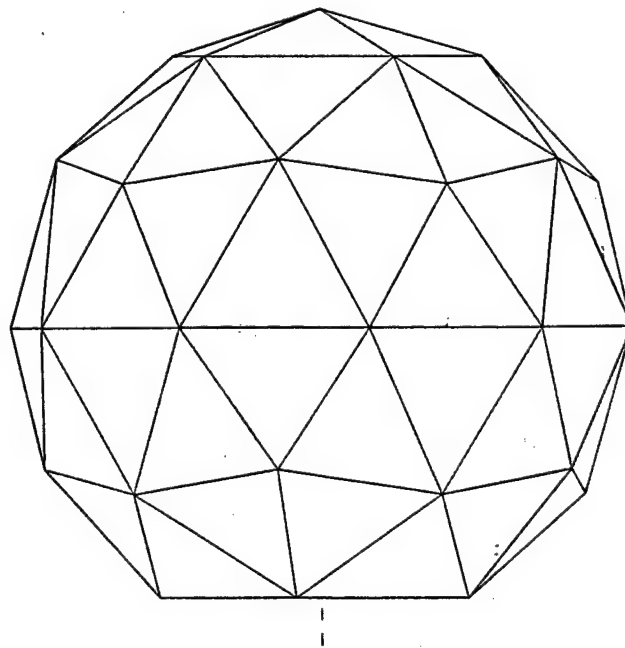


Figure 3.12: Geodesic Dome, $\nu = 2$

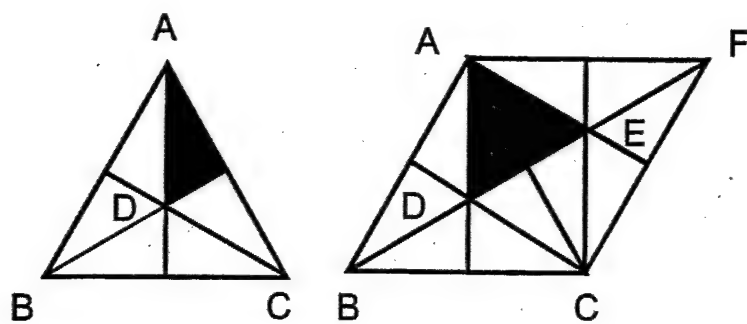


Figure 3.13: Class II- 2ν subdivision

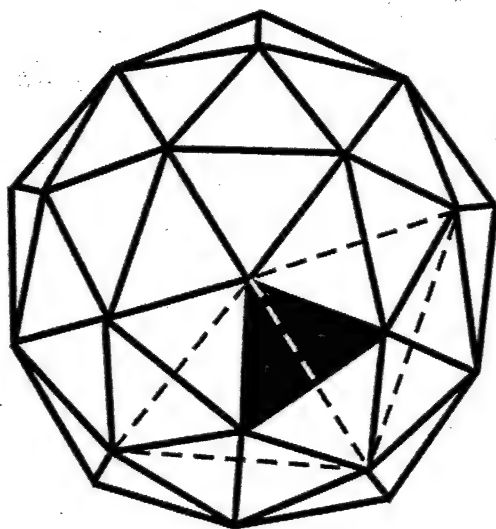


Figure 3.14: Class II- 2ν subdivision - full sphere, from [10]

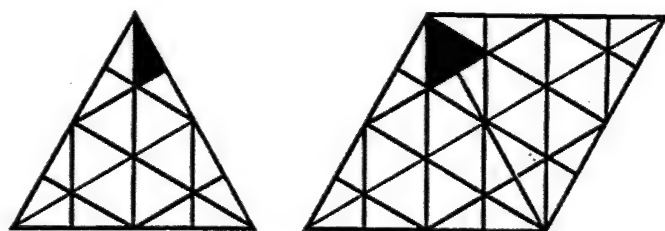


Figure 3.15: Class II- 4ν subdivision

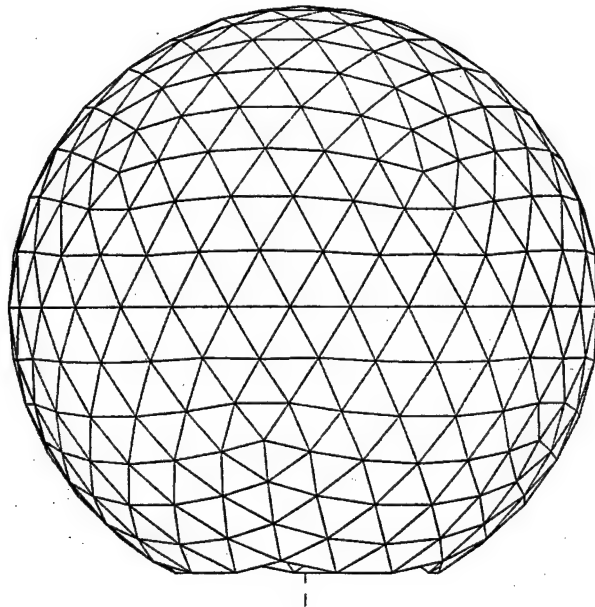


Figure 3.16: Class I - 6ν subdivision, Sphere

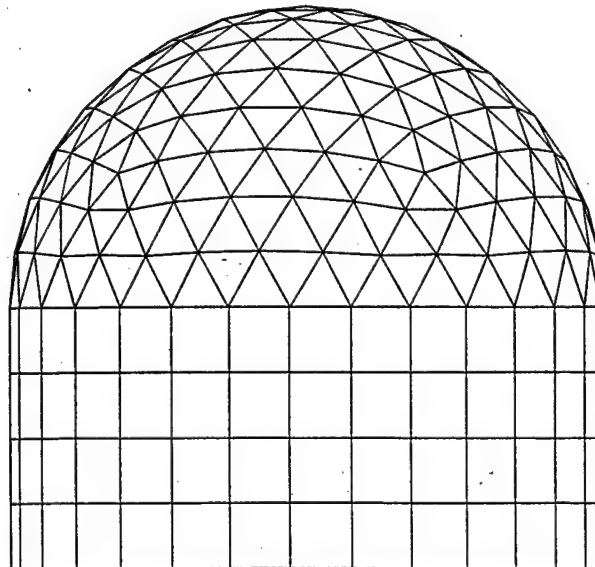


Figure 3.17: Class I - 6ν subdivision, Hemisphere/Cylinder

Chapter 4

Design of Geodesic Dome Structure

4.1 Global coordinate systems

A global coordinate system (x, y, z) with unit vectors $(\hat{x}, \hat{y}, \hat{z})$ with the origin at the center of the dome $O(0, 0, 0)$ is shown in Figure 4.1. The respective spherical coordinates (r, θ, ϕ) with unit vectors $(\hat{r}, \hat{\theta}, \hat{\phi})$ are also shown in the same figure.

4.1.1 Counting icosas's

Figure 4.2 shows the icosahedron in global coordinates. As already mentioned, the icosahedron consists of 20 equilateral triangular faces (icosas). It has 20 apexes and 30 edges. The icosas are arranged in three rows designated by index K counted from top to bottom. First row, ($K = 1$) also called top cap, contains 5 icosas. Index L specifies the location of icosas in K th row in $+\phi$ (CCW) direction starting at x - z plane. The middle section of the icosahedron ($K = 2$) has 10 icosas, while the bottom cap ($K = 3$) also contains 5 icosas. In short, each icosas is designated by two indices (K, L) where for $K = 1$ and $K = 3$, $L = 1$ to 5 and for $K = 2$, $L = 1$ to 10, as shown in Figure 4.3 and Figure 4.4.

4.1.2 Counting sub-icosas's

For 6ν subdivision, there are 36 subicosas's in each icosas, Figure 4.5. The vertices are designated by a two digit marker as shown in Figure 4.5, the top vertex being (0,0). The last point in the last row bottom row is (6,6). The icosas are also designated by two indices (N, M) where N denotes the row and M denotes the column starting at the tip of the icosas, see Figure 4.6. Note that for icosas facing up the (N, M) runs from top to bottom, left to right whereas for icosas facing down (N, M) runs from bottom to top and right to left. In this manner the (N, M) -th sub-icosas will be identical in all 20 icosas.

4.1.3 Class I, Method 1, 6ν , icosahedral coordinates

We need chord factors only for the breakdown edges that lie partially or wholly inside the symmetry triangle. For 6ν subdivision this means only the twelve edges drawn in red in Figure 4.5 for $\Delta\#1$, thus twelve out of sixty-three. Thus, the only coordinates we need are

the end points of those twelve edges; a total of ten coordinates. The rest of the system repeats symmetrically; thus (0, 0) – (1, 0) corresponds to (5, 0) – (6, 0); (6, 0) – (6, 1) corresponds to (6, 5) – (6, 6) etc. For icosahedron, Class I, Method 1 subdivision, the spherical coordinates of these vertices are given in Table 4.1. The rest of the vertex coordinates in Δ #1 can be deduced from the symmetry consideration as mentioned above. For convenience they are listed in Table 4.2. Coordinates of triangle (icosa) No. 2 shown in Figure 4.7 can be generated from data of triangle No. 1 by rotation. They are also given in Table 4.2.

With known coordinates of triangles #1 and #2, triangle sections 3, 4, 5 and 6 which are marked in red in Figure 4.8 and Figure 4.9 can be similarly obtained according to

- 3: $\phi = \phi_1 + 72^\circ$, $\theta = \theta_1$
- 4: $\phi = \phi_2 - 36^\circ$, $\theta = 180^\circ - \theta_2$
- 5: $\phi = \phi_2 + 36^\circ$, $\theta = \text{same as } \Delta \#4$
- 6: $\phi = 72^\circ + \phi_2$, $\theta = \theta_2$.

From this, the rest of the coordinates of the icosahedron can be obtained by rotation using symmetry of the structure. Thus, each triangle is specified in space by three points (corner coordinates) $P_1(R, \theta_1, \phi_1)$, $P_2(R, \theta_2, \phi_2)$ and $P_3(R, \theta_3, \phi_3)$.

Once the spherical coordinates (R, θ, ϕ) of each triangle are known, the respective coordinates in a Cartesian system $P_1(x_1, y_1, z_1)$, $P_2(x_2, y_2, z_2)$ and $P_3(x_3, y_3, z_3)$ can be found from

$$\begin{aligned} x &= R \sin \theta \cos \phi \\ y &= R \sin \theta \sin \phi \\ z &= R \sin \theta. \end{aligned} \quad (4.1)$$

4.1.4 Class I, Method 1, 6ν , chord lengths

The chord factors can be now evaluated from

$$d = \sqrt{2 - 2[\cos \theta_1 \cos \theta_2 + \cos(\phi_1 - \phi_2) \sin \theta_1 \sin \theta_2]} \quad (4.2)$$

where for θ, ϕ we insert values from the above table. Thus to calculate the distance from (0, 0) – (1, 1) we use 0 for values of ϕ_1, ϕ_2 and θ_1 , and 9.3247035 for θ_2 . The chord factor turns out to be 0.162567. Following the same procedure, the rest of the chord factors can be evaluated. They are given in Figure 4.10 for a sphere radius $R = 1$. For any other R , the chord lengths must be multiplied by R . The chord factors ($R = 1$) or the chord lengths ($R > 1$) can be also evaluated from following equations:

$$d_{ij} = \sqrt{(x_i - x_j)^2 + (y_i - y_j)^2 + (z_i - z_j)^2} \quad (4.3)$$

where as already mention (x_i, y_i, z_i) , $i = 1, 2, 3$ and (x_j, y_j, z_j) , $j = 1, 2, 3$ are coordinates of triangles.

4.1.5 Sub-icosas (panel) types

For 6ν subdivision, as illustrated in Figure 4.11, there are 6 different panel types, which for convenience we designated them from type 1 to type 6. Figure 4.11 displays all triangle types

with different color. Notice that there are two asymmetrical (mirror) triangles for types 3 and 5. Triangle types 1, 2, 4 and 6 lie on the icosahedron's symmetry axis, and because of that they are isosceles triangles. The smallest triangles are "corner" triangles (dark blue) while the largest triangle lie in the middle and are marked in red.

4.2 Local coordinate system

We introduce a local coordinate system (x_{NM}, y_{NM}, z_{NM}) with respective unit vectors $(\hat{x}_{NM}, \hat{y}_{NM}, \hat{z}_{NM})$ centered at $O_{NM}(R_{NM}, \alpha_{NM}, \beta_{NM})$ or $O_{NM}(x_0, y_0, z_0)$, Figure 4.12. The local coordinate system is oriented so that $\hat{x}_{NM} = \hat{\theta}$, $\hat{y}_{NM} = \hat{\phi}$, $\hat{z}_{NM} = \hat{r}$ at O_{NM} .

4.2.1 Sub-icosa (panel) in local coordinate system

We consider the (N, M) th subicosa or triangle (panel) with coordinates $P_1(x_1, y_1, z_1)$, $P_2(x_2, y_2, z_2)$ and $P_3(x_3, y_3, z_3)$. We define the unit normal to the plane $\mathbf{n} = \hat{x}n_x + \hat{y}n_y + \hat{z}n_z$; directional cosines (n_x, n_y, n_z) to be determined. Then, we define the line LL, with the same directional cosines (n_x, n_y, n_z) passing through the global origin O . The origin $O_{NM}(x_0, y_0, z_0)$ of the local coordinates is specified by the intersection of line LL and the triangle plane as shown in Figure 4.13. The z_{NM} -axis of the local coordinate system coincides with the normal \mathbf{n} while axis x_{NM}, y_{NM} lies in the triangle plane.

First we determine the directional cosines of the \mathbf{n} then, the location of the O_{NM} i.e., coordinates (x_0, y_0, z_0) and finally the directional cosines of the (x_{NM}, y_{NM}, z_{NM}) local axis.

Directional cosines of normal

The general equation of a plane in space is

$$Ax + By + Cz + D = 0. \quad (4.4)$$

Specifically, for the plane passing through three points in space $P_1(x_1, y_1, z_1)$, $P_2(x_2, y_2, z_2)$, $P_3(x_3, y_3, z_3)$ we may write

$$\begin{vmatrix} x - x_1 & y - y_1 & z - z_1 \\ x_2 - x_1 & y_2 - y_1 & z_2 - z_1 \\ x_3 - x_1 & y_3 - y_1 & z_3 - z_1 \end{vmatrix} = 0. \quad (4.5)$$

or

$$\begin{aligned} & (x - x_1)[(y_2 - y_1)(z_3 - z_1) - (y_3 - y_1)(z_2 - z_1)] \\ & + (y - y_1)[(-(x_2 - x_1)(z_3 - z_1) + (x_3 - x_1)(z_2 - z_1))] \\ & + (z - z_1)[(x_2 - x_1)(y_3 - y_1) - (x_3 - x_1)(y_2 - y_1)] = 0. \end{aligned} \quad (4.6)$$

In (4.4), we see that

$$\begin{aligned} A &= (y_2 - y_1)(z_3 - z_1) - (y_3 - y_1)(z_2 - z_1) \\ B &= -[-(x_2 - x_1)(z_3 - z_1) + (x_3 - x_1)(z_2 - z_1)] \\ C &= (x_2 - x_1)(y_3 - y_1) - (x_3 - x_1)(y_2 - y_1) \end{aligned} \quad (4.7)$$

and

$$D = -x_1A - y_1B + z_1C. \quad (4.8)$$

Thus the directional cosines of the normal vector \mathbf{n} to the plane are:

$$\begin{aligned} n_x &= \cos \alpha = \frac{A}{\sqrt{A^2 + B^2 + C^2}} \\ n_y &= \cos \beta = \frac{B}{\sqrt{A^2 + B^2 + C^2}} \\ n_z &= \cos \gamma = \frac{C}{\sqrt{A^2 + B^2 + C^2}}. \end{aligned} \quad (4.9)$$

Warning: (α, β, γ) in (4.9) not to be confused with $(\alpha_{NM}, \beta_{NM})$ in Figure 4.13.

Location of O_{NM} :

The general equation of a line in parametric form passing through global origin O is

$$\begin{aligned} x &= n_x t \\ y &= n_y t \\ z &= n_z t. \end{aligned} \quad (4.10)$$

Since $O_{NM}(x_0, y_0, z_0)$ lies on this line we can write

$$\begin{aligned} x_0 &= n_x t_0 \\ y_0 &= n_y t_0 \\ z_0 &= n_z t_0. \end{aligned} \quad (4.11)$$

At the same time O_{NM} also lies on the planar triangle so we can write

$$Ax_0 + By_0 + Cz_0 + D = 0 \quad (4.12)$$

or using (4.11)

$$An_x t_0 + Bn_y t_0 + Cn_z t_0 + D = 0. \quad (4.13)$$

From here

$$t_0 = -\frac{D}{An_x + Bn_y + Cn_z}. \quad (4.14)$$

Substituting (4.14) into (4.11), the global coordinates of the origin O_{NM} are

$$\begin{aligned} x_0 &= n_x t_0 \\ y_0 &= n_y t_0 \\ z_0 &= n_z t_0. \end{aligned} \quad (4.15)$$

In spherical coordinates the coordinates of $O_{NM}(R_0, \alpha_{NM}, \beta_{NM})$ are:

$$R_0 = \sqrt{x_0^2 + y_0^2 + z_0^2} \quad (4.16)$$

$$\alpha_{NM} = \arccos \frac{z_0}{R_0} \quad (4.17)$$

$$\beta_{NM} = \arctan \frac{y_0}{R_0}. \quad (4.18)$$

Local axis

Consequently, the directional cosines of local x_{NM} -axis are:

$$\begin{aligned} n_x(x_{NM}) &= \cos \alpha_{NM} \cos \beta_{NM} \\ n_y(x_{NM}) &= \cos \alpha_{NM} \sin \beta_{NM} \\ n_z(x_{NM}) &= -\sin \alpha_{NM} \end{aligned} \quad (4.19)$$

where the identity

$$\sqrt{n_x^2(x_{NM}) + n_y^2(x_{NM}) + n_z^2(x_{NM})} = 1 \quad (4.20)$$

holds. Similarly, directional cosines of the local y_{NM} -axis are:

$$\begin{aligned} n_x(y_{NM}) &= -\sin \beta_{NM} \\ n_y(y_{NM}) &= \cos \beta_{NM} \\ n_z(y_{NM}) &= 0 \end{aligned} \quad (4.21)$$

with

$$\sqrt{n_x^2(y_{NM}) + n_y^2(y_{NM}) + n_z^2(y_{NM})} = 1 \quad (4.22)$$

As mentioned \mathbf{n} coincides with the unit vector $\hat{\mathbf{z}}_{NM}$, so

$$\begin{aligned} n_x(z_{NM}) &= n_x \\ n_y(z_{NM}) &= n_y \end{aligned} \quad (4.23)$$

and

$$n_z(z_{NM}) = n_z. \quad (4.24)$$

Coordinate transformation - going from global to local

Any given point in global coordinates (x, y, z) can be transformed into local coordinates (x_{NM}, y_{NM}, z_{NM}) by following translation - rotation matrix:

$$\begin{bmatrix} x_{NM} \\ y_{NM} \\ z_{NM} \end{bmatrix} = [A] \begin{bmatrix} x - x_0 \\ y - y_0 \\ z - z_0 \end{bmatrix} \quad (4.25)$$

where

$$[A] = \begin{bmatrix} n_x(x_{NM}) & n_y(x_{NM}) & n_z(x_{NM}) \\ n_x(y_{NM}) & n_y(y_{NM}) & n_z(y_{NM}) \\ n_x(z_{NM}) & n_y(z_{NM}) & n_z(z_{NM}) \end{bmatrix}. \quad (4.26)$$

Each subicosa triangle can now be represented in local coordinates by using (4.26) for each the three corner points. Because the unit vector $\hat{\mathbf{z}}_{NM}$ is perpendicular to subicosa, $z_{NM} = 0$. Thus, one can write for the coordinates of the subicosa in local coordinate system

$$\begin{aligned} x_{NM} &= n_x(x_{NM})(x - x_0) + n_y(x_{NM})(y - y_0) + n_z(x_{NM})(z - z_0) \\ y_{NM} &= n_x(y_{NM})(x - x_0) + n_y(y_{NM})(y - y_0) + n_z(y_{NM})(z - z_0) \\ z_{NM} &= 0. \end{aligned} \quad (4.27)$$

Figure 4.14 to Figure 4.29 show all eight types of subicosas in local coordinates. As an example we selected the subicosa triangles (N, M) to be: $(1, 1)$, $(2, 1)$, $(2, 2)$, $(2, 3)$, $(3, 1)$, $(3, 2)$, $(3, 3)$, $(4, 4)$. The specific location of these triangles in the icosia triangle is also illustrated with fill-in red color in Figure 4.14 to Figure 4.29.

For each triangle point (x_{NM}, y_{NM}) coordinates are also given in Figure 4.14 to Figure 4.29. In addition chord lengths (triangle sides) are denoted with lower case Roman letters according to Figure 4.10. Chord lengths may be computed from

$$d_{ij} = \sqrt{(x_{NMi} - x_{NMj})^2 + (y_{NMi} - y_{NMj})^2} \quad (4.28)$$

where (x_{NMi}, y_{NMi}) , $i = 1, 2, 3$ and (x_{NMj}, y_{NMj}) , $j = 1, 2, 3$ are the coordinates of the subicosa triangles in local coordinate system. These chord lengths must be the same as those computed by (4.3) in global coordinates, which may be a good check for coordinate transformation and computer code.

For convenience we determine the center of mass point in local coordinates:

$$x_{NM}^c = \frac{x_{NM1} + x_{NM2} + x_{NM3}}{3} \quad (4.29)$$

$$y_{NM}^c = \frac{y_{NM1} + y_{NM2} + y_{NM3}}{3} \quad (4.30)$$

Center of mass point of every subicosa is also shown in Figure 4.14 to Figure 4.29 by a plus sign.

4.2.2 Sub-icosia base

Because the subarray must be equilateral triangular, here we determine the orientation of the largest possible equilateral triangle that fits into a subicosa triangle. Figure 4.30 shows the triangle with sides a , b and c in local coordinates. As illustrated in this figure, it is possible to fit three typical equilateral triangles within a subicosa triangle so that one side of the equilateral triangle coincides with one of the sides of the subicosa triangle. However these triangles are not the same. The largest triangle is the one that coincides with the subicosa base closest to the isosceles triangle; side b in example of Figure 4.30. If the subicosa is isosceles triangular, which are all triangles along the axis of symmetry, i.e., triangle types 1,2,4 and 6, then the base of the isosceles icosia is also a side of the equilateral triangle. For these triangles the bases are sides b , b , h , and h , respectively. For triangle type 3a and 3b, the base is chord length e , while for triangle types 5a and 5b, the base chord length is g . Thus each subicosa in a geodesic dome has one side designated as the base. The bases of subicosas (panels) in a single icosia triangle are designated in red in Figure 4.31. For convenience, the base is also marked in Figure 4.30 by the line $\overline{O_{NM}P}$ perpendicular to the base. Furthermore, using the same rule, the bases are marked for each subicosa in Figure 4.11, and in Figure 4.15 to Figure 4.29.

4.3 Reference coordinate system

We define one more coordinate system, the reference coordinate system $(x'_{NM}, y'_{NM}, z'_{NM})$ shown in Figure 4.32 and Figure 4.33. A subarray is designed and tested in the reference coordinate system. The origin of this coordinate system is at O_{NM} while the z'_{NM} axis coincides with the z_{NM} axis of the local coordinate system. As illustrated in Figure 4.33 the x'_{NM} axis coincides with line $\overline{O_{NM}P}$ and is pointing toward the tip of the equilateral triangle. Thus, the reference coordinate system can be obtained by rotating the local coordinates about the z_{NM} axis by angle φ_{NM} in the CCW direction. For subicosas along the vertical axis of symmetry, i.e., (1, 1), (2, 2), (3, 3), (4, 4), (5, 5) and (6, 6) the rotation angle is 0 or 180 deg. For other subicosas the rotation angle depends not only on azimuthal position but also on elevation. Thus, the rotation angles depend on the subicosas position within the icosahedron and on the icosahedron elevation position. We compute the rotation angles with the help of Figure 4.33. An equilateral triangle with side a_E is shown. For the sake of analysis we assume that $(x_{NM2}, y_{NM2})(x_{NM3}, y_{NM3})$ is the base. The angle that the line parallel with the base makes with respect to the $+x_{NM}$ axis is

$$\phi_{NM}^{BASE} = \arctan \frac{y_{NM3} - y_{NM2}}{x_{NM3} - x_{NM2}} \quad (4.31)$$

Then the rotation angle

$$\varphi_{NM} = \phi_{NM}^{BASE} + \pi/2. \quad (4.32)$$

Figure 4.35 shows the four basic icosas and respective subicosas. Each subicosahedron in these four basic icosahedrons has a different angle $\varphi_{NM}(K, L, N, M)$ of rotation. These angles for the four basic icosahedrons are given in Table 4.3 to Table 4.6. These four icosahedrons constitute the basic cell of the full dome, i.e., by rotating Figure 4.35 in steps of 72 deg about the z -axis, we would get full dome. Thus, the angles φ_{NM} of the rest of the subicosahedrons in the dome can be determined from those in Table 4.3 to Table 4.6, by taking into account periodicity in azimuth. Thus, we use the following identities:

$$\varphi_{NM}(1, L, N, M) = \varphi_{NM}(1, 1, N, M), \quad L = 1, 2, \dots, 5 \quad (4.33)$$

$$\varphi_{NM}(2, L, N, M) = \varphi_{NM}(2, 1, N, M), \quad L = 1, 3, \dots, 9 \quad (4.34)$$

$$\varphi_{NM}(2, L, N, M) = \varphi_{NM}(2, 2, N, M), \quad L = 2, 4, \dots, 10 \quad (4.35)$$

$$\varphi_{NM}(3, L, N, M) = \varphi_{NM}(3, 1, N, M), \quad L = 1, 2, \dots, 5. \quad (4.36)$$

Thus the reference coordinates (x'_{NM}, y'_{NM}) can be obtained by rotating the local coordinates (x_{NM}, y_{NM}) about z_{NM} axis by angle φ_{NM} in CCW direction. In reference to Figure 4.34, this transformation can be described by the following rotation matrix relation:

$$\begin{pmatrix} x'_{NM} \\ y'_{NM} \end{pmatrix} = \begin{pmatrix} \cos \varphi_{NM} & \sin \varphi_{NM} \\ -\sin \varphi_{NM} & \cos \varphi_{NM} \end{pmatrix} \begin{pmatrix} x_{NM} \\ y_{NM} \end{pmatrix}. \quad (4.37)$$

Taking the inverse of the rotation matrix the reference coordinates can be transferred back to local coordinates by using

$$\begin{pmatrix} x_{NM} \\ y_{NM} \end{pmatrix} = \begin{pmatrix} \cos \varphi_{NM} & -\sin \varphi_{NM} \\ \sin \varphi_{NM} & \cos \varphi_{NM} \end{pmatrix} \begin{pmatrix} x'_{NM} \\ y'_{NM} \end{pmatrix}. \quad (4.38)$$

4.3.1 Sub-icosas in reference coordinates

Now, we transform all subicosa triangles into reference coordinates according to the above prescription, which for the three triangle points becomes

$$\begin{aligned} x'_{NM1} &= x_{NM1} \cos \varphi_{NM} + y'_{NM1} \sin \varphi_{NM} \\ y'_{NM1} &= -x_{NM1} \sin \varphi_{NM} + y'_{NM1} \cos \varphi_{NM} \end{aligned} \quad (4.39)$$

$$\begin{aligned} x'_{NM2} &= x_{NM2} \cos \varphi_{NM} + y'_{NM2} \sin \varphi_{NM} \\ y'_{NM2} &= -x_{NM2} \sin \varphi_{NM} + y'_{NM2} \cos \varphi_{NM} \end{aligned} \quad (4.40)$$

$$\begin{aligned} x'_{NM3} &= x_{NM3} \cos \varphi_{NM} + y'_{NM3} \sin \varphi_{NM} \\ y'_{NM3} &= -x_{NM3} \sin \varphi_{NM} + y'_{NM3} \cos \varphi_{NM} \end{aligned} \quad (4.41)$$

As an illustrative example, Figure 4.38 to Figure 4.45 show all six triangle types belonging to icoso $(K, L) = (1, 1)$ in reference coordinates. Numerical values for the triangle coordinates are also given in these figures. We see that all six types differ considerably in size. For convenience the six basic types are plotted on the same axis (x'_{NM}, y'_{NM}) in Figure 4.36. Moreover, for easy comparison, we plotted the same triangles so that the bases coincide on the same horizontal line, Figure 4.37. To efficiently populate these triangles with radiating elements, it is obvious that each of them will require a different number of elements. More on this subject will be said in the next section.

4.3.2 Fitting equilateral triangle into sub-icoso triangle

In this section we determine the maximum side length of the equilateral triangle that fits into each subicosa type and the respective coordinates of the equilateral triangles in the reference coordinate system.

Type 1:

Figure 4.38 shows the subicosa in reference coordinates. We see that the maximum side of the equilateral triangle a_E is limited by the height of the subicosa. We find a_E as follows:

$$\cos \alpha = \frac{b}{2a} \quad (4.42)$$

$$h_{\Delta} = a_E \frac{\sqrt{3}}{2} = a \sin \alpha. \quad (4.43)$$

From here

$$a_E = \frac{2}{\sqrt{3}} a \sin(\arccos \frac{b}{2a}) = 0.1521. \quad (4.44)$$

Consequently, the coordinates of the equilateral triangle are:

$$\begin{aligned}(x'_{NM1E}, y'_{NM1E}) &= (x'_{NM1}, 0) \\(x'_{NM2E}, y'_{NM2E}) &= (x'_{NM2}, a_E/2) \\(x'_{NM3E}, y'_{NM3E}) &= (x'_{NM3}, -a_E/2).\end{aligned}\tag{4.45}$$

The center of mass is therefore

$$\begin{aligned}x'_{Emass} &= \frac{x'_{NM1E} + x'_{NM2E} + x'_{NM3E}}{3} \\y'_{Emass} &= 0.\end{aligned}\tag{4.46}$$

Type 2:

Following the same procedure using Figure 4.39, we get

$$a_E = \frac{2}{\sqrt{3}}c \sin(\arccos \frac{b}{2c}) = 0.1790\tag{4.47}$$

and

$$\begin{aligned}(x'_{NM1E}, y'_{NM1E}) &= (x'_{NM1}, 0) \\(x'_{NM2E}, y'_{NM2E}) &= (x'_{NM2}, a_E/2) \\(x'_{NM3E}, y'_{NM3E}) &= (x'_{NM3}, -a_E/2).\end{aligned}\tag{4.48}$$

Center of mass

$$\begin{aligned}x'_{Emass} &= \frac{x'_{NM1E} + x'_{NM2E} + x'_{NM3E}}{3} \\y'_{Emass} &= 0.\end{aligned}\tag{4.49}$$

Types 3a and 3b: Subicosas of type 3 and 5 are the triangles with all three sides different, as shown in Figure 4.40 and Figure 4.41. In type 3 subicosas the base is chord length e . The maximum size of an equilateral triangle is determined by the subicosas height h_Δ . To determine a_E we first find height h_Δ as follows:

$$\alpha = 2 \arctan \sqrt{\frac{c^2 - (e - d)^2}{(e + d)^2 - c^2}}\tag{4.50}$$

and therefore

$$h_\Delta = d \sin \alpha.\tag{4.51}$$

Finally,

$$a_E = \frac{2h}{\sqrt{3}} = 0.1781\tag{4.52}$$

$$\begin{aligned}(x'_{NM1E}, y'_{NM1E}) &= (x'_{NM1}, y'_{NM1}) \\(x'_{NM2E}, y'_{NM2E}) &= (x'_{NM2}, y'_{NM1} + a_E/2) \\(x'_{NM3E}, y'_{NM3E}) &= (x'_{NM3}, y'_{NM1} - a_E/2).\end{aligned}\tag{4.53}$$

Center of mass

$$\begin{aligned}x'_{Emass} &= \frac{x'_{NM1E} + x'_{NM2E} + x'_{NM3E}}{3} \\y'_{Emass} &= \frac{y'_{NM1E} + y'_{NM2E} + y'_{NM3E}}{3}.\end{aligned}\quad (4.54)$$

Subicosa of type 3b is the mirror image of type 3a. In reference to Figure 4.41, the same expressions as for a subicosa of type 3a can be used, giving the same a_E as in (4.52). Expressions for equilateral triangle coordinates (4.53) also apply.

Type 4:

In this case from Figure 4.42 we can write

$$a_E = \frac{2}{\sqrt{3}}f \sin(\arccos \frac{h}{2f}) = 0.2027 \quad (4.55)$$

$$\begin{aligned}(x'_{NM1E}, y'_{NM1E}) &= (x'_{NM1}, y'_{NM1}) \\(x'_{NM2E}, y'_{NM2E}) &= (x'_{NM2}, a_E/2) \\(x'_{NM3E}, y'_{NM3E}) &= (x'_{NM3}, -a_E/2).\end{aligned}\quad (4.56)$$

Center of mass

$$\begin{aligned}x'_{Emass} &= \frac{x'_{NM1E} + x'_{NM2E} + x'_{NM3E}}{3} \\y'_{Emass} &= 0.\end{aligned}\quad (4.57)$$

Types 5a and 5b: The base of this type of subicosas is chord length g . In this case the maximum length of the equilateral triangle is limited by the base length, as seen in Figure 4.43 and Figure 4.44. Thus, for triangles of type 5a and 5b, $a_E = g = 0.1980$ and

$$\begin{aligned}(x'_{NM1E}, y'_{NM1E}) &= (x'_{NM1}, -a_E/2) \\(x'_{NM2E}, y'_{NM2E}) &= (x'_{NM1} + a_E \sin(\pi/3), 0) \\(x'_{NM3E}, y'_{NM3E}) &= (x'_{NM3}, a_E/2).\end{aligned}\quad (4.58)$$

Center of mass

$$\begin{aligned}x'_{Emass} &= \frac{x'_{NM1E} + x'_{NM2E} + x'_{NM3E}}{3} \\y'_{Emass} &= 0.\end{aligned}\quad (4.59)$$

Isosceles Subicosa of Type 6, (see Figure 4.45) is limited by its base length h . Thus, in this case

$$a_E = h = 0.2154 \quad (4.60)$$

$$\begin{aligned}(x'_{NM1E}, y'_{NM1E}) &= (x'_{NM1}, a_E/2) \\(x'_{NM2E}, y'_{NM2E}) &= (x'_{NM2}, -a_E/2) \\(x'_{NM3E}, y'_{NM3E}) &= (x'_{NM1} + a_E \sin(\pi/3), 0).\end{aligned}\quad (4.61)$$

Center of mass

$$\begin{aligned} x'_{mass} &= \frac{x'_{NM1E} + x'_{NM2E} + x'_{NM3E}}{3} \\ y'_{mass} &= 0. \end{aligned} \quad (4.62)$$

All six subicosa types with their respective equilateral triangles in the reference coordinate systems are shown in Figure 4.46 to Figure 4.61. The coordinates of the triangles are also written in blue color for subicosas and in red for equilateral triangles. Figure 4.62 shows the six different equilateral triangles in the reference coordinate system. For comparison they are also shown in Figure 4.63 where the bases are aligned on the same line. As already mentioned for efficient use of the area we would like to populate these triangles with as many radiating elements as possible we can. On the other hand, a different number of elements on each panel would require different beamforming networks, which is undesirable from ease of fabrication and low cost perspective. From Figure 4.63 it is seen that equilateral triangle types 2 and 3 are very similar. Also equilateral triangles 4 and 5 are very close in size. As will be shown latter, this means that we can reduce total number of different triangles from 6 to 4.

4.3.3 Counting the array elements in reference coordinate system (x'_{NM}, y'_{NM})

Similarly as we counted subicosas in a single icosa with two indeces (N, M) where N is counted from left-to-right, M from top-to-bottom, here we designate each subarray element with two indeces (n, m) where index m runs from left-to-right, n runs from top-to-bottom, as indicated in Figure 4.65. The elements are arranged in an equilateral grid with dimensions (d_x, d_y) . There are $nmMax$ rows in a subarray (subicosa). As already mentioned we would like to place as many elements as we can in the equilateral triangle with spacing around the edges equal to equilateral cell size. Considering this,

$$nmMax = \text{lower integer} \left(\frac{a_E}{d_y} - 1 \right). \quad (4.63)$$

For geodesic dome with $R = 5m$, Table 4.7 shows the number of rows for each panel type. Figure 4.66 to Figure 4.71 show the panel with radiating elements in the reference coordinate system. The radiating elements are circular microstrip patches.

4.3.4 Location of the array elements in reference coordinates

Once the number of rows is determined for each panel (subicosa) type we can then determine the location of the array elements in reference coordinate system (x'_{NM}, y'_{NM}) . The equilateral array with $nmMax$ rows is centered with respect to center of mass point (x'_{massE}, y'_{massE}) of the equilateral triangle as shown in Figure 4.64. The radial vector from the origin of the local coordinate system $(0, 0)$ to the center of mass point (x'_{massE}, y'_{massE}) is

$$\mathbf{r}_{NM}^0 = \hat{\mathbf{x}}'_{NM} x'_{massE} + \hat{\mathbf{y}}'_{NM} y'_{massE}. \quad (4.64)$$

The vector from the center of mass point to the first array element $(n, m) = (1, 1)$ is

$$\mathbf{r}_{NM}^1 = -\frac{L}{2}(\hat{\mathbf{x}}'_{NM} \tan(\pi/6) + \hat{\mathbf{y}}'_{NM}). \quad (4.65)$$

where L is the element center-to-center distance between the first and last elements in the first row, i.e., $L = nmMax d_y$. Thus the vector from the first element $(1, 1)$ to element (n, m) is

$$\mathbf{r}_{nm}^2 = \hat{\mathbf{x}}'_{NM}(n-1)d_x + \hat{\mathbf{y}}'_{NM}[(m-1) + \frac{(n-1)}{2}]d_y \quad (4.66)$$

where d_y is the equilateral lattice grid side length and $d_x = d_y \sin(\pi/3)$. Therefore the location of element (n, m) in the reference coordinates is

$$\mathbf{r}'_{nm} = \mathbf{r}_{NM}^0 + \mathbf{r}_{NM}^1 + \mathbf{r}_{nm}^2 \quad (4.67)$$

which may be rewritten in the following form:

$$\mathbf{r}'_{nm}(x'_{NM}, y'_{NM}) = \hat{\mathbf{x}}'_{NM}x'_{NM} + \hat{\mathbf{y}}'_{NM}y'_{NM} \quad (4.68)$$

where

$$x'_{NM} = x'_{massE} - \frac{L}{2} \tan \pi/6 + (n-1)d_x \quad (4.69)$$

and

$$y'_{NM} = y'_{massE} - \frac{L}{2} + [(m-1) + \frac{(n-1)}{2}]d_y. \quad (4.70)$$

4.3.5 Location of the array elements in local coordinates

Element locations originally given in the reference coordinates can be transformed into local coordinates according to inverse rotation matrix relation (4.38)

$$\begin{bmatrix} x_{NM} \\ y_{NM} \end{bmatrix} = \begin{bmatrix} \cos \varphi_{NM} & -\sin \varphi_{NM} \\ \sin \varphi_{NM} & \cos \varphi_{NM} \end{bmatrix} \begin{bmatrix} x'_{NM} \\ y'_{NM} \end{bmatrix}. \quad (4.71)$$

Thus, in local coordinates the array elements are located at

$$\mathbf{r}'_{nm}(x_{NM}, y_{NM}) = \hat{\mathbf{x}}_{NM}x_{NM} + \hat{\mathbf{y}}_{NM}y_{NM} \quad (4.72)$$

where according to (4.71)

$$\begin{aligned} x_{NM} &= x'_{NM} \cos \varphi_{NM} - y'_{NM} \sin \varphi_{NM} \\ y_{NM} &= x'_{NM} \sin \varphi_{NM} + y'_{NM} \cos \varphi_{NM}. \end{aligned} \quad (4.73)$$

4.3.6 Location of the array elements in global coordinates

Here we transfer local coordinates of the elements into the global coordinate system (x, y, z) .

With the help of (4.25) and (4.26) we can write

$$\begin{bmatrix} x_{nm} \\ y_{nm} \\ z_{nm} \end{bmatrix} = [A]^{-1} \begin{bmatrix} x_{NM} \\ y_{NM} \\ z_{NM} \end{bmatrix} + \begin{bmatrix} x_0 \\ y_0 \\ z_0 \end{bmatrix} \quad (4.74)$$

where $[A]^{-1}$ is inverse of (4.26). Elements of $[A]^{-1}$ are

$$\begin{aligned} a_{11} &= n_y(y_{NM})n_z(z_{NM}) - n_z(y_{NM})n_y(z_{NM}) \\ a_{21} &= n_z(y_{NM})n_x(z_{NM}) - n_x(y_{NM})n_z(z_{NM}) \\ a_{31} &= n_x(y_{NM})n_y(z_{NM}) - n_y(y_{NM})n_x(z_{NM}) \end{aligned} \quad (4.75)$$

$$\begin{aligned} a_{12} &= n_z(x_{NM})n_y(z_{NM}) - n_y(x_{NM})n_z(z_{NM}) \\ a_{22} &= n_x(x_{NM})n_z(z_{NM}) - n_z(x_{NM})n_x(z_{NM}) \\ a_{32} &= n_y(x_{NM})n_x(z_{NM}) - n_x(x_{NM})n_y(z_{NM}) \end{aligned} \quad (4.76)$$

$$\begin{aligned} a_{13} &= n_y(x_{NM})n_z(y_{NM}) - n_z(x_{NM})n_y(y_{NM}) \\ a_{23} &= n_z(x_{NM})n_x(y_{NM}) - n_x(x_{NM})n_z(y_{NM}) \\ a_{33} &= n_x(x_{NM})n_y(y_{NM}) - n_y(x_{NM})n_x(y_{NM}). \end{aligned} \quad (4.77)$$

The radial vector from the origin of the global coordinate system to the (nm) th element is therefore

$$\mathbf{R}_{nm}(x, y, z) = \hat{x}x_{nm} + \hat{y}y_{nm} + \hat{z}z_{nm}. \quad (4.78)$$

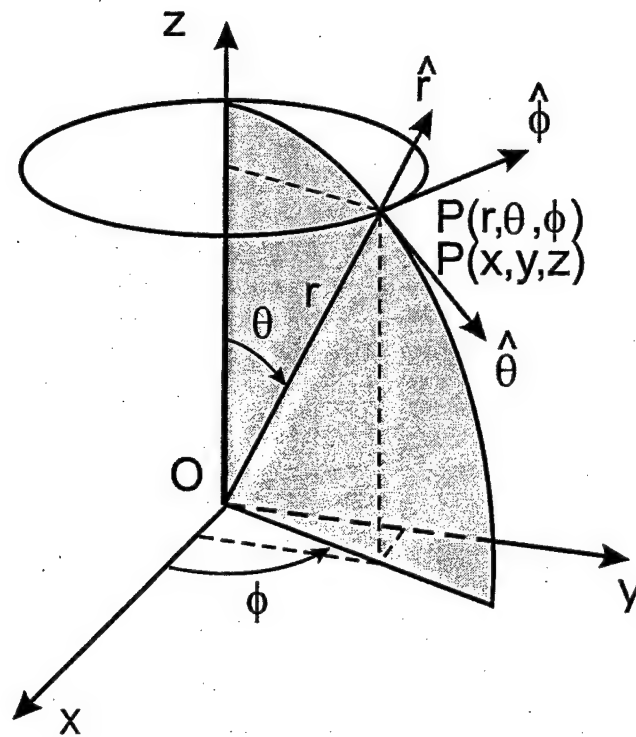


Figure 4.1: Global coordinate system (x, y, z)

Icosahedron:

20 equilateral triangular faces
12 apexes
30 edges

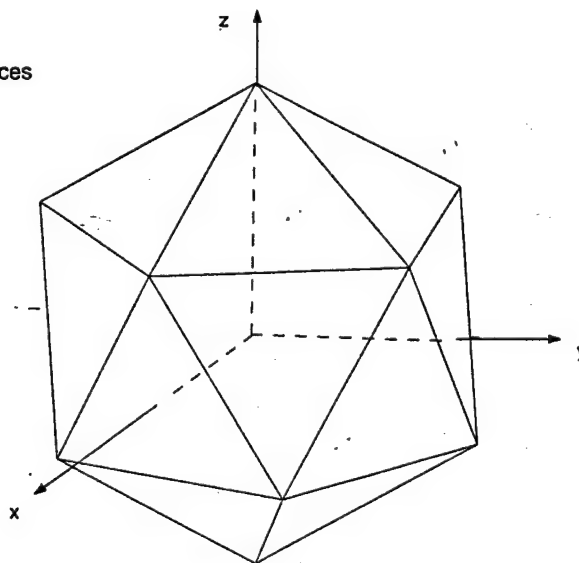
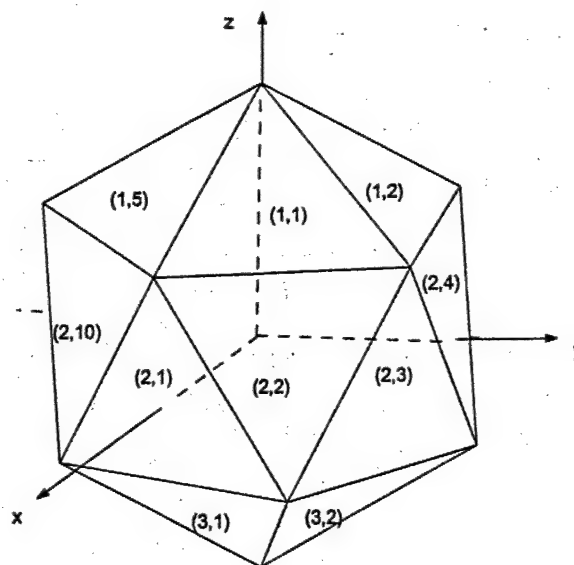


Figure 4.2: Icosahedron in global coordinates

Icosa: (K,L)

K=1, L=1 to 5
K=2, L=1 to 10
K=3, L=1 to 5



K is row counting from top to bottom
L is Icosa in Kth row counting in + ϕ direction from x-z plane

Figure 4.3: Icosahedron showing numbering of icosas - side view

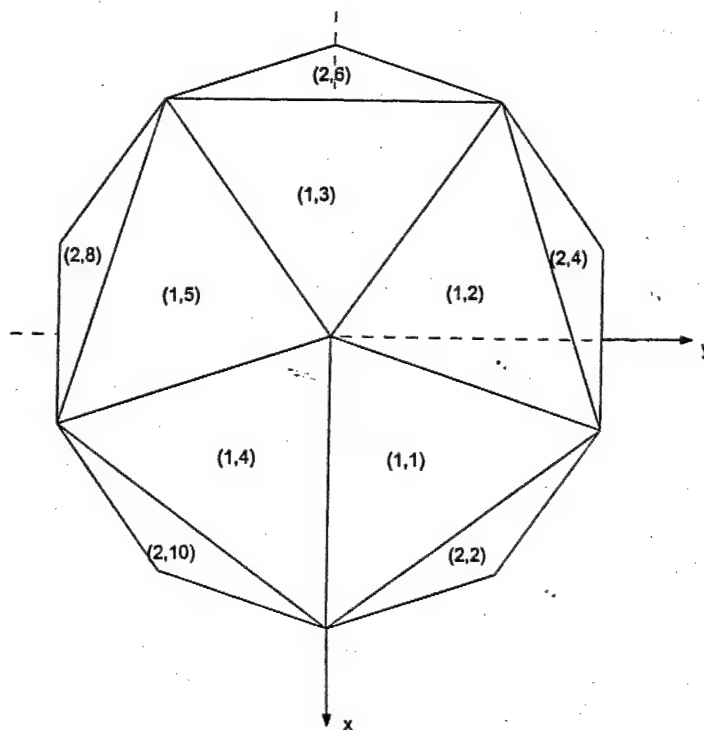


Figure 4.4: Icosahedron showing numbering of icosas - top view

Total: 63 edges and 28 vertexes
 Because of symmetry only 12 edges
 are needed or 10 vertex coordinates!

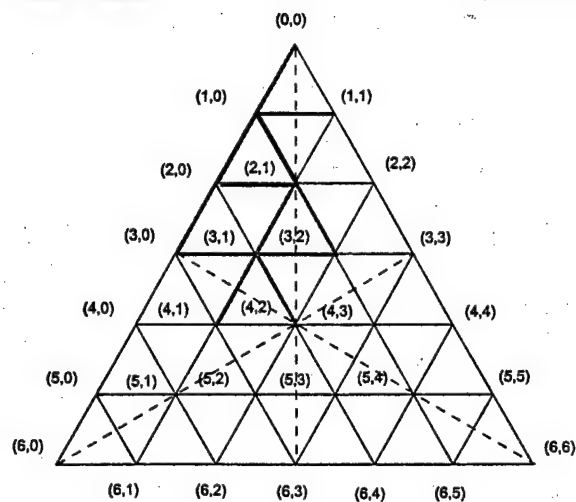
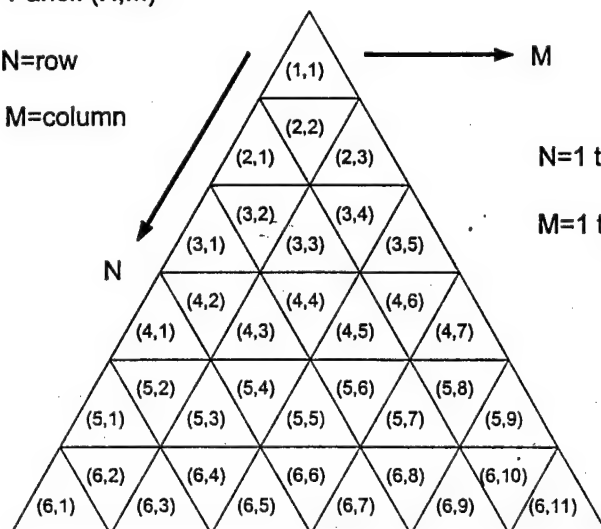


Figure 4.5: Icosa $\Delta\#1$ showing numbering of the sub-icosa's (facets) and vertices

Panel: (N,M)

N=row

M=column



N=1 to 6

M=1 to 2N-1

Figure 4.6: Icosa showing scheme for counting the sub-icosa's

Vertex	θ (deg)	ϕ (deg)
(0,0)	0	0
(1,0)	9.3247035	0
(1,1)	9.3247035	72
(2,0)	20.0767513	0
(2,1)	16.4722107	36
(3,0)	31.7174744	0
(3,1)	27.2237351	22.3861776
(3,2)	27.2237351	49.6138225
(4,1)	39.1034177	16.0353713
(4,2)	37.3773682	36

Table 4.1: Coordinates of the basic vertices for icosahedron, Class I, Method 1, 6ν frequency

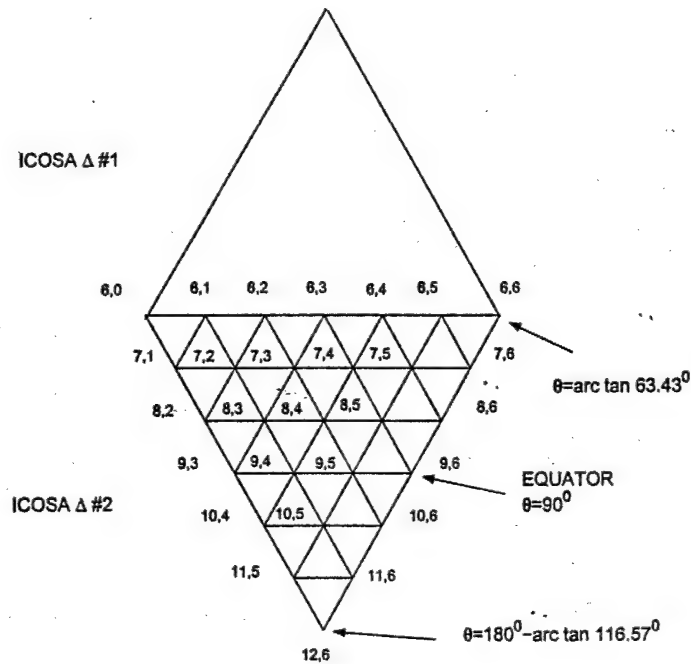


Figure 4.7: Icosa No. 2 pertaining to evaluation of respective vertex coordinates, Class I, Method 1, 6ν frequency [10]

Triangle #1, 6v		
Vertex	θ (deg)	ϕ (deg)
0,0	0.0000000	0.0000000
1,0	9.3247035	0.0000000
1,1	9.3247035	72.0000000
2,0	20.0767513	0.0000000
2,2	16.4722107	36.0000000
2,2	20.0767513	72.0000000
3,0	31.7174744	0.0000000
3,1	27.2237351	22.3861776
3,2	27.2237351	49.6138225
3,3	31.7174744	72.0000000
4,0	43.3581976	0.0000000
4,1	39.1034177	16.0353713
4,2	37.3773682	36.0000000
4,3	39.1034177	55.9646288
4,4	43.3581976	72.0000000
5,0	54.1102453	0.0000000
5,1	50.6513527	12.4463843
5,2	48.4869490	27.7323015
5,3	48.4869490	44.2676986
5,4	50.6513527	59.5536157
5,5	54.1102453	72.0000000
6,0	63.4349488	0.0000000
6,1	60.9162275	10.1562304
6,2	59.0080312	22.3861776
6,3	58.2825256	36.0000000
6,4	59.0080312	49.6138225
6,5	60.9162275	61.8437696
6,6	63.4349488	72.0000000

Triangle #2, 6v		
Vertex	θ (deg)	ϕ (deg)
7,1	71.0914502	5.7778072
7,2	69.4828700	16.7344818
7,3	68.5073635	29.3546281
7,4	68.5073635	42.6453719
7,5	69.4828700	55.2655182
7,6	71.0914502	66.2221928
8,2	80.1168545	11.8185857
8,3	79.4443283	23.3461239
8,4	79.1876831	36.0000000
8,5	79.4443283	48.6538761
8,6	80.1168545	60.1814143
9,3	90.0000000	18.0000000
9,4	90.0000000	29.8185857
9,5	90.0000000	42.1814143
9,6	90.0000000	54.0000000
10,4	99.8831455	24.1814143
10,5	100.0928406	36.0000000
10,6	99.8831455	47.8185858
11,5	108.9085499	30.2221928
11,6	108.9085499	41.7778072
12,6	116.5650512	36.0000000

Table 4.2: Coordinates of the vertices for icosas Δ #1 and Δ #2, Class I, Method 1, 6v frequency

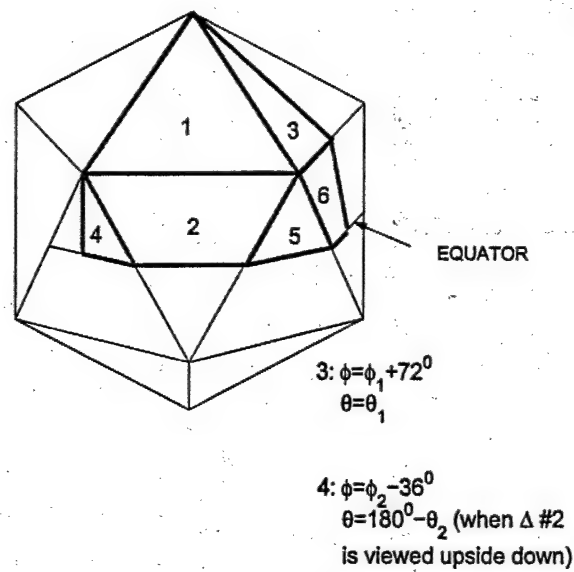


Figure 4.8: Icosahedron showing symmetry triangles [10]

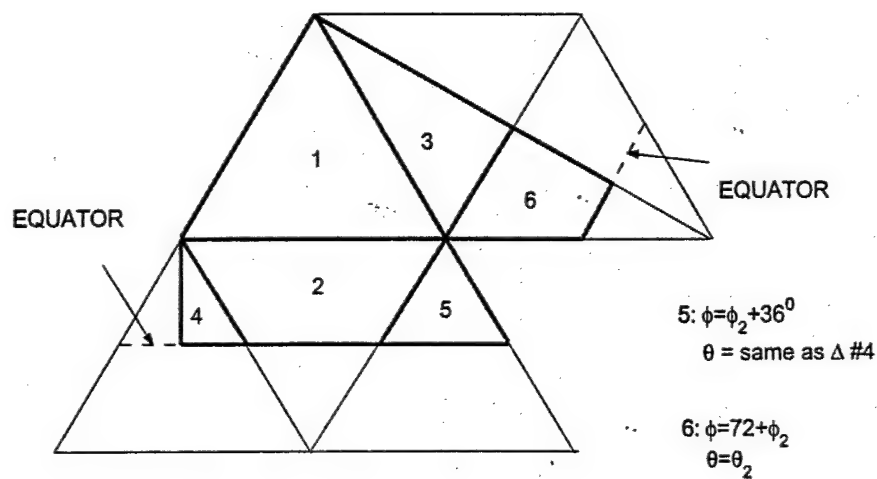


Figure 4.9: Unraveled icosahedron showing symmetry triangles [10]

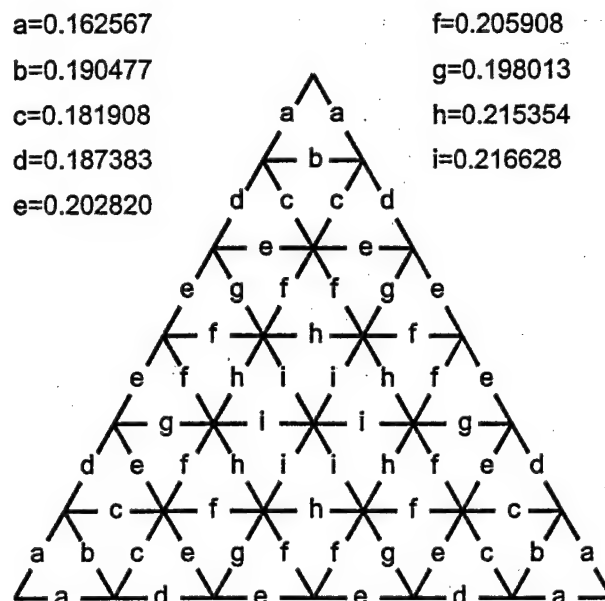


Figure 4.10: Icosahedron chord lengths, $R = 1$

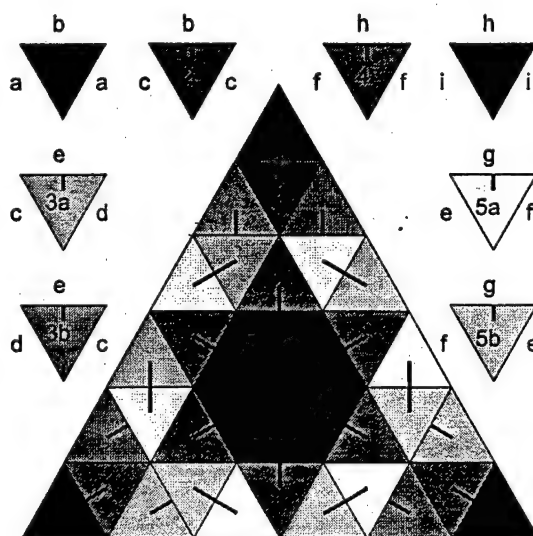


Figure 4.11: Sub-icosa (panel) types

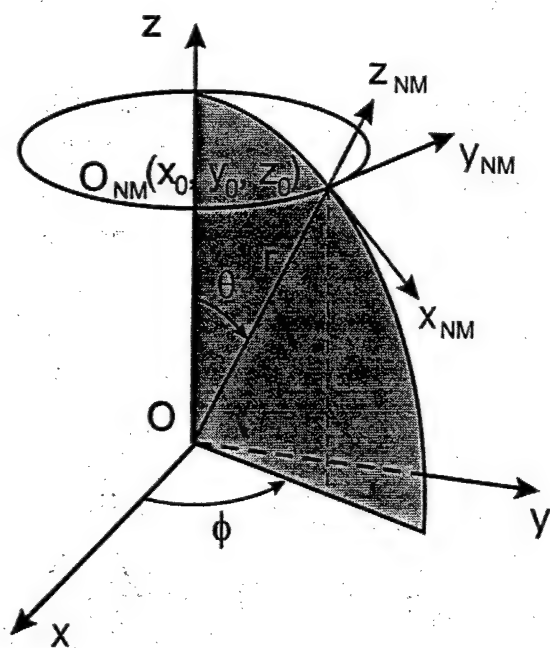


Figure 4.12: Local coordinate system (x_{NM}, y_{NM}, z_{NM})

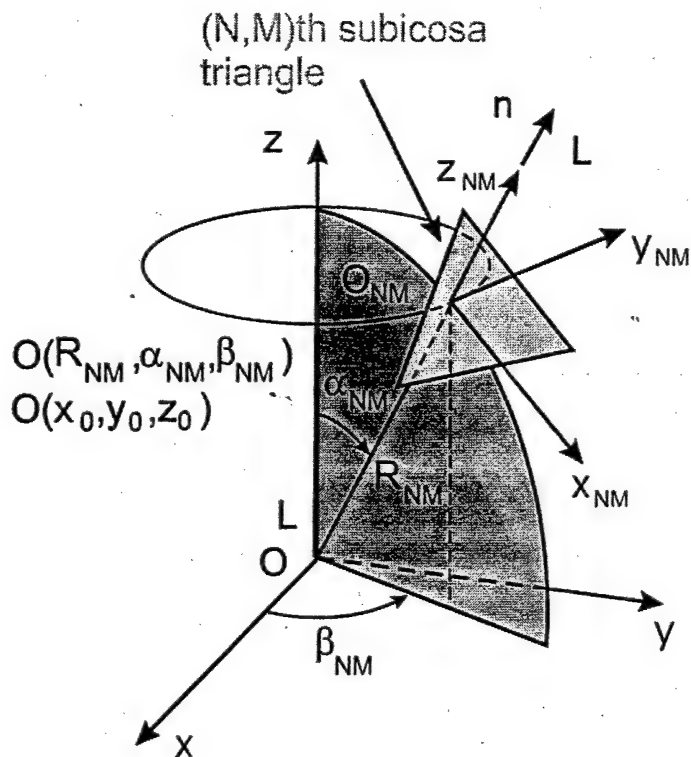


Figure 4.13: Sub-icosa and local coordinate system (x_{NM}, y_{NM}, z_{NM})

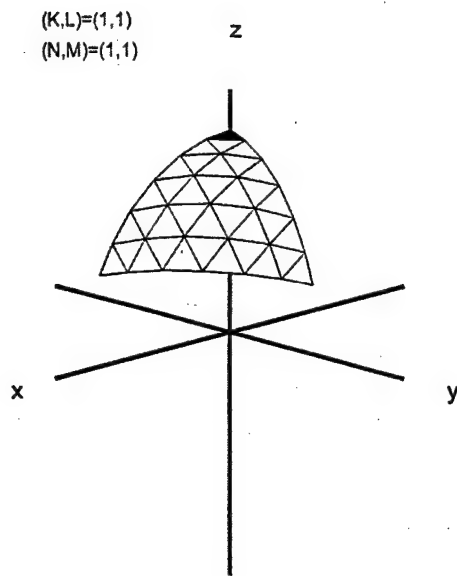


Figure 4.14: Icosa (1,1) showing subicosa location (1,1)

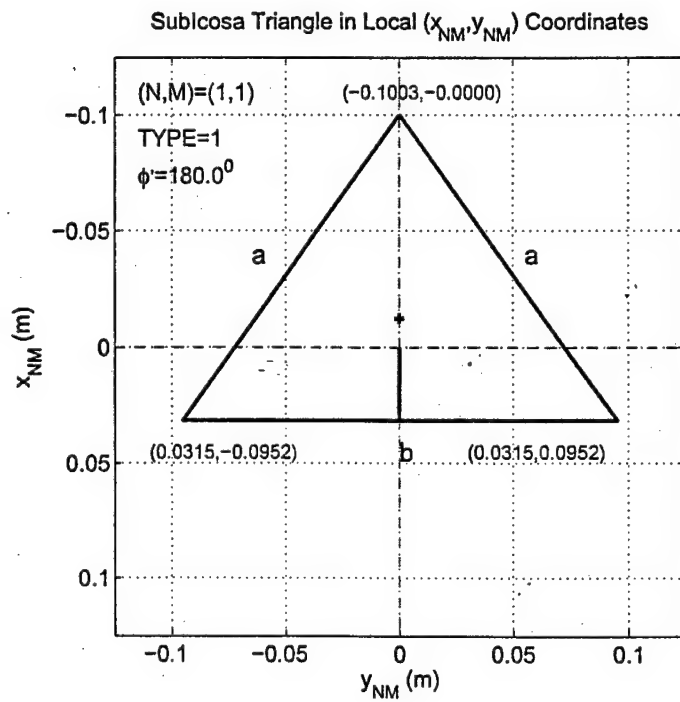


Figure 4.15: Subicosa triangle (1,1) in local (x_{NM}, y_{NM}) coordinates

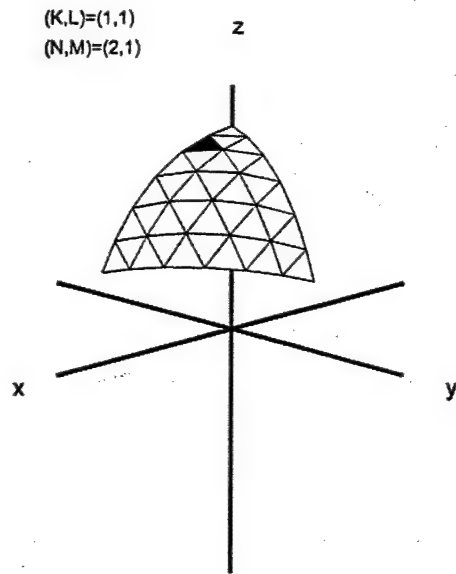


Figure 4.16: Icosa (1,1) showing subcosa location (2,1)

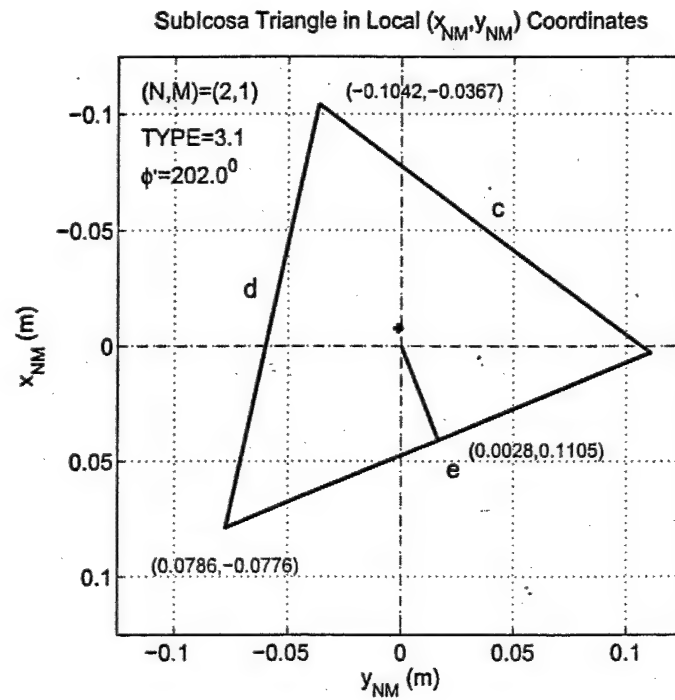


Figure 4.17: Subcosa triangle (2,1) in local (x_{NM}, y_{NM}) coordinates

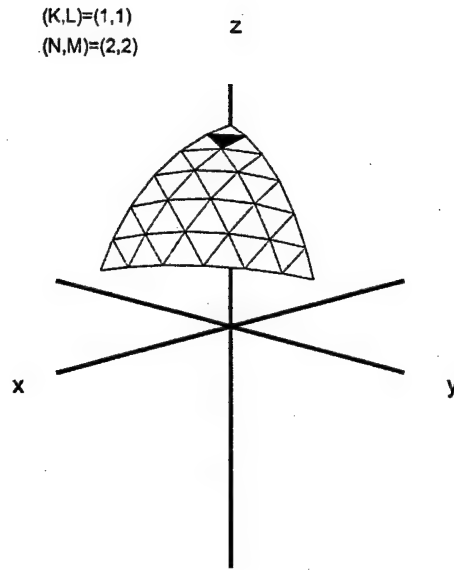


Figure 4.18: Icosa (1,1) showing subicosa location (2,2)

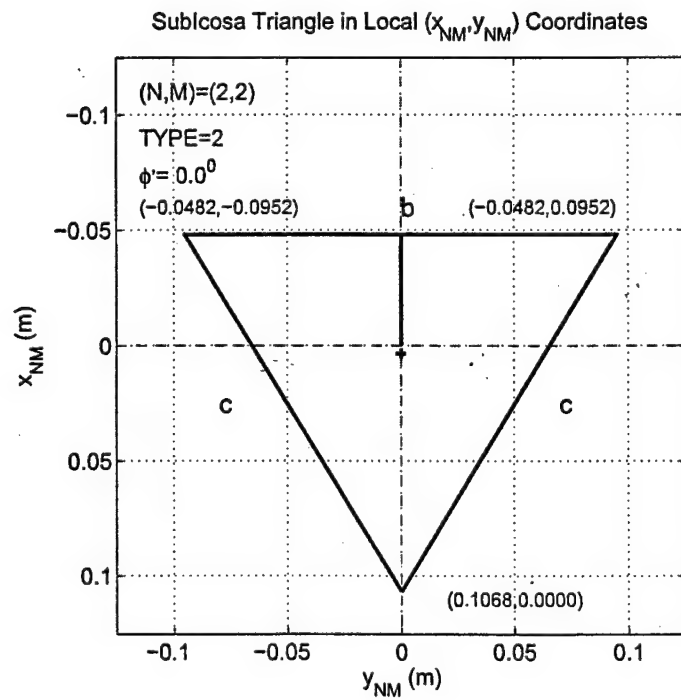


Figure 4.19: Subicosa triangle (2,2) in local (x_{NM}, y_{NM}) coordinates

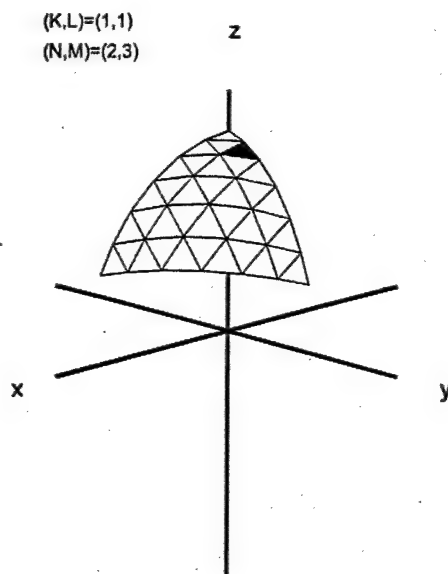


Figure 4.20: Icosa (1,1) showing subicosa location (2,3)

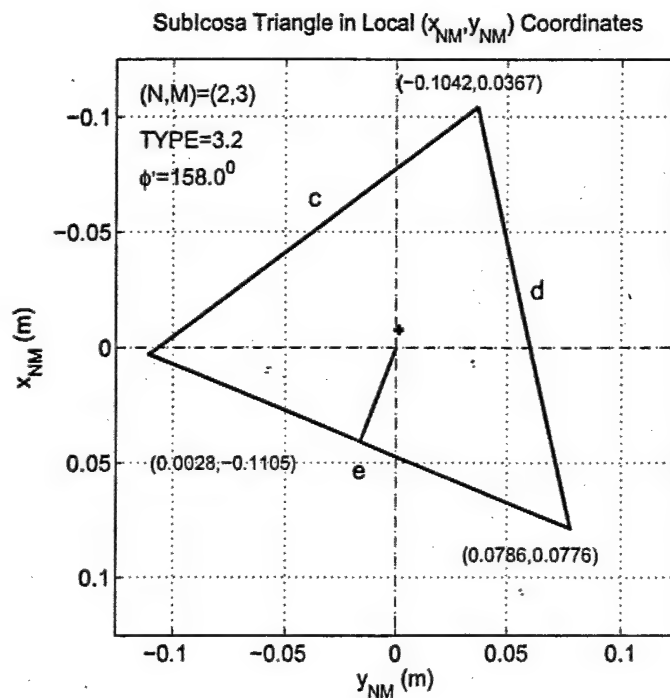
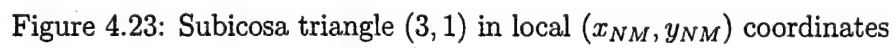
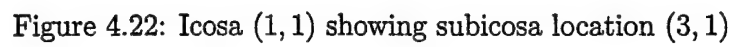


Figure 4.21: Subicosa triangle (2,3) in local (x_{NM}, y_{NM}) coordinates



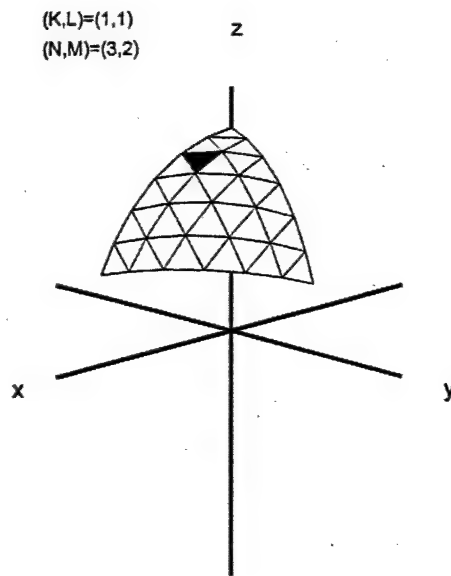


Figure 4.24: Icosa (1, 1) showing subicosah location (3, 2)

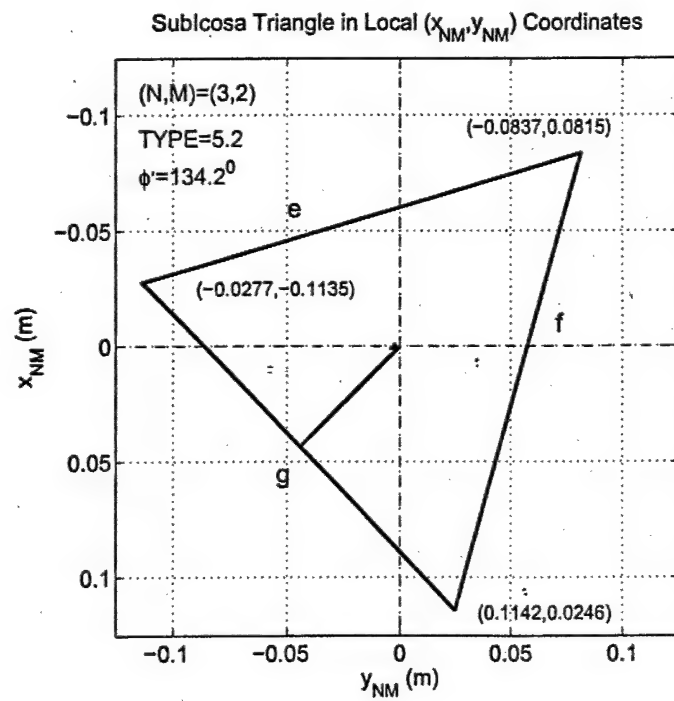


Figure 4.25: Subicosah triangle (3, 2) in local (x_{NM}, y_{NM}) coordinates

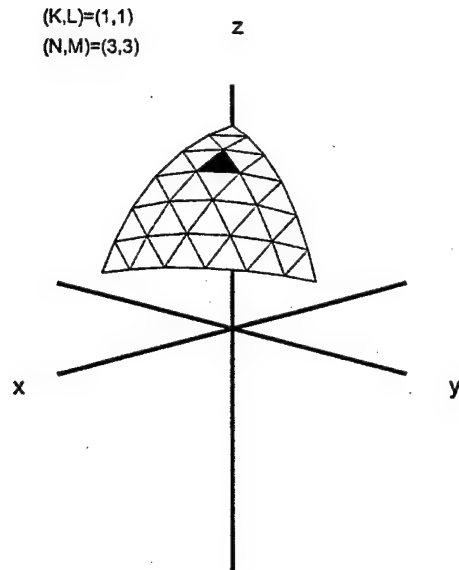


Figure 4.26: Icosa (1, 1) showing subicosa location (3, 3)

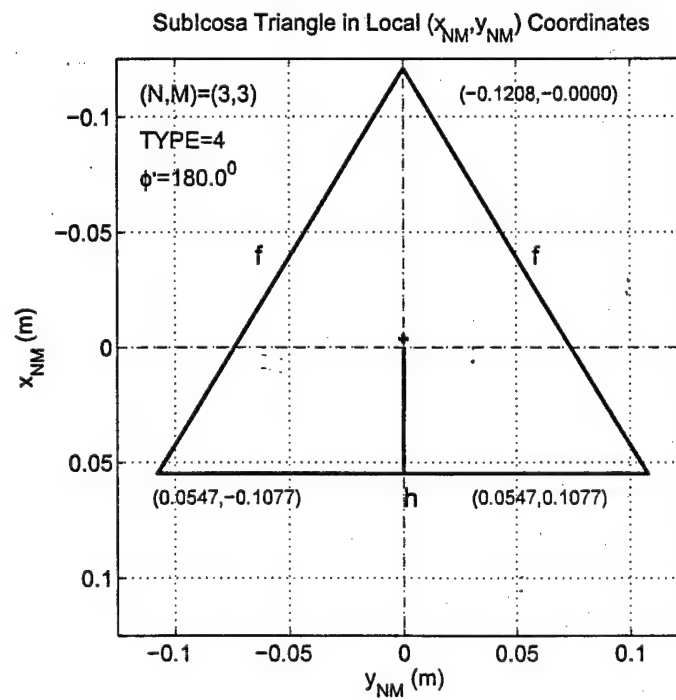


Figure 4.27: Subicosa triangle (3, 3) in local (x_{NM}, y_{NM}) coordinates

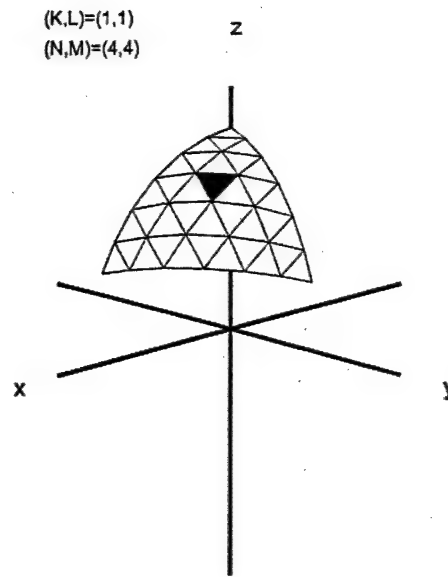


Figure 4.28: Icosa (1,1) showing subcosa location (4,4)

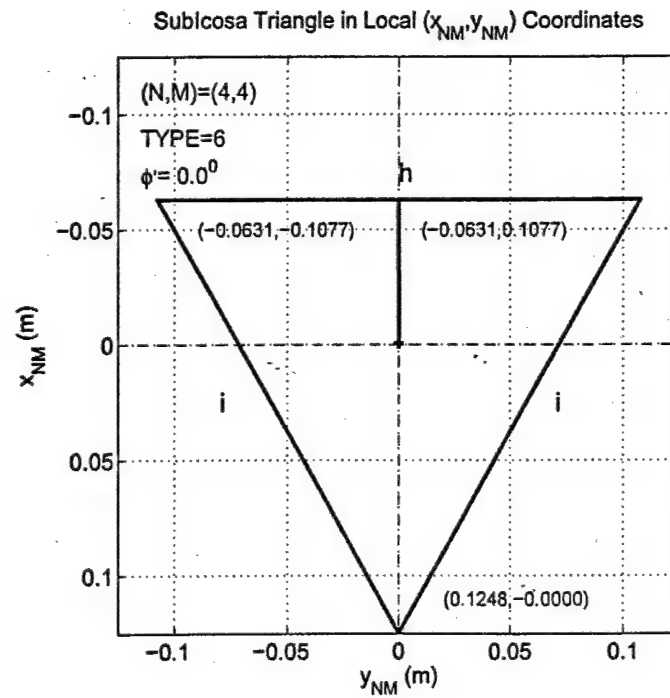


Figure 4.29: Subcosa triangle (4,4) in local (x_{NM}, y_{NM}) coordinates

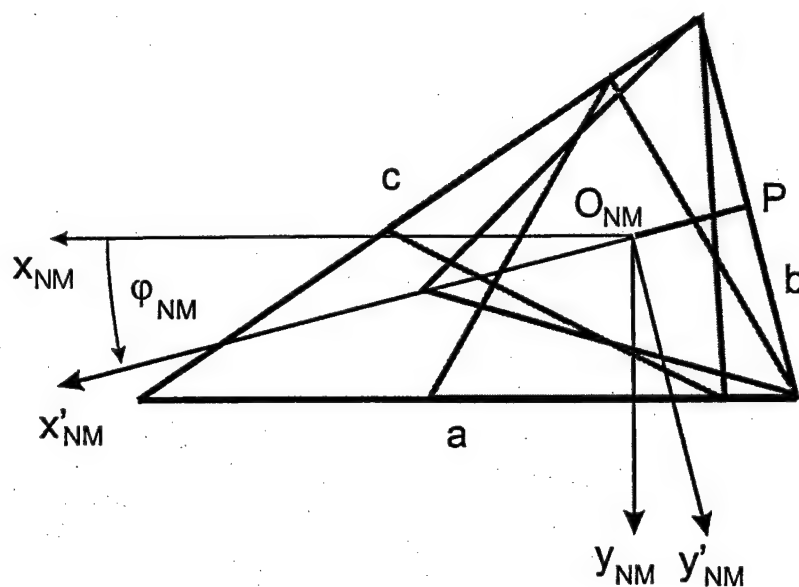


Figure 4.30: Subicosa and equilateral triangles

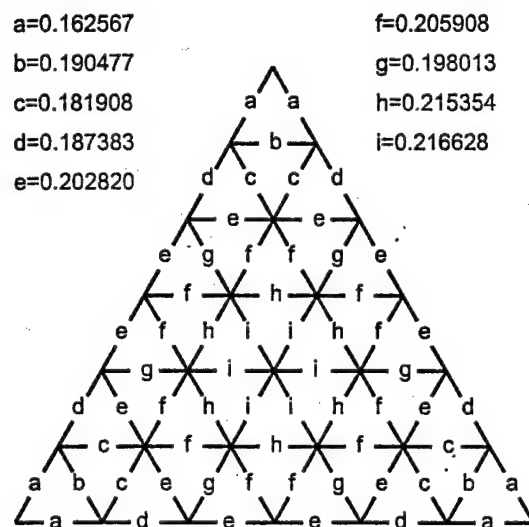


Figure 4.31: Icosahedron cord lengths indicating base-lengths

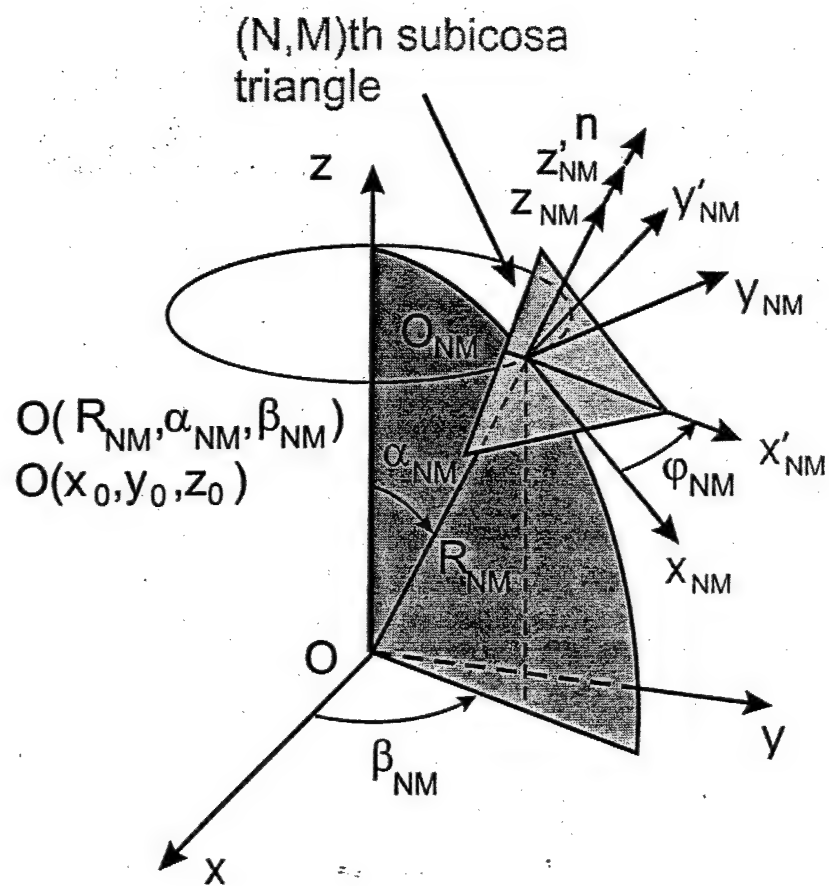


Figure 4.32: Reference coordinate system $(x'_{NM}, y'_{NM}, z'_{NM})$ pertaining to (N, M) th subicosa triangle

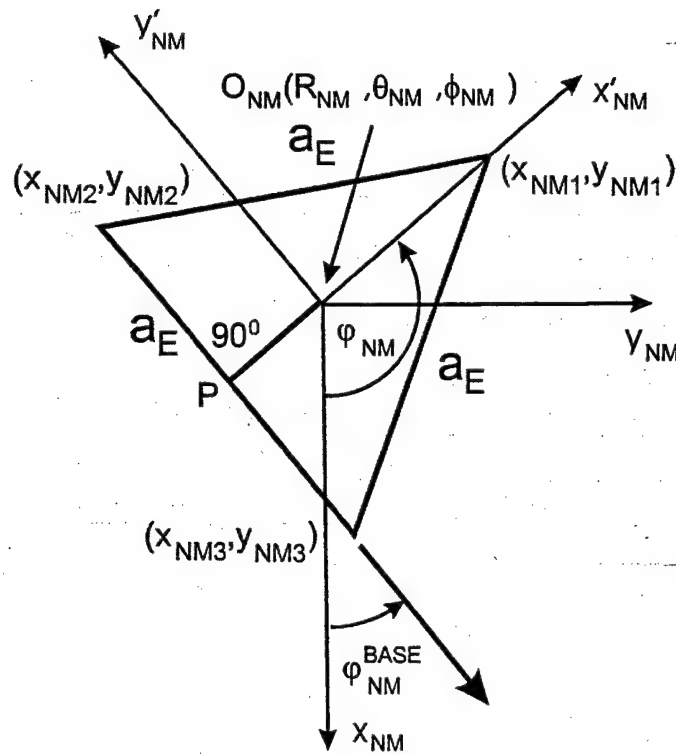


Figure 4.33: Equilateral triangle pertaining to determination of the rotation angle φ_{NM}

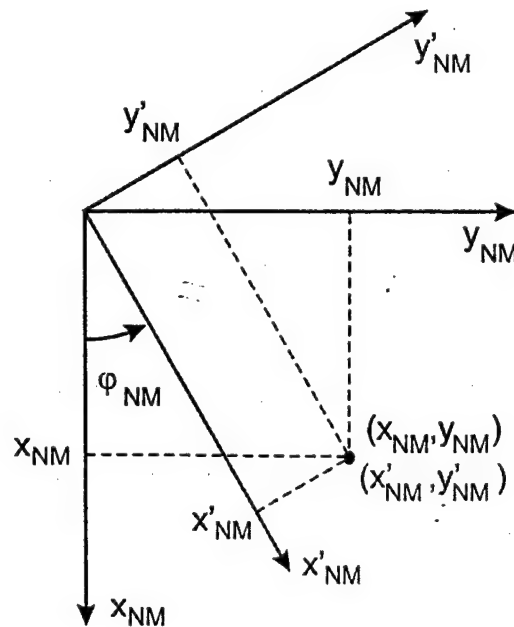


Figure 4.34: Local and reference coordinates pertaining to determination of the rotation matrix

	Rotation angle φ_{NM} for icosahedron $(K,L)=(1,1)$										
N \ M	1	2	3	4	5	6	7	8	9	10	11
1	180.0000										
2	201.9580	0.0000	158.0420								
3	-35.0368	134.2140	180.0000	225.7860	35.0368						
4	203.8554	258.9418	68.9854	0.0000	-68.9854	101.0582	156.1446				
5	-37.5512	20.7306	-47.2274	127.2897	180.0000	232.7103	47.2274	-20.7306	37.5512		
6	-37.9094	140.2243	-44.7719	250.3892	65.5333	0.0000	-65.5333	109.6108	44.7719	219.7757	37.9094

Table 4.3: Rotation angles φ_{NM} for icosahedron $(K, L) = (1, 1)$

Rotation angle φ_{NM} for icosahedron (K,L)=(2,1)										
1	2	3	4	5	6	7	8	9	10	11
180.0000										
181.0433	0.0000	178.9567								
-60.2441	119.2178	180.0000	240.7822	60.2441						
176.6323	238.4705	59.0210	0.0000	-59.0210	121.5295	183.3674				
-66.6925	-3.4444	-63.1128	118.6039	180.0000	241.3961	63.1128	3.4444	66.6925		
-69.3932	112.4914	-65.3347	235.3859	58.3393	0.0000	-58.3393	124.6141	65.3347	247.5086	69.3932

Table 4.4: Rotation angles φ_{NM} for icosahedron $(K, L) = (2, 1)$

Rotation angle φ_{NM} for icosahedron $(K,L)=(2,2)$										
1	2	3	4	5	6	7	8	9	10	11
0.0000										
1.0433	180.0000	-1.0433								
119.7559	-60.7822	0.0000	60.7822	240.2441						
-3.3674	58.4705	239.0210	180.0000	120.9790	-58.4705	3.3674				
113.3075	176.5556	116.8872	-61.3961	0.0000	61.3961	243.1128	183.4444	246.6925		
110.6068	-67.5086	114.6653	55.3859	238.3393	180.0000	121.6607	-55.3859	245.3347	67.5086	249.3932

Table 4.5: Rotation angles φ_{NM} for icosahedron $(K, L) = (2, 2)$

N \ M	Rotation angle φ_{NM} for icosahedron $(K,L)=(3,1)$										
	1	2	3	4	5	6	7	8	9	10	11
1	0.0000										
2	21.9580	180.0000	-21.9580								
3	144.9632	-45.7860	0.0000	45.7860	215.0368						
4	23.8554	78.9418	248.9854	180.0000	111.0146	-78.9418	-23.8554				
5	142.4488	200.7306	132.7726	-52.7103	0.0000	52.7103	227.2274	159.2694	217.5512		
6	142.0906	-39.7757	135.2281	70.3892	245.5333	180.0000	114.4667	-70.3892	224.7719	39.7757	217.9094

Table 4.6: Rotation angles φ_{NM} for icosahedron $(K, L) = (3, 1)$

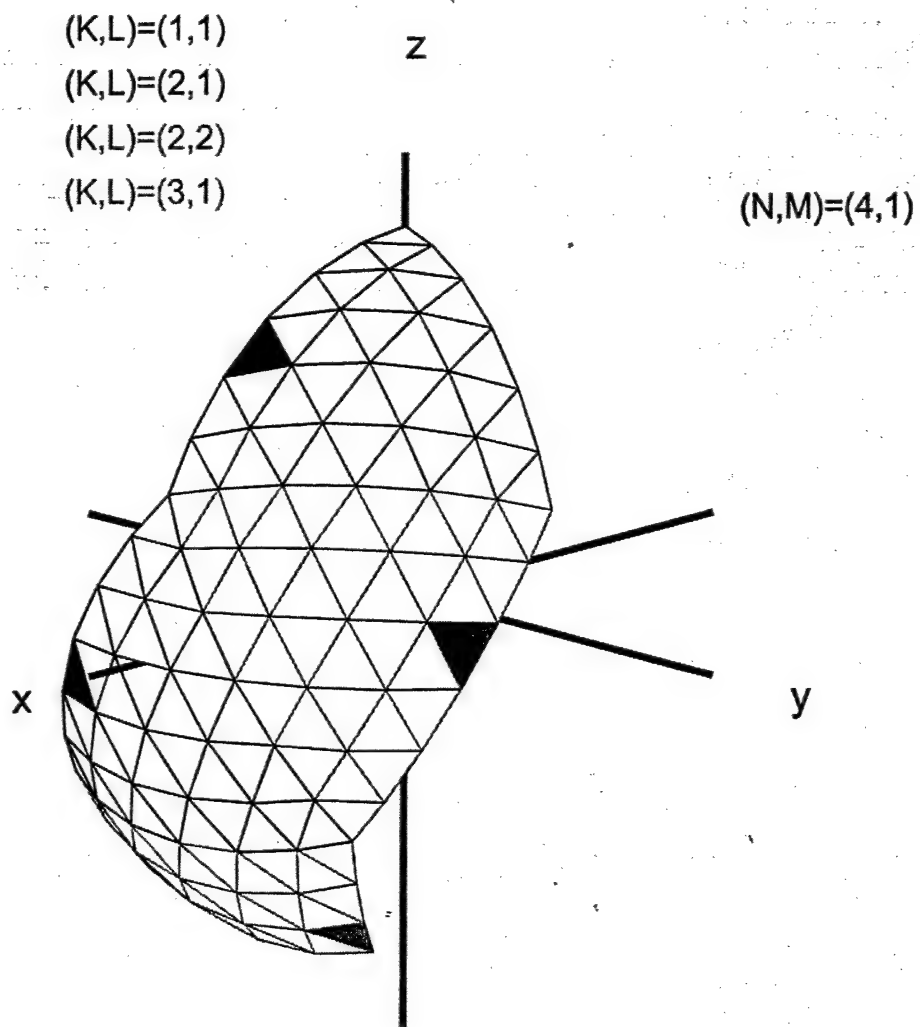


Figure 4.35: Four Basic Icosas

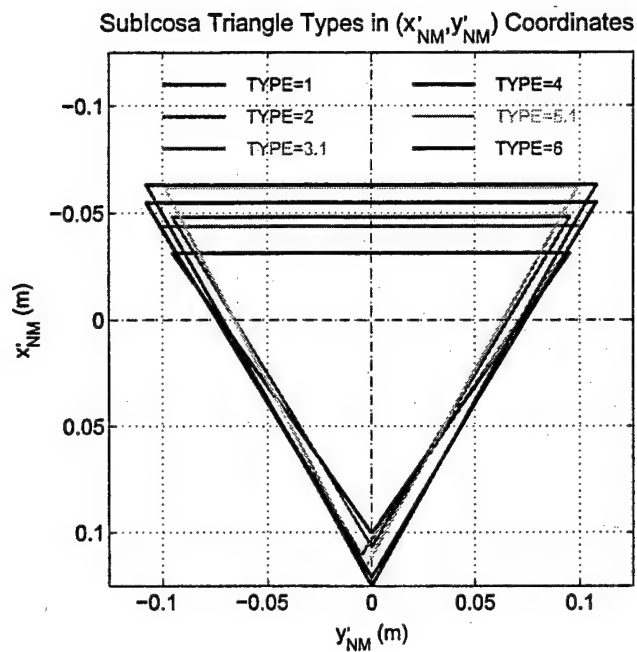


Figure 4.36: Subcosa triangles in reference (x'_{NM}, y'_{NM}) coordinates

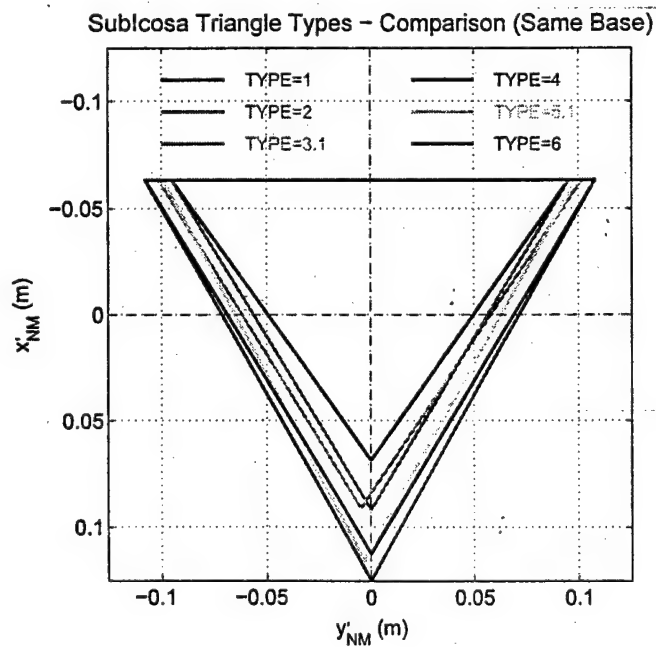


Figure 4.37: Subcosa triangle types - Comparison (Same base)

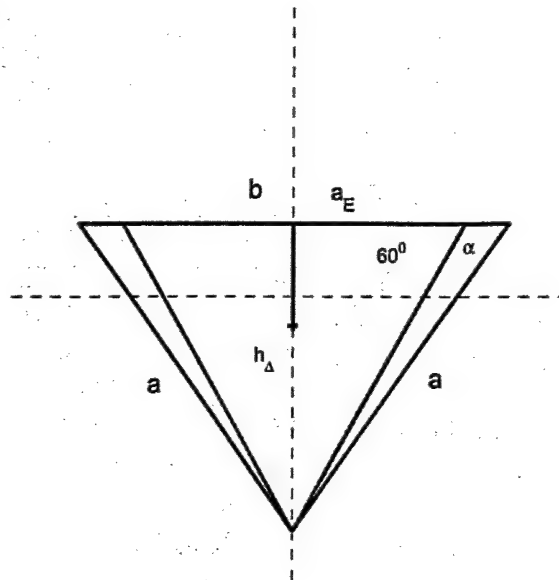


Figure 4.38: Triangle Type 1

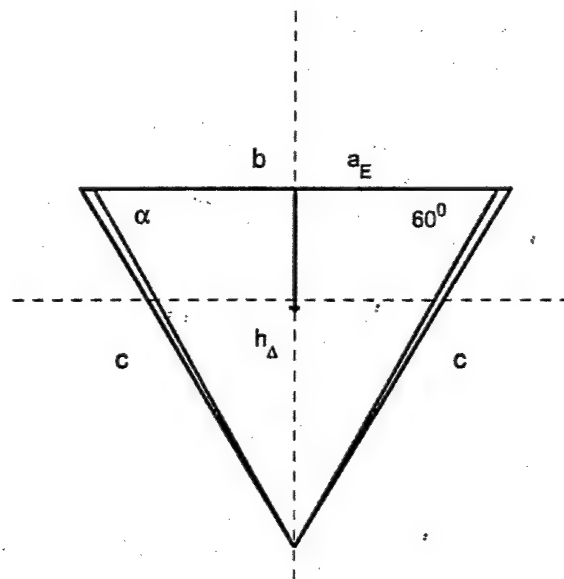


Figure 4.39: Triangle Type 2

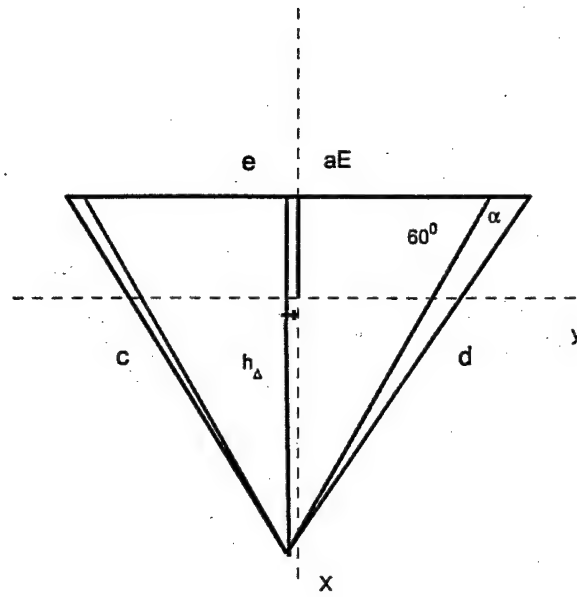


Figure 4.40: Triangle Type 3a

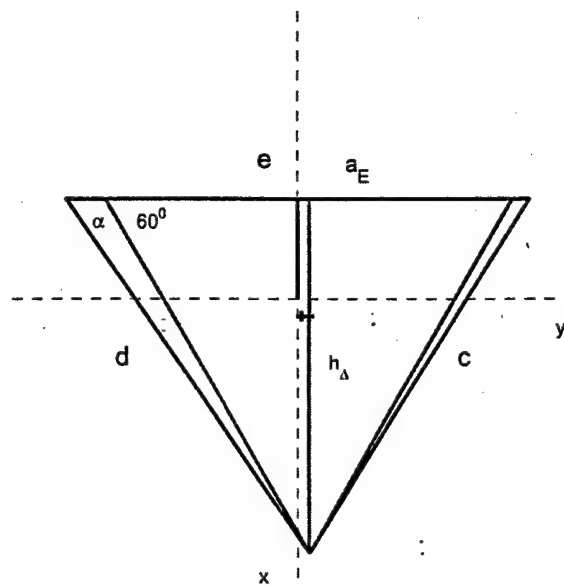


Figure 4.41: Triangle Type 3b

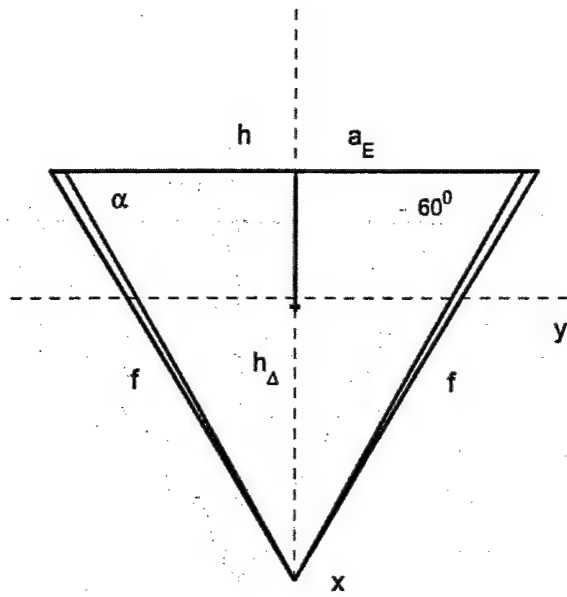


Figure 4.42: Triangle Type 4

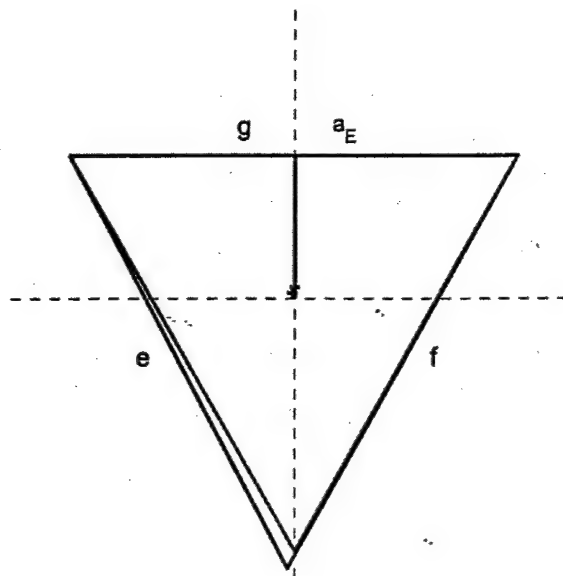


Figure 4.43: Triangle Type 5a

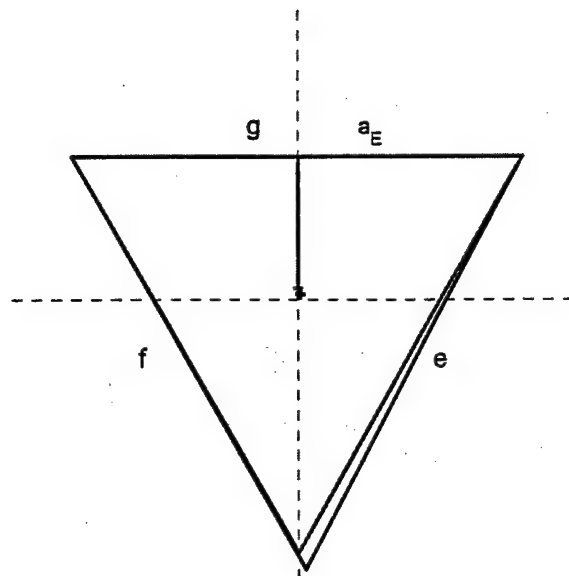


Figure 4.44: Triangle Type 5b

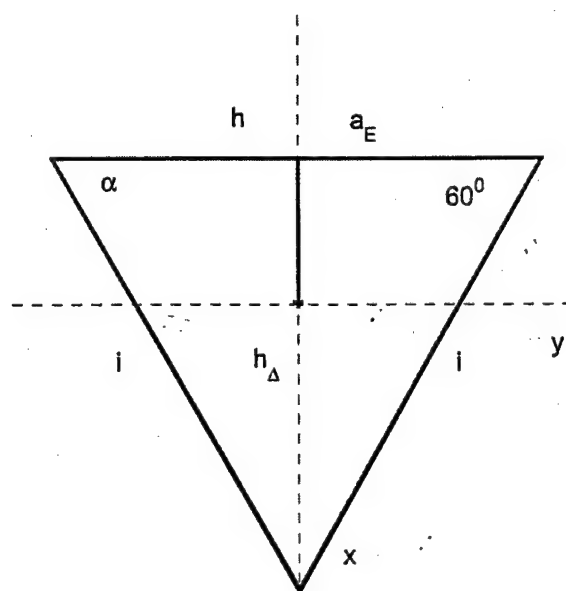


Figure 4.45: Triangle Type 6

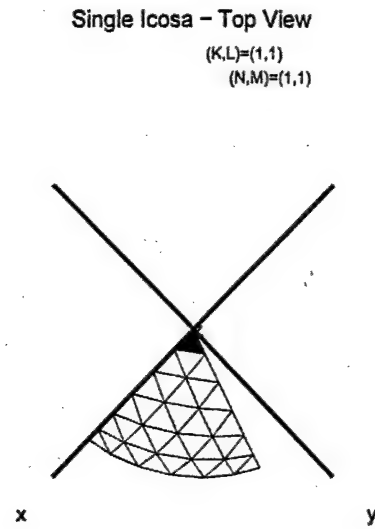


Figure 4.46: Subicosa (1, 1, 1, 1) - top view

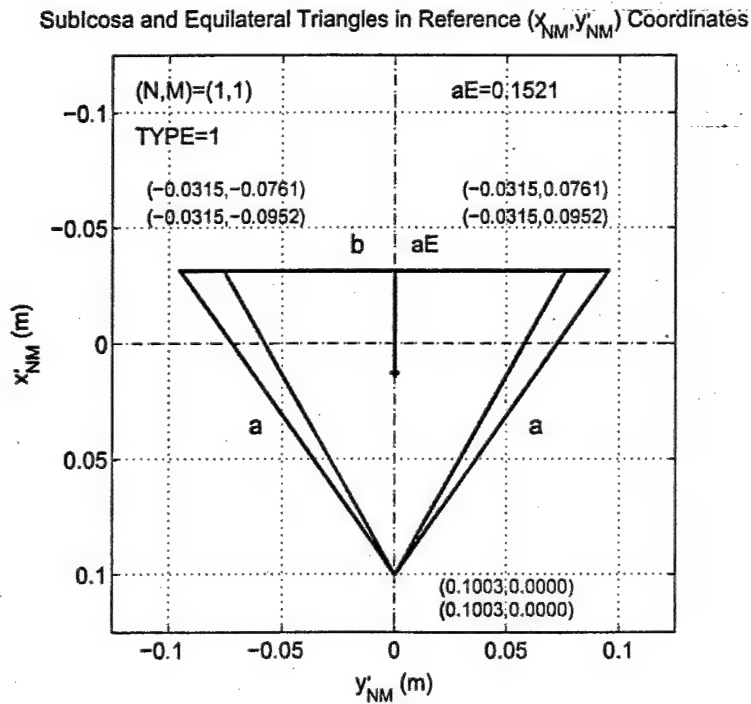


Figure 4.47: Subicosa (1, 1, 1, 1) and respective equilateral triangle in reference coordinate system (x'_{NM}, y'_{NM})

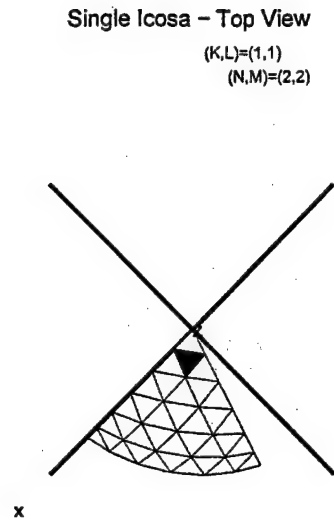


Figure 4.48: Subicosa (1, 1, 2, 2) - top view

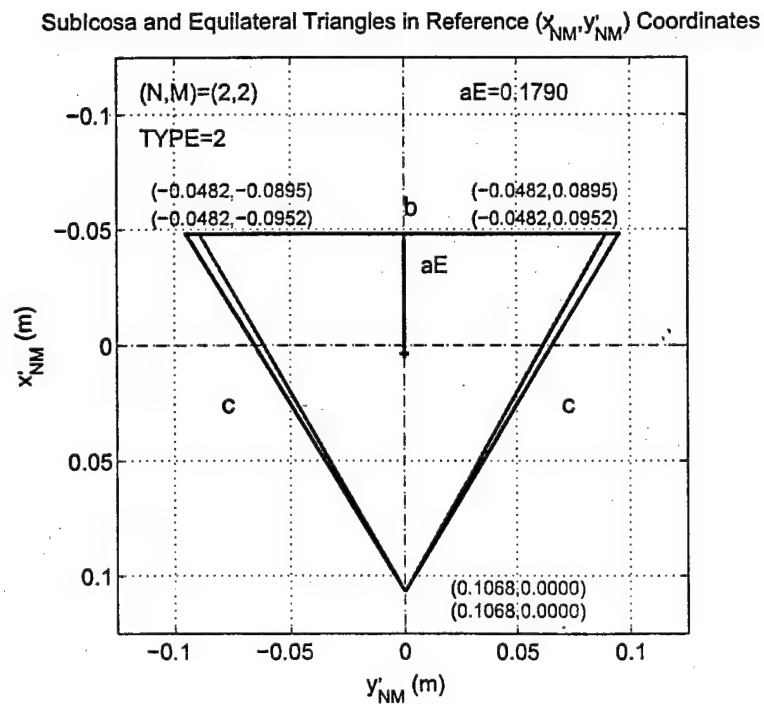


Figure 4.49: Subicosa (1, 1, 2, 2) and respective equilateral triangle in reference coordinate system (x'_{NM}, y'_{NM})

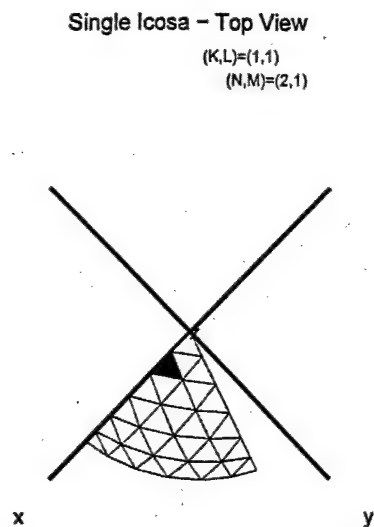


Figure 4.50: Subicosa (1, 1, 2, 1) - top view

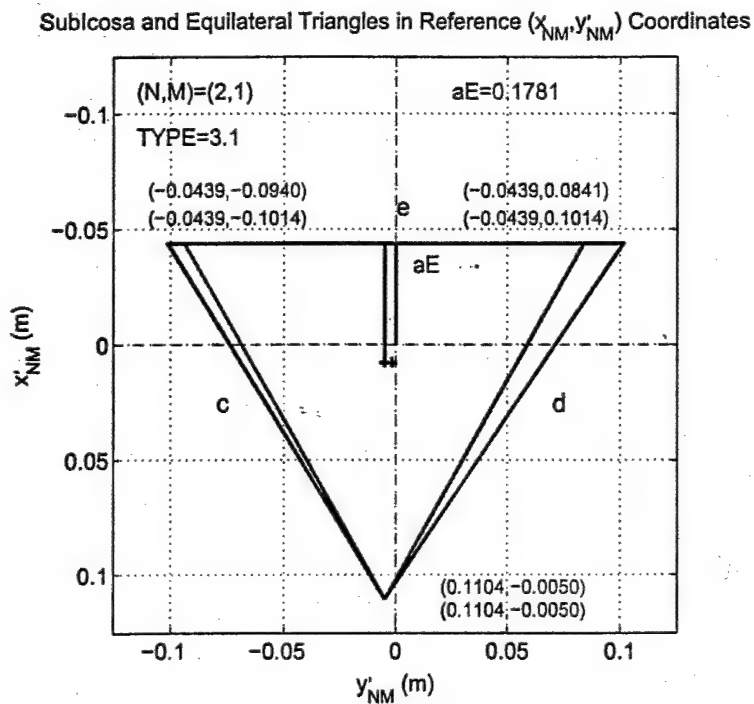


Figure 4.51: Subicosa (1, 1, 2, 1) and respective equilateral triangle in reference coordinate system (x'_{NM}, y'_{NM})

Single Icosa - Top View

(K,L)=(1,1)
(N,M)=(2,3)

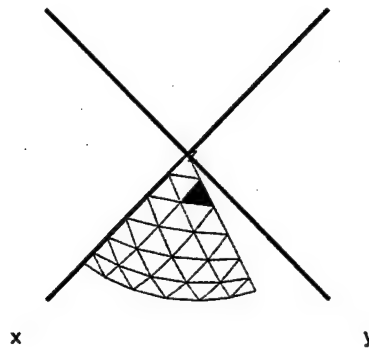


Figure 4.52: Subicosa (1, 1, 2, 3) - top view

Subicosa and Equilateral Triangles in Reference (x'_{NM}, y'_{NM}) Coordinates

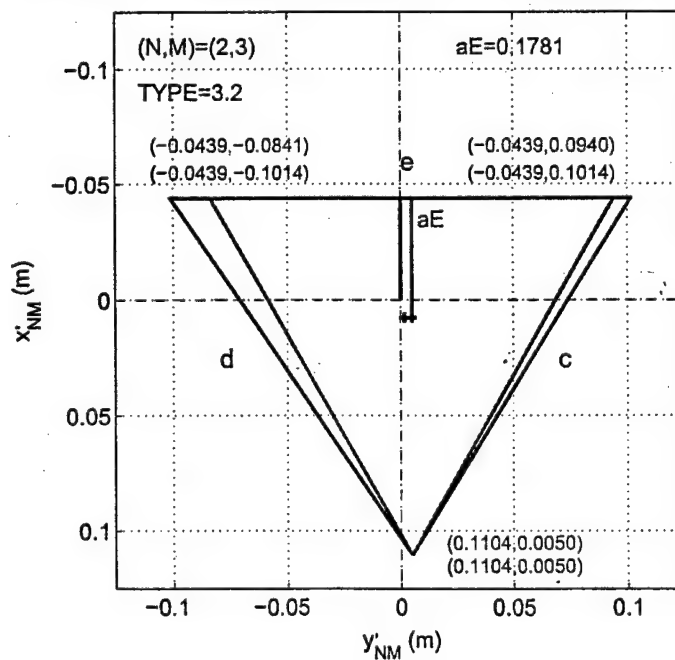


Figure 4.53: Subicosa (1, 1, 2, 3) and respective equilateral triangle in reference coordinate system (x'_{NM}, y'_{NM})

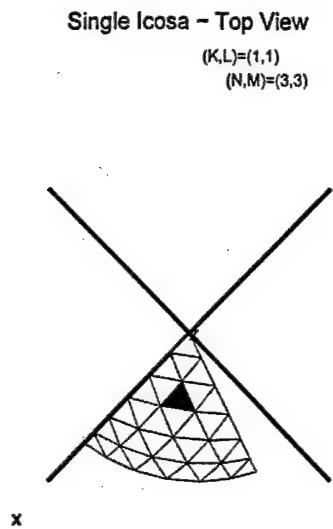


Figure 4.54: Subicosa (1, 1, 3, 3) - top view

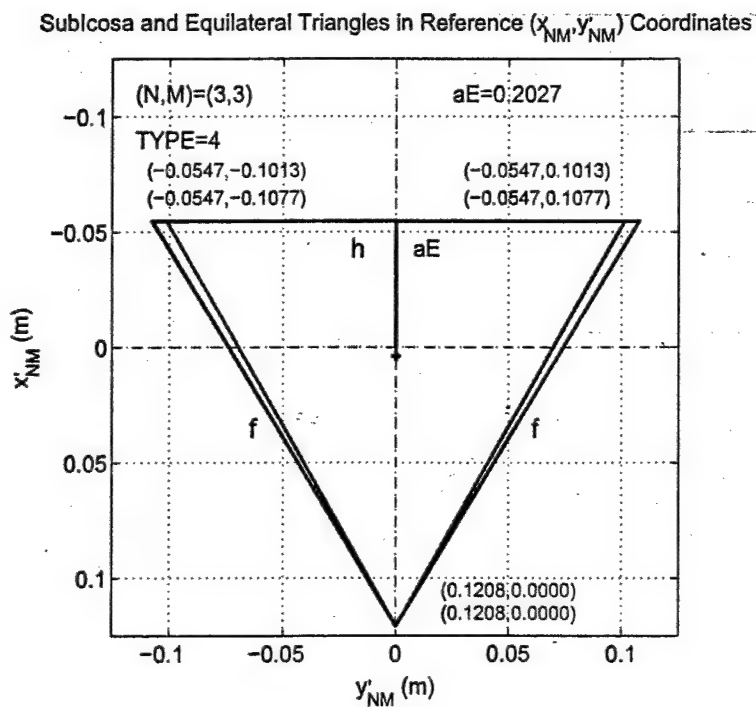


Figure 4.55: Subicosa (1, 1, 3, 3) and respective equilateral triangle in reference coordinate system (x'_{NM}, y'_{NM})

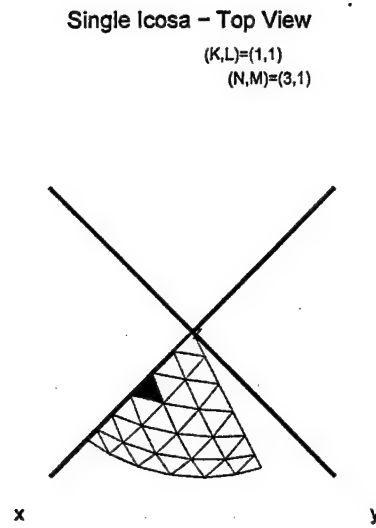


Figure 4.56: Subicosa (1, 1, 3, 1) - top view

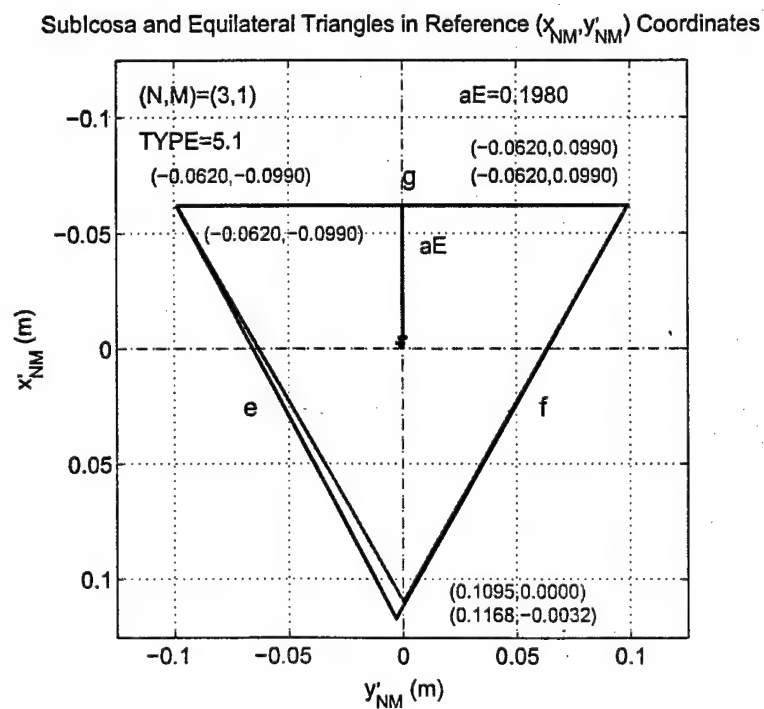


Figure 4.57: Subicosa (1, 1, 3, 1) and respective equilateral triangle in reference coordinate system (x'_{NM}, y'_{NM})

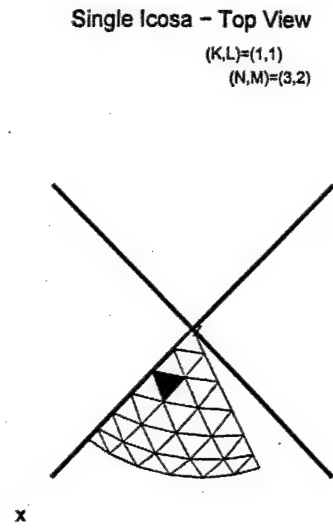


Figure 4.58: Subicosa (1, 1, 3, 2) - top view

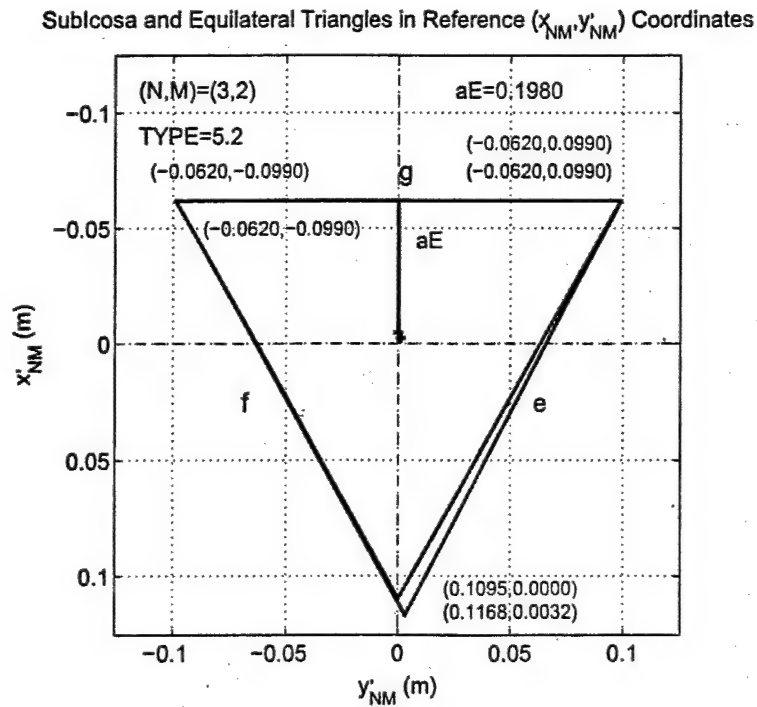


Figure 4.59: Subicosa (1, 1, 3, 2) and respective equilateral triangle in reference coordinate system (x'_{NM}, y'_{NM})

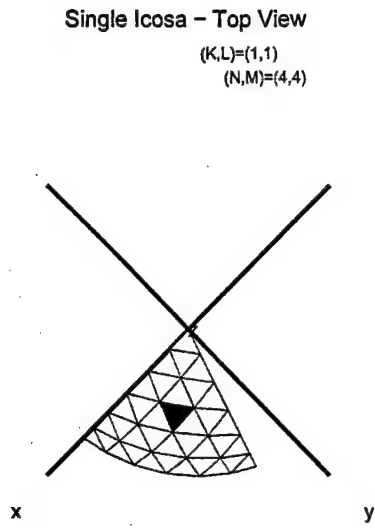


Figure 4.60: Subicosa (1, 1, 4, 4) - top view

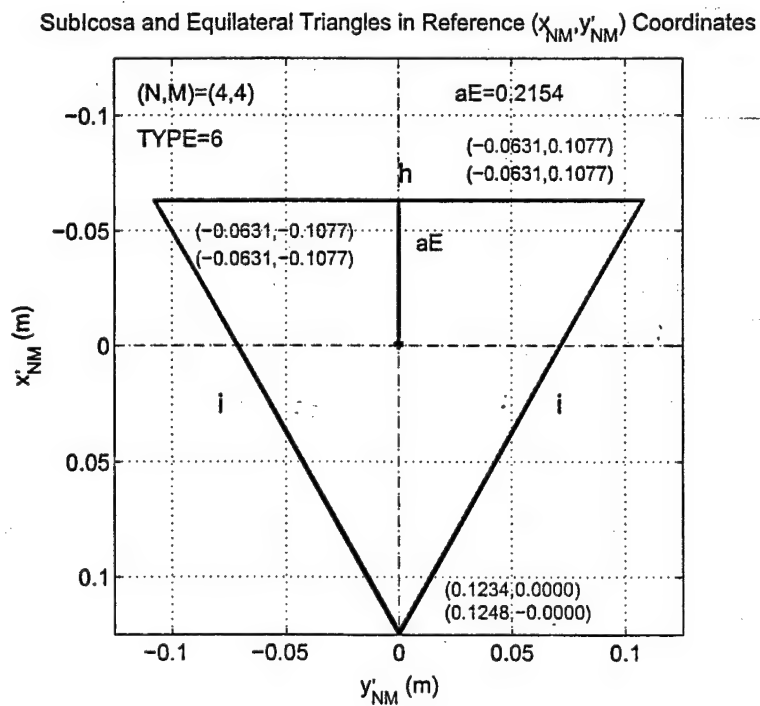


Figure 4.61: Subicosa (1, 1, 4, 4) and respective equilateral triangle in reference coordinate system (x'_{NM}, y'_{NM})

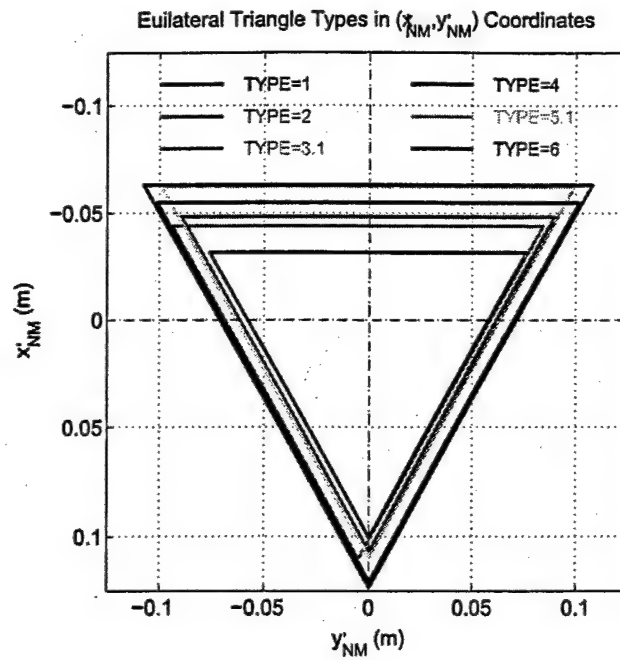


Figure 4.62: Equilateral triangle types in reference (x'_{NM}, y'_{NM}) coordinates

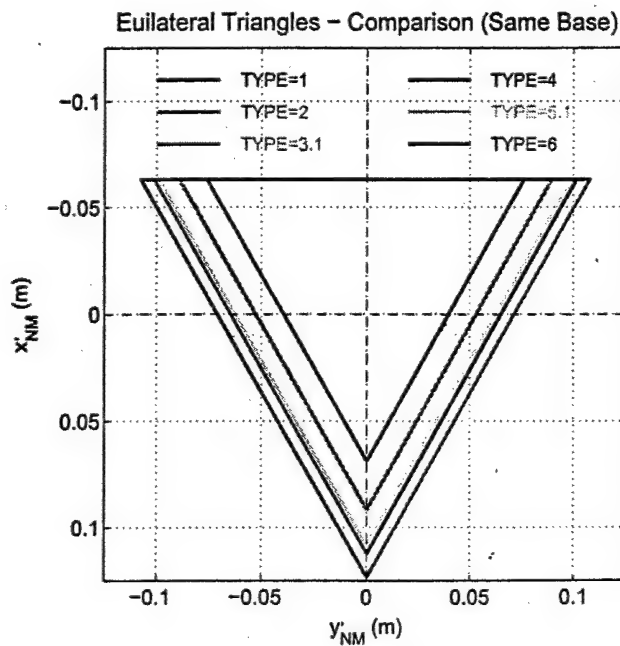


Figure 4.63: Equilateral triangle types in reference (x'_{NM}, y'_{NM}) coordinates with aligned basis for ease of comparison

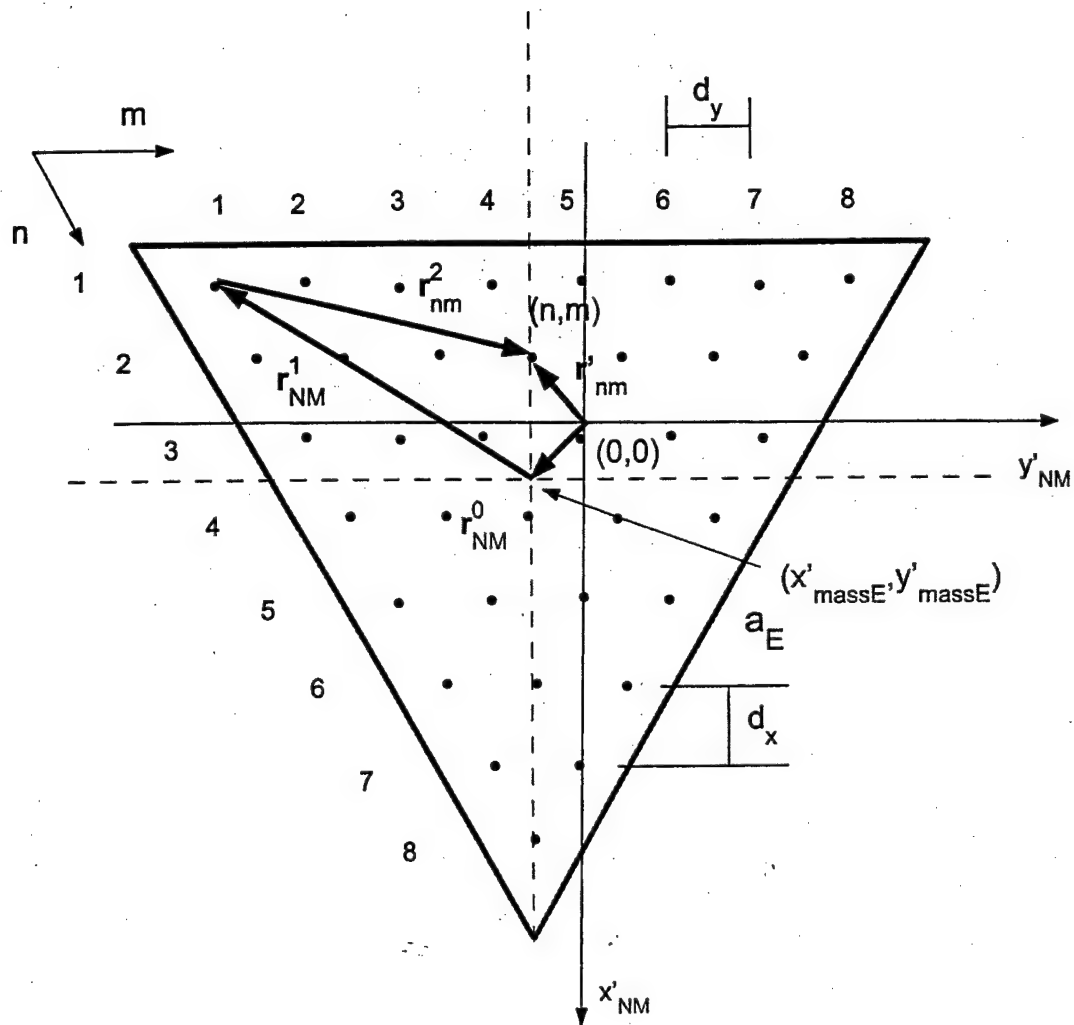


Figure 4.64: Equilateral triangle pertaining to location of array elements in reference coordinate system

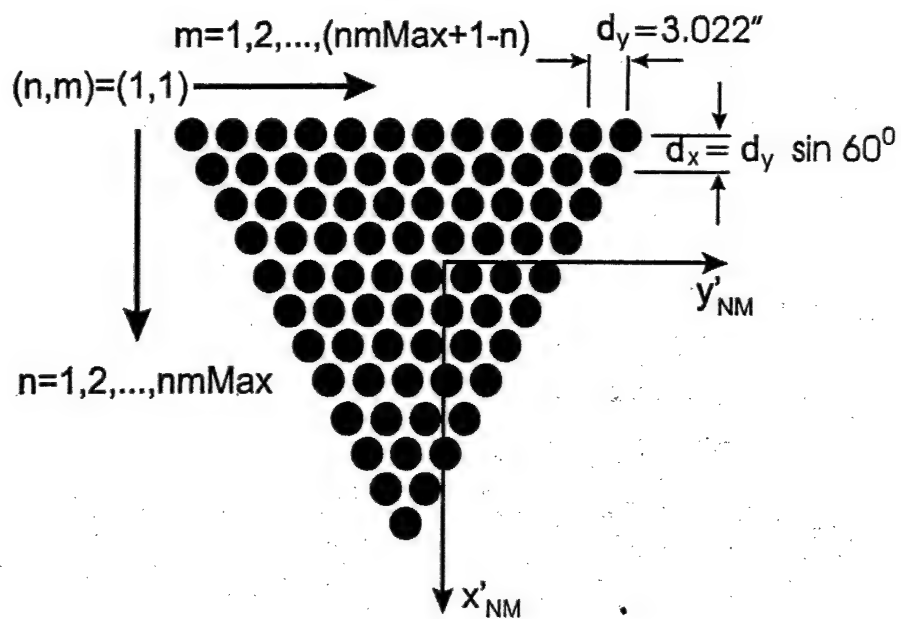


Figure 4.65: Array elements in reference coordinate system (x'_{NM}, y'_{NM})

Panel Type	(N,M)	Equilateral triangle side (m)		nmMax R=5m	No of Elements
		R=1m	R=5m		
1	(1,1)	0.1521	0.7607	8	36
2	(2,2)	0.179	0.8948	10	55
3	(2,1)	0.1781	0.8906	10	55
4	(3,3)	0.2027	1.0133	12	78
5	(3,1)	0.198	0.9901	11	66
6	(4,4)	0.2154	1.0768	13	91

Table 4.7: Number of rows and elements for 6 panel types

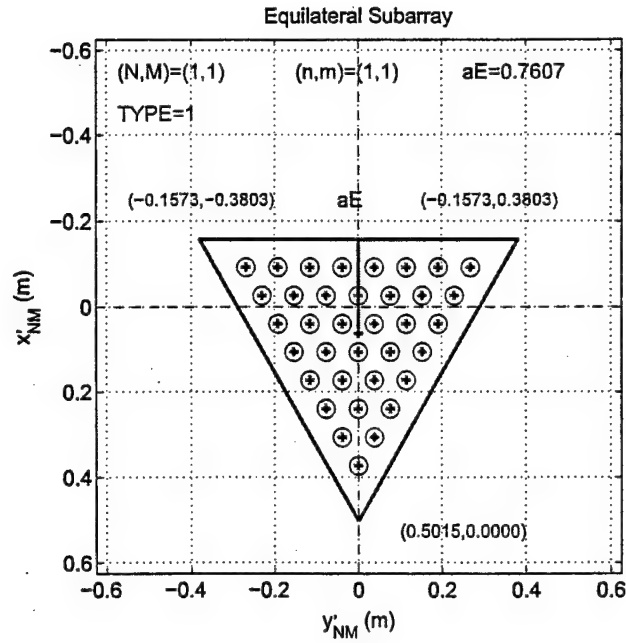


Figure 4.66: Equilateral subarray in reference (x'_{NM}, y'_{NM}) coordinates, $R = 5m$, Type 1

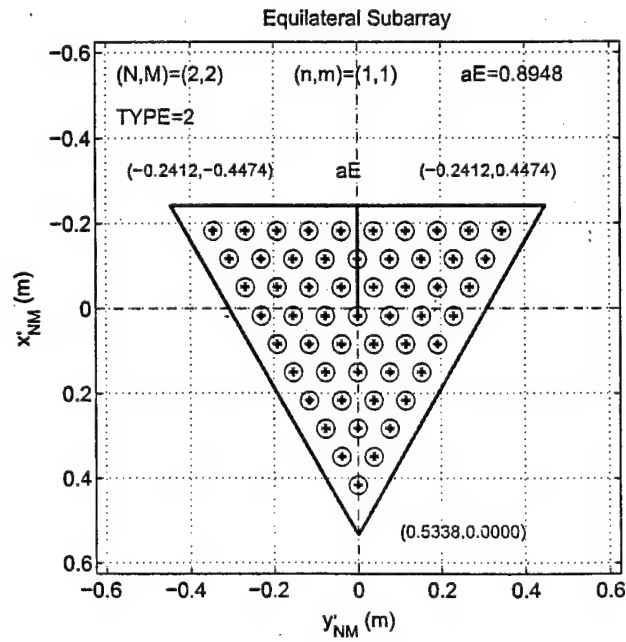


Figure 4.67: Equilateral subarray in reference (x'_{NM}, y'_{NM}) coordinates, $R = 5m$, Type 2

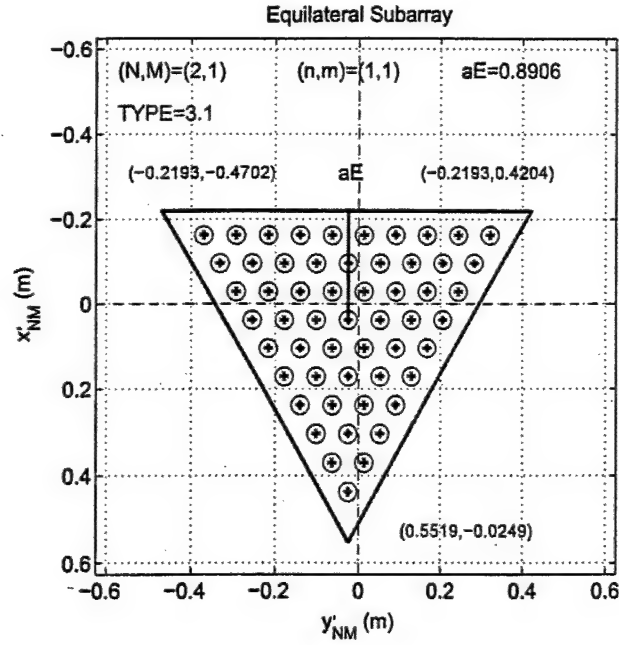


Figure 4.68: Equilateral subarray in reference (x'_{NM}, y'_{NM}) coordinates, $R = 5m$, Type 3

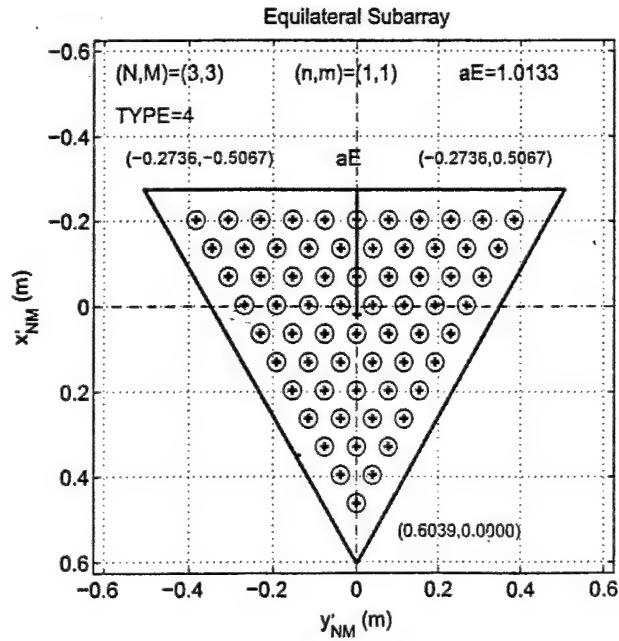


Figure 4.69: Equilateral subarray in reference (x'_{NM}, y'_{NM}) coordinates, $R = 5m$, Type 4

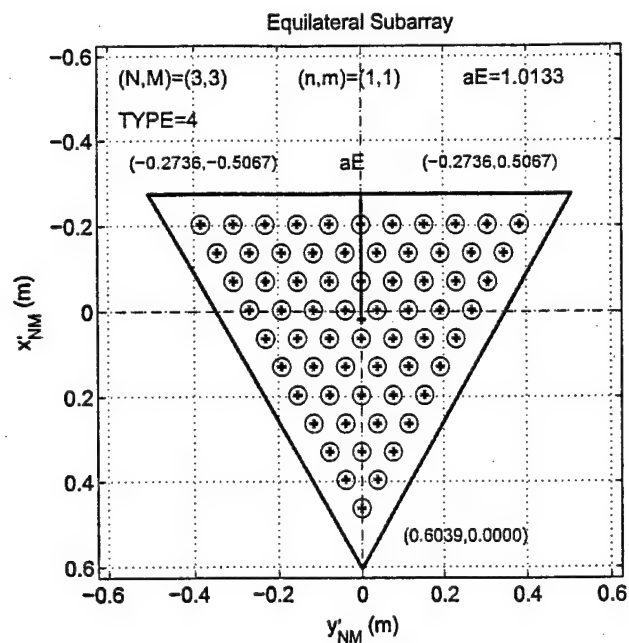


Figure 4.70: Equilateral subarray in reference (x'_{NM}, y'_{NM}) coordinates, $R = 5m$, Type 5

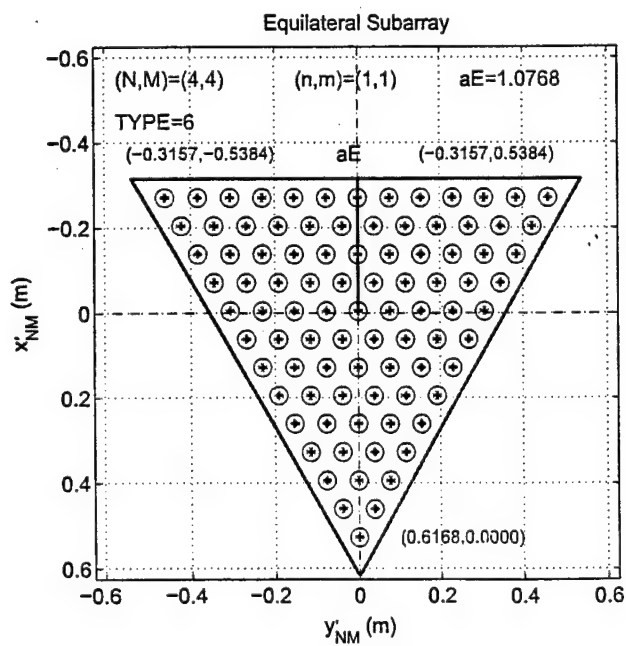


Figure 4.71: Equilateral subarray in reference (x'_{NM}, y'_{NM}) coordinates, $R = 5m$, Type 6

Chapter 5

Geodesic Dome Array Beamsteering and Radiation Patterns

5.1 Element pattern

5.1.1 Element pattern in reference coordinates

The element pattern is originally given in reference coordinate system $(x'_{NM}, y'_{NM}, z'_{NM})$ (see Figure 4.65), which for CP field can be written as

$$e_{NM}(\theta'_{NM}, \phi'_{NM}) = E_0 \sqrt{\cos \theta'_{NM}} e^{\pm j \phi'_{NM}} \frac{1}{\sqrt{2}} (\hat{\theta}'_{NM} \pm j \hat{\phi}'_{NM}) \quad (5.1)$$

where \pm refers to the LHCP and RHCP wave fields. Here, $(\theta'_{NM}, \phi'_{NM})$ are the observation angles in reference coordinates. Since every element, (nm) , on a given subcosa (subarray/facet/panel) sees the far field observation point at the same angle, in (5.1), we replaced "element" subscripts (nm) by "panel" subscripts (NM) . Furthermore, in (5.1), $(\hat{\theta}'_{NM}, \hat{\phi}'_{NM})$ are respective unit vectors as shown in Figure 5.1, and

$$E_0 = \sqrt{\frac{\zeta_0}{4\pi}} \sqrt{\frac{4\pi A_{cell}}{\lambda^2}}. \quad (5.2)$$

5.1.2 Element pattern in local coordinates

Next, we transform this element field pattern into local coordinates (x_{NM}, y_{NM}, z_{NM}) by using following identities:

$$\begin{bmatrix} \hat{\theta}'_{NM} \\ \hat{\phi}'_{NM} \end{bmatrix} = \begin{bmatrix} 1 & 0 \\ 0 & 1 \end{bmatrix} \begin{bmatrix} \hat{\theta}_{NM} \\ \hat{\phi}_{NM} \end{bmatrix} \quad (5.3)$$

$$\begin{bmatrix} x'_{NM} \\ y'_{NM} \\ z'_{NM} \end{bmatrix} = \begin{bmatrix} \cos \varphi_{NM} & \sin \varphi_{NM} & 0 \\ -\sin \varphi_{NM} & \cos \varphi_{NM} & 0 \\ 0 & 0 & 1 \end{bmatrix} \begin{bmatrix} x_{NM} \\ y_{NM} \\ z_{NM} \end{bmatrix} \quad (5.4)$$

and

$$\theta'_{NM} = \theta_{NM} \quad (5.5)$$

$$\phi'_{NM} = \phi_{NM} - \varphi_{NM}. \quad (5.6)$$

Thus, in local coordinates (see Figure 5.2), the element patterns becomes

$$\mathbf{e}_{NM}(\theta_{NM}, \phi_{NM}) = E_0 \sqrt{\cos \theta_{NM}} e^{\pm j \phi_{NM}} \frac{1}{\sqrt{2}} (\hat{\theta}_{NM} \pm j \hat{\phi}_{NM}). \quad (5.7)$$

5.1.3 Element pattern in global coordinates

The respective local unit vectors $(\hat{\mathbf{x}}_{NM}, \hat{\mathbf{y}}_{NM}, \hat{\mathbf{z}}_{NM})$ are related to the unit vectors of the global coordinate system $(\hat{\mathbf{x}}, \hat{\mathbf{y}}, \hat{\mathbf{z}})$ by the following rotation matrix equation:

$$\begin{bmatrix} \hat{\mathbf{x}}_{NM} \\ \hat{\mathbf{y}}_{NM} \\ \hat{\mathbf{z}}_{NM} \end{bmatrix} = \tilde{A}_{NM} \begin{bmatrix} \hat{\mathbf{x}} \\ \hat{\mathbf{y}} \\ \hat{\mathbf{z}} \end{bmatrix} \quad (5.8)$$

where \tilde{A} is a rotation matrix and is given by

$$\tilde{A}_{NM} = \begin{bmatrix} \cos \alpha_{NM} \cos \beta_{NM} & \cos \alpha_{NM} \sin \beta_{NM} & -\sin \alpha_{NM} \\ -\sin \beta_{NM} & \cos \beta_{NM} & 0 \\ \sin \alpha_{NM} \cos \beta_{NM} & \sin \alpha_{NM} \sin \beta_{NM} & \cos \alpha_{NM} \end{bmatrix}. \quad (5.9)$$

From Appendix B.3, the following two relations are obtained:

$$\cos \theta_{NM} = \sin \alpha_{NM} \sin \theta \cos(\phi - \beta_{NM}) + \cos \alpha_{NM} \cos \theta \quad (5.10)$$

$$\cot \phi_{NM} = \frac{\cos \alpha_{NM} \sin \theta \cos(\phi - \beta_{NM}) - \sin \alpha_{NM} \cos \theta}{\sin \theta \sin(\phi - \beta_{NM})}. \quad (5.11)$$

Similarly the local unit vectors $(\hat{\theta}_{NM}, \hat{\phi}_{NM})$ can be transformed into global coordinates via:

$$\begin{bmatrix} \hat{\theta}_{NM} \\ \hat{\phi}_{NM} \end{bmatrix} = \begin{bmatrix} -a_{NM} & b_{NM} \\ -b_{NM} & -a_{NM} \end{bmatrix} \begin{bmatrix} \hat{\theta} \\ \hat{\phi} \end{bmatrix} \quad (5.12)$$

where

$$a_{NM} = \frac{\cos \theta \sin \alpha_{NM} \cos(\phi - \beta_{NM}) - \sin \theta \cos \alpha_{NM}}{\sin \theta_{NM}} \quad (5.13)$$

and

$$b_{NM} = \frac{\sin \alpha_{NM} \sin(\phi - \beta_{NM})}{\sin \theta_{NM}}. \quad (5.14)$$

Consequently, in (5.7), as in Appendix B.6 for an array element, the factor $(\hat{\theta}_{NM} \pm j \hat{\phi}_{NM})$ becomes:

$$\hat{\theta}_{NM} \pm j \hat{\phi}_{NM} = -(\hat{\theta} \pm j \hat{\phi}) e^{\pm j \nu_{NM}} \quad (5.15)$$

where

$$\tan \nu_{NM} = \frac{b_{NM}}{a_{NM}} = \frac{\sin \alpha_{NM} \sin(\phi - \beta_{NM})}{\cos \theta \sin \alpha_{NM} \cos(\phi - \beta_{NM}) - \sin \theta \cos \alpha_{NM}}. \quad (5.16)$$

Now we can rewrite the element pattern relation (5.7) in global coordinates as

$$\mathbf{e}_{nm}(\theta, \phi) = -E_0 \sqrt{\cos \theta_{NM}} \frac{1}{\sqrt{2}} (\hat{\theta} \pm j\hat{\phi}) e^{\pm j\nu_{NM}} e^{j\psi_{nm}} e^{\pm j\phi_{NM}} \quad (5.17)$$

where $\cos \theta_{NM}$ and ϕ_{NM} are expressed in terms of (θ, ϕ) by (5.10) and (5.11). Here the phase ψ_{nm} accounts for the difference in propagation path lengths from the radiating element to the far field point and the global origin to the far field point. In reference to Figure 5.2, ψ_{nm} is

$$\psi_{nm} = k\mathbf{R}_{nm} \cdot \hat{\mathbf{r}}. \quad (5.18)$$

The radial vector specifying the location of the array elements in global coordinates, Figure 4.32 and Figure 4.64, is

$$\mathbf{R}_{nm} = \mathbf{R}_{NM} + \mathbf{r}'_{nm} \quad (5.19)$$

and is defined in (4.78) as

$$\mathbf{R}_{nm} = \hat{\mathbf{x}}x_{nm} + \hat{\mathbf{y}}y_{nm} + \hat{\mathbf{z}}z_{nm} \quad (5.20)$$

where (x_{nm}, y_{nm}, z_{nm}) are the coordinates of the array elements in global coordinates. Since,

$$\hat{\mathbf{r}} = \hat{\mathbf{x}} \sin \theta \cos \phi + \hat{\mathbf{y}} \sin \theta \sin \phi + \hat{\mathbf{z}} \cos \theta \quad (5.21)$$

from (5.18) using (5.19) and (5.21) we get

$$\psi = k(x_{nm} \sin \theta \cos \phi + y_{nm} \sin \theta \sin \phi + z_{nm} \cos \theta). \quad (5.22)$$

Notice that in (5.17) we re-introduced subscripts (n, m) , i.e., we replaced \mathbf{e}_{NM} by \mathbf{e}_{nm} because factor ψ_{nm} depends on (nm) .

5.2 Far-field

Array far-field (in global coordinates):

$$\mathbf{E}(\mathbf{r}; t) = \mathbf{E}(\theta, \phi) \frac{e^{j(\omega t - kr)}}{r} \quad (5.23)$$

where

$$\mathbf{E}(\theta, \phi) = \hat{\theta} E_{\theta}(\theta, \phi) + \hat{\phi} E_{\phi}(\theta, \phi) = \sum_{nm} \mathbf{E}_{nm}(\theta, \phi) \quad (5.24)$$

and, the field due to a single element in the array environment is

$$\mathbf{E}_{nm}(\theta, \phi) = \delta_{nm} c_{nm}(\theta_0, \phi_0) \mathbf{e}_{nm}(\theta, \phi). \quad (5.25)$$

with \mathbf{e}_{nm} given by (5.17).

5.2.1 On-Off switch:

In (5.25), the Kronecker delta δ_{nm} defines the active sector on the array. In other words it is a switch turning on and off the array elements as beam scans. We used two criteria to determine the active sector: (a) element level and (b) panel or subarray level.

(a) **element level:** In this case all elements within the cone angle α_{max} are on, while all others are turned off, Figure 5.3 and Figure 5.4. The axis of the cone coincides with the main beam direction. This criteria gives smooth edges to the active "spherical" sector which means it can potentially produce a low sidelobe radiation pattern if required. The drawback of this criteria is, however, that since some of the elements located on the "edge" panels (subarrays) will be turned on and some will be turned off, there will be degradation of the S/N or G/T on the panel level in the receive case or reduced efficiency in the transmit case. We assumed that each panel has one output per beam and that all subarray elements are fed by the corporate RF manifold. In addition, this scheme requires more computational power in the beamsteering algorithm than the scheme (b) which for a large array may be undesirable. It may be interesting to point out that the edge elements on different panels see the far field at the peak of the beam at slightly different angles (within few degrees) with respect to the local normal. For example, if we set $\alpha_{max} = 60^\circ$, the local observation angles of the edge elements will have different values in the vicinity of 60° plus/minus a couple of degrees so the edge circle may exhibit a small discontinuity as it crosses from one to neighboring panel. Thus, we define

$$\delta_{nm} = \begin{cases} 1 & \text{if } \gamma_{nm} \leq \alpha_{max} \\ 0 & \text{otherwise} \end{cases} \quad (5.26)$$

where γ_{nm} is the angle between the axis of the cone and the radial line passing through the element (nm) as shown in Figure 5.3. To determine γ_{nm} we write

$$\cos \gamma_{nm} = \hat{\mathbf{r}}_0 \cdot \hat{\mathbf{r}}_{nm} \quad (5.27)$$

Here, the unit vector in direction of (n, m) element is

$$\hat{\mathbf{r}}_{nm} = \frac{\mathbf{R}_{nm}}{R_{nm}} \quad (5.28)$$

where \mathbf{R}_{nm} is defined by (5.20) and the distance between the element (nm) and the origin of the global coordinate system is

$$R_{nm} = \sqrt{x_{nm}^2 + y_{nm}^2 + z_{nm}^2} \quad (5.29)$$

Furthermore in (5.27), $\hat{\mathbf{r}}_0$ is the unit vector in the main beam direction (θ_0, ϕ_0) , thus

$$\hat{\mathbf{r}}_0 = \hat{\mathbf{x}} \sin \theta_0 \cos \phi_0 + \hat{\mathbf{y}} \sin \theta_0 \sin \phi_0 + \hat{\mathbf{z}} \cos \theta_0. \quad (5.30)$$

Substituting (5.20) and (5.29) into (5.28) and then (5.28) and (5.30) into (5.27), we get

$$\cos \gamma_{nm} = \frac{x_{nm}}{R_{nm}} \sin \theta_0 \cos \phi_0 + \frac{y_{nm}}{R_{nm}} \sin \theta_0 \sin \phi_0 + \frac{z_{nm}}{R_{nm}} \cos \theta_0. \quad (5.31)$$

(a) **panel level:** In this case δ_{nm} in (5.25) is replaced by δ_{NM} where (NM) refers to the subarray containing element (nm) . In this scheme the active sector on the dome consists of a fixed number of active panels while all other panels are completely off. As a beam scans across the sky, some of the edge panels will be switched off while some panels that were off will be switched on. It is clear that this scheme is simpler than scheme (a), therefore it requires less computational power for the beamsteering. Also, compared to scheme (a), there is no additional RF loss in the edge panels because each individual panel has either all elements turned on or off. The drawback of this scheme is that the active sector's edges are rough and because of that the beam shape won't be uniform. Also it may not give very low sidelobes especially for small active areas on the dome. In this case,

$$\delta_{NM} = \begin{cases} 1 & \text{if } \gamma_{NM} \leq \alpha_{max} \\ 0 & \text{otherwise} \end{cases} \quad (5.32)$$

where γ_{NM} is the angle between the beam axis and the radial line passing thru the origin of the local coordinate system $O_{NM}(R_{NM}, \alpha_{NM}, \beta_{NM})$. Thus all panels with O_{NM} falling inside the cone angle α_{max} will be turned on while all others will be off. In reference to Figure 5.5 and Figure 5.6, γ_{NM} is

$$\cos \gamma_{NM} = \hat{\mathbf{r}}_0 \cdot \hat{\mathbf{r}}_{NM} \quad (5.33)$$

where

$$\hat{\mathbf{r}}_{NM} = \hat{\mathbf{x}} \sin \alpha_{NM} \cos \beta_{NM} + \hat{\mathbf{y}} \sin \alpha_{NM} \sin \beta_{NM} + \hat{\mathbf{z}} \cos \alpha_{NM}. \quad (5.34)$$

Substituting (5.30) and (5.34) into (5.33), we get

$$\cos \gamma_{NM} = \sin \theta_0 \cos \phi_0 \sin \alpha_{NM} \cos \beta_{NM} + \sin \theta_0 \sin \phi_0 \sin \alpha_{NM} \sin \beta_{NM} + \cos \theta_0 \cos \alpha_{NM}. \quad (5.35)$$

In (5.35), see Figure 5.5, α_{max} determines the size of the active sector. Typically, $\alpha_{max} \leq 60^\circ$. In this case the array elements on the edge panels will see the beam observation point at local angles 60° or less, but not more than α_{max} . Local observation angles are equivalent to planar subarray scan angles measured from local broadside. As is known, the planar array impedance and the radiation and polarization properties rapidly degrade after 60° scan, so it is not advisable to set α_{max} greater than 60° . So, in this scheme, the maximum scan angle of the subarray is equal or less than α_{max} . This is an important parameter to know in the design procedure of the subarray.

The panel level scheme also has the advantage that the numbers of beams provided by subarray/panel can be doubled or quadrupled with very small additional cost. To elaborate on this, we assume that each panel's BFN consists of two transmit and two receive RF manifolds. This means that the panel can produce four simultaneous independent beams (two transmit and two receive beams). However, not all satellite links require full size aperture. Satellites in deep space GEO or HEO may need full dome aperture, but MEO and LEO satellites may need only a fraction of the full size aperture (six or twelve panels for example). The geodesic dome antenna can provide "gain on demand", i.e., the $EIRP$ for transmit beams and G/T for receive beams can be adjusted to meet specific satellite link requirements. This is done by varying size of the active sector as illustrated in Figure 5.9 for two independent transmit beams, TX1-A and TX2-A.

The geodesic dome array based on icosahedron structure with 6ν subdivision frequency consists of 675 subarrays/panels. As already mentioned, panels for a given beam in an active sector are turned on while all others are off. Panel beam-ports that are off can be used to form an additional four or more beams. This can be done simply by adding four single-pol double-throw RF switches at the panel output beam ports and four 1:675 RF manifolds as illustrated in Figure 5.8 for the special case where we double the number of transmit and receive beams. The two additional transmit beams are designated by TX1-B and TX2-B in Figure 5.9. It is important to mention that the active areas of two beams from the same subarray beamport can not overlap. The TX1-B and TX2-B are completely independent beams, however the active sector of TX1-B can not overlap with TX1-A and active sector of TX2-B can not overlap with TX2-A. Thus, in this case the geodesic dome can support four transmit beams and four receive beams, two transmit and two receive beams being completely independent while the other four beams (two Tx and two Rx) are conditionally independent.

In practice, since the satellites are roughly uniformly distributed in a hemisphere, using the antenna resource management computer (smart time and space satellite link management and scheduling) the conditional independence can be met most of the time. In the case this condition can't be satisfied at first, beam re-assignment on the fly may be required (switching with another beam/satellite). If the independence condition between the two beams is still not met, then one can resolve this situation by moving one or both relevant active sectors off conical axis (away from each other). Consequently, the two beams in conflict are no longer broadside but are skewed with respect to their cone axis (broadside) and therefore will suffer small scan losses. The antenna resource management computer can compensate this losses by adding one or two panels to their active areas needed at broadside.

5.2.2 Element voltage excitation coefficients

In (5.25), c_{nm} are the element voltage excitation coefficients

$$c_{nm}(\theta_0, \phi_0) = |c_{nm}(\theta_0, \phi_0)| e^{j\chi_{nm}(\theta_0, \phi_0)} \quad (5.36)$$

where $|c_{nm}|$ is the desired aperture illumination function.

From (5.25) and (5.17) it is seen that to point the beam in (θ_0, ϕ_0) direction, Figure 5.7, χ_{nm} must be

$$\chi_{nm}(\theta_0, \phi_0) = -[\psi_{nm}(\theta_0, \phi_0) \pm \nu_{NM}(\theta_0, \phi_0) \pm \phi_{nm}(\theta_0, \phi_0)]. \quad (5.37)$$

5.3 Array Gain

The array gain is

$$G(\theta, \phi) = \frac{\mathbf{E}(\mathbf{r}) \cdot \mathbf{E}^*(\mathbf{r})}{\zeta_0 P_0} \quad (5.38)$$

where free space impedance $\zeta_0 = 376.7$ ohms, and P_0 is isotropic source power density, i.e.,

$$P_0 = \frac{\sum_{nm} \delta_{nm} |c_{nm}|^2}{4\pi r^2}. \quad (5.39)$$

Thus,

$$G(\theta, \phi) = \frac{4\pi}{\zeta_0} \frac{|\sum_{nm} \delta_{nm} c_{nm} \mathbf{e}_{nm}(\theta, \phi)|^2}{\sum_{nm} \delta_{nm} |c_{nm}|^2}. \quad (5.40)$$

From here, peak array gain is

$$G(\theta_0, \phi_0) = \frac{4\pi}{\zeta_0} \frac{[\sum_{nm} \delta_{nm} |c_{nm}| |\mathbf{e}_{nm}(\theta_0, \phi_0)|]^2}{\sum_{nm} \delta_{nm} |c_{nm}|^2}. \quad (5.41)$$

It is important to keep in mind that in (5.41), for example for icosahedron with subdivision frequency $\nu = 6$, using Class I, Method 1, subdivision scheme

$$\sum_{nm} = \sum_{K=1}^3 \sum_{L=1}^{5(10)} \sum_{N=1}^6 \sum_{M=1}^{2N-1} \sum_{n=1}^{nmMax} \sum_{m=1}^{nmMax+1-n} \quad (5.42)$$

where as already discussed (KL) denotes ico of the icosahedron, (NM) denotes the sub-ico or subarray panel (facet) and (nm) denotes the radiating element on this subarray. If $K=1$ or 2 , $L=1$ to 5 , and if $K=2$ then L varies from 1 to 10 .

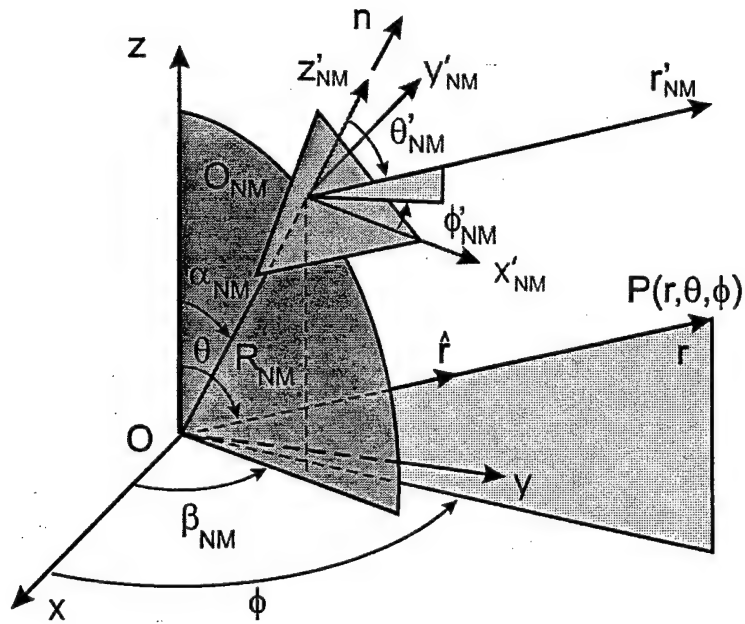


Figure 5.1: Observation angles $(\theta'_{NM}, \phi'_{NM})$ in reference coordinates

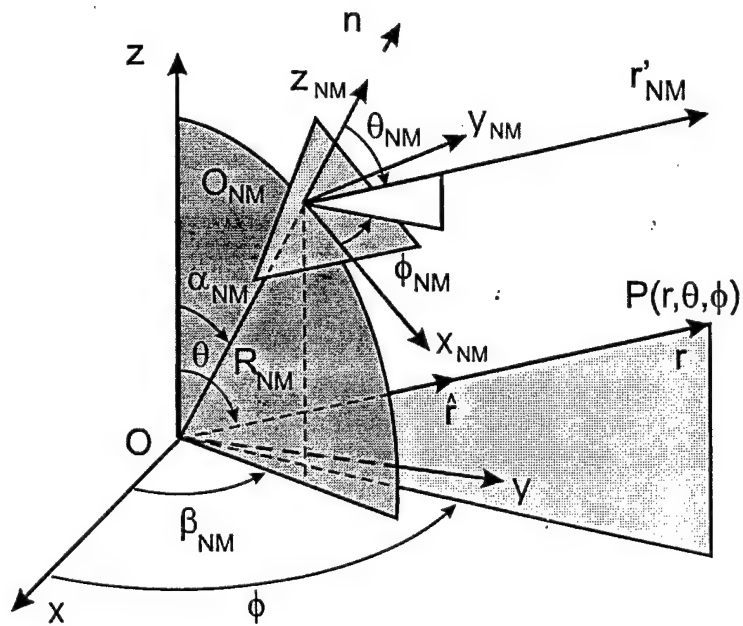


Figure 5.2: Observation angles (θ_{NM}, ϕ_{NM}) in local coordinates

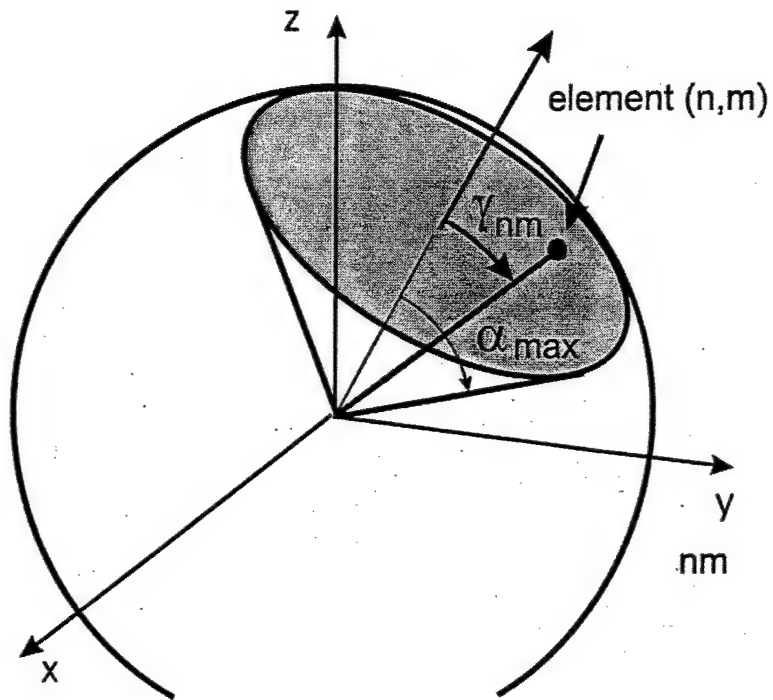


Figure 5.3: Active array sector - element level

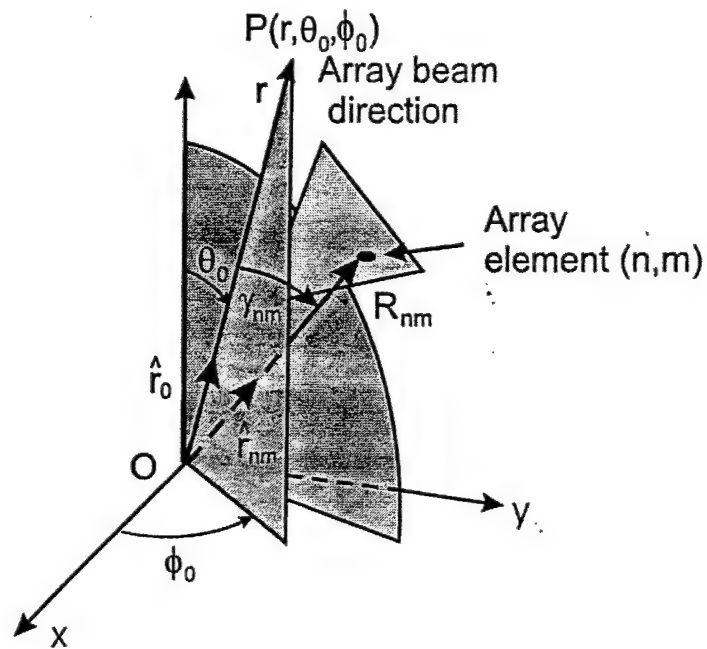


Figure 5.4: Geometry pertaining to evaluation of γ_{nm}

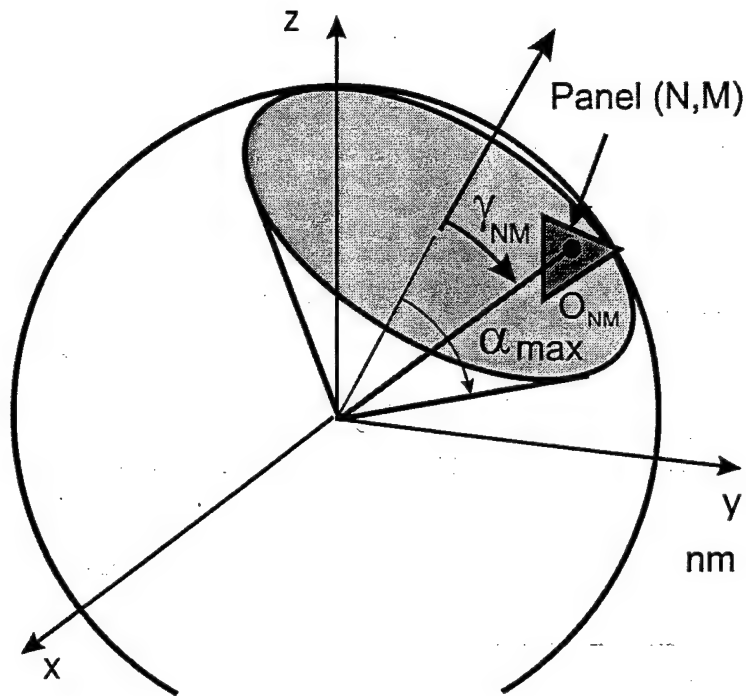


Figure 5.5: Active array sector - panel level

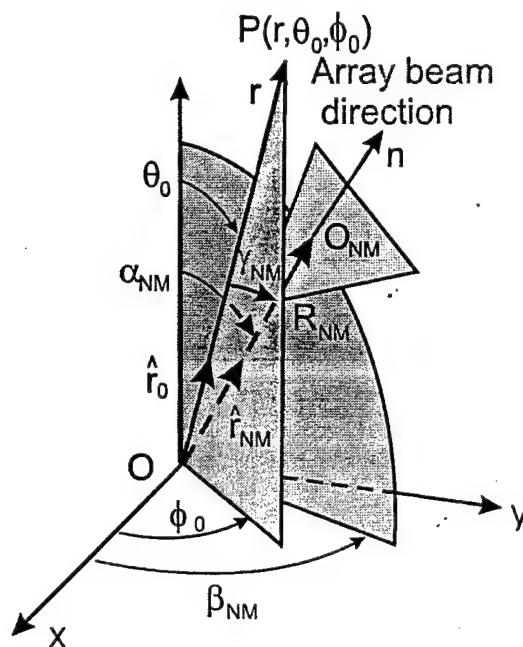


Figure 5.6: Geometry pertaining to evaluation of γ_{NM}

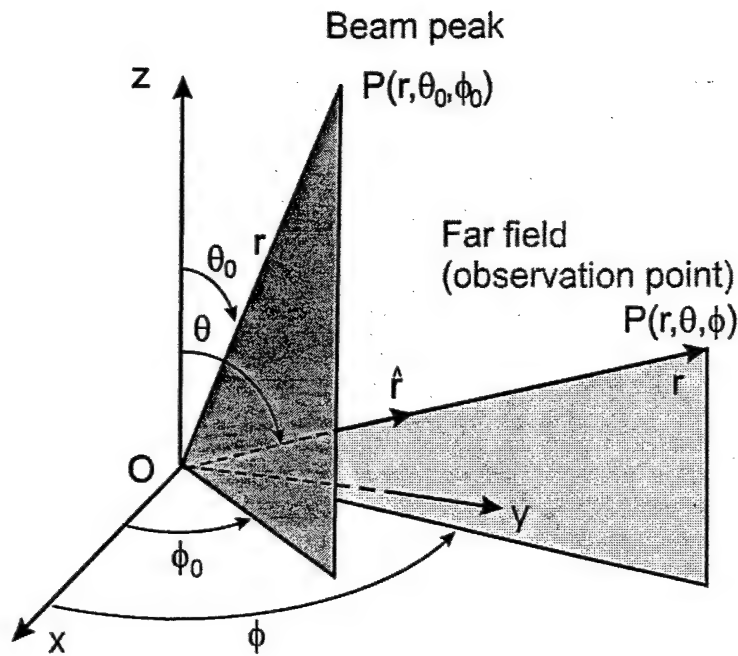


Figure 5.7: Far field observation angles (θ, ϕ) and beam direction angles (θ_0, ϕ_0) in global coordinate system

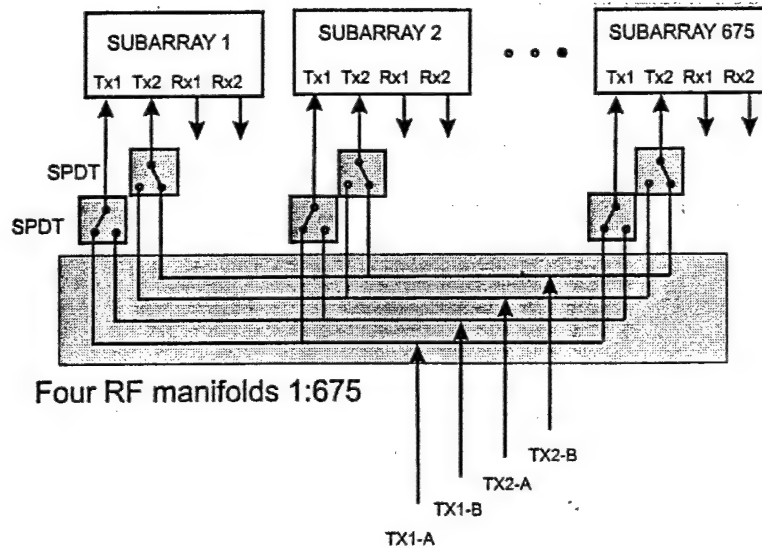


Figure 5.8: Subarray feed network supporting four simultaneous transmit and four simultaneous receive beams (switch positions shown are arbitrary and do not correspond to on/off panels in Figure 5.9)

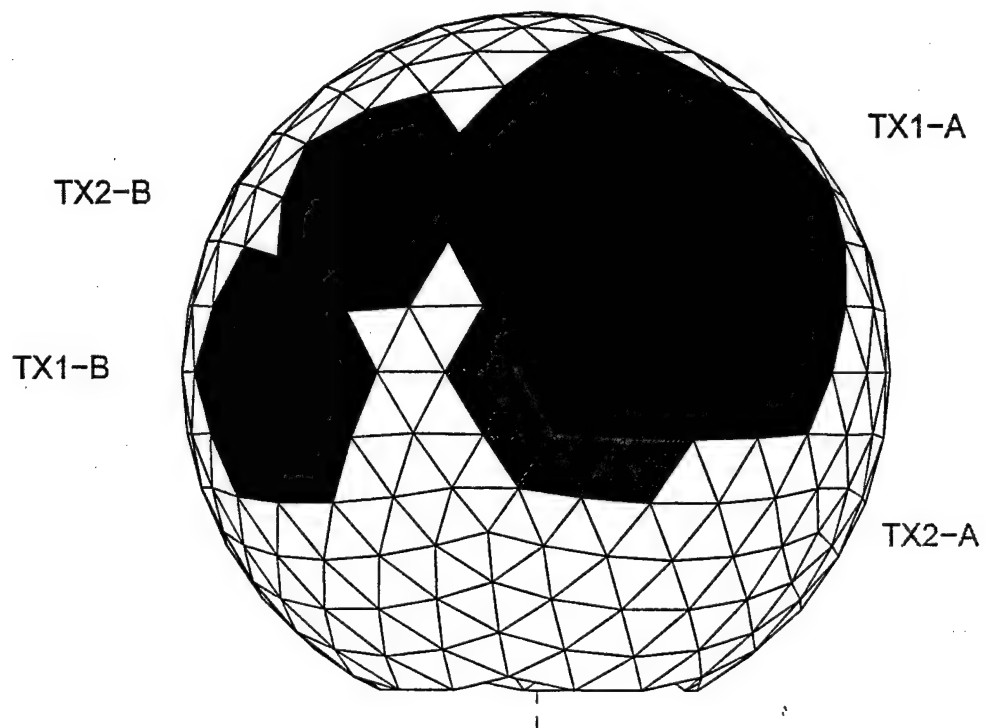


Figure 5.9: Geodesic dome showing active sectors of four simultaneous transmit beams (four receive beams not shown)

Chapter 6

Computer Codes

6.1 Code 1

6.1.1 Input

Based on the theory presented above, we have developed a MATLAB code "boris5.m" that evaluates all relevant geometrical parameters necessary for the construction geometry and beamsteering of the geodesic dome antenna. For a given dome radius, this code needs to be run only once. The code saves all output data into file "dataGD5.mat".

Input parameters can be entered via the GUI shown in Figure 6.1. For a selected icosahedron (K, L), and subicosahedron (N, M), and radiating element (n, m) the code produces a number of plots that may be useful for the design of a geodesic dome. For example it plots the icosahedron and subicosahedron, and the respective radiating elements on a 3D dome. By zooming into a subicosahedron one may see all radiating elements where the selected element (n, m) is fleshed out. Furthermore, the selected subicosahedron is plotted in the local coordinate system as well as in the reference coordinates. The respective triangle coordinates are printed. Similarly, the equilateral triangles and array elements are plotted in reference coordinates.

There is one single input parameter, i.e., array radius R . The code is valid for subdivision frequency 6, class I. The code saves output data if "Save Data" button is checked on.

6.1.2 Output

The output data file saves the following parameters:

$X1\ Y1\ Z1\ X2\ Y2\ Z2\ X3\ Y3\ Z3 = (x, y, z)$ coordinates of subicosahedron's (GD panels). It evaluates equation (4.1). The 4D arrays are of the size DIM(K,L,N,M)

$X0\ Y0\ Z0 = (x_0, y_0, z_0)$ coordinates of the origin of local coordinate system (x_{NM}, y_{NM}, z_{NM}). See equation (4.15). DIM(K,L,N,M)

$R0\ ALPHA\ BETA = (R_{NM}, \alpha_{NM}, \beta_{NM})$ coordinates of the origin of local coordinate system (x_{NM}, y_{NM}, z_{NM}). Eqs. (4.16) to (4.18). DIM(K,L,N,M).

$LX\ MX\ NX\ LY\ MY\ NY\ LZ\ MZ\ NZ$ =directional cosines of local (x_{NM}, y_{NM}, z_{NM}) axes,

DIM(K,L,N,M). Eqs. (4.19), (4.21), (4.23) and (4.24).

TYPE = panel (subicosa) type, DIM(N,M), see Figure 4.11.

PhiP = rotation angle φ_{NM} in radians, (angle between x_{NM} and x'_{NM}), DIM(K,L,N,M). Equation (4.32).

aE = equilateral triangle side length, DIM(K,L,N,M), See Section 4.3.2.

XCEm YCEm = center of mass for the equilateral triangle in reference coordinate system ($x'_{NM}, y'_{NM}, z'_{NM}$), DIM(K,L,N,M), see Section 4.3.2..

nmMax = Number of array rows in a panel, DIM(N,M), equation (4.63)

xEL yEL zEL = array element location in global (x, y, z) coordinate system, DIM(K,L,N,M,n,m), eq. (4.74).

The user friendly code was generated and tested in Matlab 6.5, Release 13. To run the code the user should go to the command window and type boris5.m - Enter. Then the GUI window will pop up. Set the input parameters as desired and press the run button. It is suggested that the user should first run the code with default input parameters and compare the output data with the original values and plots in Figure 6.2 to Figure 6.9.

By selecting different (K, L, N, M, n, m) one may observe specific panel and element locations on the dome. Coordinates and all relevant geometrical parameters can be read either from the plots for selected (K, L, N, M, n, m), or by going to the Matlab workspace to read the above output parameters which are written in a multidimensional array form. Leave the "Save Data" button off all the time except when the output data must be stored in output file dataGD5.mat. In principle, for given sphere radius R , the code needs to be executed only once.

6.2 Code 2

The second Matlab code "Tomas5.m" evaluates the required element phasing for a beam in the desired (θ_0, ϕ_0) direction; radiation patterns are also generated. The code reads the input data file "dataGD5.mat" that contains all necessary array geometry for beamsteering and calculation of the far-field. The code plots a full dome array with all radiating elements. The elements in an active sector are plotted in red while elements turned off are in green. Using the Matlab zoom command and object rotation, the user can interactively focus on specific area of interest around the dome. Since there are tens of thousands of elements in the array, the interactive plotting routine is unfortunately slow, but the graphics are useful for understanding and visualizing the geodesic dome array in action.

6.2.1 Input

Similarly as in Code 1, the input parameters can be entered via the GUI shown in Figure 6.10. The first column in Figure 6.10 specifies the selected panel and element on the dome. The

selected panel and element will be fleshed out in red in the dome plot. The second column in Figure 6.10 sets the array radius, frequency, the beam pointing direction (θ_0, ϕ_0) , the active sector angle α_{max} , and the ϕ =constant plane in which the radiation pattern will be evaluated and plotted. If the user wants to capture the peak of the beam, then one must set $\phi = \phi_0$. Finally, third column in GUI Figure 6.10, defines two aperture illuminations, uniform and $\sqrt{\cos\theta}$. If some other low-sidelobe aperture taper is needed then it is easy to modify the program accordingly. Then we have a choice of two criteria for the active sector: criteria based on the element or on the panel level. Furthermore, we have two choices for the polarization, circular or elliptical; and a choice whether we want to plot both the radiation pattern and the full geodesic dome or just the pattern.

6.2.2 Output

The GUI in Figure 6.10 shows the default input parameters. Figure 6.11 shows the respective active sector on the dome. Figure 6.11 and Figure 6.12 zoom in on the selected panel, while Figure 6.14 plots the radiation pattern for input of Figure 6.10.

Figure 6.15 shows the same GUI except the active sector is defined on the panel level. For an active sector with $\alpha_{max} = 60^\circ$, and $(\theta_0, \phi_0) = (0, 0)$, the sector is in a pentagon shape as shown in Figure 6.16 and in zoom in version in Figure 6.17. The respective radiation pattern is shown in Figure 6.18. Figure 6.20 and Figure 6.21 are output plots with input parameters given in GUI on Figure 6.19. This case is the same as that of Figure 6.15 except here $\theta_0 = 45^\circ$. Comparing Figure 6.18 and Figure 6.21 we see that the radiation pattern is practically independent of scan, which is an expected and desirable feature of the spherical arrays. Figure 6.22 to Figure 6.25 shows the same except in this case we apply panel level active sector criteria. The active sector for this case is shown in Figure 6.23 with the respective radiation pattern shown in Figure 6.25. Notice, by comparing Figure 6.21 and Figure 6.25, we see that for a large active sector there is not much difference in the radiation patterns between the two criteria.

For LEO satellites, the EIRP and G/T link requirements are much lower than for GEO satellites, and therefore the active sector on the dome could be much smaller than in previous examples. For example, the active sector of an equivalent 4m dish is shown in Figure 6.26. This spot will give roughly $G/T = 11\text{dB/K}$ enough for most low-flying birds. The active spot has a smooth contour which indicates that we used element level criteria to determine the active sector. The respective radiation pattern is shown in Figure 6.27. Figure 6.28 to Figure 6.35 show the same in scan intervals in elevation of 5 deg. Note the radiation pattern and peak gain as beam sweeps from $\theta_0 = 37.38$ deg to 57.38 deg are fairly scan independent.

To see the rough edge effects on radiation pattern and peak gain we run the same case but the active sector is determined based on whole panel criteria. As seen from Figure 6.36 to Figure 6.45 the peak gain is fairly constant while sidelobes are little higher than in the previous smooth-edge case.

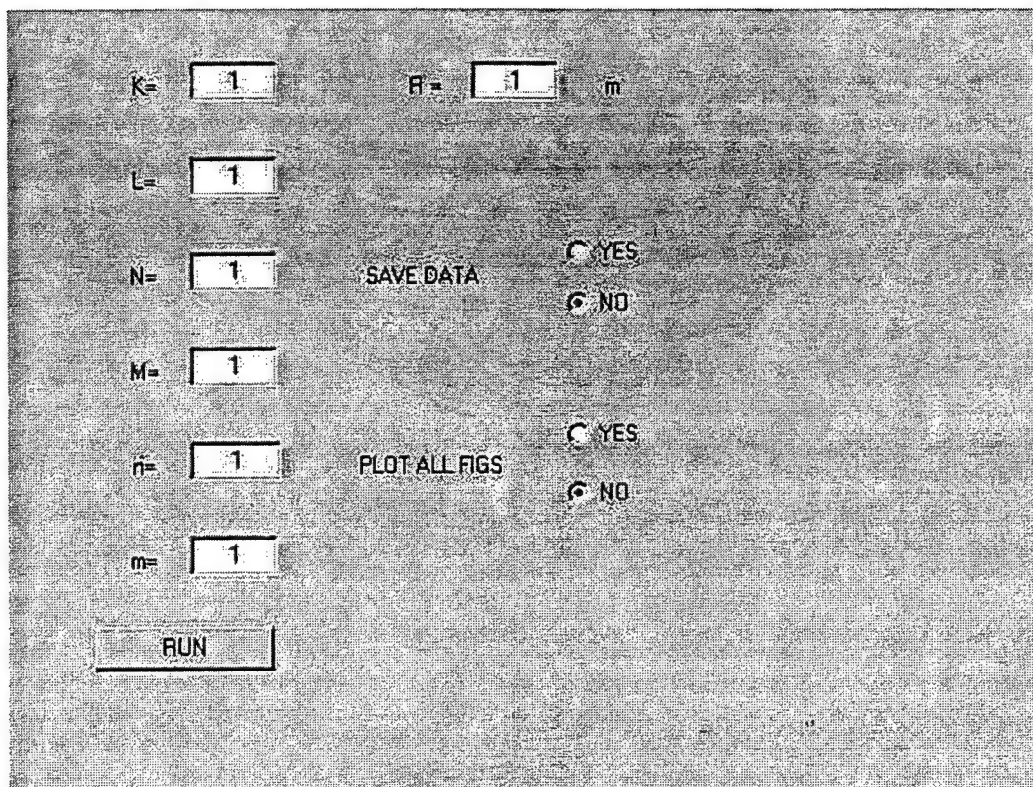


Figure 6.1: GUI for input parameters

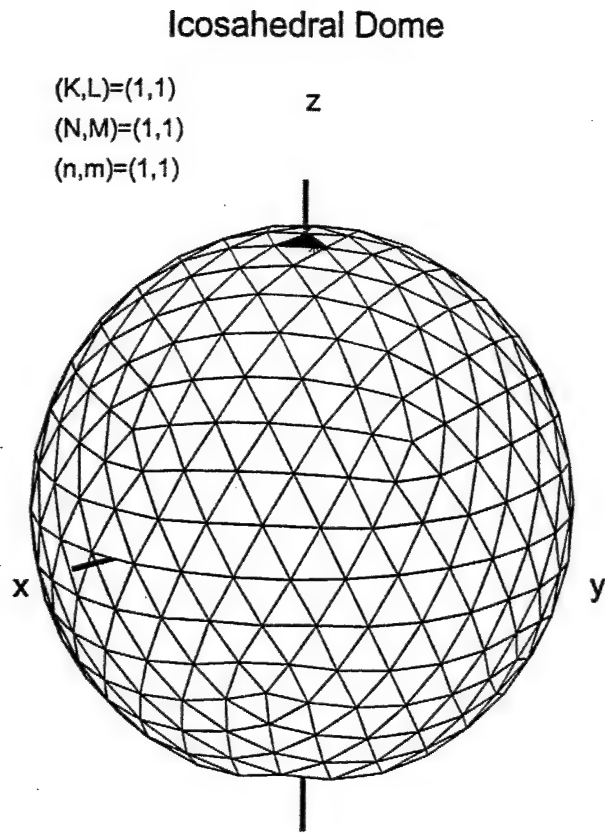


Figure 6.2: Icosahedral dome in perspective indicating selected icosahedra

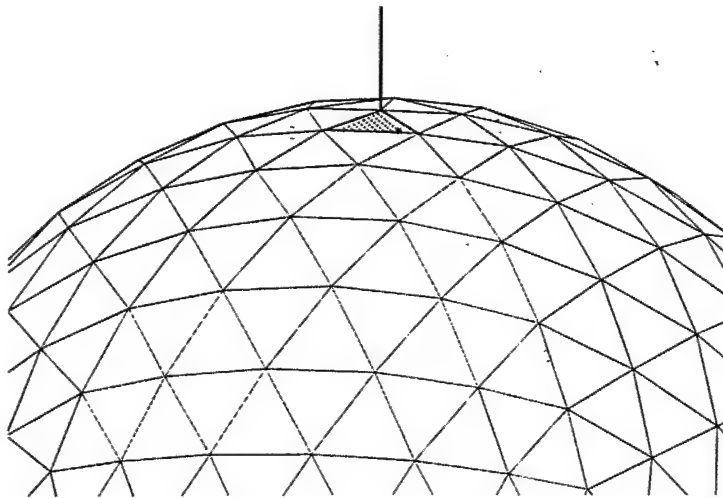


Figure 6.3: Zoom in of Figure 6.2

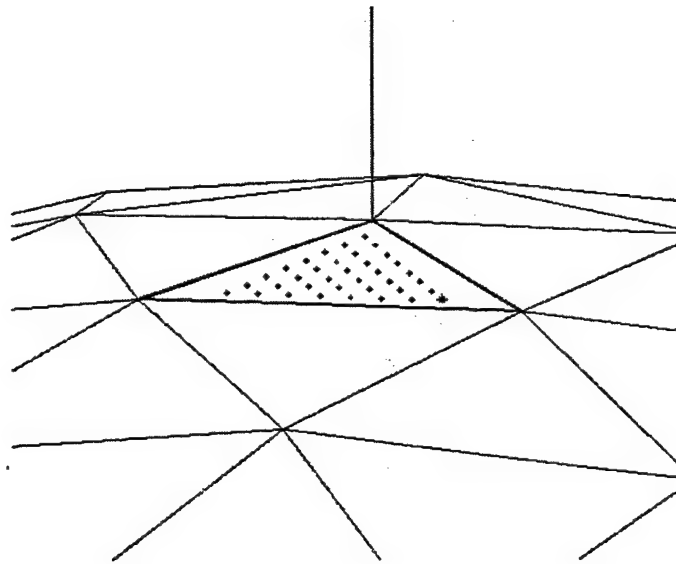


Figure 6.4: Zoom in of Figure 6.3

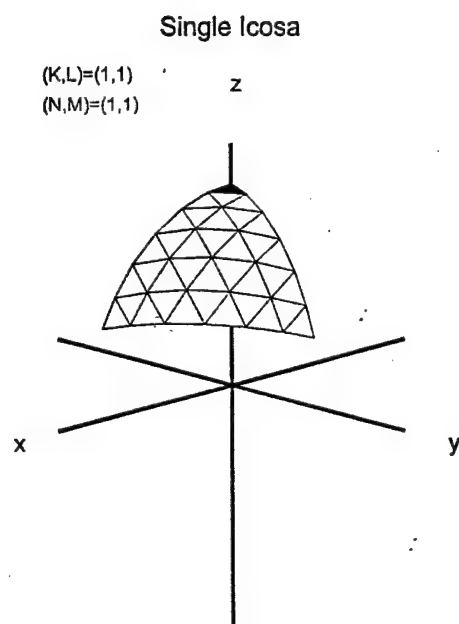


Figure 6.5: Single Icosa

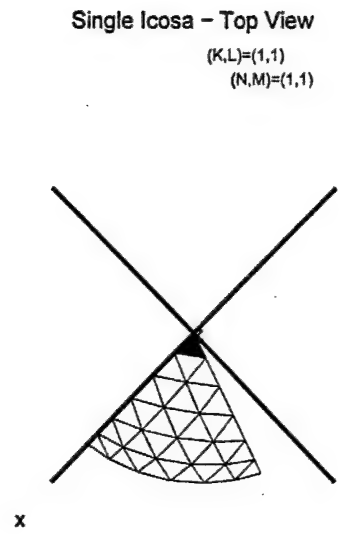


Figure 6.6: Single Icosa - Top view

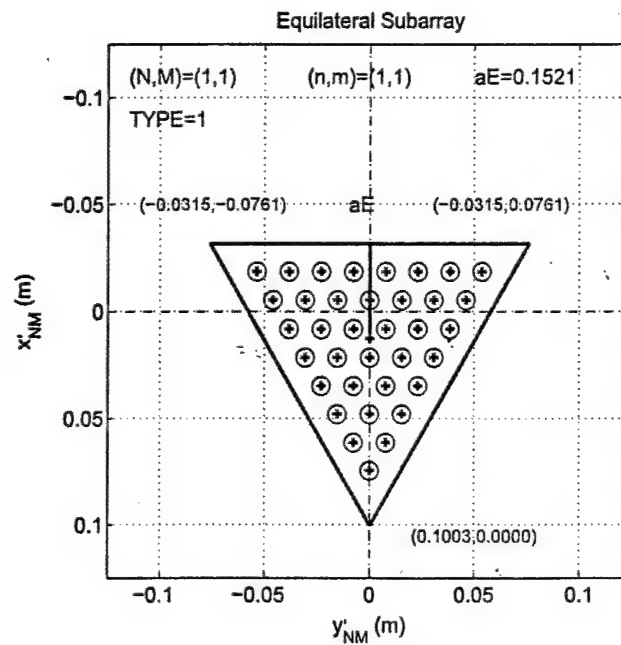


Figure 6.7: Equilateral subarray indicating $(n,m)=(1,1)$ element location

Subicosa and Equilateral Triangles in Reference (x_{NM}, y_{NM}) Coordinates

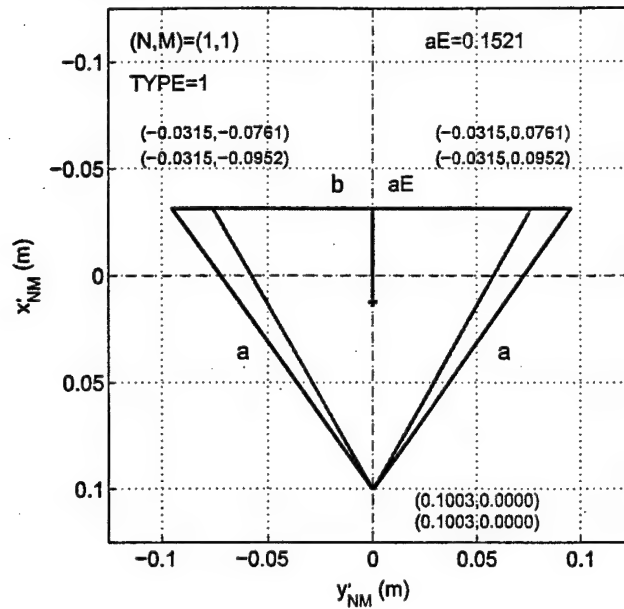


Figure 6.8: Subicosa $(K, L, N, M) = (1, 1, 1, 1)$ and respective equilateral triangle in reference coordinates

Subicosa Triangle in Local (x_{NM}, y_{NM}) Coordinates

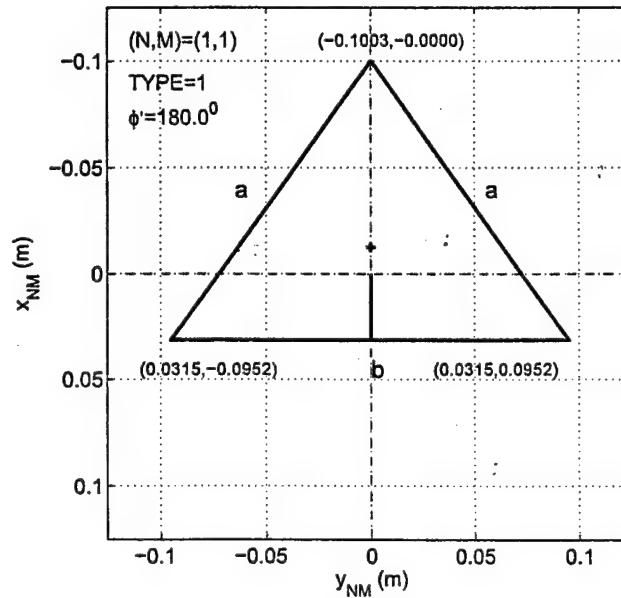


Figure 6.9: Subicosa $(K, L, N, M) = (1, 1, 1, 1)$ in local coordinates

K = <input type="text" value="1"/>	R = <input type="text" value="5"/> m	Mag Excitation	<input checked="" type="radio"/> UNITY
L = <input type="text" value="1"/>	f0 = <input type="text" value="2.000"/> GHz		<input type="radio"/> SQRT(COS TH)
N = <input type="text" value="1"/>	f = <input type="text" value="2.000"/> GHz	Active Sector	<input checked="" type="radio"/> ELEMENT
M = <input type="text" value="1"/>	Th0 = <input type="text" value="0"/> deg		<input type="radio"/> PANEL
n = <input type="text" value="1"/>	Phi0 = <input type="text" value="0"/> deg	Polarization	<input checked="" type="radio"/> CIRCULAR
m = <input type="text" value="1"/>	ActAngle = <input type="text" value="60"/> deg		<input type="radio"/> ELLIPTICAL
	PhiCut = <input type="text" value="0"/> deg	Plot Rad Pattern	<input checked="" type="radio"/> YES
			<input type="radio"/> NO
		Plot GD Array	<input type="radio"/> YES
			<input checked="" type="radio"/> NO
<input type="button" value="RUN"/>			

Figure 6.10: GUI Code 2

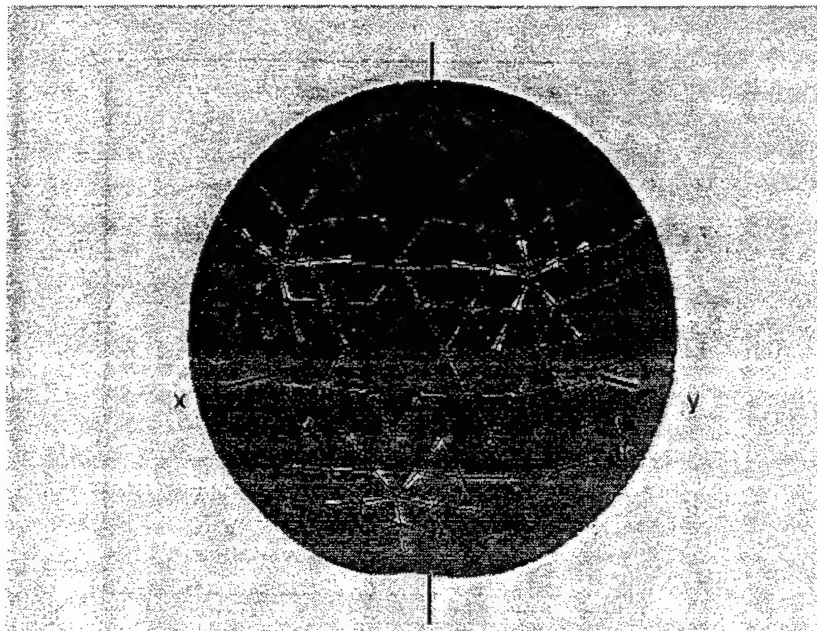


Figure 6.11: Full dome showing $\alpha_{max} = 60^\circ$ active sector in red

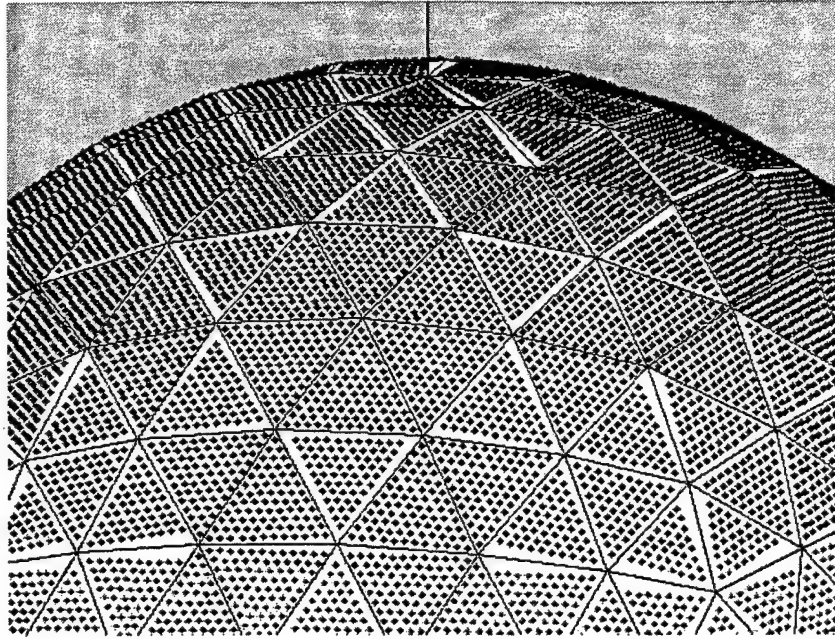


Figure 6.12: same Figure 6.11 -zoom in indicating selected panel $(K, L, N, M) = (1, 1, 1, 1)$

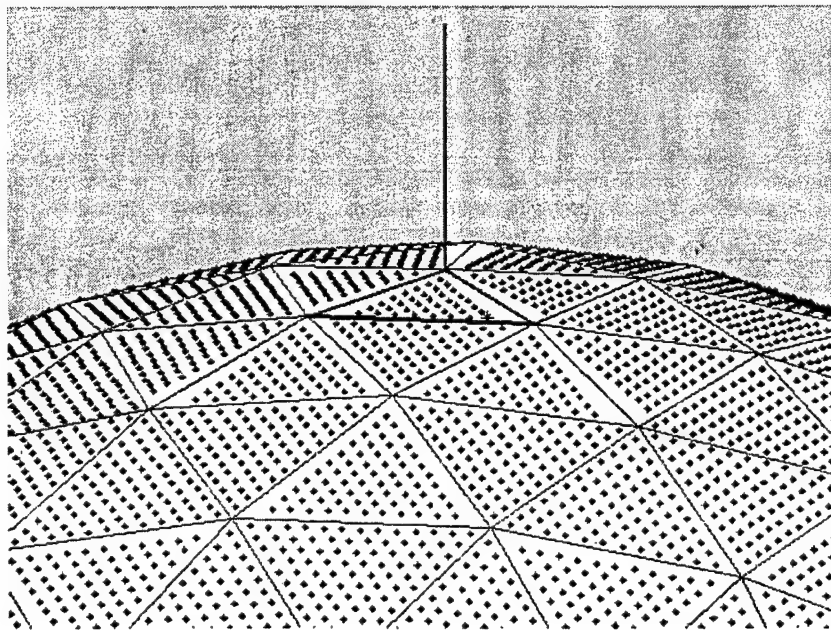


Figure 6.13: same as Figure 6.12 - zoom in indicating radiating element $(K, L, N, M, n, m) = (1, 1, 1, 1, 1, 1)$

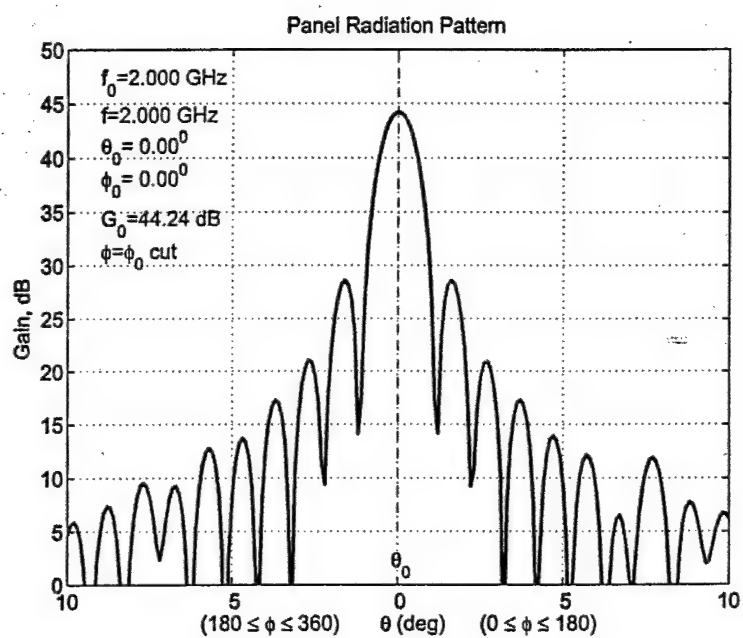


Figure 6.14: Radiation pattern pertaining to input parameters of Figure 6.10 - default input values

K =	<input type="text" value="1"/>	R =	<input type="text" value="5"/>	m	Mag Excitation	<input checked="" type="radio"/> UNITY
L =	<input type="text" value="1"/>	f0 =	<input type="text" value="2.000"/>	GHz		<input type="radio"/> SQRT(COS TH)
N =	<input type="text" value="1"/>	f =	<input type="text" value="2.000"/>	GHz	Active Sector	<input type="radio"/> ELEMENT
M =	<input type="text" value="1"/>	Th0 =	<input type="text" value="0"/>	deg		<input checked="" type="radio"/> PANEL
n =	<input type="text" value="1"/>	Phi0 =	<input type="text" value="0"/>	deg	Polarization	<input checked="" type="radio"/> CIRCULAR
m =	<input type="text" value="1"/>	ActAngle =	<input type="text" value="60"/>	deg		<input type="radio"/> ELLIPTICAL
		PhiCut =	<input type="text" value="0"/>	deg	Plot Rad Pattern	<input checked="" type="radio"/> YES
						<input type="radio"/> NO
					Plot GD Array	<input type="radio"/> YES
						<input checked="" type="radio"/> NO

Figure 6.15: GUI Code 2

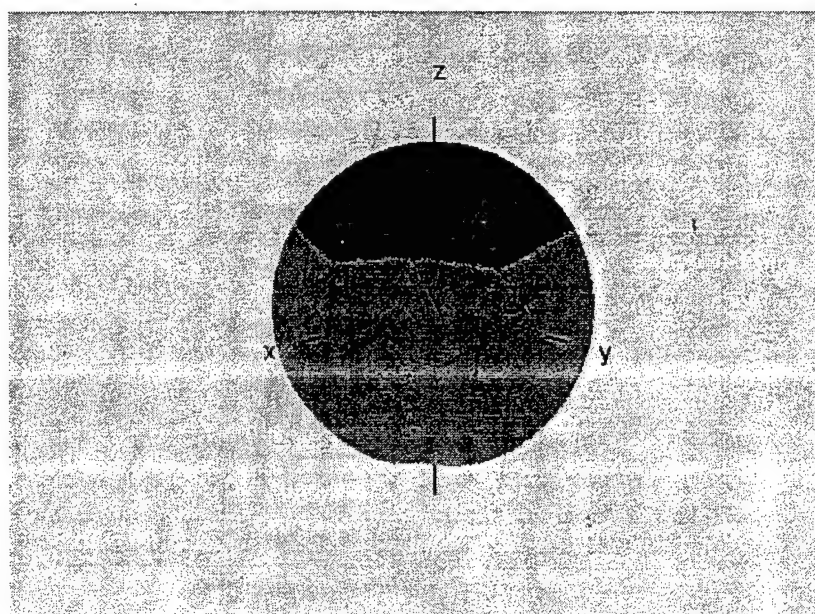


Figure 6.16: Active sector on a full dome, $\alpha_{max} = 60^\circ$, panel criteria

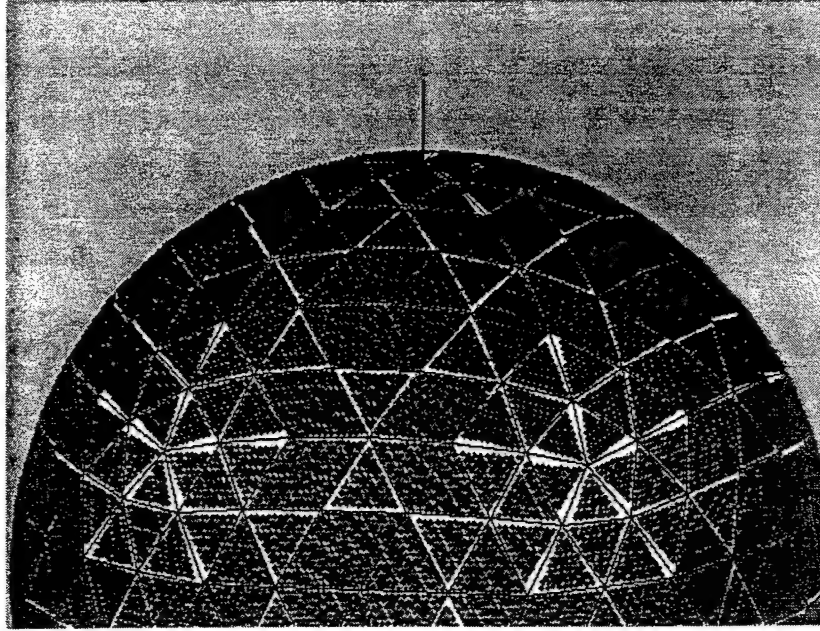


Figure 6.17: Zoom in of Figure 6.16

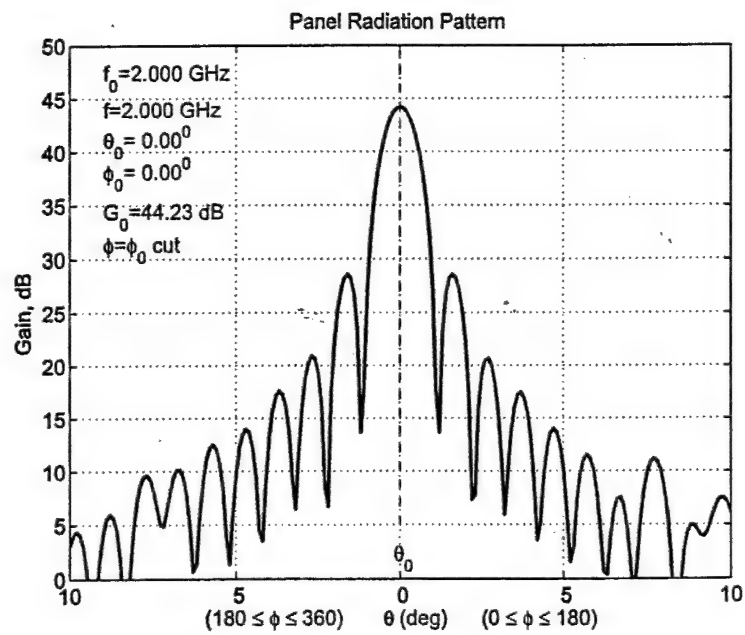


Figure 6.18: Radiation pattern pertaining to GUI of Figure 6.15

K =	<input type="text" value="2"/>	R =	<input type="text" value="5"/>	m	Mag Excitation	<input checked="" type="radio"/> UNITY
L =	<input type="text" value="2"/>	f0 =	<input type="text" value="2.000"/>	GHz		<input type="radio"/> SQRT(COS TH)
N =	<input type="text" value="5"/>	f =	<input type="text" value="2.000"/>	GHz	Active Sector	<input checked="" type="radio"/> ELEMENT
M =	<input type="text" value="3"/>	Th0 =	<input type="text" value="45"/>	deg		<input type="radio"/> PANEL
n =	<input type="text" value="2"/>	Phi0 =	<input type="text" value="0"/>	deg	Polarization	<input checked="" type="radio"/> CIRCULAR
m =	<input type="text" value="1"/>	ActAngle =	<input type="text" value="60"/>	deg		<input type="radio"/> ELLIPTICAL
		PhiCut =	<input type="text" value="0"/>	deg	Plot Rad Pattern	<input checked="" type="radio"/> YES
						<input type="radio"/> NO
					Plot GD Array	<input checked="" type="radio"/> YES
						<input type="radio"/> NO
<input type="button" value="RUN"/>						

Figure 6.19: GUI 45 degree scan - active sector "element"

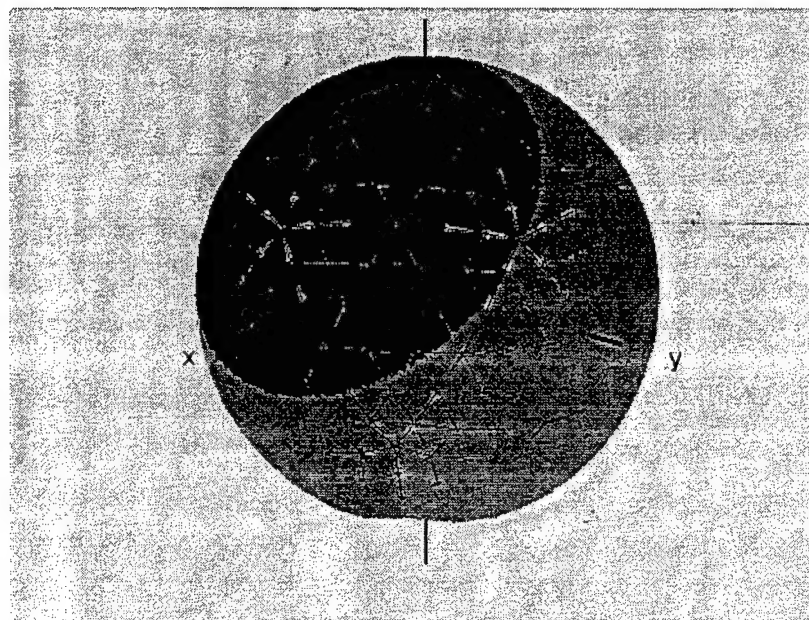


Figure 6.20: Active sector corresponding to input data of Figure 6.19

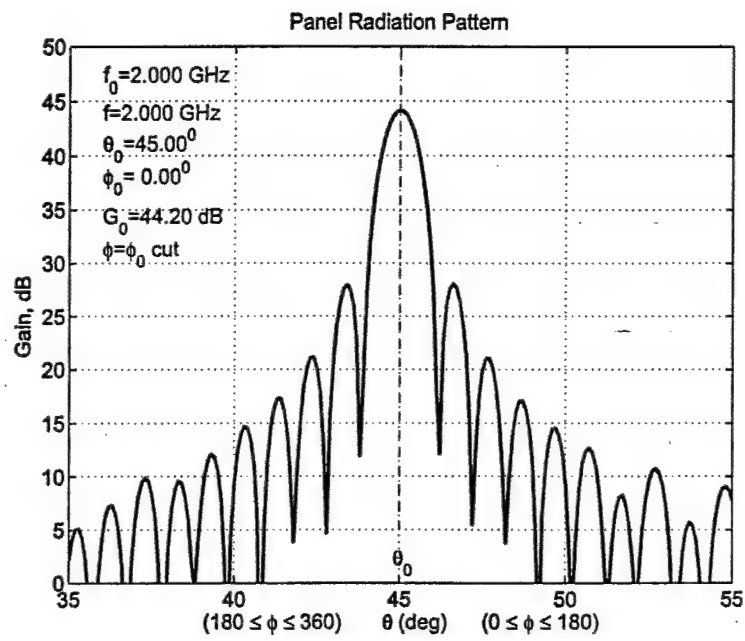


Figure 6.21: Rad pattern, 45 deg scan

K =	<input type="text" value="2"/>	R =	<input type="text" value="5"/>	m	Mag Excitation	<input checked="" type="radio"/> UNITY
L =	<input type="text" value="2"/>	f0 =	<input type="text" value="2000"/>	GHz		<input type="radio"/> SQRT(COS TH)
N =	<input type="text" value="5"/>	f =	<input type="text" value="2000"/>	GHz	Active Sector	<input type="radio"/> ELEMENT
M =	<input type="text" value="3"/>	Th0 =	<input type="text" value="45"/>	deg		<input checked="" type="radio"/> PANEL
n =	<input type="text" value="2"/>	Phi0 =	<input type="text" value="0"/>	deg	Polarization	<input type="radio"/> CIRCULAR
m =	<input type="text" value="1"/>	ActAngle =	<input type="text" value="60"/>	deg		<input type="radio"/> ELLIPTICAL
		PhiCut =	<input type="text" value="0"/>	deg	Plot Rad Pattern	<input checked="" type="radio"/> YES
						<input type="radio"/> NO
					Plot GD Array	<input checked="" type="radio"/> YES
						<input type="radio"/> NO

Figure 6.22: GUI 45 degree scan - active sector "panel"

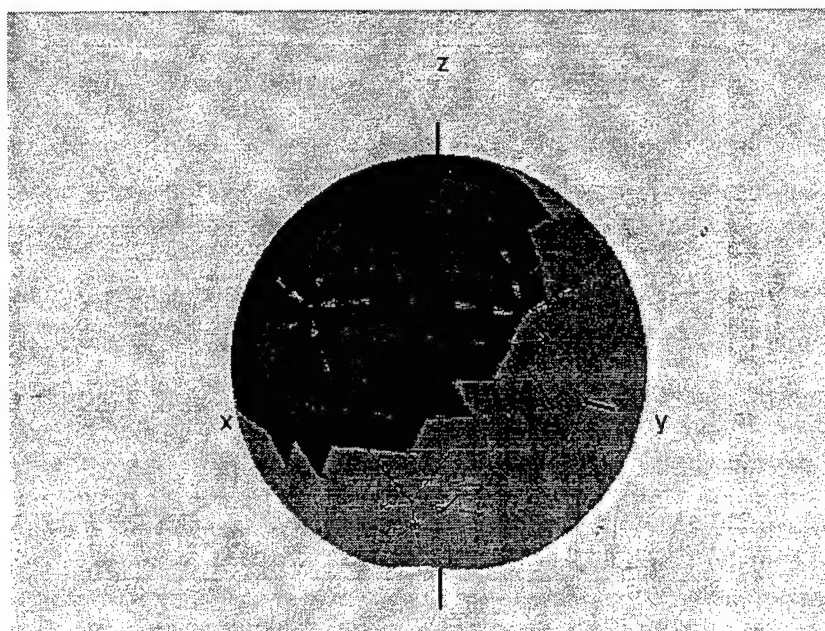


Figure 6.23: Active sector of Figure 6.22

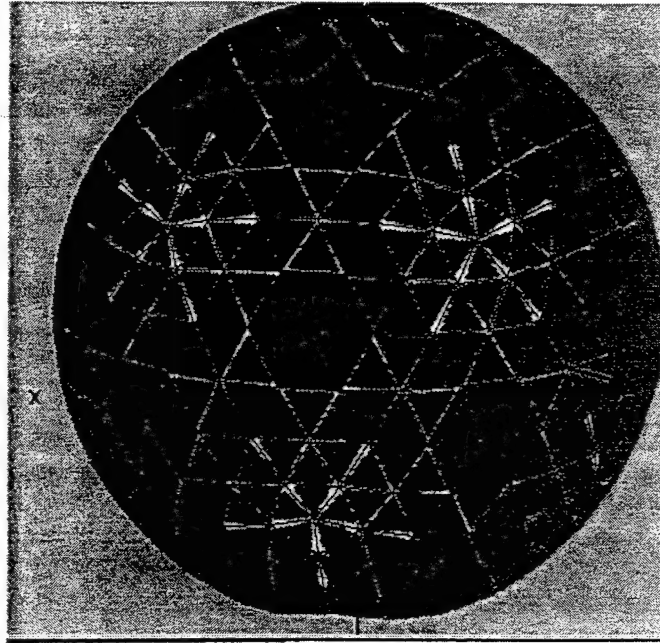


Figure 6.24: Active sector, zoom in of Figure 6.23

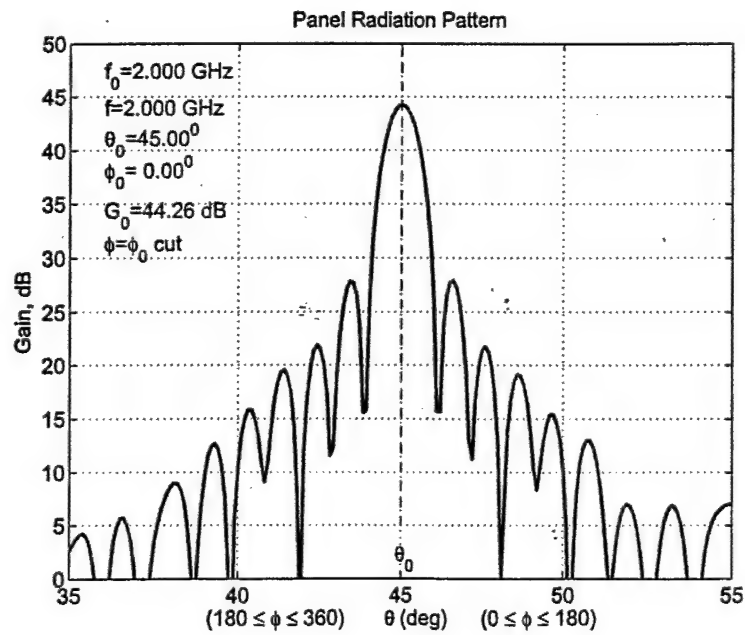


Figure 6.25: Radiation Pattern of Figure 6.22

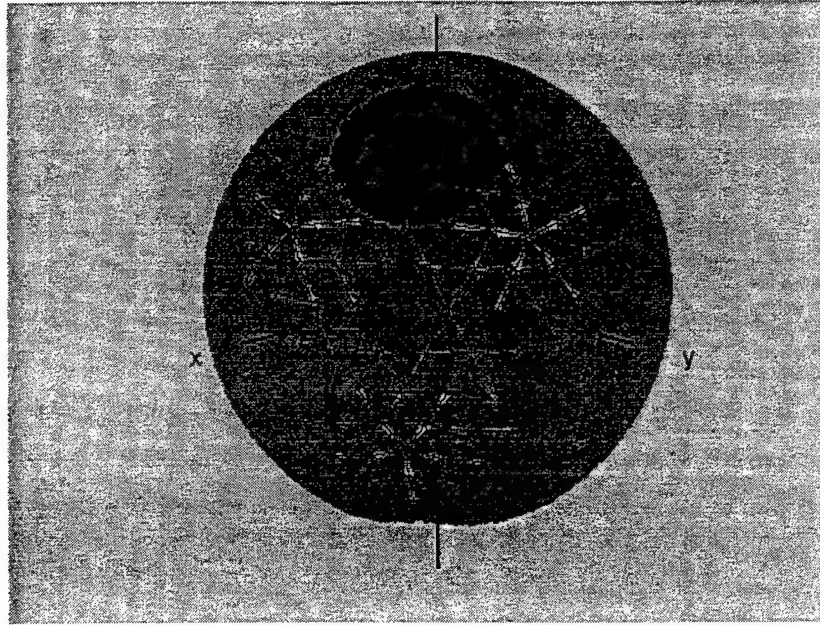


Figure 6.26: Active sector based on element criteria, $\alpha_{max} = 22^\circ, (\theta_0, \phi_0) = (37.38^\circ, 36^\circ)$

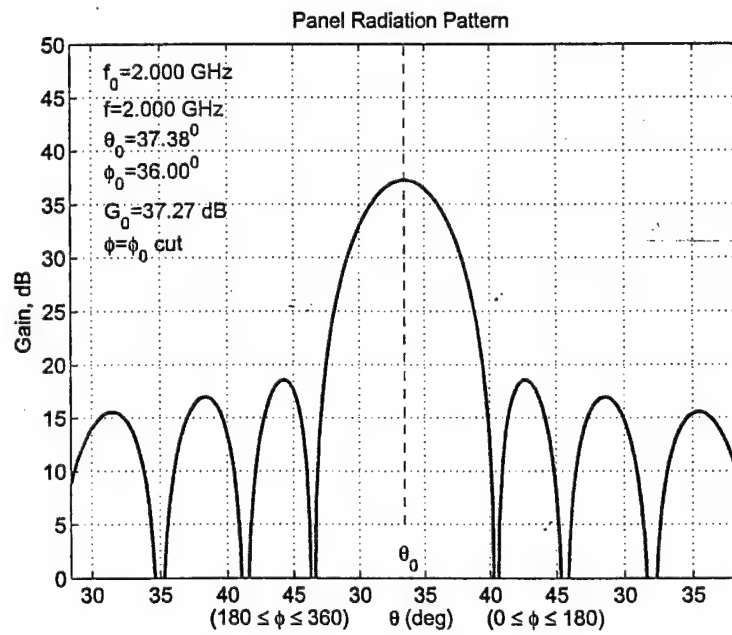


Figure 6.27: Array pattern pertaining to active sector of Figure 6.26 , $(\theta_0, \phi_0) = (37.38^\circ, 36^\circ)$

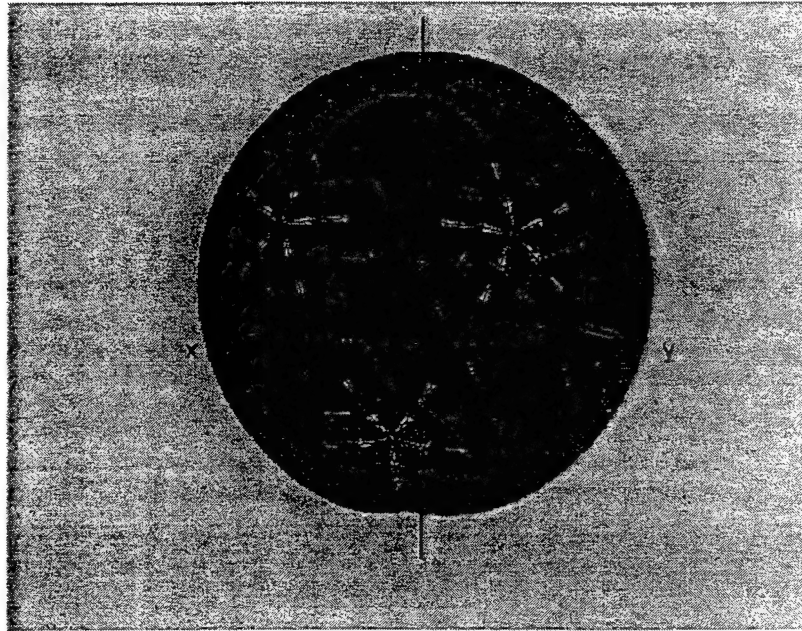


Figure 6.28: Active sector based on element criteria, $\alpha_{max} = 22^\circ, (\theta_0, \phi_0) = (42.38^\circ, 36^\circ)$

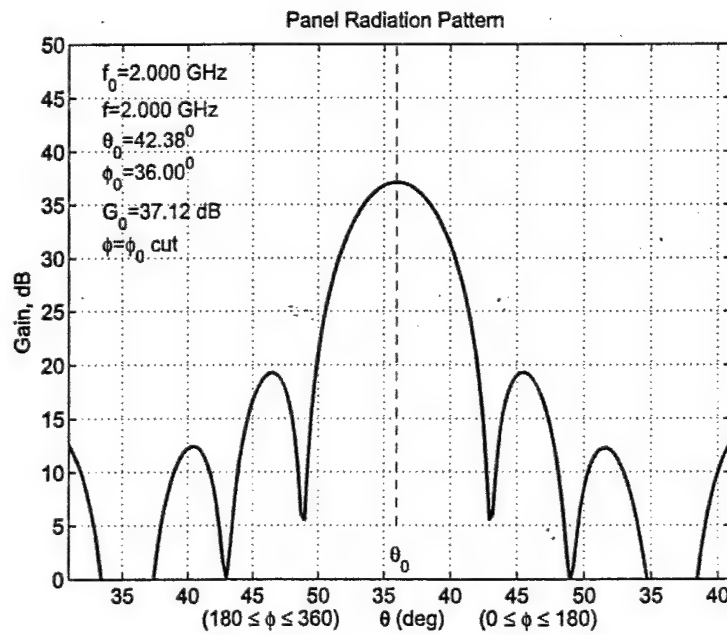


Figure 6.29: Array pattern pertaining to active sector of Figure 6.28, $(\theta_0, \phi_0) = (42.38^\circ, 36^\circ)$

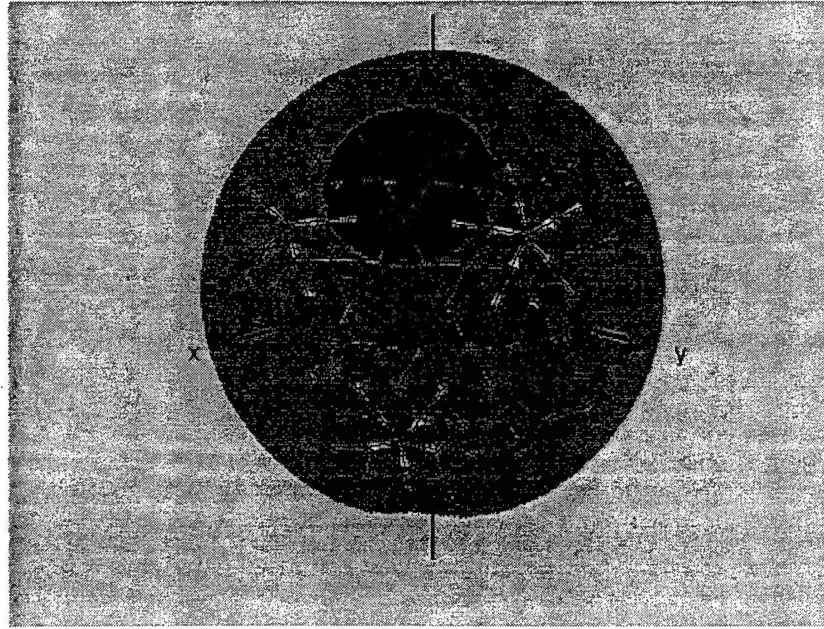


Figure 6.30: Active sector based on element criteria, $\alpha_{max} = 22^\circ, (\theta_0, \phi_0) = (47.38^\circ, 36^\circ)$

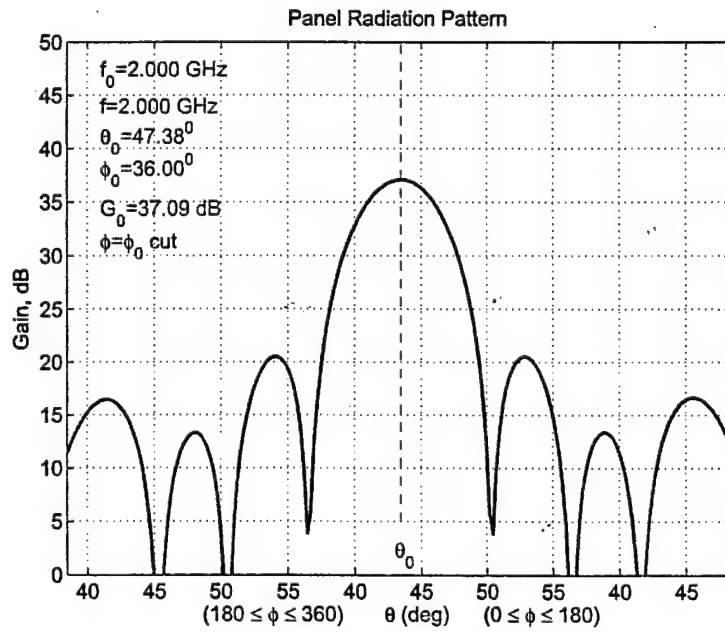


Figure 6.31: Array pattern pertaining to active sector of Figure 6.30, $(\theta_0, \phi_0) = (47.38^\circ, 36^\circ)$

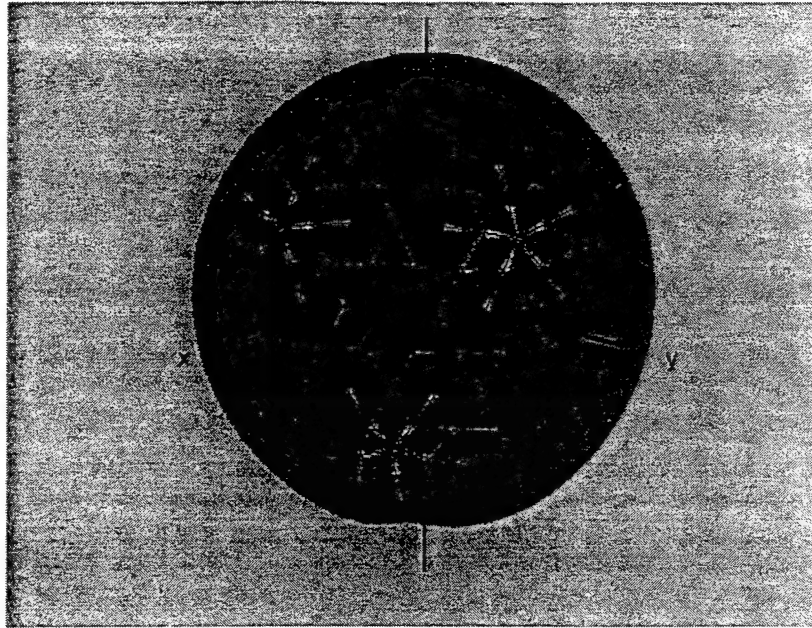


Figure 6.32: Active sector based on element criteria, $\alpha_{max} = 22^\circ, (\theta_0, \phi_0) = (52.38^\circ, 36^\circ)$

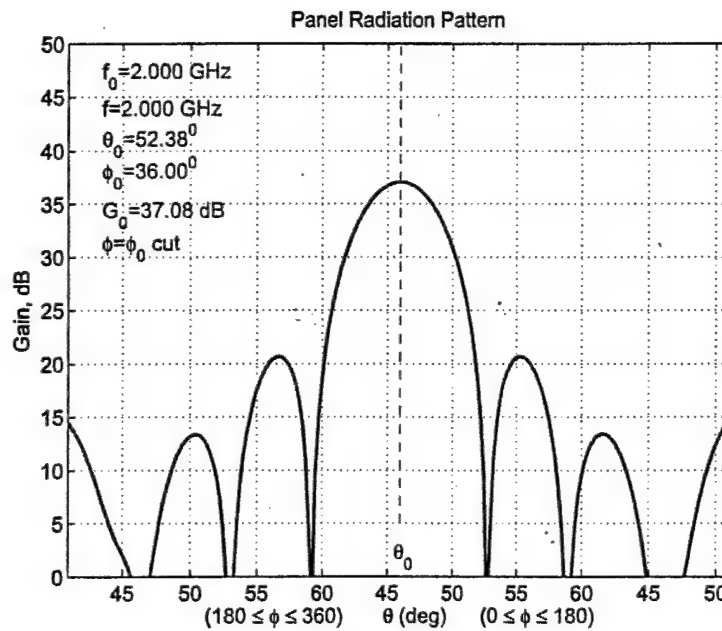


Figure 6.33: Array pattern pertaining to active sector of Figure 6.32, $(\theta_0, \phi_0) = (52.38^\circ, 36^\circ)$

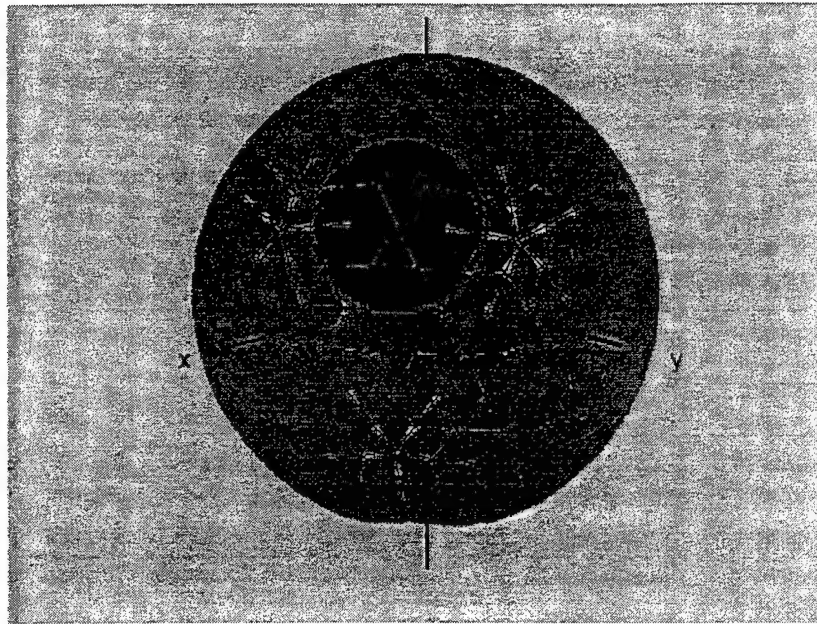


Figure 6.34: Active sector based on element criteria, $\alpha_{max} = 22^\circ, (\theta_0, \phi_0) = (57.38^\circ, 36^\circ)$

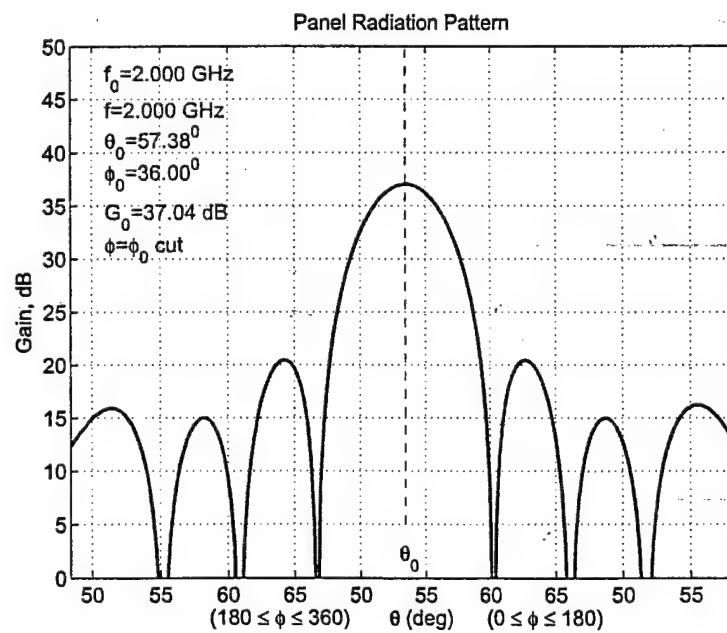


Figure 6.35: Array pattern pertaining to active sector of Figure 6.34, $(\theta_0, \phi_0) = (57.38^\circ, 36^\circ)$

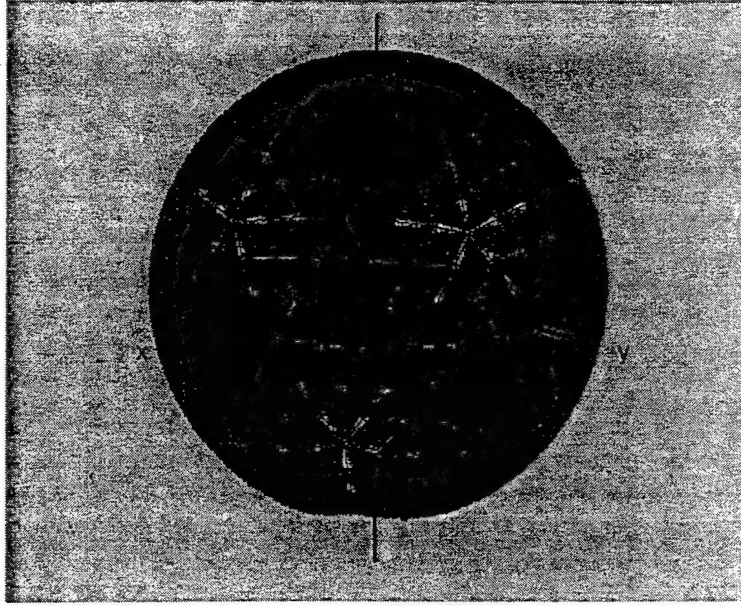


Figure 6.36: Active sector based on panel criteria, $\alpha_{max} = 22^\circ, (\theta_0, \phi_0) = (37.38^\circ, 36^\circ)$

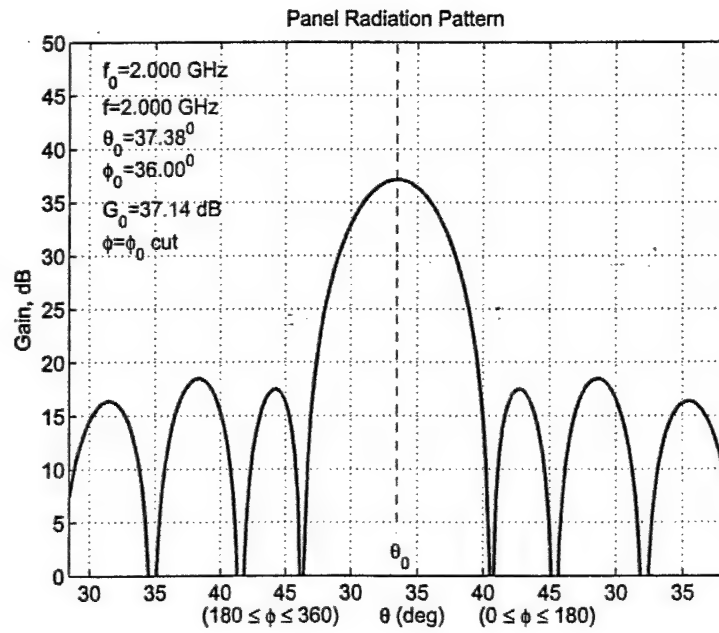


Figure 6.37: Array pattern pertaining to active sector of Figure 6.36, $(\theta_0, \phi_0) = (37.38^\circ, 36^\circ)$

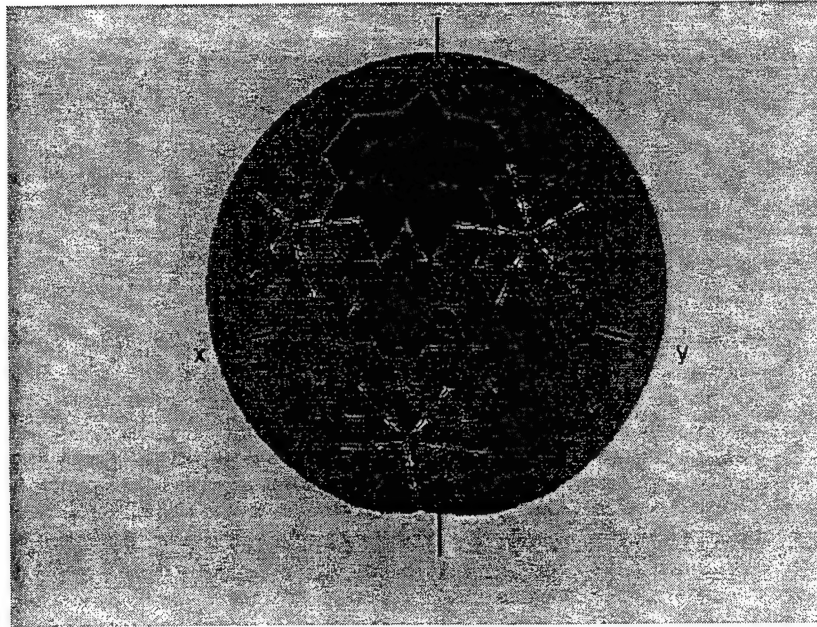


Figure 6.38: Active sector based on panel criteria, $\alpha_{max} = 22^\circ, (\theta_0, \phi_0) = (42.38^\circ, 36^\circ)$

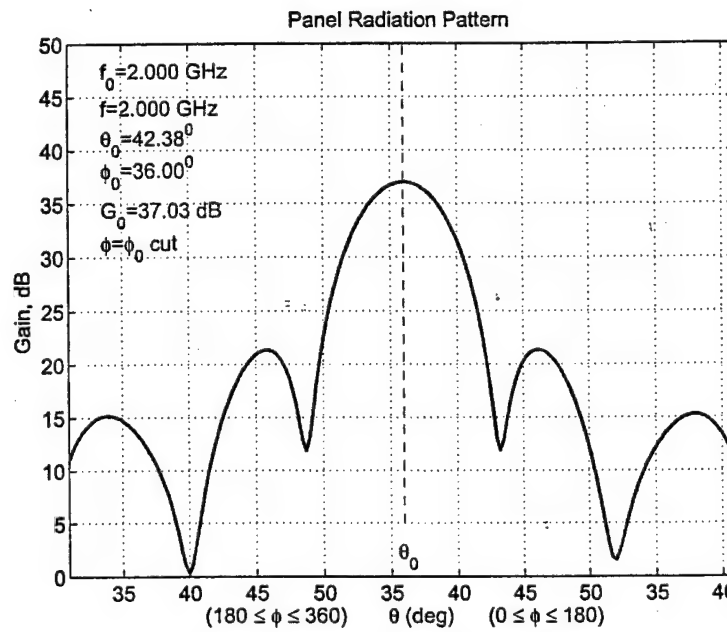


Figure 6.39: Array pattern pertaining to active sector of Figure 6.38, $(\theta_0, \phi_0) = (42.38^\circ, 36^\circ)$

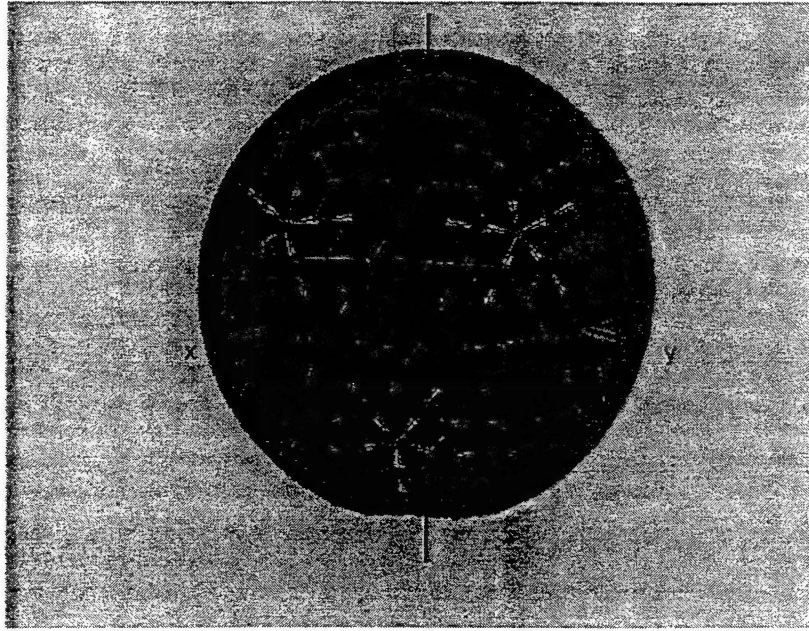


Figure 6.40: Active sector based on panel criteria, $\alpha_{max} = 22^\circ, (\theta_0, \phi_0) = (47.38^\circ, 36^\circ)$

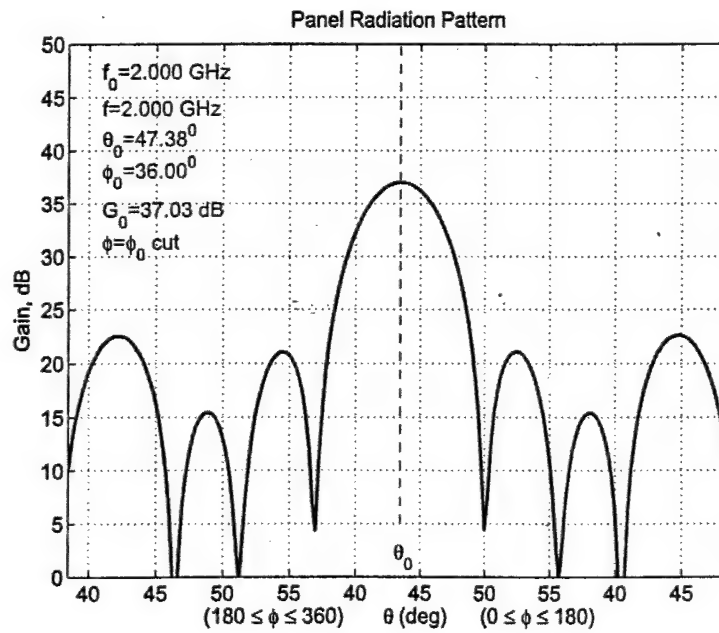


Figure 6.41: Array pattern pertaining to active sector of Figure 6.40, $(\theta_0, \phi_0) = (47.38^\circ, 36^\circ)$

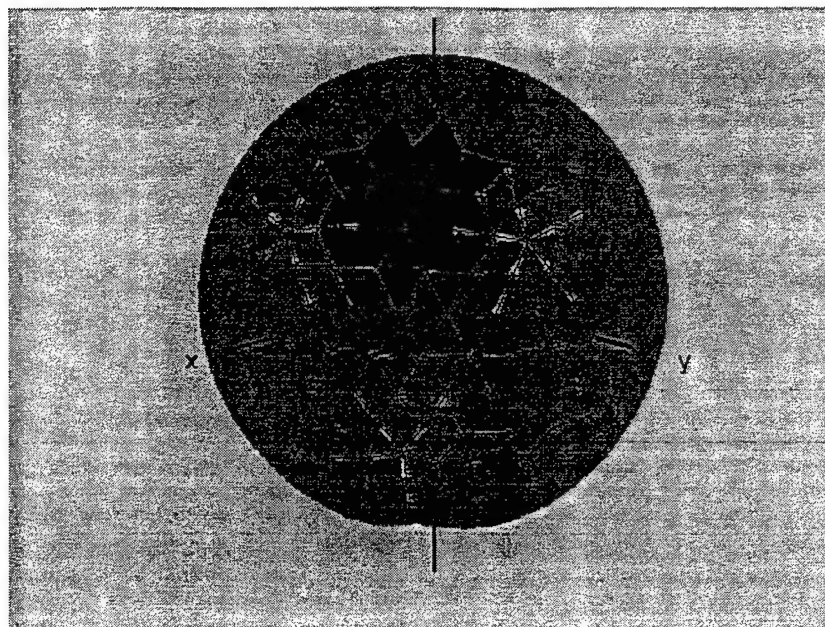


Figure 6.42: Active sector based on panel criteria, $\alpha_{max} = 22^\circ, (\theta_0, \phi_0) = (52.38^\circ, 36^\circ)$

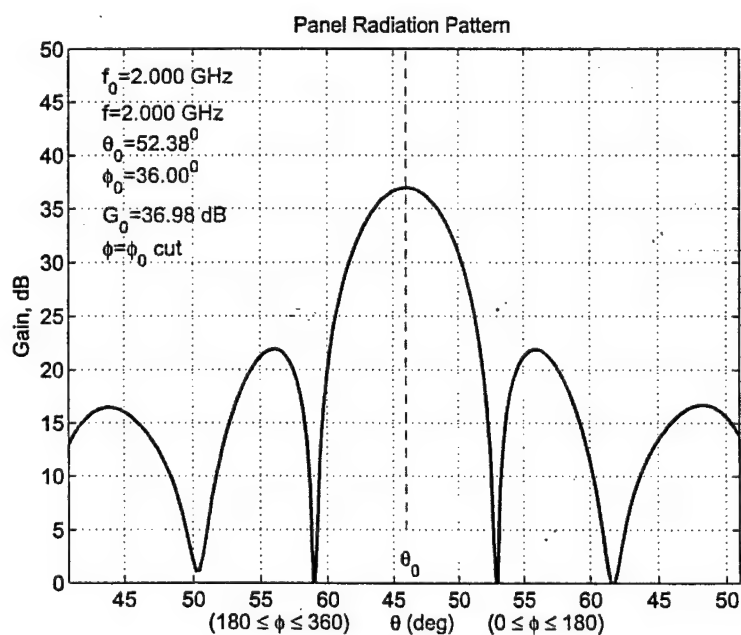


Figure 6.43: Array pattern pertaining to active sector of Figure 6.42, $(\theta_0, \phi_0) = (52.38^\circ, 36^\circ)$

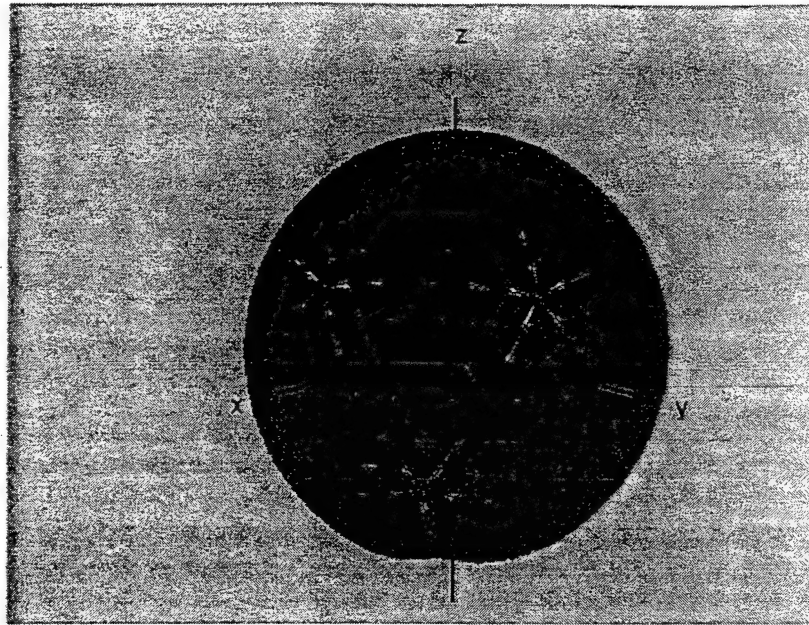


Figure 6.44: Active sector based on panel criteria, $\alpha_{max} = 22^\circ, (\theta_0, \phi_0) = (57.38^\circ, 36^\circ)$

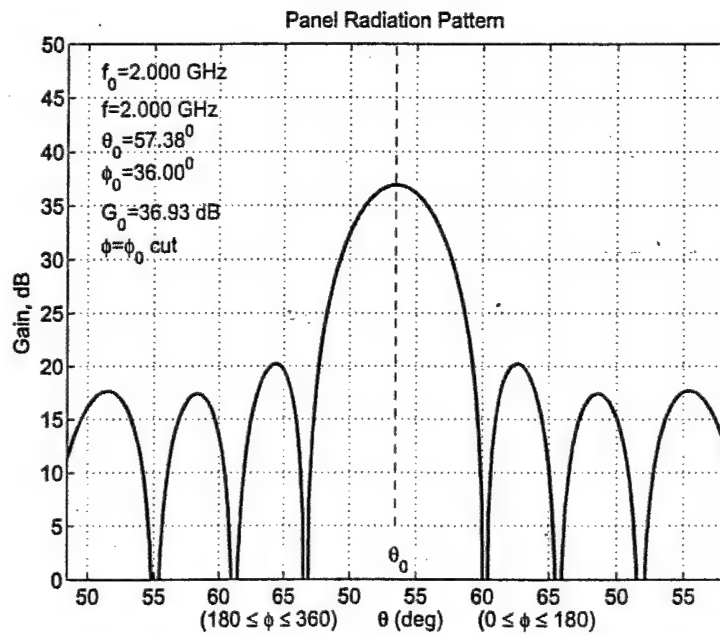


Figure 6.45: Array pattern pertaining to active sector of Figure 6.44, $(\theta_0, \phi_0) = (57.38^\circ, 36^\circ)$

Appendix A

Element Patterns in source (local) coordinates

A.1 Far-field of two crossed dipoles

We evaluate the far-field due to two crossed infinitesimal dipoles, $\lambda/4$ above an infinite conducting ground. First dipole points in the x -direction with current I_0 while second the dipole points in y -direction with current $I_0 \exp(\pm j\pi/2)$. The far field is

$$\mathbf{E}(r, \theta, \phi) = E_0 \frac{e^{-jkr}}{r} \sin\left(\frac{\pi}{2} \cos \theta\right) e^{\pm j\phi} (\hat{\theta} \cos \theta \pm j\hat{\phi}) \quad (\text{A.1})$$

where

$$E_0 = \zeta_0 \frac{k I_0}{2\pi} \quad (\text{A.2})$$

and $+/-$ denotes, in general, left/right handed elliptically polarized wave, and when $\theta = 0$, LHCP/RHCP wave.

In (A.1), it is convenient to replace $\sin(\pi/2 \cos \theta)$ with $\cos^{(1/2)} \theta$. This approximation is adequate for most practical applications and it is exact at $\theta = 0$ and $\theta = \pi/3$. Thus,

$$\mathbf{E}(r, \theta, \phi) = E_0 \frac{e^{-jkr}}{r} \sqrt{\cos \theta} e^{\pm j\phi} (\hat{\theta} \cos \theta \pm j\hat{\phi}). \quad (\text{A.3})$$

This expression can be further simplified by assuming a CP wave for all (θ, ϕ) as follows

$$\mathbf{E}(r, \theta, \phi) = E_0 \frac{e^{-jkr}}{r} \sqrt{\cos \theta} e^{\pm j\phi} (\hat{\theta} \pm j\hat{\phi}) \quad (\text{A.4})$$

or in the theoretical limit for isotropic CP source

$$\mathbf{E}(r, \theta, \phi) = E_0 \frac{e^{-jkr}}{r} e^{\pm j\phi} (\hat{\theta} \pm j\hat{\phi}). \quad (\text{A.5})$$

A.2 Approximate expressions for array element patterns

For a precise, low sidelobe design, one needs to know the radiation and impedance properties of the array element in a mutually coupled spherical array environment. This requires a rigorous analysis for the specific element and array geometry [36, 37]. For a sphere with large radius, the local spherical array geometry can be approximated by an equivalent infinite planar array. Furthermore, if high accuracy is not desired, or for a rough array performance estimation, one can use the single mode theory of the uniform infinite planar arrays, which gives reasonable but simple expressions for the element magnitude and phase patterns. For a fundamental radiator, two crossed dipoles above the ground plane, the approximate expression for the far field due to (n, m) element is

$$\mathbf{E}_{nm}(r, \theta, \phi) = a_{nm} \mathbf{e}(\theta, \phi) \frac{e^{-jk r_{nm}}}{r_{nm}} \quad (\text{A.6})$$

where a_{nm} are the complex excitation coefficients and $\mathbf{e}(\theta, \phi)$ is the element pattern which can be written in the following form:

$$\mathbf{e}(\theta, \phi) = \frac{\zeta_0}{4\pi} \sqrt{\left(\frac{4\pi A_{cell}}{\lambda^2}\right)} (1 - |\Gamma_a(\theta_0, \phi_0)|^2) \sqrt{\cos \theta} e^{\pm j\phi} \frac{1}{\sqrt{2}} (\hat{\theta} \cos \theta \pm j \hat{\phi}). \quad (\text{A.7})$$

Consequently, the respective element gain is

$$G(\theta, \phi) = G_{cell} (1 - |\Gamma_a(\theta_0, \phi_0)|^2) \cos \theta \frac{1}{2} (1 + \cos^2 \theta). \quad (\text{A.8})$$

Each term in the equations above has a distinct physical meaning:

$$G_{cell} = \frac{4\pi A_{cell}}{\lambda^2} \quad (\text{A.9})$$

is the unit cell area gain, $\cos \theta$ accounts for the reduction of the projected unit cell area for off-broadside field points, $(1 - |\Gamma(\theta_0, \phi_0)|^2)$ takes into account the reduction of element gain due to active impedance input mismatch losses at scan angles (θ_0, ϕ_0) while $(1 + \cos^2 \theta)/2$ represents polarization losses.

Appendix B

Spherical Array Analysis

B.1 Array model

A typical spherical array is shown in Figure B.1. The antenna elements are placed on the surface of radius R . The distribution of the elements may be general; however, in Figure B.1 to Figure B.3 we show the arrangement where the elements are aligned along $z=\text{constant}$ circles. The angular spacing in elevation between the circles is uniform. The azimuthal element spacing on each circle is also uniform but slightly differ from circle to circle due to different circle radii. The number of elements on each circle was determined so that the azimuth element spacing on each circle is roughly the same although periodic. Each element is designated by two indices (n, m) where n designates the circle (row) counting from the z -axis and m designates the element on a n th circle counting from x - z plane according to "right-hand screw" rule pointing into $+z$ direction. Therefore the $(n, m) = (0, 0)$ is the top element located on z -axis. Each element is assumed to produce an elliptically polarized radiation having a maximum along its own radial direction. The antenna elements are phased such that the pattern produced by the array has a maximum along the (θ_0, ϕ_0) direction, as the position of a typical element at P_{nm} on the spherical surface is represented by the coordinates $(R, \alpha_n, \beta_{nm})$ as shown in Figure B.4. The coordinates of a far-field point P are (r, θ, ϕ) and the beam pointing direction is specified by (θ_0, ϕ_0) as illustrated in Figure B.5.

B.2 Global and Local Coordinate Systems

We define a global rectangular coordinate system (x, y, z) with unit vectors $(\hat{x}, \hat{y}, \hat{z})$, and corresponding spherical coordinates (r, θ, ϕ) with respective unit vectors $(\hat{r}, \hat{\theta}, \hat{\phi})$. The far-field observation point is $P(r, \theta, \phi)$ or in vector form $P(\mathbf{r})$ where $\mathbf{r} = \hat{r}r$ as shown in Figure B.4.

At each element (n, m) we also define the local coordinate system (x_{nm}, y_{nm}, z_{nm}) (drawn in red color) with unit vectors $(\hat{x}_{nm}, \hat{y}_{nm}, \hat{z}_{nm})$ and corresponding spherical coordinates $(r_{nm}, \theta_{nm}, \phi_{nm})$ with unit vectors $(\hat{r}_{nm}, \hat{\theta}_{nm}, \hat{\phi}_{nm})$. In local coordinates the far-field observation point is $P(r_{nm}, \theta_{nm}, \phi_{nm})$, see Figure B.4.

B.3 Coordinate Transformation Relations

The field produced by a typical element at P_{nm} , is initially expressed in the local coordinate system (x_{nm}, y_{nm}, z_{nm}) , with the origin at P_{nm} and the z_{nm} axis being normal to the spherical surface as shown in Figure B.4. The transformation relations for going from the (nm)th local to global coordinates can be obtained by using the general method of orthogonal transformation of coordinates. In general, (θ_{nm}, ϕ_{nm}) can be expressed as [38] to [41]

$$\cos \theta_{nm} = \hat{\mathbf{r}} \cdot \hat{\mathbf{z}}_{nm} \quad (\text{B.1})$$

$$\cot \phi_{nm} = \frac{\hat{\mathbf{r}} \cdot \hat{\mathbf{x}}_{nm}}{\hat{\mathbf{r}} \cdot \hat{\mathbf{y}}_{nm}} \quad (\text{B.2})$$

where $(\hat{\mathbf{x}}_{nm}, \hat{\mathbf{y}}_{nm}, \hat{\mathbf{z}}_{nm})$ are unit vectors in (x_{nm}, y_{nm}, z_{nm}) directions, and

$$\hat{\mathbf{r}} = \hat{\mathbf{x}} \sin \theta \cos \phi + \hat{\mathbf{y}} \sin \theta \sin \phi + \hat{\mathbf{z}} \cos \theta. \quad (\text{B.3})$$

The respective local unit vectors $(\hat{\mathbf{x}}_{nm}, \hat{\mathbf{y}}_{nm}, \hat{\mathbf{z}}_{nm})$ are related to the unit vectors of the global coordinate system $(\hat{\mathbf{x}}, \hat{\mathbf{y}}, \hat{\mathbf{z}})$ by the following matrix equation:

$$\begin{bmatrix} \hat{\mathbf{x}}_{nm} \\ \hat{\mathbf{y}}_{nm} \\ \hat{\mathbf{z}}_{nm} \end{bmatrix} = \bar{A}_{nm} \begin{bmatrix} \hat{\mathbf{x}} \\ \hat{\mathbf{y}} \\ \hat{\mathbf{z}} \end{bmatrix} \quad (\text{B.4})$$

where \bar{A}_{nm} is a rotation matrix and is given by

$$\bar{A}_{nm} = \begin{bmatrix} \cos \alpha_n \cos \beta_{nm} & \cos \alpha_n \sin \beta_{nm} & -\sin \alpha_n \\ -\sin \beta_{nm} & \cos \beta_{nm} & 0 \\ \sin \alpha_n \cos \beta_{nm} & \sin \alpha_n \sin \beta_{nm} & \cos \alpha_n \end{bmatrix}. \quad (\text{B.5})$$

After using (B.1) to (B.5), the following two relations are obtained:

$$\cos \theta_{nm} = \sin \alpha_n \sin \theta \cos(\phi - \beta_{nm}) + \cos \alpha_n \cos \theta \quad (\text{B.6})$$

$$\cot \phi_{nm} = \frac{\cos \alpha_n \sin \theta \cos(\phi - \beta_{nm}) - \sin \alpha_n \cos \theta}{\sin \theta \sin(\phi - \beta_{nm})}. \quad (\text{B.7})$$

Similarly, the local unit vectors $(\hat{\theta}_{nm}, \hat{\phi}_{nm})$ can be transformed into global coordinates via:

$$\begin{bmatrix} \hat{\theta}_{nm} \\ \hat{\phi}_{nm} \end{bmatrix} = \begin{bmatrix} -a_{nm} & b_{nm} \\ -b_{nm} & -a_{nm} \end{bmatrix} \begin{bmatrix} \hat{\theta} \\ \hat{\phi} \end{bmatrix} \quad (\text{B.8})$$

where

$$a_{nm} = \frac{\cos \theta \sin \alpha_n \cos(\phi - \beta_{nm}) - \sin \theta \cos \alpha_n}{\sin \theta_{nm}} \quad (\text{B.9})$$

$$b_{nm} = \frac{\sin \alpha_n \sin(\phi - \beta_{nm})}{\sin \theta_{nm}} \quad (\text{B.10})$$

and

$$\sin \theta_{nm} = \sqrt{1 - \cos^2 \theta_{nm}}. \quad (\text{B.11})$$

Taking inverse of (B.8) where determinant $\Delta = a_{nm}^2 + b_{nm}^2 = 1$, we obtain

$$\begin{bmatrix} \hat{\theta} \\ \hat{\phi} \end{bmatrix} = \begin{bmatrix} -a_{nm} & -b_{nm} \\ b_{nm} & -a_{nm} \end{bmatrix} \begin{bmatrix} \hat{\theta}_{nm} \\ \hat{\phi}_{nm} \end{bmatrix}. \quad (\text{B.12})$$

B.4 Element patterns in local coordinates

The far electric field produced by a single element at the field point $P(r, \theta, \phi)$ can be written as follows

$$\mathbf{E}_{nm}(r_{nm}, \theta_{nm}, \phi_{nm}; t) = \mathbf{e}_{nm}(\theta_{nm}, \phi_{nm}) \frac{e^{j(\omega t - kr_{nm})}}{r_{nm}} \quad (\text{B.13})$$

with

$$\mathbf{e}_{nm}(\theta_{nm}, \phi_{nm}) = \hat{\boldsymbol{\theta}}_{nm} e_{\theta nm}(\theta_{nm}, \phi_{nm}) + \hat{\boldsymbol{\phi}}_{nm} e_{\phi nm}(\theta_{nm}, \phi_{nm}) \quad (\text{B.14})$$

where $e_{\theta nm}$ and $e_{\phi nm}$ are the complex element pattern factors of the two field components. Basically they represent the field produced by a single element in a match-terminated spherical array environment. In general $e_{\theta nm}$ and $e_{\phi nm}$ are of the form

$$e_{\theta nm}(\theta_{nm}, \phi_{nm}) = |e_{\theta nm}(\theta_{nm}, \phi_{nm})| e^{j\vartheta_{nm}(\theta_{nm}, \phi_{nm})} \quad (\text{B.15})$$

$$e_{\phi nm}(\theta_{nm}, \phi_{nm}) = |e_{\phi nm}(\theta_{nm}, \phi_{nm})| e^{j\varphi_{nm}(\theta_{nm}, \phi_{nm})} e^{j\delta} \quad (\text{B.16})$$

Here, δ is the phase difference between the two components of the field. In general the field is elliptically polarized. For a circularly polarized field $e_{\theta nm} = e_{\phi nm}$ and $\delta = \pm\pi/2$ where a plus sign corresponds to RHCP and a minus sign to LHCP outgoing wave.

B.5 Element patterns in global coordinates

The field in (B.13) can be expressed in global coordinates using the coordinate transformation relation (B.8) as follows:

$$\mathbf{E}_{nm}(r, \theta, \phi; t) = \mathbf{e}_{nm}(\theta, \phi) \frac{e^{j(\omega t - kr)}}{r} \quad (\text{B.17})$$

where

$$\mathbf{e}_{nm}(\theta, \phi) = [\hat{\boldsymbol{\theta}} e_{\theta nm}(\theta, \phi) + \hat{\boldsymbol{\phi}} e_{\phi nm}(\theta, \phi)] e^{j\psi_{nm}} \quad (\text{B.18})$$

and (from (B.12))

$$e_{\theta nm}(\theta, \phi) = -a_{nm} e_{\theta nm}(\theta_{nm}, \phi_{nm}) + b_{nm} e_{\phi nm}(\theta_{nm}, \phi_{nm}) \quad (\text{B.19})$$

$$e_{\phi nm}(\theta, \phi) = -b_{nm} e_{\theta nm}(\theta_{nm}, \phi_{nm}) - a_{nm} e_{\phi nm}(\theta_{nm}, \phi_{nm}) \quad (\text{B.20})$$

with

$$\psi_{nm} = k \boldsymbol{\rho}_{nm} \cdot \hat{\mathbf{r}} = kR [\sin \alpha_n \sin \theta \cos(\phi - \beta_{nm}) + \cos \alpha_n \cos \theta]. \quad (\text{B.21})$$

To facilitate the computation of the element excitation coefficients, we rewrite (B.19) and (B.20) in the form

$$e_{\theta nm}(\theta, \phi) = |e_{\theta nm}(\theta, \phi)| e^{j\vartheta_{nm}(\theta, \phi)} \quad (\text{B.22})$$

$$e_{\phi nm}(\theta, \phi) = |e_{\phi nm}(\theta, \phi)| e^{j\varphi_{nm}(\theta, \phi)} e^{j\delta} \quad (\text{B.23})$$

and then

$$\mathbf{e}_{nm}(\theta, \phi) = [\hat{\boldsymbol{\theta}} |e_{\theta nm}(\theta, \phi)| e^{j\vartheta_{nm}(\theta, \phi)} + \hat{\boldsymbol{\phi}} |e_{\phi nm}(\theta, \phi)| e^{j\varphi_{nm}(\theta, \phi)} e^{j\delta}] e^{j\psi_{nm}}. \quad (\text{B.24})$$

To form a beam in the (θ_0, ϕ_0) direction, all element contributions must coherently add up in the far zone. This means that the phase of the element excitation coefficients must be the negative of the phase of the e_{nm} . For CP, we must have $|e_{\theta nm}(\theta_0, \phi_0)| = |e_{\phi nm}(\theta_0, \phi_0)|$, $\vartheta_{nm}(\theta_0, \phi_0) = \varphi_{nm}(\theta_0, \phi_0)$ and $\delta = \pm\pi/2$. This would require separate magnitude and phase/time controls for each field component which is not practical. A single magnitude and phase/time control per element is instead used resulting in some acceptable polarization loss.

In the above expressions $e_{\theta nm}$ and $e_{\phi nm}$ must be known whether by EM simulation, by measurements or by some kind of realistic approximation.

B.6 An Example

Two examples will be presented. In the first example we consider a CP isotropic (nm) th array element on the sphere with element pattern given in local coordinates as

$$e_{nm}(\theta_{nm}, \phi_{nm}) = E_0(\hat{\theta}_{nm} \pm j\hat{\phi}_{nm}) e^{\pm j\phi_{nm}}. \quad (B.25)$$

In this case we can write

$$e_{\theta nm}(\theta_{nm}, \phi_{nm}) = 1 \quad (B.26)$$

$$e_{\phi nm}(\theta_{nm}, \phi_{nm}) = \pm j \quad (B.27)$$

Applying coordinate transformation (B.19) and (B.20) yields

$$e_{\theta nm}(\theta, \phi) = -(a_{nm} \pm j b_{nm}) \quad (B.28)$$

$$e_{\phi nm}(\theta, \phi) = -(a_{nm} \pm j b_{nm})(\pm j). \quad (B.29)$$

Next, we rewrite (B.28) and (B.29) in the form

$$e_{\theta nm}(\theta, \phi) = -|e_{\theta nm}(\theta, \phi)| e^{\pm j\vartheta_{nm}(\theta, \phi)} \quad (B.30)$$

$$e_{\phi nm}(\theta, \phi) = -(\pm j)|e_{\phi nm}(\theta, \phi)| e^{\pm j\varphi_{nm}(\theta, \phi)}. \quad (B.31)$$

Noting that

$$|a_{nm} \pm j b_{nm}| = 1 \quad (B.32)$$

and

$$\tan \nu_{nm}(\theta, \phi) = \tan \vartheta_{nm}(\theta, \phi) = \tan \varphi_{nm}(\theta, \phi) = \frac{b_{nm}}{a_{nm}} \quad (B.33)$$

which after substituting (B.9) and (B.10) into (B.33) becomes

$$\tan \nu_{nm}(\theta, \phi) = \frac{\sin \alpha_n \sin(\phi - \beta_{nm})}{\cos \theta \sin \alpha_n \cos(\phi - \beta_{nm}) - \sin \theta \cos \alpha_n}. \quad (B.34)$$

(B.30) and (B.31) can be written in the form

$$e_{\theta nm}(\theta, \phi) = -e^{\pm j\nu_{nm}(\theta, \phi)} \quad (B.35)$$

and

$$e_{\phi nm}(\theta, \phi) = -(\pm j) e^{\pm j\nu_{nm}(\theta, \phi)}. \quad (\text{B.36})$$

The element pattern (B.25) can be now rewritten in global coordinates as

$$\mathbf{e}_{nm}(\theta, \phi) = -E_0(\hat{\theta} \pm j\hat{\phi}) e^{\pm j\nu_{nm}(\theta, \phi)} e^{j\psi_{nm}} e^{\pm j\phi_{nm}}. \quad (\text{B.37})$$

As a second example we consider a typical and simple approximation for e_θ and e_ϕ as given by (A.3). Although the phase $\delta = \pm\pi/2$ the wave is CP only on the element radial axis, i.e., when $\theta_{nm} = 0$. Thus we write

$$\mathbf{e}_{nm}(\theta_{nm}, \phi_{nm}) = E_0 (\hat{\theta}_{nm} \cos \theta_{nm} \pm j\hat{\phi}_{nm}) e^{\pm j\phi_{nm}} \quad (\text{B.38})$$

$$e_{\theta nm}(\theta_{nm}, \phi_{nm}) = \cos \theta_{nm} \quad (\text{B.39})$$

$$e_{\phi nm}(\theta_{nm}, \phi_{nm}) = \pm j \quad (\text{B.40})$$

where $e_{\theta nm} = e_{\phi nm} = 0$ for $\theta_{nm} > \pi/2$.

Following the same procedure of first example, we get

$$e_{\theta nm}(\theta, \phi) = - |e_{\theta nm}(\theta, \phi)| e^{\pm j\vartheta_{nm}(\theta, \phi)} \quad (\text{B.41})$$

$$e_{\phi nm}(\theta, \phi) = -(\pm j) |e_{\phi nm}(\theta, \phi)| e^{\pm j\varphi_{nm}(\theta, \phi)} \quad (\text{B.42})$$

where

$$|e_{\theta nm}(\theta, \phi)| = |a_{nm} \cos \theta_{nm} \pm j b_{nm}| \quad (\text{B.43})$$

$$|e_{\phi nm}(\theta, \phi)| = |a_{nm} \pm j b_{nm} \cos \theta_{nm}| \quad (\text{B.44})$$

and

$$\tan \vartheta_{nm} = \frac{b_{nm}}{a_{nm} \cos \theta_{nm}} \quad (\text{B.45})$$

$$\tan \varphi_{nm} = \frac{b_{nm} \cos \theta_{nm}}{a_{nm}}. \quad (\text{B.46})$$

Then, (B.38) can be rewritten in global coordinates as

$$\mathbf{e}_{nm}(\theta, \phi) = -E_0 [\hat{\theta} |e_{\theta nm}(\theta, \phi)| e^{\pm j\vartheta_{nm}(\theta, \phi)} \pm j\hat{\phi} |e_{\phi nm}(\theta, \phi)| e^{\pm j\varphi_{nm}(\theta, \phi)}] e^{j\psi_{nm}} e^{\pm j\phi_{nm}} \quad (\text{B.47})$$

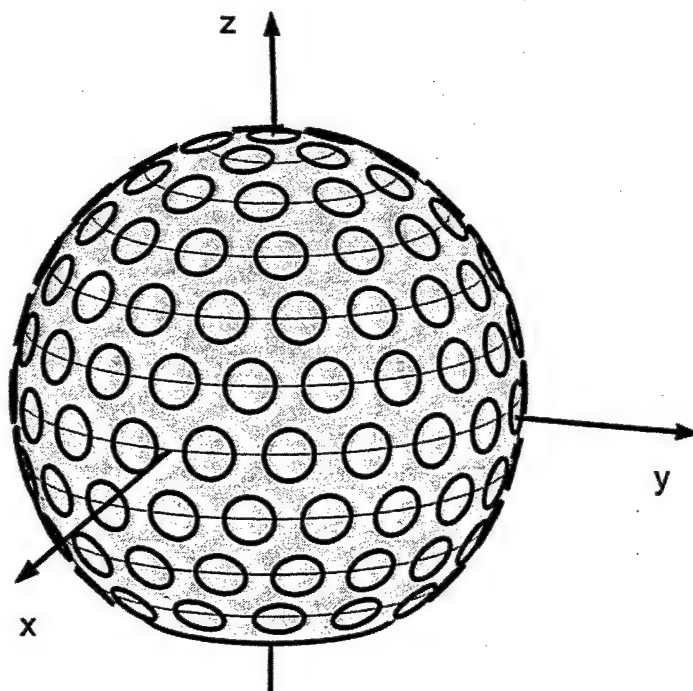


Figure B.1: Spherical array

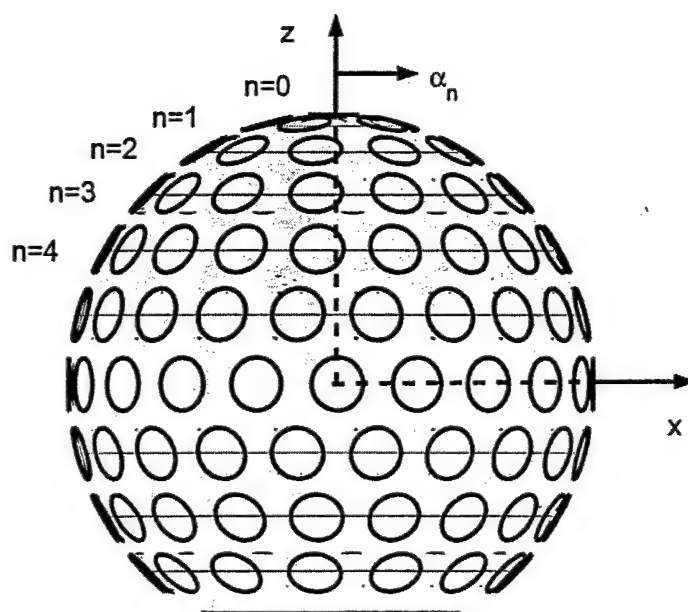


Figure B.2: Spherical array, side view

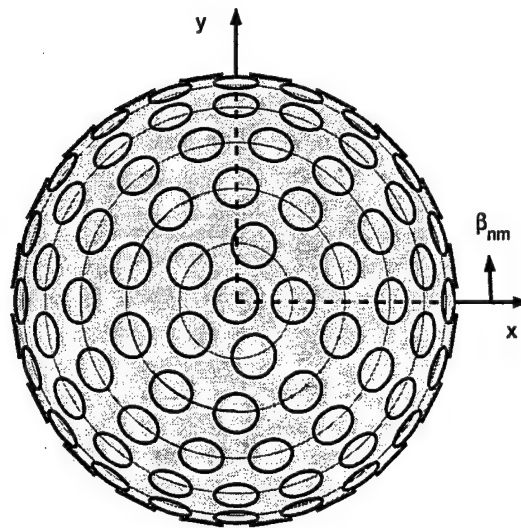


Figure B.3: Spherical array, top view

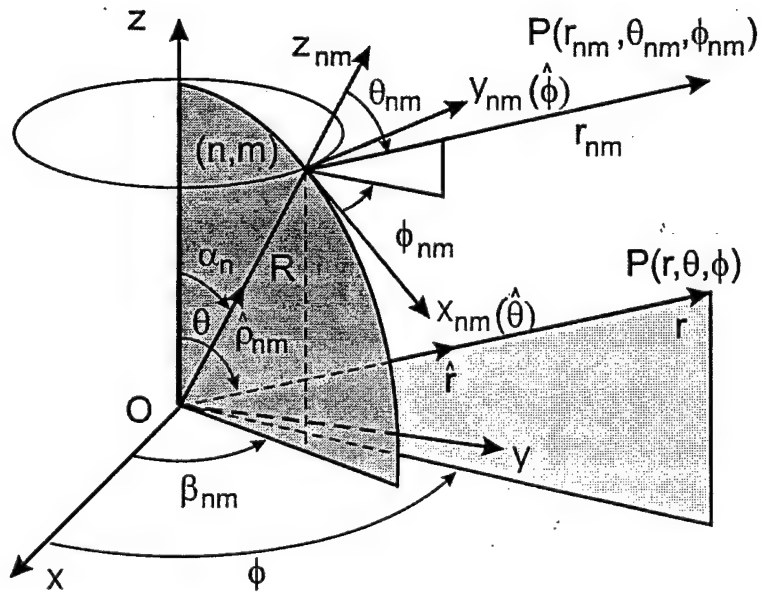


Figure B.4: Global and local coordinate systems

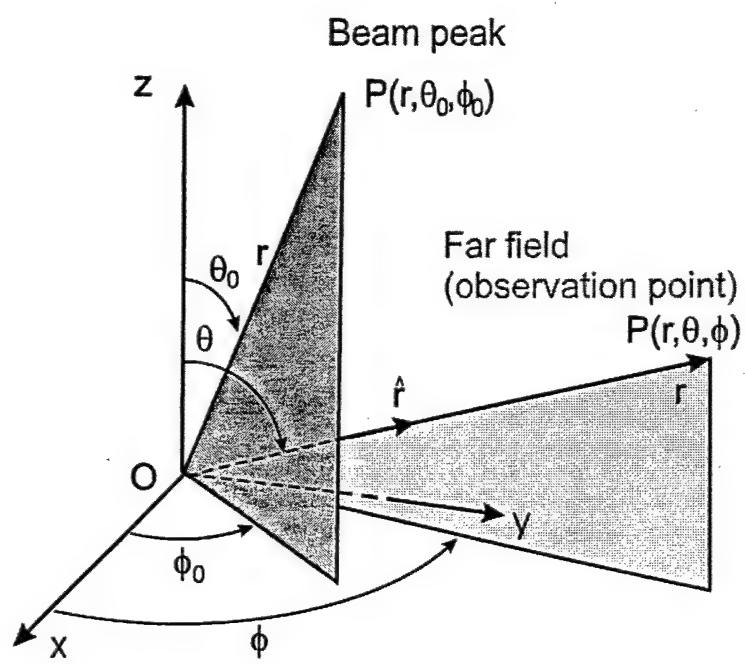


Figure B.5: Polar coordinates pertaining to far field point and beam peak

Appendix C

Maximum Gain Theorem for Conformal Arrays

The optimization problem for antenna arrays has been treated by many authors in the past. The first solution was given by [15] where it is shown that in the absence of mutual coupling, the maximum directivity is equal to the sum of the directivities of the individual radiators. For example, for arrays of N isotropic sources with element spacing $d = \lambda/2$ the maximum directivity $D_{max} = N$. If there is a mutual power exchange between the array elements, as shown in [15] the highest D_{max} may be obtained, usually for element spacing $d < \lambda/2$, and in the limiting case as $d \rightarrow 0$, $D_{max} \rightarrow N^2$. These, so called super gain-arrays, as is well known, require large element currents distributions, with inter-element phase close to 180 deg yielding low efficiency and extremely narrow frequency bandwidth, and therefore, they are not practical. Over the years, this work has been followed by many papers dealing with the optimization of the performance of arbitrary antenna arrays most of them focusing on end-fire arrays [16]. A notable theorem concerning the maximum realized gain of arbitrary broadside arrays is proven in [17]. The theorem basically states that the maximum gain of a nonuniform conformal array is equal to a sum of the array element gain pattern values in the main beam direction. This is obtained with the following characteristic excitation: complex voltage excitation coefficients are proportional to the complex element (field) pattern values in the main beam direction and a phase factor accounting for the different element propagation paths to a common phase front. The theorem does not apply to end-fire and super-gain arrays.

For convenience, below we re-derive the excitation criteria for maximum gain of the non-uniform, an arbitrary curved-surface arrays originally presented in [17].

C.1 The Theorem

We consider an arbitrary array of N elements as shown in Figure C.1. The array elements are fed by voltage generators V_{gi} , with impedance Z_{gi} , where $i = 1, \dots, N$ denotes the element serial number. The a_i and b_i , in Figure C.1, are the voltages of incident and reflected signals at the array element terminals. The a_i are also called the array excitation coefficients. Each array element is characterized by its element gain pattern $g_i(\theta, \phi)$, where the angles θ, ϕ

define the far field observation direction in spherical coordinates. It is important to mention that g_i represents the element gain pattern of the i th element in a mutually coupled array environment (which can be measured when element i is excited while all other array elements are match-loaded). For simplicity, it is assumed that the array elements are lossless.

The Maximum Gain Theorem for conformal arrays states that the maximum possible gain (for a particular polarization) of a conformal array in the main beam direction (θ_0, ϕ_0) is the sum of individual element gain values in this direction, i.e.,

$$G(\theta_0, \phi_0)_{max} = \sum_{i=1}^N g_i(\theta_0, \phi_0). \quad (C.1)$$

This can be achieved if the magnitudes of the excitation coefficients are proportional to the element gain values in the (θ_0, ϕ_0) direction, i.e.,

$$|a_i| \propto \sqrt{g_i(\theta_0, \phi_0)} \quad (C.2)$$

and the phase of the excitation coefficients is such as to constructively add all element field contributions in the same direction.

C.2 Proof

To prove (C.2), we consider an arbitrary array of N elements as shown in Figure C.1. In this figure, \mathbf{r}_i is the position vector of the i -th element with respect to the origin of the spherical coordinate system (r, θ, ϕ) . In this case the far field due to element i is

$$E_i(r_i, \theta, \phi) = a_i e_i(\theta, \phi) \frac{e^{-jkr_i}}{r_i} \quad (C.3)$$

where a_i are incident complex excitation coefficients

$$a_i = |a_i| e^{j\alpha_i} \quad (C.4)$$

and

$$e_i(\theta, \phi) = |e_i(\theta, \phi)| e^{j\psi_i(\theta, \phi)} \quad (C.5)$$

are the complex element patterns. In general the vector element patterns are different for each element and represent the radiation pattern of a single element in a mutually coupled array environment. Furthermore in (C.3), r_i is the distance between the i -th element and the far-field observation point (r, θ, ϕ) . Consequently, the element gain is

$$g_i(\theta, \phi) = \frac{E_i(r_i, \theta, \phi) E_i^*(r_i, \theta, \phi)}{\zeta_0 P_{0i}} \quad (C.6)$$

where

$$P_{0i} = \frac{|a_i|^2}{4\pi r_i^2} \quad (C.7)$$

and $\zeta_0 = 376.7 \Omega$ is the free space impedance. For simplicity, we assume that $Z_{gi} = 1$, thus in (4b), $|a_i|^2$ represents the total incident (available) power in the i th element. Substituting (3a) into (4a), the element gain becomes

$$g_i(\theta, \phi) = \frac{4\pi}{\zeta_0} |e_i(\theta, \phi)|^2. \quad (C.8)$$

Using (C.3), by superposition, the total array far field is

$$E(\mathbf{r}) = \frac{e^{-jkr}}{r} \sum_{i=1}^N a_i e_i(\theta, \phi) e^{jkr'_i \cdot \hat{\mathbf{r}}} \quad (C.9)$$

where $\hat{\mathbf{r}} = \mathbf{r}/r$ is the unit vector toward the observation point (r, θ, ϕ) . In this expression we have used the approximation $r_i \simeq r$ in the amplitude factor $1/r_i$. Consequently, the array gain is

$$G(\theta, \phi) = \frac{E(\mathbf{r})E^*(\mathbf{r})}{\zeta_0 P_0} \quad (C.10)$$

where

$$P_0 = \frac{\sum_{i=1}^N |a_i|^2}{4\pi r^2}. \quad (C.11)$$

Substituting (C.9) into (C.10), the array gain becomes

$$G(\theta, \phi) = \frac{4\pi}{\zeta_0} \frac{|\sum_{i=1}^N a_i e_i(\theta, \phi) e^{jkr'_i \cdot \mathbf{r}_0}|^2}{\sum_{i=1}^N |a_i|^2}. \quad (C.12)$$

To prove the maximum gain theorem we address the following question: for a given e_i , what a_i 's are required to achieve a maximum array gain in the particular (θ_0, ϕ_0) direction. Thus, we must maximize $G(\theta_0, \phi_0)$ as given by (C.12) with respect to $|a_i|$ and α_i . This is done in two steps.

step 1: For the moment we assume that the $|a_i|$ are known. In this case in view of (C.4) and (C.5) we see that (C.12) is a maximum when

$$kr'_i \cdot \mathbf{r}_0 + \psi_i(\theta_0, \phi_0) + \alpha_i = 0 \quad (C.13)$$

from where

$$\alpha_i = -kr'_i \cdot \mathbf{r}_0 - \psi_i(\theta_0, \phi_0). \quad (C.14)$$

As expected, the first term in (C.14) accounts for the different propagation path lengths while the second term takes into account the different element phase pattern values in the (θ_0, ϕ_0) direction. With such α_i , all array element far-field contributions will add up in phase.

step 2: With α_i of (C.14), relation (C.12) can be written in the following form:

$$G(\theta_0, \phi_0) = \frac{4\pi}{\zeta_0} \frac{|\sum_{i=1}^N |a_i| e_i(\theta_0, \phi_0)|^2}{\sum_{i=1}^N |a_i|^2}. \quad (C.15)$$

In order to determine the $|a_i|$ that gives the maximum $G(\theta_0, \phi_0)$ it is convenient to renormalize $|a_i|$ according to

$$|\hat{a}_i| = \frac{|a_i|}{\sqrt{\sum_{i=1}^N |a_i|^2}}. \quad (\text{C.16})$$

In this case (C.15) becomes

$$G(\theta_0, \phi_0) = \frac{4\pi}{\zeta_0} \left[\sum_{i=1}^N |\hat{a}_i| |e_i(\theta_0, \phi_0)| \right]^2. \quad (\text{C.17})$$

By introducing the excitation vector

$$\hat{\mathbf{a}} = (|\hat{a}_1|, |\hat{a}_2|, \dots, |\hat{a}_N|) \quad (\text{C.18})$$

and the element pattern vector

$$\mathbf{e} = (|e_1(\theta_0, \phi_0)|, |e_2(\theta_0, \phi_0)|, \dots, |e_N(\theta_0, \phi_0)|) \quad (\text{C.19})$$

(C.17) can be further rewritten as the complex scalar product

$$G(\theta_0, \phi_0) = \frac{4\pi}{\zeta_0} [\hat{\mathbf{a}} \cdot \mathbf{e}]^2. \quad (\text{C.20})$$

Using Schwartz's inequality $|\hat{\mathbf{a}} \cdot \mathbf{e}| \leq |\hat{\mathbf{a}}| |\mathbf{e}|$, we see that the excitation vector which yields the maximum gain is determined by $|\hat{\mathbf{a}}| = C |\mathbf{e}|$, where C is the constant to be determined. In component form this can be written as

$$|\hat{a}_i| = C |e_i(\theta_0, \phi_0)| \quad (\text{C.21})$$

where C is the proportionality constant to be determined. Thus,

$$G(\theta_0, \phi_0)_{\max} = C^2 \frac{4\pi}{\zeta_0} \left[\sum_{i=1}^N |e_i(\theta_0, \phi_0)|^2 \right]^2. \quad (\text{C.22})$$

To determine C we write

$$|\hat{a}_i|^2 = C^2 |e_i(\theta_0, \phi_0)|^2 \quad (\text{C.23})$$

from which

$$\sum_{i=1}^N |\hat{a}_i|^2 = C^2 \sum_{i=1}^N |e_i(\theta_0, \phi_0)|^2. \quad (\text{C.24})$$

With the help of (C.16) we find that the left hand side of (C.24) is

$$\sum_{i=1}^N |\hat{a}_i|^2 = \sum_{i=1}^N \left(\frac{|a_i|}{\sqrt{\sum_{j=1}^N |a_j|^2}} \right)^2 = \sum_{i=1}^N \frac{|a_i|^2}{\sum_{j=1}^N |a_j|^2} = 1. \quad (\text{C.25})$$

Substitution of (C.25) into (2.23) yields

$$1 = C^2 \sum_{i=1}^N |e_i(\theta_0, \phi_0)|^2 \quad (\text{C.26})$$

so that

$$C^2 = \frac{1}{\sum_{i=1}^N |e_i(\theta_0, \phi_0)|^2}. \quad (\text{C.27})$$

Therefore, substituting (C.27) into (C.22), the maximum gain is

$$G(\theta_0, \phi_0)_{\max} = \frac{4\pi}{\zeta_0} \sum_{i=1}^N |e_i(\theta_0, \phi_0)|^2 \quad (\text{C.28})$$

or in terms of the element gain pattern as given by (C.8)

$$G(\theta_0, \phi_0)_{\max} = \sum_{i=1}^N g_i(\theta_0, \phi_0). \quad (\text{C.29})$$

As shown, this can be achieved if the amplitudes $|a_i|$ and phases α_i of the complex excitation coefficients a_i satisfy (C.21) and (C.14), respectively. To elaborate on the former we write

$$|\hat{a}_i| = C |e_i(\theta_0, \phi_0)| = \frac{|e_i(\theta_0, \phi_0)|}{\sqrt{\sum_{j=1}^N |e_j(\theta_0, \phi_0)|^2}}. \quad (\text{C.30})$$

For convenience, we normalize (C.30) with respect to the first array element, which yields

$$\frac{|\hat{a}_i|}{|\hat{a}_1|} = \frac{|a_i|}{|a_1|} = \frac{|e_i(\theta_0, \phi_0)|}{|e_1(\theta_0, \phi_0)|} = \sqrt{\frac{g_i(\theta_0, \phi_0)}{g_1(\theta_0, \phi_0)}}. \quad (\text{C.31})$$

Thus, to obtain the maximum gain of the conformal array we have found that the magnitude of the excitation coefficients must be

$$|a_i| = |a_1| \sqrt{\frac{g_i(\theta_0, \phi_0)}{g_1(\theta_0, \phi_0)}} \quad (\text{C.32})$$

Q.E.D.

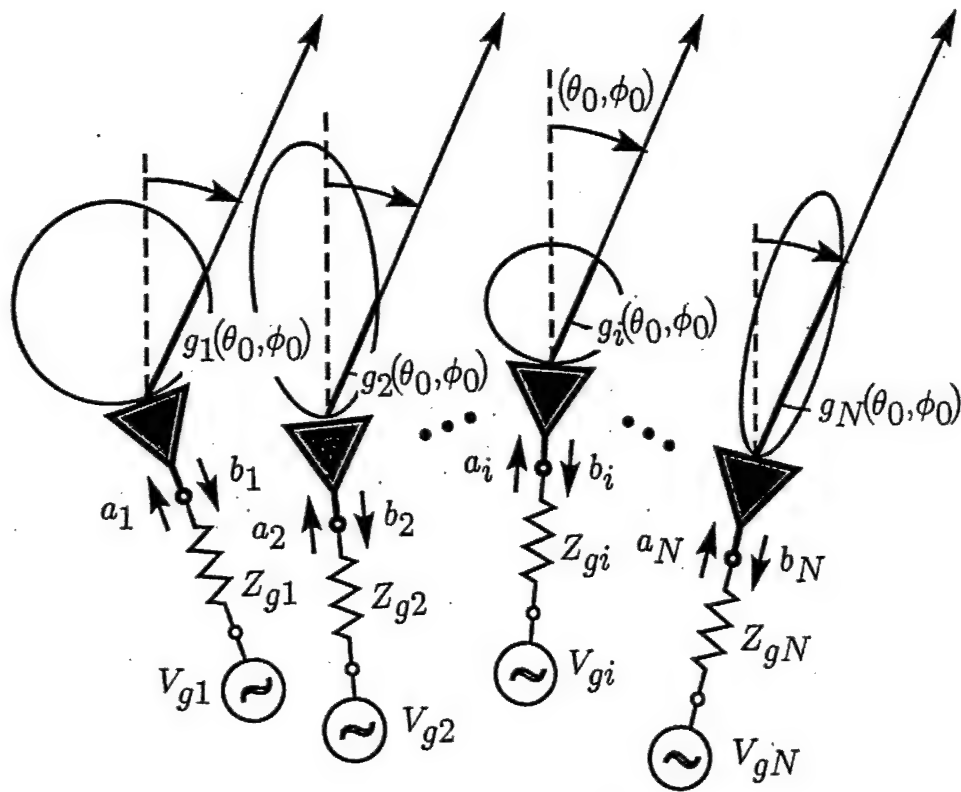


Figure C.1: Finite conformal array

Bibliography

- [1] B. Miller, "Satellite Free Mobile Phone," IEEE Spectrum, March 1998.
- [2] B. Tomasic, "Analysis and Design Trade-Offs of Candidate Phased Array Architectures for AFSCN Application," Presentation to the Second AFSCN Phased Array Antenna Workshop, Hanscom AFB, 31 March - 1 April 1998.
- [3] B. Tomasic, "Analysis and Design Trade-Offs of Candidate Phased Array Antenna Architectures for AFSCN," Report - memo to SMC, May 1998.
- [4] B. Tomasic and S. Liu, "Phased Arrays for Ground Based Satellite Payload and Control Applications," USNC/URSI Radio Science Meeting, Orlando, FL, July 1999.
- [5] D.L. Sengupta, T.M. Smith and R.W. Larson, "Radiation Characteristics of a Spherical Array of Circularly Polarized Elements," IEEE Trans. on Antennas and Prop., Vol. AP-16, No.1, January 1968.
- [6] H.E. Schrank, "Basic Theoretical Aspects of Spherical Phased Arrays," Phased Array Antennas, pp. 323-327, Artech House, Inc., 1972.
- [7] A.K. Chan, "Experimental Investigation on Spherical Arrays," IEEE Trans. on Antennas and Prop., May 1969.
- [8] Buckminster Fuller, R. "The Age of the Dome," Build. Int. July/Aug., 7-15, 1969.
- [9] Z.S. Makowski, "Analysis, Design and Construction of Braced Domes," Nichols Publishing Company, New York, NY 1984.
- [10] H. Kenner, "Geodesic Math and How to Use it," University of California Press, Ltd. Berkeley and Los Angeles, CA 1976.
- [11] W.D. Teter and R.L. Nichols, "A computer Program for Geodesic Dome Geometries," Univ. of Delaware, Newark, DE, 1998.
- [12] R.J. Mailloux, "Phased Array Antenna Handbook," Artech House, Inc., 1993.
- [13] R.C. Hansen, "Phased Array Antennas," John Wiley & Sons, Inc., 1997.
- [14] Conformal Antenna Array - Design Handbook, Naval Air Systems Command, Editor R.C. Hansen, Sept. 1981.

- [15] Uzkov, A.I., "An Approach to the Problem of Optimum Directive Antennae Design," *Comptes Rendus (Doklady) de l'Academie des Sciences de l'URSS*, Vol 53, pp. 35-38, 1946.
- [16] R.E. Collin and F.J. Zucker, "Antenna Theory - Part 1," McGraw-Hill, Inc., 1969.
- [17] A. Hessel and J.C. Sureau, "On the Realized Gain of Arrays," *IEEE Trans. on Antennas and Prop.*, Jan. 1971.
- [18] J. Frank, "Bandwidth Criteria for Phased Array Antennas," *Phased Array Antennas*, Edited by A.A. Oliner and G.H. Knittel, Artech House, Inc., Mass. 1972.
- [19] B. Tomasic, J. Turtle and S. Liu, "A Geodesic Sphere Phased Array Antenna for Satellite Control and Communication," *International Union of Radio Science, XXVIIth General Assembly*, Maastricht, The Netherlands, August 2002.
- [20] B. Tomasic, J. Turtle, S. Liu, R. Schmier, S. Bharj, and P. Oleski, "The Geodesic Dome Phased Array Antenna for Satellite Control and Communication - Subarray Design, Development and Demonstration," *IEEE International Symposium on Phased Array Systems and Technology 2003*. Boston, USA, October 2003., pp. 411-416.
- [21] B. Tomasic, J. Turtle and S. Liu, "The Geodesic sphere phased array antenna for satellite operation and air/space surveillance," *2001 Core Technologies for Space Systems Conference*, Nov. 28-30, 2001, Colorado Springs, CO.
- [22] S. Bharj, A. Merzhevskiy, P. Oleski and B. Tomasic, "Affordable Antenna Array for Multiple Satellite Links," *Proceedings of the 2000 Antenna Applications Symposium*, Allerton Park, Monticello IL, September 2000, pp. 401-414.
- [23] S. Bharj, A. Merzhevskiy, P. Oleski, B. Tomasic, S. Liu, J. Turtle and N. Patel, "Low cost transmit/receive module for space ground link subsystem," *2002 Antenna Application Symposium*, Monticello, IL, Sep. 2002.
- [24] S. Liu, B. Tomasic J. Turtle, D. Mulligan, "Geodesic phased array antenna and demonstration for satellite control," *Colorado Springs, CO, 2002 Core Technologies for Space Systems Conference*, Nov. 2002.
- [25] S. Bharj, P. Oleski B. Tomasic, J. Turtle, S. Liu, N. Patel, A. Merzhevskiy, L. Qu and M. Thaduri, "Multi-beam transmit receive module for USB and SGLS band satellite links," *2003 Antenna Application Symposium*, Monticello, IL, Sep. 2003.
- [26] B. Tomasic, J. Turtle, R. Schmier, S. Bharj, S. Liu and P. Oleski, "Transmit-receive isolation in phased array antennas for duplex communication systems," *17th International Conference on Applied Electromagnetics and Communications*, Dubrovnik, Croatia, Oct. 2003.
- [27] G.H. Knittel, "Choosing the Number of Faces of a Phased-Array Antenna for Hemisphere Scan Coverage," *IEEE Trans. Ant. Propagat.*, Vol. AP-13, No.6, pp.878-882, November 1965.

- [28] J.L. Kmentzo, "An Analytical Approach to the Coverage of a Hemisphere by N Planar Phased Arrays," IEEE Trans. Ant. Propagat., Vol.AP-15, No.3, pp.367-371, May 1967. pp.367-371
- [29] J.J. Stangel and P.A. Valentine, "Phased Array Fed Lens Antenna," US Patent No. 3,755,815, August 28, 1973.
- [30] P.M. Liebman, et al, "Dome Radar- A New Phased Array System," Digest of IEEE International Radar Conference, Washington, D.C., April 1975.
- [31] R. Kinsey, "An Objective Comparison of the Dome Antenna and a Conventional Four-Face Planar Array," Antenna Application Symposium 2000, Allerton, IL, September 2000.
- [32] T.K. Wu, "Phased Array Antenna for Tracking and Communication with LEO Satellites," 1996 IEEE International Symposium on Phased Array Technology, Boston, MA, Oct. 1996.
- [33] V. Jamnejad, J. Huang and R.J. Cesarone, "A study of Phased Array Antennas for NASA's Deep Space Network," Proceedings of the 2001 Antenna Applications Symposium - Vol. II, September 2001.
- [34] D. Loffler and W. Wiesbeck, "Considerations and Restrictions for Conformal Antennas," Proceeding of the "2nd European Workshop on Conformal Antennas", The Hague, The Netherlands, April 2001.
- [35] H. Southal, R. Mailloux and J.P. Turtle, "Coverage analysis of airborne SATCOM phased array antennas," Microwave Journal, September 1995, pp. 132-138.
- [36] P.K.Bondyopadhyay, "Analysis of Rotationall Symmetric Arrays of Apertures on Conducting Spherical Surfaces," IEEE Trans on Antennas and Prop., Vol 40, No 8, Aug. 1992., pp. 857-866.
- [37] Z. Sipus, N. Burun and R. Zentner, "Analysis of Curved Microstrip Antennas," EOARD Technical Report, Contract Number F61775-010WE024, April 2003.
- [38] D.L. Sengupta, J.E. Ferris, R.W. Larson and T.M. Smith, "Azimuth and Elevation Finder Study," Technical Quarterly Report ECOM-01499-1, The University of Michigan Radiation Laboratory, Dept. of El. Eng., Ann, Arbor, Michigan, Dec. 1965.
- [39] D.L. Sengupta, J.E. Ferris, G. Hok, R.W. Larson and T.M. Smith, "Azimuth and Elevation Finder Study," Technical Quarterly Report ECOM-01499-2, The University of Michigan Radiation Laboratory, Dept. of El. Eng., Ann, Arbor, Michigan, March. 1966.
- [40] D.L. Sengupta, J.E. Ferris, G. Hok, R.W. Larson and T.M. Smith, "Azimuth and Elevation Finder Study," Technical Quarterly Report ECOM-01499-3, The University of Michigan Radiation Laboratory, Dept. of El. Eng., Ann, Arbor, Michigan, June 1966.

- [41] D.L. Sengupta, J.E. Ferris, R.W. Larson G. Hok and T.M. Smith, "Azimuth and Elevation Finder Study," Technical Final Report ECOM-01499-4, The University of Michigan Radiation Laboratory, Dept. of El. Eng., Ann, Arbor, Michigan, Sep. 1966.